

MONTE CARLO SIMULATIONS FOR CLASSICAL  
TWO-DIMENSIONAL DIPOLAR ANTIFERROMAGNETIC  
SYSTEMS ON A SQUARE LATTICE

CENTRE FOR NEWFOUNDLAND STUDIES

---

TOTAL OF 10 PAGES ONLY  
MAY BE XEROXED

(Without Author's Permission)

ABDEL-RAHMAN MUSTAFA ABU-LABDEH









Library and  
Archives Canada

Bibliothèque et  
Archives Canada

Published Heritage  
Branch

Direction du  
Patrimoine de l'édition

395 Wellington Street  
Ottawa ON K1A 0N4  
Canada

395, rue Wellington  
Ottawa ON K1A 0N4  
Canada

*Your file* *Votre référence*

*ISBN: 0-612-99577-1*

*Our file* *Notre référence*

*ISBN: 0-612-99577-1*

#### NOTICE:

The author has granted a non-exclusive license allowing Library and Archives Canada to reproduce, publish, archive, preserve, conserve, communicate to the public by telecommunication or on the Internet, loan, distribute and sell theses worldwide, for commercial or non-commercial purposes, in microform, paper, electronic and/or any other formats.

The author retains copyright ownership and moral rights in this thesis. Neither the thesis nor substantial extracts from it may be printed or otherwise reproduced without the author's permission.

#### AVIS:

L'auteur a accordé une licence non exclusive permettant à la Bibliothèque et Archives Canada de reproduire, publier, archiver, sauvegarder, conserver, transmettre au public par télécommunication ou par l'Internet, prêter, distribuer et vendre des thèses partout dans le monde, à des fins commerciales ou autres, sur support microforme, papier, électronique et/ou autres formats.

L'auteur conserve la propriété du droit d'auteur et des droits moraux qui protègent cette thèse. Ni la thèse ni des extraits substantiels de celle-ci ne doivent être imprimés ou autrement reproduits sans son autorisation.

---

In compliance with the Canadian Privacy Act some supporting forms may have been removed from this thesis.

Conformément à la loi canadienne sur la protection de la vie privée, quelques formulaires secondaires ont été enlevés de cette thèse.

While these forms may be included in the document page count, their removal does not represent any loss of content from the thesis.

Bien que ces formulaires aient inclus dans la pagination, il n'y aura aucun contenu manquant.

  
**Canada**



# Monte Carlo Simulations for Classical Two-dimensional Dipolar Antiferromagnetic Systems on a Square Lattice

by

©Abdel-Rahman Mustafa Abu-Labdeh, B.Sc., M.Sc.

A thesis submitted to the School of Graduate  
Studies in conformity with the requirements for the  
Degree of Doctor of Philosophy

Faculty of Science  
Memorial University of Newfoundland  
January 2004

St. John's      Newfoundland and Labrador      Canada

*I dedicate this thesis to my parents, to my wife, to my daughters, to my sisters, and to my brothers.*

## Abstract

In this research, the phase behavior of a lattice-based model for a classical two-dimensional dipolar antiferromagnet on a square lattice is determined using Monte Carlo simulations. Four different systems are investigated, with the magnetic phase diagram for each system being established for both zero and finite temperature. The results are compared to earlier theoretical and experimental results on low-dimensional magnetic systems.

The first model is the Heisenberg system in which the three-dimensional classical spins interact through both nearest-neighbor antiferromagnetic exchange and long-range dipolar interactions. The magnetic phase diagram for this system was determined as a function of both  $T/g$  and  $|J|/g$ , where  $T$  is the temperature in units of  $1/k_B$  such that  $k_B$  is the Boltzmann constant,  $J$  is the strength of the antiferromagnetic exchange interaction, and  $g$  is the strength of the dipolar interaction. At low temperatures, this phase diagram shows a dipolar planar antiferromagnetic phase for low values of  $|J|/g$ , and a simple perpendicular antiferromagnetic phase for large values of  $|J|/g$ . The reorientation transition value of the exchange interaction,  $J_R(T)$ , on the phase boundary separating these two ordered phases, shows only a weak dependence on temperature. The data also indicate that the dipolar planar antiferromagnetic phase separates into two distinct phases in which the orientation of the spins depends on the value of the  $|J|/g$ .

The second model is the plane rotator system in which the two-dimensional classical spin rotors are confined to the plane of the system and interact through both nearest-neighbor antiferromagnetic exchange and long-range dipolar interactions. The phase diagram of this system was constructed as a function of both  $T/g$  and  $|J|/g$ . The results for the plane rotator system are compared to the results obtained for the Heisenberg system. This comparison clarifies the role played by the

out-of-plane degree of freedom of spins in determining the structure of the dipolar planar antiferromagnetic phase.

The third model is the anisotropic Heisenberg system with fixed  $\kappa$  (where  $\kappa$  is the strength of the planar magnetic surface anisotropy). In this system, the three-dimensional classical spins interact through nearest-neighbor antiferromagnetic exchange and long-range dipolar interactions, as well as by a weak planar magnetic surface anisotropy (i.e.,  $\kappa = -1.0g$ ). Again, the magnetic phase diagram for this system was determined as a function of both  $T/g$  and  $|J|/g$ . This phase diagram shows similar behavior to that of the Heisenberg system, except that there exists a range of  $|J|/g$  in which the system exhibits a reorientation transition from the dipolar planar antiferromagnetic phase to the simple perpendicular antiferromagnetic phase with increasing temperature.

Finally, the fourth model is the anisotropic Heisenberg system with fixed  $J$ . In this system, the three-dimensional classical spins interact through a short-range antiferromagnetic exchange interaction, a planar magnetic surface anisotropy and a long-range dipolar interaction. The simulations focus on the exchange-dominated regime in which the strength of the exchange interaction is significantly greater than both the dipolar interaction and the magnetic surface anisotropy. The magnetic phase diagram for this system was then established as a function of both  $T/g$  and  $|\kappa|/g$ , for a fixed value of the exchange constant (i.e.,  $J = -10.0g$ ). This phase diagram shows that there exists a range of the  $|\kappa|/g$  in which the system exhibits a reorientation transition from the simple planar antiferromagnetic phase to the simple perpendicular antiferromagnetic phase with increasing temperature. Finally, some implications of these findings are presented.

# Acknowledgements

I would like to take this opportunity to express my sincere gratitude to all the individuals who supported this work.

I wish to express my sincere thanks to my parents (Mustafa and Aqleh) for their encouragement, understanding, and forbearance. They deserve my deep admiration and love. I extend my heart-felt thanks to my wife (Manal) and to my daughters (Razan, Ahlam, and Ruhuf) for their strength, patience, and support. I also extend my thanks to my sisters and brothers for their encouragement and help.

I thank Dr. John Whitehead (my supervisor) for his suggestions, contributions, and help in this research project. I would also like to thank the members of my supervisory committee (Drs. Mark Whitmore and Guy Quirion) and the members of my examiner committee (Drs. Michael Cottam, Kristin Poduska, and John Lewis) for their suggestions and comments. I extend my thanks to Drs. Keith De'Bell and Allen MacIsaac for their cooperation. I extend my thanks for the technical support provided by Fred Perry, Chris Stevenson, and Darryl Reid in the Physics Department. I also extend my thanks to Paul Chaif (summer student) for his computational work on the free energy of the planar system. Also, I would like to thank Lester Marshal (learning specialist at Memorial University) for his feedback on the writing style.

I also wish to acknowledge access to computing systems provided through C3.ca at Memorial University of Newfoundland, University of Calgary and University of Alberta.

I would like to acknowledge the financial assistance provided by the School of Graduate Studies, Department of Physics, and Dr. John Whitehead's NSERC research grant in the form of graduate fellowships and teaching assistantships.

Finally, I would like to thank all of my friends who helped me in different ways.

# Contents

<b>Abstract</b>	<b>i</b>
<b>Acknowledgements</b>	<b>iii</b>
<b>Contents</b>	<b>iv</b>
<b>List of Figures</b>	<b>vi</b>
<b>List of Tables</b>	<b>xv</b>
<b>1 Introduction</b>	<b>1</b>
<b>2 The Model in General Terms</b>	<b>19</b>
2.1 The Energy of the General Model . . . . .	19
2.2 The Dipole-dipole Interaction and Ewald Summation Technique . . .	27
2.3 Systems of Interest . . . . .	31
<b>3 Monte Carlo Methods</b>	<b>33</b>
3.1 Importance Sampling and the Metropolis Algorithm . . . . .	34
3.2 Boundary Conditions and Long-range Dipolar Interactions . . . . .	39
3.3 Computational Aspects . . . . .	49
3.4 Benchmarks . . . . .	55
<b>4 The Heisenberg System</b>	<b>59</b>
4.1 Introduction . . . . .	59
4.2 Ground State Properties . . . . .	60
4.3 Finite Temperature Properties . . . . .	66
4.4 The Phase Diagram . . . . .	83
4.5 Low Temperature Order Parameter . . . . .	88
4.6 Discussion . . . . .	93

4.7	Summary . . . . .	97
<b>5</b>	<b>The Plane Rotator System</b>	<b>99</b>
5.1	Introduction . . . . .	99
5.2	Ground state properties . . . . .	101
5.3	The phase diagram . . . . .	103
5.4	Free energy . . . . .	113
5.5	Summary . . . . .	114
<b>6</b>	<b>The Anisotropic Heisenberg System: Fixed <math>\kappa</math></b>	<b>117</b>
6.1	Introduction . . . . .	117
6.2	The Ground State . . . . .	119
6.3	Finite Temperature Properties . . . . .	120
6.4	The Phase Diagram . . . . .	129
6.5	The Low Temperature Order Parameter . . . . .	132
6.6	Summary . . . . .	134
<b>7</b>	<b>The Anisotropic Heisenberg System: Fixed <math>J</math></b>	<b>138</b>
7.1	Introduction . . . . .	138
7.2	Magnetic Properties . . . . .	139
7.3	The Phase Diagram . . . . .	152
7.4	The Temperature Dependence of the Order Parameters in the Limit $T \rightarrow 0$ . . . . .	156
7.5	Summary . . . . .	159
<b>8</b>	<b>Conclusions and Future Research Directions</b>	<b>161</b>
8.1	Summary of Results . . . . .	164
8.2	Future Research Directions . . . . .	168
<b>A</b>	<b>Free Energy</b>	<b>170</b>
<b>B</b>	<b>Slope of the Coexistence Line</b>	<b>183</b>
B.1	Slope of the Coexistence Line: $J_R(T)$ . . . . .	183
B.2	Slope of the Coexistence Line: $\kappa_R(T)$ . . . . .	185
	<b>Bibliography</b>	<b>188</b>

# List of Figures

2.1	Schematic diagram of a direct exchange (a), an indirect exchange (b), and a superexchange interaction (c). In this Figure, M=magnetic ion, N=non-magnetic ion, and CE=conduction electrons. . . . .	21
2.2	The magnetic field for an isolated magnetic dipole moment located at the origin. . . . .	23
3.1	An infinite plane from replicas of a finite system (indicated by dark lines). All interactions between spins outside the finite system are included in an effective interaction between spins within the dark unit cell. In this Figure, $x$ and $y$ denote the the two in-plane directions of the square lattice, $\vec{r}$ is to the position of the $i^{th}$ lattice site within the finite system, $\vec{G}$ is the translation lattice distance, and $\vec{R}$ is the to the position of the equivalent $i^{th}$ lattice site in one of the replicas of a finite system. . . . .	41
3.2	A uniform distribution of the randomly selected orientations of the target spins along the arc of a ring with radius 1. . . . .	46
3.3	The spherical coordinates ( $ \vec{\sigma}_i $ , $\theta$ , and $\phi$ ) for the target spin, $\vec{\sigma}_i$ . . . .	47
3.4	A uniform distribution of the randomly selected orientations of the target spins over the surface of a sphere with radius 1. . . . .	48

3.5	Average internal energy, $\langle E/g \rangle$ , per spin as a function of time, $MCS/site$ , for the Heisenberg model with $J = -10.0g$ , $\kappa = -1.5g$ , and $L = 64$ at four different values of temperature, $T = 0.05g, 0.1g, 0.15g, 0.2g$ , from the start of the simulation. The final spin configuration at any of these fixed temperatures is considered as an initial state or the next nearest temperature. . . . .	52
3.6	A comparison between the obtained (o) heat capacity, $C_v$ , per spin as a function of temperature, $T/g$ , and the results (★) obtained by Rastelli <i>et al.</i> for the pure dipolar plane rotator system on a two-dimensional square lattice with $L = 32$ . . . . .	56
3.7	A comparison between the obtained (o) perpendicular order parameter, $M_{\perp}$ , per spin as a function of temperature, $T/g$ , and the results (★) found by Gouvêa <i>et al.</i> for the Heisenberg system on a two-dimensional square lattice with $L = 64$ , $g = 0$ , and where $J^x = J^y = \frac{1}{1.05}J^z$ . . . . .	57
4.1	Two planar ground state spin configurations. In one (a) the spins are aligned along the x-axis in the other (b) they are oriented at $\pm\pi/4$ to the x-axis. . . . .	61
4.2	A schematic of the magnetic unit cell used to describe the magnetic order showing the four magnetic sub-lattices and labels attached to them. In this Figure, $x$ and $y$ denote the two in-plane directions of the square lattice. The energy of the spin configuration is independent of the angle $\phi$ shown in the Figure. . . . .	62
4.3	The perpendicular ground state spin configuration in the case of the large value of $ J /g$ , where $x$ and $y$ denote the two in-plane directions of the square lattice. . . . .	64
4.4	A plot of the parallel and perpendicular order parameters, $M_{AF_{\parallel}}$ and $M_{AA_{\perp}}$ , per spin as a function of temperature, $T/g$ , for (a) $ J  = 0.4g$ and (b) $ J  = 1.0g$ with $L = 32$ and $104$ . . . . .	68

4.5	A plot of the parallel and perpendicular susceptibilities, $\chi_{AF_{\parallel}}$ and $\chi_{AA_{\perp}}$ , per spin as a function of temperature, $T/g$ , for (a) $ J  = 0.4g$ and (b) $ J  = 1.0g$ with $L = 32$ and $104$ . . . . .	69
4.6	A plot of the average internal energy, $\langle E/g \rangle$ , per spin as a function of temperature, $T/g$ , for (a) $ J  = 0.4g$ and (b) $ J  = 1.0g$ with $L = 32$ and $104$ . . . . .	70
4.7	A plot of the heat capacity, $C_v$ , per spin as a function of temperature, $T/g$ , for (a) $ J  = 0.4g$ and (b) $ J  = 1.0g$ with $L = 32$ and $104$ . . . . .	71
4.8	Snapshots of two typical spin configurations at $T = 0.15g$ for (a) $ J  = 0.4g$ and (b) $ J  = 1.0g$ with $L = 104$ . . . . .	73
4.9	A plot of the angle $\phi_{\alpha}$ , for each of the sub-lattice magnetization as a function of temperature, $T/g$ , for (a) $ J  = 0.4g$ and (b) $ J  = 1.0g$ with $L = 104$ . . . . .	74
4.10	A plot of the perpendicular and parallel order parameters, $M_{AA_{\perp}}$ and $M_{AF_{\parallel}}$ , per spin as a function of temperature, $T/g$ , for $ J  = 2.0g$ with $L = 32$ and $104$ . . . . .	75
4.11	A plot of the heat capacity, $C_v$ , per spin as a function of temperature, $T/g$ , for $ J  = 2.0g$ with $L = 32$ and $104$ . . . . .	77
4.12	A plot of the perpendicular and parallel susceptibilities, $\chi_{AA_{\perp}}$ and $\chi_{AF_{\parallel}}$ , per spin as a function of temperature, $T/g$ , for $ J  = 2.0g$ with $L = 32$ and $104$ . . . . .	78
4.13	A plot of the average internal energy, $\langle E/g \rangle$ , per spin as a function of temperature, $T/g$ , for $ J  = 2.0g$ with $L = 32$ and $104$ . . . . .	79
4.14	A plot of the parallel and perpendicular order parameters, $M_{AA_{\perp}}$ and $M_{AF_{\parallel}}$ , per spin as a function of the exchange constant, $J/g$ , for $T = 0.4g$ with $L = 104$ . . . . .	80
4.15	A plot of the average internal energy, $\langle E/g \rangle$ , per spin as a function of the exchange constant, $J/g$ , for $T = 0.4g$ with $L = 104$ . . . . .	81

4.16	A plot of the exchange energy, $\langle E_{ex}/g \rangle$ , and the dipolar energy, $\langle E_{dd}/g \rangle$ , energies per spin as a function of the exchange constant, $J/g$ , for $T = 0.4g$ with $L = 104$ . . . . .	82
4.17	A plot of the perpendicular (a) and the parallel (b) susceptibilities, $\chi_{AA_{\perp}}$ and $\chi_{AF_{\parallel}}$ , per spin as a function of the exchange constant, $J/g$ , for $T = 0.4g$ with $L = 104$ . Both the perpendicular and parallel susceptibilities exhibit peaks at the in-plane to out-of-plane transition. The parallel susceptibility exhibits a second peak corresponding to the in-plane reorientation transition. . . . .	84
4.18	The magnetic phase diagram, based on the Monte Carlo simulations, for the dipolar antiferromagnetic Heisenberg system with $\kappa = 0$ as a function of increasing and decreasing both $ J /g$ and $T/g$ for $N = L \times L = 32^2, 64^2, 104^2$ . Region I is the dipolar planar antiferromagnetic phase ( $AF_{\parallel}$ phase), Region II is the simple perpendicular antiferromagnetic phase ( $AA_{\perp}$ phase), and Region III is the paramagnetic phase (disordered phase). The two solid lines highlight the two lines of second-ordered transitions from the paramagnetic phase to the two ordered phases. The dashed line highlight the line of first-ordered reorientation transition from one order state to the other ( $AF_{\parallel}$ , $AA_{\perp}$ ). The dotted line separates the two planar phases ( $AF_{\parallel}1$ , $AF_{\parallel}2$ ). . . . .	85
4.19	A plot of $ J /T_N$ as a function of $\ln( J /g)$ for $ J  > J_0$ with $L = 104$ . . . . .	87
4.20	A plot of the perpendicular order parameter, $M_{AA_{\perp}}$ , per spin as a function of the the temperature, $T/g$ , for several values of $ J  > J_0$ with $L = 104$ . . . . .	89
4.21	A plot of the low temperature slope, $ dM_{AA_{\perp}}/dT $ , as a function of the exchange interaction, $ J /g$ , for $ J  > J_0$ with $L = 104$ . . . . .	91
4.22	A plot of the ratio $g(1 - M_{AF_{\parallel}})/T$ as a function of the the temperature, $T/g$ , for $ J  < J_0$ with $L = 104$ . . . . .	92

5.1	The planar antiferromagnetic ( $AA_{\parallel}$ ) ground state spin configuration, where $x$ and $y$ denote the two in-plane directions of the square lattice.	102
5.2	The magnetic phase diagram, based on the Monte Carlo simulations, for the dipolar antiferromagnetic plane rotator system as a function of increasing and decreasing both $ J /g$ and $T/g$ for $N = L \times L = 32^2, 64^2, 104^2$ . Region I is the dipolar planar antiferromagnetic phase ( $AF_{\parallel}$ phase), Region II is the simple parallel antiferromagnetic phase ( $AA_{\parallel}$ phase), and Region III is the paramagnetic phase (disordered phase). The two solid lines highlight the two lines of second-ordered transitions from the paramagnetic phase to the two ordered phases. The dashed line highlight the line of first-ordered reorientation transition from one order state to the other ( $AF_{\parallel 1}$ , $AF_{\parallel 2}$ ). The two dotted lines separate the two planar phases ( $AF_{\parallel 1}$ , $AF_{\parallel 2}$ ).	104
5.3	The two order parameters, $M_{AF_{\parallel}}$ and $M_{AA_{\parallel}}$ , per spin as a function of $J/g$ for $T = 0.4g$ with $L = 104$ . The transition region is shown in the inset and displays the hysteresis characteristic of a first-order transition.	105
5.4	The two order parameters, $M_{AF_{\parallel}}$ and $M_{AA_{\parallel}}$ , per spin as a function of $T/g$ for (a) $ J  = 0.2g$ , (b) $ J  = 1.5g$ , (c) $ J  = 2.7g$ , and (d) $ J  = 5.0g$ with $L = 104$ .	107
5.5	The heat capacity, $C_v$ , per spin as a function of $T/g$ for (a) $ J  = 0.2g$ , (b) $ J  = 1.5g$ , (c) $ J  = 2.7g$ and, (d) $ J  = 5.0g$ with $L = 104$ .	108
5.6	A plot of the angle $\phi_{\alpha}$ , for each of the four sub-lattice magnetisations as a function of temperature, $T/g$ , for (a) $ J  = 0.2g$ , (b) $ J  = 1.5g$ , and (c) $ J  = 2.7g$ with $L = 104$ .	109
5.7	Snapshots of three typical spin configurations at $T = 0.15g$ for (a) $ J  = 0.2g$ , (b) $ J  = 1.5g$ , and (c) $ J  = 2.7g$ with $L = 104$ .	110
5.8	The conjugate field, $P$ , per spin as a function of temperature, $T/g$ , for several values of $ J /g$ with $L = 104$ .	112

5.9	The free energy as a function of the exchange constant, $ J /g$ , for $T = 0.2g$ with $L = 64$ . (The solid lines shown in the figure are simply a guide to the eye.) . . . . .	115
6.1	The two order parameters, $M_{AF_{\parallel}}$ and $M_{AA_{\perp}}$ , per spin as a function of the temperature $T/g$ for (a) $ J  = 0.2g$ , (b) $ J  = 1.2g$ , (c) $ J  = 1.7g$ , and (d) $ J  = 2.5g$ with $L = 104$ . . . . .	121
6.2	A plot of the (a) two order parameters, $M_{AA_{\perp}}$ and $M_{AF_{\parallel}}$ , and (b) the total average internal energy, $\langle E/g \rangle$ , per spin as a function of temperature, $T/g$ , for $ J  = 1.7g$ with $L = 104$ . . . . .	123
6.3	A plot of the (a) parallel and (b) the perpendicular susceptibilities, $\chi_{AA_{\perp}}$ and $\chi_{AF_{\parallel}}$ , per spin as a function of temperature, $T/g$ , for $ J  = 1.7g$ with $L = 104$ . . . . .	124
6.4	The heat capacity, $C_v$ , per spin as a function of temperature, $T/g$ , for (a) $ J  = 0.2g$ , (b) $ J  = 1.2g$ , (c) $ J  = 1.7g$ and (d) $ J  = 2.5g$ with $L = 104$ . . . . .	126
6.5	Snapshots of two typical spin configurations at $T = 0.15g$ for (a) $ J  = 0.2g$ and (b) $ J  = 1.2g$ with $L = 104$ . . . . .	127
6.6	The angle $\phi_{\alpha}$ , for each of the four sub-lattice magnetisations as a function of temperature, $T/g$ , for (a) $ J  = 0.2g$ , and (b) $ J  = 1.2g$ with $L = 104$ . . . . .	128

6.7	The magnetic phase diagram, based on the Monte Carlo simulations, for the dipolar antiferromagnetic Heisenberg system with $\kappa = -1.0g$ as a function of increasing and decreasing both $ J /g$ and $T/g$ for $N = L \times L = 32^2, 64^2, 104^2$ . Region I is the dipolar planar antiferromagnetic phase ( $AF_{\parallel}$ phase), Region II is the simple perpendicular antiferromagnetic phase ( $AA_{\perp}$ phase), and Region III is the paramagnetic phase (disordered phase). The two solid lines highlight the two lines of second-order transitions from the paramagnetic phase to the two ordered phases. The dashed line highlights the line of first-order reorientation transitions from one ordered state to the other ( $AF_{\parallel}, AA_{\perp}$ ). The dotted line separates the two planar phases ( $AF_{\parallel 1}, AF_{\parallel 2}$ ). . . . .	130
6.8	A schematic phase diagrams for (a) $\kappa = 0$ and (b) $\kappa = -1.0g$ as a function of both $ J /g$ and $T/g$ . Region I is the dipolar planar antiferromagnetic ordered phase ( $AF_{\parallel}$ ), Region II is the simple out-of-plane antiferromagnetic ordered phase ( $AA_{\perp}$ ), and Region III is the paramagnetic phase (disordered phase). . . . .	131
6.9	A plot of the perpendicular order parameter, $M_{AA_{\perp}}$ , per spin as a function of the temperature, $T/g$ , for several values of $ J  > J_0$ with $L = 104$ . . . . .	133
6.10	A plot of the low temperature slope, $ dM_{AA_{\perp}}/dT $ , as a function of the the exchange interaction $ J /g$ , for $ J  > J_0$ with $L = 104$ . . . . .	135
6.11	A plot of the ratio $g(1 - M_{AF_{\parallel}})/T$ as a function of the temperature, $T/g$ , for $ J  < J_0$ with $L = 104$ . . . . .	136
7.1	A plot of the two order parameters, $M_{AA_{\perp}}$ and $M_{AA_{\parallel}}$ , per spin as a function of temperature, $T/g$ , for (a) $ \kappa  = 1.5g$ and (b) $ \kappa  = 7.0g$ with $L = 104$ . . . . .	143
7.2	A plot of the heat capacity, $C_v$ , per spin as a function of temperature, $T/g$ , for (a) $ \kappa  = 1.5g$ and (b) $ \kappa  = 7.0g$ with $L = 104$ . . . . .	144

7.3	A plot of the two order parameters, $M_{AA_{\perp}}$ and $M_{AA_{\parallel}}$ , per spin as a function temperature, $T/g$ , for $ \kappa  = 4.1g$ with $L = 104$ . . . . .	146
7.4	A plot of (a) the two order parameters, $M_{AA_{\perp}}$ and $M_{AA_{\parallel}}$ , and (b) the total average internal energy, $\langle E/g \rangle$ , per spin as a function of both increasing and decreasing temperature for $ \kappa  = 4.1g$ with $L = 104$ . . . . .	147
7.5	A plot of the heat capacity, $C_v$ , per spin as a function temperature, $T/g$ , for $ \kappa  = 4.1g$ with $L = 104$ . . . . .	148
7.6	A plot of (a) the parallel susceptibility, $\chi_{AA_{\parallel}}$ , and (b) the perpendicular susceptibility, $\chi_{AA_{\perp}}$ , per spin as a function temperature, $T/g$ , for $ \kappa  = 4.1g$ with $L = 104$ . . . . .	150
7.7	A plot of the two conjugate fields, $P_{xy}$ and $P_z$ , per spin as a function of temperature, $T/g$ , for $ \kappa  = 4.1g$ with $L = 104$ . . . . .	151
7.8	The magnetic phase diagram, based on the Monte Carlo simulations, for the dipolar antiferromagnetic Heisenberg system with $\kappa \leq 0$ for $J = -10.0g$ as a function of $ \kappa /g$ and $T/g$ for $N = L \times L = 32^2, 64^2, 104^2$ . Region I is the simple perpendicular antiferromagnetic phase ( $AA_{\perp}$ phase), Region II is the simple parallel antiferromagnetic phase ( $AA_{\parallel}$ phase), and Region III is the paramagnetic phase (disordered phase). The two solid lines highlight the two lines of second-ordered transitions from the paramagnetic phase to the two ordered phases. The dashed line highlight the line of first-ordered reorientation transition from one order state to the other ( $AA_{\perp}, AA_{\parallel}$ ). . . . .	153
7.9	A plot of (a) the average internal energy, $\langle E/g \rangle$ , and (b) the average magnetic surface anisotropy energy, $\langle E_{\kappa/g} \rangle$ , per spin for $ \kappa  = 4.2g$ as a function of temperature, $T/g$ , with $L = 104$ . . . . .	155
7.10	A plot of (a) the perpendicular order parameter, $M_{AA_{\perp}}$ , per spin for several values of $ \kappa  < \kappa_0$ and (b) the planar order parameter, $M_{AA_{\parallel}}$ , per spin for several values of $ \kappa  > \kappa_0$ as a function of temperature, $T/g$ , with $L = 104$ . . . . .	157

7.11	A plot of the low temperature slope, $ dM_{AA_{\perp}}/dT $ , and the low temperature slope, $ dM_{AA_{\parallel}}/dT $ , as a function of the anisotropy constant, $ \kappa /g$ , with $L = 104$ . . . . .	158
A.1	The change in the free energy as a function of the exchange constant over the range where $0 <  J  < 0.7g$ , for several values of $J_o/g$ at $T = 0.2g$ with $L = 64$ . . . . .	173
A.2	The change in the free energy for the points selected from the curves shown in Figure A.1 at $T = 0.2g$ with $L = 64$ , where lower case letters denote these selected points. . . . .	174
A.3	The change in the free energy for the points selected from the curves shown in Figure A.1 after the combination of the points selected for the curve where $J_o = 0.0$ with the points selected from the curve where $J_o = -0.2g$ at $T = 0.2g$ with $L = 64$ . . . . .	176
A.4	The change in the free energy for the points selected from the curves shown in Figure A.1 after the combination of the new points selected from the curve where $J_o = -0.2g$ with the points selected from the curve where $J_o = -0.4g$ at $T = 0.2g$ with $L = 64$ . . . . .	177
A.5	The corrected free energy as a function of the exchange constant over the range $0 <  J  < 0.7g$ , for several values of $J_o/g$ at $T = 0.2g$ with $L = 64$ . . . . .	178
A.6	The corrected free energy as a function of the exchange constant over the range $0.7g <  J  < 2.1g$ , for several values of $J_o/g$ at $T = 0.2g$ with $L = 64$ . . . . .	179
A.7	The corrected free energy as a function of the exchange constant over the range $2.1 <  J /g < 3.2$ , for several values of $J_o/g$ at $T = 0.2g$ . . .	180
A.8	The free energy with respect to a common value, $F_o$ , as a function of the exchange constant at $T = 0.2g$ . (The solid lines shown in the figure are simply a guide to the eye.) . . . . .	181

# List of Tables

2.1	The dipolar energy calculated for a number of important antiferromagnetic spin configurations on a two-dimensional square lattice. The subscripts $x$ and $y$ denote the square lattice axes, $z$ denotes the axis perpendicular to lattice, and $(n_x, n_y)$ denotes the coordinates of the spin variable on the lattice. . . . .	30
-----	--	----

# Chapter 1

## Introduction

Magnetism results from the effects of both the spin and orbital degrees of freedom of the electron, and is influenced by the structure, composition and dimensionality of the system. Magnetism has been investigated in both bulk and reduced-dimensional materials. While extensive research has been carried out on bulk magnetic materials, in recent decades reduced-dimensional spin systems have received much greater attention among researchers due to their magnetic properties, which are distinctively different from those of their bulk counterparts. This has recently led to significant advances in technological applications such as magnetic sensors, recording, and storage media [1, 2].

One important class of the reduced-dimensional magnetic systems is quasi-two-dimensional materials. These materials show a wide range of ordering effects and related pattern-formation phenomena which potentially have a number of interesting technological applications. A number of experimental and theoretical studies have reported on the interesting and unusual magnetic properties of these quasi-two-dimensional systems [3]. These studies have been motivated both by the technological

importance of these systems and by the insight that they can provide into the fundamental role of interactions at the atomic level in determining macroscopic properties.

Three important magnetic systems can be considered to be quasi-two-dimensional. The first are ultra thin magnetic films. The field of ultra thin magnetic films continues to be an exciting and rapidly expanding one, from both technical and fundamental viewpoints. Ultra thin magnetic films consist of several mono-layers (i.e., a few atomic layers) of magnetic atoms deposited on a non-magnetic substrate [4, 5]. In many cases the magnetic spins of such films are observed to be magnetically ordered at low temperatures, and show a variety of interesting ordered phases. One important phenomenon found to occur in the ferromagnetic thin films is a reorientation transition (switching transition) in which the magnetization switches from out-of-plane to in-plane or vice versa. Using both spin scanning electron microscopy with polarization analysis and the surface magneto-optic Kerr effect, experimental studies conclude that these films exhibit a reorientation transition either above a critical temperature,  $T_R$ , at constant film thickness [6, 7, 8, 9], or above critical film thickness,  $d_R$ , at constant temperature [6, 7, 8, 10, 11, 12]. Moreover, it was found that the  $T_R$  decreases with the increasing film thickness. These experimental results indicate that the region between the two ordered states consists of domains where the magnetic moments are arranged such that the net magnetization of the system is essentially zero. While the transition from out-of-plane to in-plane is typical of most ferromagnetic films, the opposite sequence has also been observed, as in Ni on Cu(001) substrate and Gd on W(110) substrate [13, 14, 15]. Experimentally, it is believed that the ferromagnetic ultrathin films have a dominant ferromagnetic exchange interaction, a strong magnetic surface anisotropy, and a weak dipolar interaction.

In recent years, ultra thin ferromagnetic films have become an interesting area of research for several reasons. First, advances in film growth techniques such as atomic or molecular beam epitaxy have made ultra thin ferromagnetic films easier to fabricate [10, 16]. Second, enhancements in characterization methods, such as the surface magneto-optic Kerr effect, have made it easier to investigate the magnetic properties of ultra thin ferromagnetic films [8, 9, 17]. Third, researchers are able to construct high quality ultra thin ferromagnetic films for study and are able to characterize their magnetic properties [6, 18]. Fourth, ferromagnetic thin films have considerable technological interest because of their wide range of applications in electronics, data storage, processing, recording media, catalysis, and in biotechnology and pharmacology [19, 20, 21]. Moreover, the rich variety of spatially modulated phases which can be found in the thin magnetic films also makes them ideal systems for the study of pattern formation [22, 23, 24] and self-organized behavior [25].

A particularly important and scientifically challenging area of research in the context of the current work involve antiferromagnetic thin films, which are used in exchange bias (spin valve) applications [1, 2, 26, 27, 28, 29, 30]. Exchange bias is used to magnetically pin a ferromagnetic layer to an adjacent antiferromagnet, thereby acting as a reference layer in a magnetic device that is important in the magnetic storage industry. In addition, applications for spin-valve structures are expanding. Important applications include magnetic field sensors [31], read heads for hard drives, galvanic isolators, and magnetoresistive random access memory [1].

Despite the technological importance of the spin valve, the study of antiferromagnetic surfaces and interfaces has posed a significant challenge due to the inability of

conventional methods such as optical, x-ray, and neutron techniques to spatially determine the microscopic magnetic structure of the antiferromagnetic thin films [32]. Although the antiferromagnetic domain structure in bulk single crystals has been studied since the late 1950s [33, 34], little is known about the domain structure in thin films. Recently, this limitation has been partially overcome by the use of x-ray magnetic linear dichroism (XMLD) spectroscopy [35, 36, 37, 38]. In view of this, antiferromagnetic thin films remain an experimental and theoretical challenge.

The second important class of quasi-two-dimensional system consists of layered magnetic compounds such as the rare earth (RE) ions in the family of compounds,  $\text{REBa}_2\text{Cu}_3\text{O}_{7-\delta}$  ( $0 \lesssim \delta \lesssim 1$ ). Following the discovery of high-temperature superconductivity (i.e., with critical temperature  $80 \text{ K} < T_c < 90 \text{ K}$ ) in the perovskite structure,  $\text{YBa}_2\text{Cu}_3\text{O}_{7-\delta}$  [39], it was found that the  $\text{Y}^{3+}$  ions could be fully replaced by most of the RE ions (typically from the lanthanide series) without significantly affecting  $T_c$  or the superconducting behavior of the parent compound [40, 41, 42, 43, 44, 45, 46, 47, 48].

The interest in these rare earth compounds arises because nearly all rare earth ions in such compounds show antiferromagnetic ordering at low temperatures (typically  $\lesssim 2 \text{ K}$ ), and this ordered state coexists with the superconducting state. This observation indicates that these rare earth compounds are strong candidates for investigating the interplay between magnetism and superconductivity. For this reason the detailed studies of magnetic effects in these materials are of considerable importance.

For rare earth compounds, the perovskite structure consists of the  $ab$  planes of RE ions each of which lie between two double copper oxide layers. In these compounds there is one rare earth ion per chemical unit cell, and the  $c$ -axis is approximately three

times as long as the  $a$  and  $b$ -axes. This suggests that these rare earth compounds are quasi-two-dimensional magnetic systems [49, 50]. For example, the observation of two-dimensional antiferromagnetic ordering on  $\text{ErBa}_2\text{Cu}_3\text{O}_7$  with Néel temperature,  $T_N \approx 0.5$  K, has been confirmed experimentally using the neutron-scattering technique [51, 52, 53, 54, 55, 56]. In this case the magnetic spins are observed to be ordered within the  $ab$ -plane, in which they are aligned ferromagnetically in the  $b$  direction and antiferromagnetically in the  $a$  direction (denoted as the dipolar planar antiferromagnetic phase). Neutron-scattering experiments also show clear evidence of two-dimensional antiferromagnetic ordering on  $\text{DyBa}_2\text{Cu}_3\text{O}_7$  at  $T_N \approx 0.95$  K [57], and on  $\text{GdBa}_2\text{Cu}_3\text{O}_7$  at  $T_N \approx 2.2$  K [58, 59, 60, 61]. Unlike the Er compounds, the spins of these two compounds are aligned along the  $c$ -axis, in which they are ordered antiferromagnetically in both the  $a$  and  $b$  directions (denoted as the simple perpendicular antiferromagnetic phase).

The third important class of quasi-two-dimensional system consists of arrays of magnetic wires with diameters of only a few micro [62, 63] or nanometers [64, 65, 66, 67]. While the arrays of nanowires are of particular value in the design and optimization of magnetoresistive heads for ultra high-density data storage applications [62], arrays of glass-coated microwires are potential candidates for many sensor applications [68, 69, 70].

The magnetostatic interactions among these micro or nanowires can play a fundamental role in the magnetization reversal process and domain structures of the individual elements, which consequently influence the macroscopic magnetic response of the system. In particular, it was found that the dipolar interaction between such wires has a similar effect on its magnetic properties as do classical spins interacting

through long-range interactions [71]. Therefore, the interactions among these wires can be best described by a two-dimensional model. This makes it possible to test micromagnetic predictions and verify the best conditions for optimizing the macroscopic magnetic behavior of specific applications.

As in thin magnetic films, a reorientation transition has been predicted and observed in micro or nanomagnetic dot array systems [72]. For example, in arrays of small (micro or nanometers) magnetic dots, a reorientation transition from perpendicular to in-plane has been shown to occur for dots with perpendicular anisotropy [73] as temperature is decreased using a self-consistent mean-field calculation of the field and a temperature-dependent magnetization process.

The development of the quasi-two-dimensional systems for specific applications, requires a detailed understanding of their microscopic interactions and of the influences of such factors as composition and preparation of these interactions. These, in turn, determine the macroscopic properties of the material. For example, variations in the non-magnetic overlayers of the magnetic film can be used for developing sensitive magnetic-field sensors such as the ones employed in magnetic storage devices, as well as for magnetic recording [74]. The operating parameters for such devices are often predetermined or constrained, and hence the ability to design a material to meet these constraints and optimize performance can be of significant technological benefit. Furthermore, most of the recent explosive growth in electro magnetic media has been due to new discoveries and better understanding of the magnetic and electronic properties of complex thin magnetic films. Therefore, this research serves as an important study to develop both the micro and macroscopic understanding of the magnetic phenomena for these reduced-dimensional spin systems. In this research,

classical two-dimensional dipolar antiferromagnetic spin systems on a square lattice have been investigated using Monte Carlo simulations.

In addition to the dimensionality of the lattice, the spin dimensionality is an important parameter in determining the phase behavior of such magnetic spin systems. Theoretical studies have identified models that effectively divide such magnetic systems into three main types based on the classical dimensionality of the spins. These are the Ising (uniaxial) model, the plane rotator (XY) model, and the anisotropic Heisenberg model. In the case of the two-dimensional Ising model, the classical spins are constrained to be aligned along the axis perpendicular to the plane of the system due to the strong perpendicular (uniaxial) magnetic surface anisotropy, while in the case of the two-dimensional XY-model the classical spins are confined to the plane of the system due to the strong planar magnetic surface anisotropy. However, in the case of the two-dimensional anisotropic Heisenberg model, the classical spins are three dimensional due to a finite value of magnetic surface anisotropy. This means that the uniaxial and the plane rotator models can be considered as two important limiting cases of the anisotropic Heisenberg model. It is worth noting that in the limit where the magnetic surface anisotropy is zero the spins are fully three dimensional and the model is the so-called isotropic Heisenberg model (or simply the Heisenberg model).

The inherently anisotropic long-range dipolar interaction, which is often ignored in theoretical studies of magnetic systems, can play a significant role in the structural properties of low-dimensional magnetic systems. It can stabilize long-range magnetic order at finite temperature and give rise to magnetization switching between in-plane and out-of-plane ordered phases. This means that the nature and morphology of the ordered phases arising in low-dimensional magnetic systems result from the

subtle combination of the dipolar interaction with competing interactions like the magnetocrystalline interaction (due to the structure of the crystal or the presence of a low-dimensional surface), exchange interaction, or external magnetic field [50, 75]. Therefore, any theoretical description of low-dimensional magnetic systems must include a consideration of all these fundamental interactions- the isotropic short-range exchange interaction, the anisotropic long-range dipolar interaction and the localized (on-site) magnetocrystalline interaction.

Perhaps the earliest model of a two-dimensional spin system was the Ising model. In this model, the magnetic system is considered to be an array of  $N$  fixed points called lattice sites which form a periodic lattice in two dimensions. Associated with each lattice site is an ion which has a spin variable,  $\sigma$ . Each spin variable is a number that is either  $\pm 1$  (due to the very strong uniaxial magnetic surface anisotropy) and interacts with other spins via short-range exchange interactions.

The literature on the Ising model has increased immensely [76] since the original contribution of Ising in 1925 [77]. In three-dimensional lattices, the Ising model is so complicated that no exact solution has ever been found, while in one- and two-dimensional lattices exact solutions have been derived. These exact solutions can be distinguished insofar as the one-dimensional Ising model does not undergo a phase transition, whereas the two-dimensional model has a sharp order-disorder phase transition and also has many unique physical properties as calculated by Onsager [78].

In addition to any short-range exchange interaction, a dipolar interaction exists between the moments of real magnetic ions, as mentioned above. Consequently, the ground state of a two-dimensional uniaxial system, as determined by the exchange interaction alone, differs from the ground state of a system as determined by the

dipolar interaction alone. It is found that in the absence of the dipolar interaction, the ground state of a two-dimensional Ising system is either ferromagnetic, where all the spins are aligned in parallel, or simple antiferromagnetic as in open lattices (e.g., the square lattice) where all the nearest-neighbor pairs of spins are antiparallel [79, 80, 81, 82]. With respect to the pure dipolar case, however, the ground state of the system on a square lattice depends on the type of the magnetic surface anisotropy. For large uniaxial anisotropy, the ground state is an out-of-plane antiferromagnet where each spin is oriented antiparallel to its four nearest neighbours. For large planar anisotropy, the ground state is an in-plane antiferromagnet where the spins form ferromagnetic rows along either of the two axes of the lattice and are ordered antiferromagnetically along the other one [83].

When both the exchange and dipolar interactions are present the system is inherently frustrated. Ground state energy calculations [84, 85, 86, 87, 88, 89, 90], renormalization-group-based arguments [91], and Monte Carlo simulations [25, 83, 92, 93] all predict the existence of a striped phase at low temperatures in the ferromagnetic systems. It is believed that the stability of these stripe domains can be understood, qualitatively, as a compromise between the increase in the exchange energy due to the formation of domain walls, and the decrease in the dipolar energy due to the interaction between magnetization currents generated at the domain walls.

Also, Whitehead and his co-workers [83, 90, 92] have shown that, in the case of large stripe widths, the equilibrium width of a stripe in the ground state grows exponentially as a function of the ratio of the strength of the exchange interaction to the strength of the dipolar interaction. Therefore, the stripe width of the ground state for a system with large ferromagnetic exchange interactions is predicted to be

much larger than found in any particular laboratory sample size [90, 94], and hence the system is characterized by a single domain phase in which the system has a net spontaneous magnetization. As the temperature is increased, the system loses its net magnetization due to the onset of multiple domains in the striped phase, domains that are oriented along a common crystallographic axis. With further increases in temperature, the number of domains increases exponentially [25, 83, 91, 92]. As the temperature is increased further, the striped phase is replaced by a phase in which the magnetic domains are no longer oriented along a common axis but, instead, manifest the symmetry of the underlying lattice. As the temperature is further increased, the intermediate phase decays into a true paramagnetic phase where the typical sharp order-disorder phase transition commonly associated with an Ising model having only a short-range exchange interaction is absent. Instead, a broad peak is found in which the specific heat and the detailed nature of the transition to the fully disordered phase remains unclear. These stages in the evolution of the domain structures are generally consistent with what is observed in the experimental studies of systems that remain uniaxial, using either direct images [7, 10, 95] or magnetic measurements [6, 9, 96].

In addition, both neutron scattering experiments and low-temperature specific heat moments provide strong evidence that the sublattice magnetization of the  $\text{ErBa}_2\text{Cu}_3\text{O}_7$ ,  $\text{DyBa}_2\text{Cu}_3\text{O}_7$ , and  $\text{GdBa}_2\text{Cu}_3\text{O}_7$  rare earth compounds is well fitted by using the Onsager solution for the two-dimensional Ising model [58, 59, 60, 97, 98, 99, 100].

In contrast to the Ising Model, the spins of the plane rotator model are constrained to rotating in the plane of the lattice. This model is peculiar because it has no quantum counterpart. It was first pointed out by Bloch [101] and later proved rigorously by

Mermin and Wagner [102] that the short-range isotropic exchange interaction was insufficient for establishing a spontaneous or sublattice spontaneous magnetization (i.e., of long-range magnetic order) at any finite temperature within a two-dimensional system whose spin dynamics were invariant under a continuous global rotation of the spins, as in the plane rotator model. However, based on renormalization group analysis [103, 104], high temperature series expansions [105], and Monte Carlo simulations [106, 107] it is now known that this model exhibits a topological Kosterlitz-Thouless transition from a low-temperature phase to a high-temperature phase at a finite transition temperature,  $T_{KT}$ . Below  $T_{KT}$ , a metastable phase corresponding to bound vortex-antivortex pairs in this system, having a two-point correlation function which exhibits a power-law decay. Above  $T_{KT}$ , these vortices unbind and the two-point correlation function decays exponentially. When the long-range ferromagnetic exchange interaction is considered, it is found that different magnetic behaviors are expected. As shown using renormalization-group analysis [108] and Monte Carlo simulations (S. Romano, Nuovo Cimento B 100B, 447, 1987 cited in [109]), a model with only long-range ferromagnetic exchange interactions exhibits spontaneous long-range order. In contrast, a model with only the long-range antiferromagnetic exchange interactions does not exhibit any long-range order based on research using Monte Carlo simulations [110], linearized spin-wave approximations [110], and renormalized spin-wave approximations [111].

Different and interesting scenarios appear in the plane rotator model when the dipolar interaction is included. The ground state of the pure dipolar system of magnetic moments located at the sites of a square lattice was investigated by Belobrova *et al.* [112] using the Luttinger and Tisza method [113]. Belobrova *et al.* found that the

ground state of this system is continuously degenerate and consists of four sublattices where the magnetic moment of these sublattices make angles  $\phi$ ,  $-\phi$ ,  $\pi + \phi$ , and  $\pi - \phi$  with the  $x$ -axis,  $\phi$  being arbitrary. Because the Hamiltonian of the dipolar model is not invariant during a global rotation of the spins, the ground-state degeneracy does not arise as a consequence of an exact symmetry of the Hamiltonian, but instead is a peculiarity of the dipolar interaction. Using the mean-field approach as well as Monte Carlo simulations, Zimmerman *et al.* [114] confirmed the existence of such continuous degeneracy in a classical dipolar planar model on the honeycomb lattice, and also predicted the existence of an ordered phase at low temperature.

The work of Zimmerman *et al.* was expanded upon by Henley [115, 116], who introduced the concept of ‘order from disorder’ in which fluctuations (e.g., thermal, quantum, or dilution) lift the degeneracy of the ground state. Furthermore, Prakash and Henley [117] investigated both square and honeycomb plane rotator models having only nearest neighbour portion of the dipolar interaction. In their study, the free energy of both models was calculated within the context of linearized spin-wave approximations. In both cases, Prakash and Henley found that thermal fluctuations and dilution give rise to terms in the free energy that favor particular states, reducing the continuous degeneracy to a discrete symmetry. Whereas in the square system both perturbations were found to reduce the continuous degeneracy of the ground state to a discrete fourfold symmetry, in the honeycomb system both perturbations reduce the continuous degeneracy of the ground state to a discrete sixfold symmetry. In the case of a square lattice, they also showed that while the thermal fluctuations favor a dipolar phase wherein spins are aligned in parallel ferromagnetically along one of the two axes of the lattice and antiferromagnetically along the other axis, the dilution

favors a dipolar phase wherein the spins are oriented at  $\pi/4$  to the  $x$  and  $y$ -axes.

The square plane rotator model having pure long-range dipolar interactions was investigated by both Monte Carlo simulations [118, 119] and linearized spin-wave approximations [118, 119]. Both Monte Carlo simulations and the evaluation of the free energy using the linearized spin-wave approximations provide evidence of the existence of long-range magnetic order in such systems, even though the order parameter evaluated within the linearized spin-wave approximation is actually zero at any finite temperature [118, 119]. To overcome this apparent contradiction, it is necessary to consider higher order approximations in the calculations. Indeed, based on renormalized spin-wave approximations, some authors [120, 109] have shown that higher order corrections to the Hamiltonian will induce a gap in the spin-wave spectra. The appearance of such a temperature-dependent gap renders the ensemble average of the spin-wave amplitude finite, and leads to the appearance of long-range magnetic order at lower temperature. However, the order parameters and the heat capacity exhibit nonanalytic behaviour at low temperature.

The generalization of plane rotator model to include both the long-range dipolar and the short-range antiferromagnetic exchange interactions is presented in chapter 4 [121]. Using both Monte Carlo simulations and spin-wave approximations, independent results on the same system but which treat a long-range antiferromagnetic exchange interaction have been presented by Rastelli *et al.* [121]. These two independent studies showed that the continuous degeneracy is lifted at any non-zero temperature, and that long-range order is supported by thermal fluctuations. Indeed, the characteristics of the low temperature ordered phase depend on the relative strength of the exchange antiferromagnetic and dipole parameters. At low temperatures and

for large values of exchange interactions, the system has a simple parallel antiferromagnetic phase, while for low values of the exchange interaction, the system has a dipolar planar antiferromagnetic phase in which the orientation of the spins depends on the value of the exchange interaction. This will be shown in chapter 5 where the Monte Carlo results for the dipolar plane antiferromagnetic system are presented and discussed.

While the studies of these two previous models (i.e., uniaxial and planar models) provide some understanding of the magnetic properties of quasi-two-dimensional magnetic systems, a detailed description requires a detailed treatment of the magnetic surface anisotropy. This can be done through study of the third model (i.e., the anisotropic Heisenberg model). In this model, the spins are considered to be three-dimensional classical vectors that interact via exchange and dipolar interactions as well as via a magnetic surface anisotropy.

As in the planar model, the long-range magnetic order which breaks a continuous symmetry cannot be sustained in the two-dimensional Heisenberg model having only short-range exchange interactions [102]. Previous studies have shown that, when only a ferromagnetic exchange interaction and a magnetic surface anisotropy are included, the system will order in accord with a transition temperature that is determined by the ratio of the exchange interaction and the magnetic surface anisotropy. For uniaxial magnetic surface anisotropy, there is a second-order phase transition to the ferromagnetic state, which is in the Ising universality class [122, 123]. Meanwhile, for planar magnetic surface anisotropy, the system behaves similarly to the classical XY-model and exhibits a Kosterlitz-Thouless transition [122].

The effect of the long-range dipolar interaction on a system with short-range

exchange interactions was investigated using spin-wave approximations by both Maleev [124] and Pich and Schwabl [125]. While Maleev considered the case of the long-range dipolar interaction along with a dominant ferromagnetic exchange interaction, Pich and Schwabl considered the case of the long-range dipolar interaction along with a dominant antiferromagnetic exchange interaction. Both studies showed that the dipolar interaction modifies the spin-wave spectra by breaking the rotational invariance of the exchange interaction and removing the degeneracy within the magnetic ground state. In the antiferromagnetic case this introduces a gap in the spin-wave spectrum, which renders the magnetic fluctuations finite and stabilizes the long-range magnetic order at finite temperature. In the ferromagnetic case Maleev shows that the long range character of the dipolar interaction modifies the spin-wave spectra in the long wavelength limit such that  $\lim_{q \rightarrow 0} \omega(q) \approx \sqrt{q}$ . This also renders the magnetic fluctuations finite and stabilizes the long-range magnetic order at finite temperature. It is worth noting in these two studies that, while in the first case the ground state is planar ferromagnetic, the ground state in the second case is a perpendicular antiferromagnet.

Heisenberg ferromagnetic systems that include all three interactions - the ferromagnetic exchange interaction, the dipolar interaction, and the uniaxial magnetic surface anisotropy - have been studied extensively using methods such as renormalization group calculations [126, 127, 128, 129], mean-field calculations [130, 131, 132, 133, 134], Monte Carlo simulations [135, 136, 137, 138, 139], and spin-wave analysis [140, 141, 142, 143]. In general, these studies predict the existence of a reorientation transition from an out-of-plane ferromagnetic state at low temperatures to an

in-plane ferromagnetic state as the temperature increases for some ratios of the magnetic surface anisotropy parameter to the dipolar interaction parameter. This agrees well with the experimental findings from most of the research with ferromagnetic ultrathin films.

Using Monte Carlo simulations, MacIsaac and his co-workers also studied the structures and phase diagrams of the dipolar Heisenberg model having zero [144] and intermediate [144] ferromagnetic exchange interactions. In these two studies, the authors showed that there exists a range of values for the ratio of the magnetic surface anisotropy parameter to the dipolar interaction parameter in which the system exhibits a reorientation transition from in-plane at low temperatures to out-of-plane as the temperature increases. However, it is worth noting that, in carrying out the work of this thesis, the nonuniform sampling technique used by MacIsaac *et al.* in these two studies resulted in an additional temperature-dependent effective anisotropy.

For the case of the dominant ferromagnetic exchange interaction, the origin of the reorientation transition is believed to result from competition between the magnetic surface anisotropy, which favors an out-of-plane orientation for the magnetic spins, and the dipolar interaction which favors an in-plane orientation for the moments. Pescia and Pokrovsky [126] argued that the reorientation transition occurs in such systems because the magnitude of the dipolar anisotropy decreases more slowly than the uniaxial anisotropy with increasing temperature. Jensen and Bennemann [145, 146] also claimed that the increased entropy in the planar orientation plays a key role in such a reorientation transition. Furthermore, the effective anisotropy term that arises from the combination of these two interactions may depend on both the temperature [13, 14, 15] and the thickness of the film [12, 13, 15, 133, 147, 148, 140,

149, 150, 151].

While extensive work has been done on the behaviour of low-dimensional ferromagnetic systems [3, 18, 17], little systematic work has been carried out on low-dimensional antiferromagnetic systems [125, 152, 153, 154]. In particular, little is known about the effects that arise from the interplay of the exchange, dipolar, and magnetic surface anisotropy in the antiferromagnetic case. In this thesis, to obtain a better understanding of both the low temperature properties and the nature of the phase transitions within the low-dimensional antiferromagnetic systems, several Monte Carlo simulations are carried out on the classical two-dimensional dipolar antiferromagnetic systems, each on a square lattice. Results are presented for different values of the short-range antiferromagnetic exchange constant and magnetic surface anisotropy in the presence of the long-range dipolar interaction over a range of temperatures for three different lattice sizes ( $N = L \times L = 32^2, 64^2, 104^2$ ). The code used in the study of these systems has been modified from that originally written by MacIsaac and his co-workers [155, 156]. From the results of these simulations the phase diagram for each investigated system is constructed both at  $T = 0$  and at finite temperature.

The outline of this thesis, thus, is as follows: Chapter 2 provides a general introduction to the model of interest. It also gives a brief description of the Ewald summation technique. Chapter 3 then gives a brief introduction to Monte Carlo simulations and how MacIsaac and his co-workers [155, 156] included the long-range dipolar energy in finite temperature Monte Carlo simulations based on the Ewald summation technique. The chapter concludes by providing the computational aspects and benchmarks needed for applying the code.

Given the complexity of the general model on a square lattice, chapters 4, 5, 6, and 7 present the more specific results obtained from this research. In chapter 4, results are presented for the case of the Heisenberg system (previously published [157]) in which the three-dimensional classical spin vectors interact through both the long-range dipolar and the short-range antiferromagnetic exchange interactions. In chapter 5, results are presented for the plane rotator system (previously published [158]) in which the classical spin vectors are restricted to lying within the plane of the lattice and interact through long-range dipolar and short-range antiferromagnetic exchange interactions. In chapter 6, results are presented for the anisotropic Heisenberg system in which the three-dimensional classical spin vectors interact through long-range dipolar and short-range antiferromagnetic exchange interactions as well as by a fixed value of the planar magnetic surface anisotropy. Finally, results are presented in chapter 7 (previously published [159]) for the anisotropic Heisenberg system in which the three-dimensional classical spin vectors interact through the long-range dipolar interaction and through the planar magnetic surface anisotropy along with a fixed value of the antiferromagnetic exchange constant. Chapter 8 provides a summary of the main findings and explores some of the interesting implications for conducting further research in the field of low-dimensional magnetic systems.

# Chapter 2

## The Model in General Terms

### 2.1 The Energy of the General Model

Even though magnetism is an intrinsically quantum mechanical phenomenon, the systems considered in this study are all based on two-dimensional classical spin systems on a square lattice. This is because classical spin systems can often provide insight into the phase behavior of the equivalent quantum mechanical systems and, as well, the difficulties associated with the analysis of quantum spin systems can be overcome by the simulation of the equivalent classical spin systems [160].

In the model of interest, the two in-plane directions of the square lattice are denoted by  $\hat{x}$  and  $\hat{y}$  respectively, and the direction perpendicular to the plane is denoted by  $\hat{z}$ . Each lattice site,  $i$ , is associated with an ion which has a total magnetic moment,  $\vec{\mu}$ , and a total spin,  $\vec{S}$ . In this model, the magnetic ions interact through the exchange interaction ( $E_{ex}$ ), the dipolar interaction ( $E_{dd}$ ), and the magnetic surface anisotropy ( $E_{\kappa}$ ). Thus, the general energy of the considered model can be written in simple terms as

$$E = E_{ex} + E_{dd} + E_{\kappa}. \quad (2.1.1)$$

The first term in Equation 2.1.1,  $E_{ex}$ , is the exchange interaction. The exchange interaction is typically subdivided into one of three energies: direct exchange, indirect exchange, and superexchange. The direct exchange interaction arises from the direct Coulomb interaction among the electrons of two adjacent ions, as shown in Figure 2.1a. The indirect exchange interaction arises where the electrons of the partially filled  $f$ -shells, as present in the rare earth metals, are coupled due to their interaction with the conduction electrons, as shown in Figure 2.1b. The superexchange interaction occurs when the electrons of a nonmagnetic ion interact with the electrons of the first magnetic ion, and also with the electrons of the second magnetic ion, as shown in Figure 2.1c.

The exchange interaction has two important properties. First, it decays exponentially with increasing distance between the magnetic ions of the lattice and, as such, it is a short-range interaction extending over a few atomic radii. Given this characteristic, only the nearest-neighbor exchange interactions, and no superexchange interactions, are considered in this research. Second, the interaction depends only on the relative angle between the spins. Because of this property, the exchange coupling is said to be isotropic. With these two properties, the exchange energy term may be written as

$$E_{ex} = -\mathcal{J} \sum_{\langle i,j \rangle} \vec{S}(\vec{R}_i) \cdot \vec{S}(\vec{R}_j), \quad (2.1.2)$$

where the sum is the overall nearest-neighbor pairs of sites  $\langle i, j \rangle$ ,  $\vec{S}(\vec{R}_i)$  is the classical spin vector at site  $i$ , and  $\mathcal{J}$  is the strength of the exchange interaction (i.e., the exchange coupling constant or parameter). A positive  $\mathcal{J}$  gives a ferromagnetic ground state so that the spins are all aligned in parallel, while a negative  $\mathcal{J}$  gives an anti-ferromagnetic ground state on open lattices (such as the square lattice) in which all

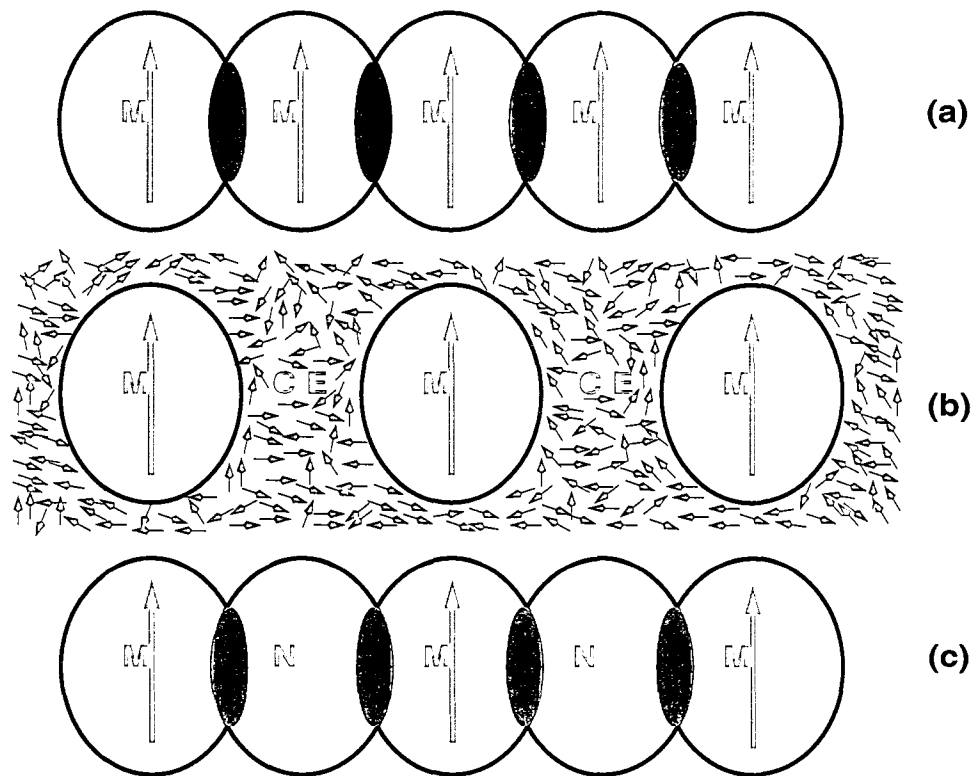


Figure 2.1: Schematic diagram of a direct exchange (a), an indirect exchange (b), and a superexchange interaction (c). In this Figure, M=magnetic ion, N=non-magnetic ion, and CE=conduction electrons.

nearest-neighbor pairs of spins are anti-parallel [102, 161, 162].

The second term in Equation 2.1.1,  $E_{dd}$ , is the dipole-dipole interaction. The dipolar energy for neighboring moments is typically smaller than the exchange interaction often by many orders of magnitude [163]. Also, the dipolar interaction between any two moments on the lattice decays as the inverse cube of the distance between them. For this reason, the dipole-dipole interaction decays slowly with distance between any two magnetic ions, and therefore it is a long-range interaction where each moment interacts with all the other moments in the lattice. Unlike the exchange interaction, the dipolar interaction between any two moments not only depends on the relative orientation of the two moments but also depends on their orientation relative to the vector joining the two corresponding sites. In this sense, the dipolar coupling is said to be anisotropic. Schematically, Figure 2.2 shows the magnetic field produced by an isolated magnetic dipole.

The contribution of the dipolar energy to the general energy given by Equation 2.1.1 can then be written as

$$E_{dd} = \frac{1}{2} \sum_{i \neq j} \left( \frac{\vec{\mu}(\vec{R}_i) \cdot \vec{\mu}(\vec{R}_j)}{|\vec{R}_{ij}|^3} - 3 \frac{(\vec{\mu}(\vec{R}_i) \cdot \vec{R}_{ij})(\vec{\mu}(\vec{R}_j) \cdot \vec{R}_{ij})}{|\vec{R}_{ij}|^5} \right), \quad (2.1.3)$$

where the sum is over all possible pairs of sites in the lattice except  $i = j$ ,  $|\vec{R}_{ij}|$  is the distance between site  $i$  and site  $j$ , and  $\vec{\mu}(\vec{R}_i)$  is the classical moment vector at site  $i$  [161].

Finally, the third term of Equation 2.1.1,  $E_{\kappa}$ , is the magnetic surface anisotropy which arises due to the spin interaction with the crystal environment [164, 165]. This coupling can result in a preferred axis or axes (i.e., easy axis or axes) about which the system may be favorably ordered energetically. The existence of such an easy axis or axes can have any one of a number of causes. For example, the spin-orbit coupling

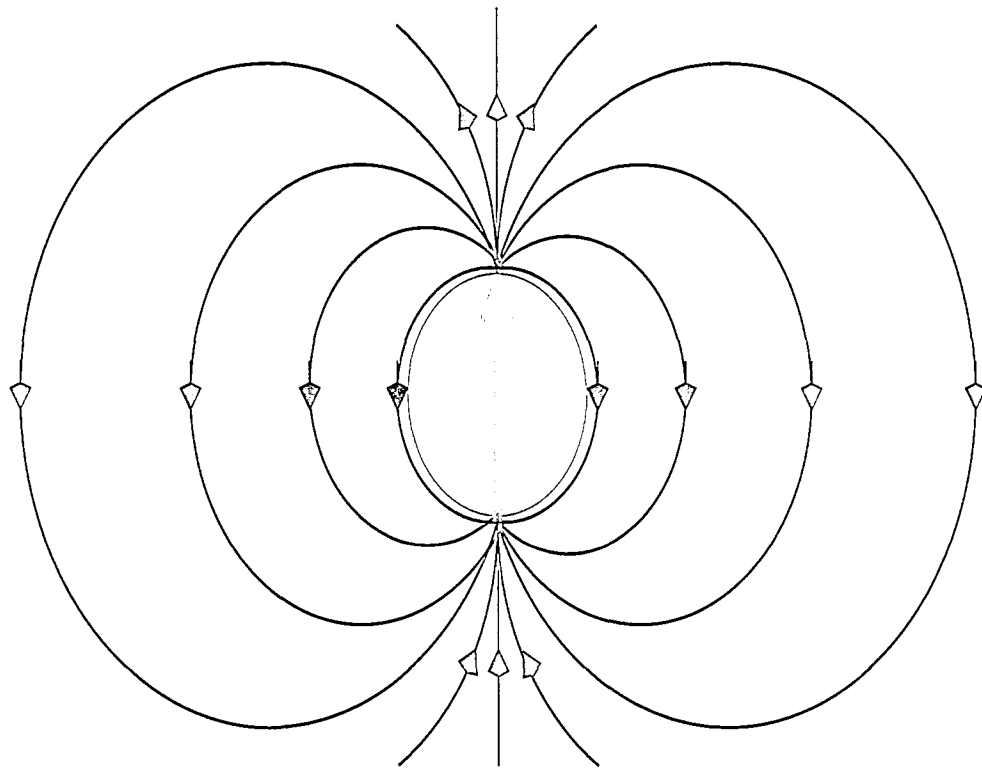


Figure 2.2: The magnetic field for an isolated magnetic dipole moment located at the origin.

which arises from the lack of spherical symmetry in the charge overlap between ions can lead to a preferred orientation for the magnetic ion as in the case of cobalt crystals [162, 166]. Another possible cause is the effect of the crystalline electric field such as found in heavy rare earth and transition metals [167, 168]. The effects of the crystalline electric field, however, will be much stronger in magnetic systems that consist of transition metals than in those systems that include rare earth ions. In the transition ions it is the outer shell, the  $3d$ -shell, which is responsible for the magnetic moment, while in the rare earth ions it is the inner  $4f$  shell.

Because the  $E_\kappa$  term is a surface effect, it may best be observed experimentally in systems with a high surface-to-volume ratio such as magnetic ultrathin films or multilayer compounds. Theoretically, it is convenient to include this term when a two-dimensional (monolayer) system is examined. For the magnetic systems investigated in this research, it is sufficient to consider only the case where the anisotropic term couples exclusively to the component of the magnetic moment that is perpendicular to the surface, due to the symmetry between the two in-plane directions [147, 164, 16].

With the  $z$ -axis perpendicular to the surface of the system, as chosen above, the magnetic surface anisotropy may be written as

$$E_\kappa = -\lambda \sum_i \mu^z(\vec{R}_i)^2, \quad (2.1.4)$$

where the sum is over all sites in the lattice,  $\mu^z(\vec{R}_i)$  is the  $\hat{z}$  component of the moment vector at site  $i$ , and  $\lambda$  is the strength of the magnetic surface anisotropy. A positive value of  $\lambda$  yields an easy axis along  $\hat{z}$ , while a negative value gives an easy plane within the system.

To use Equation 2.1.1 in the Monte Carlo simulations, Equations 2.1.2, 2.1.3, and 2.1.4 may be written in terms of the dimensionless quantities such that  $\vec{\mu}$  and  $\vec{S}$

at site  $i$  can be rewritten as

$$\vec{\mu}(\vec{R}_i) = \mu_{\text{eff}} \vec{\sigma}(\vec{R}_i), \quad (2.1.5)$$

and

$$\vec{S}(\vec{R}_i) = S_{\text{eff}} \vec{\sigma}(\vec{R}_i), \quad (2.1.6)$$

such that

$$|\vec{\sigma}(\vec{R}_i)| = 1. \quad (2.1.7)$$

Also, all distances are scaled by the lattice constant,  $a$ , and thus  $\vec{R}_i \rightarrow \vec{R}_i/a$ . Substituting these new definitions into Equations 2.1.2, 2.1.3, and 2.1.4 then gives

$$E_{ex} = -\mathcal{J} S_{\text{eff}}^2 \sum_{\langle i,j \rangle} \vec{\sigma}(\vec{R}_i) \cdot \vec{\sigma}(\vec{R}_j), \quad (2.1.8)$$

$$E_{dd} = \frac{\mu_{\text{eff}}^2}{2a^3} \sum_{i \neq j} \left( \frac{\vec{\sigma}(\vec{R}_i) \cdot \vec{\sigma}(\vec{R}_j)}{|\vec{R}_{ij}|^3} - 3 \frac{(\vec{\sigma}(\vec{R}_i) \cdot \vec{R}_{ij})(\vec{\sigma}(\vec{R}_j) \cdot \vec{R}_{ij})}{|\vec{R}_{ij}|^5} \right), \quad (2.1.9)$$

and

$$E_{\kappa} = -\lambda (\mu_{\text{eff}}^z)^2 \sum_i \sigma^z(\vec{R}_i)^2. \quad (2.1.10)$$

Moreover, the new coupling parameters

$$J = \mathcal{J} S_{\text{eff}}^2, \quad (2.1.11)$$

$$g = \frac{\mu_{\text{eff}}^2}{2a^3}, \quad (2.1.12)$$

and

$$\kappa = (\mu_{\text{eff}}^z)^2 \lambda \quad (2.1.13)$$

are defined so that Equations 2.1.8, 2.1.9, and 2.1.10 can be rewritten as

$$E_{ex} = -J \sum_{\langle i,j \rangle} \vec{\sigma}(\vec{R}_i) \cdot \vec{\sigma}(\vec{R}_j), \quad (2.1.14)$$

$$E_{dd} = g \sum_{i \neq j} \left( \frac{\vec{\sigma}(\vec{R}_i) \cdot \vec{\sigma}(\vec{R}_j)}{|\vec{R}_{ij}|^3} - 3 \frac{(\vec{\sigma}(\vec{R}_i) \cdot \vec{R}_{ij})(\vec{\sigma}(\vec{R}_j) \cdot \vec{R}_{ij})}{|\vec{R}_{ij}|^5} \right), \quad (2.1.15)$$

and

$$E_{\kappa} = -\kappa \sum_i \sigma^z(\vec{R}_i)^2. \quad (2.1.16)$$

Finally, substituting Equations 2.1.14, 2.1.15, and 2.1.16 into Equation 2.1.1 yields

$$\begin{aligned} E = & g \sum_{i \neq j} \left( \frac{\vec{\sigma}(\vec{R}_i) \cdot \vec{\sigma}(\vec{R}_j)}{|\vec{R}_{ij}|^3} - 3 \frac{(\vec{\sigma}(\vec{R}_i) \cdot \vec{R}_{ij})(\vec{\sigma}(\vec{R}_j) \cdot \vec{R}_{ij})}{|\vec{R}_{ij}|^5} \right) \\ & - J \sum_{\langle i,j \rangle} \vec{\sigma}(\vec{R}_i) \cdot \vec{\sigma}(\vec{R}_j) - \kappa \sum_i \sigma^z(\vec{R}_i)^2. \end{aligned} \quad (2.1.17)$$

In the present research, the two coupling parameters,  $J$  and  $\kappa$ , appearing in Equation 2.1.17, are measured in units such that  $g = \mu_{\text{eff}}^2/2a = 1$ .

As summarized in chapter 1, there are three important and much-studied limiting cases of the general model given by Equation 2.1.17:

1. At the limit of strong perpendicular magnetic surface anisotropy (i.e.,  $\kappa \rightarrow \infty$ ), the spins are constrained to be aligned along the axis perpendicular to the plane of the system. This may be described by the two-dimensional classical Ising Model.
2. At the limit of strong planar magnetic surface anisotropy (i.e.,  $\kappa \rightarrow -\infty$ ), the spins are confined to the plane and thus they become two dimensional. This may be described in terms of the two-dimensional classical XY-model.

3. In the case of zero magnetic surface anisotropy, the spins are fully three dimensional, and the system is described by the two-dimensional classical Heisenberg model.

## 2.2 The Dipole-dipole Interaction and Ewald Summation Technique

The dipolar interaction is always present between the magnetic moments in all real magnetic materials. Despite its small value, it may lead to critical behavior significantly different from that found in materials that have only short-range interactions. Indeed, in the case of quasi-two-dimensional magnetic systems, the dipolar interaction has been found to play an essential role in determining the magnetic properties [169, 170]. Thus, the dipolar interaction should be included in any considered model that attempts to represent the magnetic properties of two-dimensional spin systems.

The evaluation of the contribution of the dipole-dipole interaction to the magnetic energy is complicated by its slow convergence, and an efficient method is needed for calculating this sum for particular spin configurations. Such a sum is best treated using one of the variants of the Ewald summation technique described in earlier work [155, 171]. The basic idea behind this method is to employ the properties of theta functions under Jacobi imaginary transformations to convert the slowly converging lattice sum to a rapidly convergent form.

In the case of the dipolar interaction, the appropriate way to apply the Ewald summation technique is to separate the dipolar energy into two parts. The first part

represents a localized part of the dipolar interaction and this part converges rapidly in real space. The second part is a long-range component of the dipolar interaction which converges rapidly in momentum ( $\vec{q}$ ) space. For this reason it is better to start from a differential form of the dipolar interaction. This can be done by rewriting the dipolar energy given by Equation 2.1.15 as

$$E_{dd} = -\frac{g}{2} \sum_{i \neq j} \sum_{\alpha, \beta} \sigma^\alpha(\vec{R}_i) \sigma^\beta(\vec{R}_j) \lim_{\vec{r} \rightarrow 0} \frac{\partial}{\partial r^\alpha} \frac{\partial}{\partial r^\beta} \left( \frac{1}{|\vec{R}_{ij} + \vec{r}|} \right), \quad (2.2.1)$$

where  $\alpha$  and  $\beta$  denote components of the spin vectors.

The Ewald summation technique used to perform the previous sum is based on the integral representation

$$\begin{aligned} \frac{1}{|\vec{R}|} &= \frac{2}{\sqrt{\pi}} \int_0^\infty d\rho \exp(-\rho^2 |\vec{R}|^2) \\ &= \frac{2}{\sqrt{\pi}} \left( \int_0^\eta d\rho \exp(-\rho^2 |\vec{R}|^2) + \int_\eta^\infty d\rho \exp(-\rho^2 |\vec{R}|^2) \right), \end{aligned} \quad (2.2.2)$$

where  $\eta$  is an arbitrary constant typically chosen to be of order 1. Comparing Equation 2.2.2 with the expression for the dipolar sum given by Equation 2.2.1 we obtain

$$E_{dd} = E_1 + E_2, \quad (2.2.3)$$

where the  $E_1$  term denotes the integration over the interval  $0 < \rho < \eta$ , and the  $E_2$  term represents the integration over the interval  $\eta < \rho < \infty$ .

The  $E_2$  term can be readily evaluated as

$$E_2 = -\frac{g}{2} \sum_{i \neq j} \sum_{\alpha, \beta} \sigma^\alpha(\vec{R}_i) \gamma_2^{\alpha\beta}(\vec{R}_{ij}) \sigma^\beta(\vec{R}_j), \quad (2.2.4)$$

where  $\gamma_2^{\alpha\beta}(\vec{R}_{ij})$  is given by

$$\gamma_2^{\alpha\beta}(\vec{R}_{ij}) = \lim_{\vec{r} \rightarrow 0} \frac{\partial}{\partial r^\alpha} \frac{\partial}{\partial r^\beta} \left( \frac{\text{erfc}(\eta |\vec{R}_{ij} + \vec{r}|)}{|\vec{R}_{ij} + \vec{r}|} \right), \quad (2.2.5)$$

where  $\text{erfc}(x)$  is the complimentary error function. Since  $\text{erfc}(x)$  damps exponentially for large values of  $x$  as

$$\lim_{x \rightarrow \infty} \text{erfc}(x) \approx \frac{\exp(-x^2)}{\sqrt{\pi}x}, \quad (2.2.6)$$

the  $E_2$  term can be readily evaluated numerically for different spin configurations.

In contrast, the  $E_1$  term is evaluated in  $\vec{q}$  space using the Fourier transformation of the spin configuration,

$$\sigma^\alpha(\vec{q}) = \frac{1}{\sqrt{N}} \sum_i \sigma^\alpha(\vec{R}_i) \exp(i\vec{q} \cdot \vec{R}_i). \quad (2.2.7)$$

By transforming the sum over lattice vectors  $\{\vec{R}\}$  to one over reciprocal lattice vectors  $\{\vec{Q}\}$ , the resultant expression for the  $E_1$  term may then be written as

$$E_1 = \frac{g}{2} \sum_{\vec{q}} \sum_{\alpha, \beta} \sigma^\alpha(\vec{q}) \gamma_1^{\alpha\beta}(\vec{q}) \sigma^\beta(-\vec{q}). \quad (2.2.8)$$

In the case of the rectangular lattice,  $\gamma_1^{\alpha\beta}(\vec{q})$  has the form

$$\begin{aligned} \gamma_1^{\alpha\beta}(\vec{q}) = & -2\pi \sum_{\vec{Q}} \left( z^\alpha z^\beta |\vec{q} - \vec{Q}| - \frac{(q^\alpha - Q^\alpha)(q^\beta - Q^\beta)}{|\vec{q} - \vec{Q}|} \right) \text{erfc}\left(\frac{|\vec{q} - \vec{Q}|}{2\eta}\right) \\ & - \frac{4\eta^3}{3\sqrt{\pi}} \left( \delta_{\alpha\beta} - z^\alpha z^\beta \frac{3\pi}{\eta^2} \sum_{\vec{Q}} \exp(-|\vec{q} - \vec{Q}|^2/4\eta^2) \right), \end{aligned} \quad (2.2.9)$$

where  $z^\alpha$  denotes the  $\alpha$  component of the unit vector perpendicular to the surface. Again, the existence of  $\text{erfc}(x)$  in the previous sum ensures rapid convergence for large values of  $\vec{q}$ . Careful analysis for the long wavelength limit has to be taken into account since the term corresponding to  $Q = 0$  in the series contains a non-analytic contribution denoted by  $q^\alpha q^\beta / |\vec{q}|$ .

One important application of this Ewald summation technique is in the determination of the dipolar contribution to the ground state energy for some important

spin configurations. Generalizations of the above technique for a simple antiferromagnet on a two-dimensional square lattice [49], yield the dipolar contribution to several important spin configurations as shown in Table 2.1 [50]. In both the  $AA_{\parallel}$  and the  $AF_{\parallel 1}$  phases, the spins are aligned within the plane of the lattice. While in the  $AA_{\parallel}$  phase each spin is ordered anti-parallel to each of its nearest neighbors, in the  $AF_{\parallel 1}$  phase the spins are ordered ferromagnetically along one of the two axes of the lattice and antiferromagnetically along the other axis. In contrast to the  $AA_{\parallel}$  and  $AF_{\parallel 1}$  phases, the spins in the  $AA_{\perp}$  are ordered perpendicular to the plane of the lattice with each spin aligned anti-parallel to each of its nearest neighbors. The Ewald summation technique is also used in treating the dipolar interaction when there are periodic boundary conditions as will be presented in the following chapter.

System	Spin configuration	Energy per spin
Planar antiferromagnetic ( $AA_{\parallel}$ ) phase	$\sigma^x = (-1)^{n_x+n_y}$ $\sigma^y = 0$ $\sigma^z = 0$	$E = 1.3229g$
Planar antiferromagnetic ( $AF_{\parallel 1}$ ) phase	$\sigma^x = (-1)^{n_y}$ $\sigma^y = 0$ $\sigma^z = 0$ or $\sigma^x = 0$ $\sigma^y = (-1)^{n_x}$ $\sigma^z = 0$	$E = -5.0989g$
Uniaxial antiferromagnetic ( $AA_{\perp}$ ) phase	$\sigma^x = 0$ $\sigma^y = 0$ $\sigma^z = (-1)^{n_x+n_y}$	$E = -2.6459g$

Table 2.1: The dipolar energy calculated for a number of important antiferromagnetic spin configurations on a two-dimensional square lattice. The subscripts  $x$  and  $y$  denote the square lattice axes,  $z$  denotes the axis perpendicular to lattice, and  $(n_x, n_y)$  denotes the coordinates of the spin variable on the lattice.

## 2.3 Systems of Interest

This thesis presents the results from several series of Monte Carlo simulations on models of antiferromagnetic spin systems. The purpose of these simulation studies is to better understand both the low temperature magnetic properties of these systems and their phase behavior. The simulations are performed on a two-dimensional square lattice of length  $L$  with the spin represented by  $N$  vectors of fixed magnitude ( $N = L \times L = 32^2, 64^2, 104^2$ ). Depending on the choice of parameters, the ground state for each system is one of those listed in Table 2.1.

The first system to be analyzed is the dipolar Heisenberg system without magnetic surface anisotropy (i.e.,  $\kappa = 0$ ). In this system, the spin variables are fully three-dimensional classical vectors, and interact through both the long-range dipolar and the short-range antiferromagnetic exchange interactions. The phase behavior is determined by the competition between dipolar and exchange interactions. Based on the Monte Carlo data, the magnetic phase diagram, constructed as a function of both  $|J|/g$  and  $T/g$ , will be presented in chapter 4.

The second is the plane rotator system. This system has infinite planar anisotropy (i.e.,  $\kappa \rightarrow -\infty$ ) and its classical spin vectors are restricted to lying within the plane of the lattice and have full rotational freedom in that plane. Again the spin vectors interact via long-range dipolar and short-range antiferromagnetic exchange interactions. From Monte Carlo simulations, the phase diagram of this system is determined as a function of both  $|J|/g$  and  $T/g$  as will be shown in chapter 5.

The third is the anisotropic Heisenberg system with a fixed value of the planar anisotropy. This system is similar to the first system except that the spin vectors of this system are subject to a weak planar magnetic surface anisotropy (i.e.,  $\kappa = -1.0g$ ).

Using the Monte Carlo results, the phase diagram is established as a function of both  $|J|/g$  and  $T/g$  as will be presented in chapter 6.

Finally, the fourth system is the anisotropic Heisenberg system in which the spin vectors are subject to a range of planar magnetic surface anisotropy (*i.e.*,  $\kappa < 0$ ) and have long-range dipolar interactions, as well as a dominant short-range antiferromagnetic exchange interaction ( $J = -10.0g$ ). Based on the Monte Carlo calculations, the phase diagram of this system is constructed as a function of both  $|\kappa|/g$  and  $T/g$  as will be presented in chapter 7.

# Chapter 3

## Monte Carlo Methods

In recent years the method of computer simulation has become a bridge that connects the theoretical and experimental branches of science. In simulations, the model that is used to describe the system can be studied without recourse to further approximation techniques. This can allow us to discover and investigate new phenomena as revealed through simulation. Computer simulation, therefore, complements both theoretical and experimental research, and provides a third branch of scientific investigation. The three branches would be analogous to the vertices of a triangle where each vertex seems distinct but at the same time is strongly connected to the other two [172].

One of the most important simulation techniques is the Monte Carlo technique, which is widely used for solving problems in statistical physics. The basic idea is to evaluate thermal equilibrium averages of materials by statistically sampling the significance region of the phase space of a model using a computer. This implies that the use of probability and statistics is essential in Monte Carlo physics [173].

The fast growth of computational resources and the development of new algorithms allow Monte Carlo simulations to look deeper and deeper into subjects of statistical physics by offering great improvements in the accuracy of results [172].

However, the limitations of computer speed and computer memory can still make computational simulations difficult and challenging. In the case of magnetic systems for example, much less simulation work has been carried out on spin systems that include long-range interactions [93, 135, 136, 156, 174] as compared to those systems that include only short-range interactions [123, 172, 173, 175, 176, 177].

Because most of the results in the present research are based on Monte Carlo simulations, this chapter looks briefly at the general ideas behind equilibrium thermal Monte Carlo methods. Four important ideas about Monte Carlo techniques are introduced in this chapter: importance sampling, transition probability, detailed balance, and the Metropolis algorithm. This chapter also contains a brief description of how MacIsaac and his co-workers [155, 156] treated the long-range nature of dipolar interactions in Monte Carlo simulations. This approach forms the basis of the Monte Carlo Code written by MacIsaac *et al.*, used with some modifications in this study. Moreover, this chapter presents a typical simulation and the important benchmarks used in this research.

### 3.1 Importance Sampling and the Metropolis Algorithm

The goal of equilibrium statistical mechanics is to calculate observable thermal quantities of a material, such as a magnetization in a magnetic model. In the canonical ensemble this requires that we average an observable quantity,  $Q$ , over all of the states of the system, weighting each by the Boltzmann probability

$$P(\nu) \propto \exp(-E_\nu/T), \tag{3.1.1}$$

where  $E_\nu$  is the energy of the system in state  $\nu$ ,  $T$  is the temperature measured in units of  $1/k_B$ , where  $k_B$  is the Boltzmann constant. Therefore, the average value of  $Q$  is given by

$$\langle Q \rangle = \frac{\sum_\nu Q_\nu \exp(-E_\nu/T)}{\sum_\nu \exp(-E_\nu/T)}, \quad (3.1.2)$$

such that  $Q_\nu$  is the value of  $Q$  at some state  $\nu$ .

Except for a few systems, the exact evaluation of such quantities is impossible and approximations are required to obtain estimates of important thermodynamical variables. One approach is to evaluate the quantity given in Equation 3.1.2 by summing over a large but finite number of states, an approach made feasible with the advent of modern computers. The question we would like to answer now is how should we choose a finite number of states in order to obtain an accurate estimate of  $\langle Q \rangle$ ? While the simplest choice is to pick all of these states at random with equal probability from the phase space of the system, averaging over them is unlikely to yield any reasonable estimate of the average value of  $Q$ , since most of these randomly chosen states will not make a statistically significant contribution to the sums given by Equation 3.1.2. This means that a few terms of the sums given by Equation 3.1.2 will be dominant. For example, at low temperatures, the system spends almost all of its time in the ground state, or at one of the lowest excited states, because there is not enough thermal agitation to excite the system to the higher states. Consequently, it cannot be assumed that the system passes through every state during the measurement, even though every state appears in the sums of Equation 3.1.2. However, if instead of choosing the states at random with equal probability, they are selected according to some probability distribution,  $P(\nu)$ , which we specify, then it is possible to significantly improve the reliability of the estimate provided by averaging over these states.

The significance of this approach lies in the ability to choose the probability  $P(\nu)$  such that the selected states used in the evaluation of  $\langle Q \rangle$  are statistically significant. This approach is referred to as importance sampling.

Suppose we choose a subset  $\{\nu_1, \nu_2, \dots, \nu_{\mathcal{M}}\}$  at random, each with probability  $\{P(\nu_1), P(\nu_2), \dots, P(\nu_{\mathcal{M}})\}$ , then the best estimate of  $Q$  will be given by

$$\langle Q \rangle_{\mathcal{M}} = \frac{\sum_{\nu_l=1}^{\mathcal{M}} Q_{\nu_l} P_{\nu_l}^{-1} \exp(-E_{\nu_l}/T)}{\sum_{\nu_l=1}^{\mathcal{M}} P_{\nu_l}^{-1} \exp(-E_{\nu_l}/T)}. \quad (3.1.3)$$

Equation 3.1.3 tells us that the  $\langle Q \rangle_{\mathcal{M}}$  becomes a more and more accurate estimate of  $\langle Q \rangle$  as the number of the selected states  $\mathcal{M}$  increases. In addition, when  $\mathcal{M}$  goes to infinity,  $\langle Q \rangle_{\mathcal{M}}$  goes to  $\langle Q \rangle$ . A simple and effective choice for  $P_{\nu}$  in Equation 3.1.3 would be the Boltzmann distribution given by Equation 3.1.1. Then,  $\langle Q \rangle_{\mathcal{M}}$  becomes just a simple arithmetic average

$$\langle Q \rangle_{\mathcal{M}} = \frac{\sum_{\nu_l=1}^{\mathcal{M}} Q_{\nu_l}}{\mathcal{M}}. \quad (3.1.4)$$

The choice of the Boltzmann distribution also ensures that the average of  $Q$  is calculated using the most statistically significant states.

The question which arises is how to find a procedure that selects states according to the Boltzmann probability. The idea is to use a Markov process. In this process, successive states,  $\nu_{l+1}$ , are generated from previous states,  $\nu_l$ , through a transition probability,  $W(\nu_l \rightarrow \nu_{l+1})$ , such that in the limit,  $\mathcal{M} \rightarrow \infty$ , the distribution function of the states generated by this Markov is given by the Boltzmann distribution.

Such a process should satisfy the following four conditions:

1. The state,  $\nu_{l+1}$ , is generated every time it is determined by the state,  $\nu_l$ .

2. The transition probabilities must satisfy the constraint

$$\sum_l W(\nu_l \rightarrow \nu_{l+1}) = 1. \quad (3.1.5)$$

3. Reaching any state of the system from any other state is possible if the program is run for a long enough time (i.e., the condition of ergodicity).

4. In equilibrium, the rate at which the system makes transitions into and out of any state,  $\nu$ , must be equal (i.e., the condition of the detailed balance). Mathematically, this condition can be written as

$$P(\nu_l)W(\nu_l \rightarrow \nu_{l+1}) = P(\nu_{l+1})W(\nu_{l+1} \rightarrow \nu_l). \quad (3.1.6)$$

Using the Boltzmann probability distribution given by Equation 3.1.1, Equation 3.1.6 thus gives

$$\frac{W(\nu_l \rightarrow \nu_{l+1})}{W(\nu_{l+1} \rightarrow \nu_l)} = \frac{P(\nu_{l+1})}{P(\nu_l)} = \exp(-(E_{\nu_{l+1}} - E_{\nu_l})/T). \quad (3.1.7)$$

Equation 3.1.7 indicates that the transition probability ratio for a move from state  $\nu_l$  to  $\nu_{l+1}$  depends only on the energy change,  $E_{\nu_{l+1}} - E_{\nu_l}$ .

One simple and efficient choice for the transition probability which satisfies Equation 3.1.7 is the Metropolis algorithm. This algorithm was proposed by Metropolis and his co-workers in 1953 in the simulation of hard-sphere gases [178]. In this optimal algorithm the transition probability is given by

$$W(\nu_l \rightarrow \nu_{l+1}) = \left\{ \begin{array}{ll} \exp(-(E_{\nu_{l+1}} - E_{\nu_l})/T), & \text{if } E_{\nu_{l+1}} > E_{\nu_l} \\ 1, & \text{if } E_{\nu_{l+1}} \leq E_{\nu_l} \end{array} \right\} \quad (3.1.8)$$

This means that if we select a new state,  $\nu_{l+1}$ , which has an energy lower than or equal to the present state,  $\nu_l$ , then we accept the transition to that state. If the

new state has a higher energy then we may accept it with the probability given in Equation 3.1.8.

To accept or reject a new state which has a higher energy than the previous one, we choose a uniform random number,  $Z$ , between zero and one. If the transition probability is greater than  $Z$ , then we accept the new state and the system moves to the  $\nu_{l+1}$  state. Other than this we reject the new state and the system stays in the  $\nu_l$  state.

Actually, there is much freedom of choice in moving from states  $\nu_l$  to  $\nu_{l+1}$ , which are only restricted by the condition that the  $W_{\Delta E=0}$  is symmetric (i.e.,  $W_{\Delta E=0}(\nu_l \rightarrow \nu_{l+1}) = W_{\Delta E=0}(\nu_{l+1} \rightarrow \nu_l)$ ). Changing many degrees of freedom simultaneously, however, leads to an extremely small value for the transition probability, and hence, most of the desired moves would not be selected at all such that the system may largely remain in its previous state. Therefore, one efficient and common strategy is to change only one degree of freedom, such as rotating a single spin in the case of the plane rotator system; or change only two degrees of freedom, such as rotating a single spin in the case of the Heisenberg system.

Thus, the optimal Metropolis algorithm used in this work proceeds according to the following nine steps:

1. Choose the initial state,  $\nu_l$ , of the system.
2. Randomly select the target spin,  $\vec{\sigma}(\vec{r}_i)$ , where  $i \in (1, 2, 3, 4, \dots, N = L \times L)$ .
3. Generate a new state,  $\nu_{l+1}$ , randomly by changing the orientation of the selected spin  $\vec{\sigma}(\vec{r}_i)$  to  $\vec{\sigma}'(\vec{r}_i)$  such that

$$\vec{\sigma}'(\vec{r}_i) = \vec{\sigma}(\vec{r}_i) + \Delta\vec{\sigma}(\vec{r}_i). \quad (3.1.9)$$

4. Compute the difference in the energy,  $\Delta E$ , between the new state and the old one (i.e.,  $\Delta E = E_{\nu_{l+1}} - E_{\nu_l}$ ).
5. Calculate the transition probability according to Equation 3.1.8.
6. Generate a uniform distribution random number,  $Z$ , between zero and one.
7. Compare  $Z$  with the calculated  $W(\nu_l \rightarrow \nu_{l+1})$ . If  $W(\nu_l \rightarrow \nu_{l+1})$  is greater than  $Z$  accept the move, otherwise leave the spin as it is and retain the old spin configuration.
8. Repeat steps 2 – 7 as necessary.
9. Store the required observable quantities of the system every  $n^{\text{th}}$  Monte Carlo step per lattice site ( $MCS/site$ ) to calculate the averages.

For more details about the Monte Carlo procedure, however, the reader is referred to some excellent texts on this subject [172, 173, 179].

## 3.2 Boundary Conditions and Long-range Dipolar Interactions

Since simulations are applied to finite systems, one important question which arises is how to treat the boundaries of the lattice.

When only the short-range exchange interactions are involved in the simulations, problems of finite size may be treated easily by applying periodic boundary conditions. Then, by using finite-size scaling analysis, these finite size systems can be extrapolated to infinite systems [180, 181]. With these periodic boundary conditions, the spins

along one edge of the lattice are neighbours of corresponding spins along the other edge. This ensures that each spin has the same number of neighbours and local geometry such that all the spins are equivalent.

However, including the dipolar interactions in Monte Carlo simulations makes such techniques less straightforward since the dipole-dipole interaction is not a simple nearest neighbour interaction, but instead is a long-range interaction in which each spin interacts with every other spin. Despite these difficulties, earlier studies with long-range dipolar interactions on three-dimensional systems [182] and on square two-dimensional systems [155, 156] showed that the finite size effect can best be treated by constructing an infinite plane from replicas of a finite system. Such a replication is shown in Figure 3.1, where the finite system is denoted by dark lines and is assumed to be a two-dimensional square with lattice constant,  $a$ . By scaling all distances with the lattice constant,  $a$ , one can define  $L$  as an integer number characterizing the periodicity of the allowed configurations. Based on this definition, the finite system (i.e., unit cell) contains  $L \times L$  magnetic spins, where the  $x$  and  $y$  axes are the two axes of the square lattice and the  $z$  axis is perpendicular to it.

Knowing the state of each spin in a finite  $L \times L$  system means that one knows the state of every spin in the infinite system. This suggests that the spin configurations of the infinite system can be specified in terms of the  $L^2$  spins of the  $L \times L$  unit cell. The dipolar part of the general energy, therefore, can be rewritten such that the spins outside the finite system can be replaced with the equivalent spins from inside the unit cell. To achieve this for the case of a two-dimensional square lattice, the only spin configurations included in the calculation are those which satisfy the condition

$$\sigma^\alpha(\vec{R}_i) = \sigma^\alpha(\vec{r}_i), \quad (3.2.1)$$

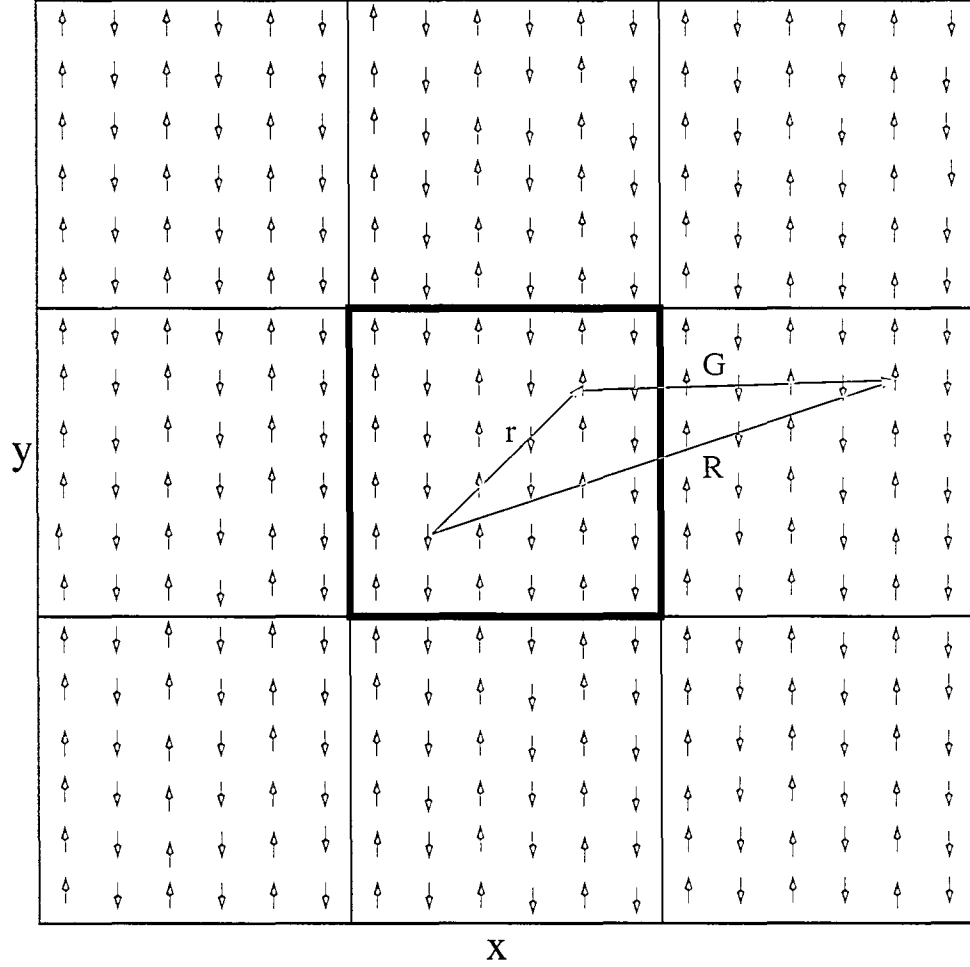


Figure 3.1: An infinite plane from replicas of a finite system (indicated by dark lines). All interactions between spins outside the finite system are included in an effective interaction between spins within the dark unit cell. In this Figure,  $x$  and  $y$  denote the two in-plane directions of the square lattice,  $\vec{r}$  is to the position of the  $i^{th}$  lattice site within the finite system,  $\vec{G}$  is the translation lattice distance, and  $\vec{R}$  is the to the position of the equivalent  $i^{th}$  lattice site in one of the replicas of a finite system.

with

$$\vec{R}_i = \vec{r}_i + \vec{G}, \quad (3.2.2)$$

where  $\vec{r}_i$  refers to the position of the  $i^{\text{th}}$  lattice site within the finite system and  $\vec{G}$  is the translation lattice vector given by

$$\vec{G} = L(n_1\hat{x} + n_2\hat{y}), \quad (3.2.3)$$

such that

$$n_1, n_2 = 0, \pm 1, \pm 2, \dots, \quad (3.2.4)$$

as shown in Figure 3.1. This assumed periodicity presents no problems for treating the short-range exchange interactions, the magnetic surface anisotropy, or even the externally applied magnetic fields because it is equivalent to the application of periodic boundary conditions.

Imposing the periodic boundary conditions given by Equation 3.2.1, the dipolar energy given by Equation 2.1.15 can be rewritten as [155, 156]

$$E_{dd} = \frac{g}{2} \left( C + \sum_{i \neq j} \sum_{\alpha, \beta} \sigma^\alpha(\vec{r}_i) \mathcal{W}^{\alpha\beta}(\vec{r}_{ij}) \sigma^\beta(\vec{r}_j) \right). \quad (3.2.5)$$

Here,  $C$  is a constant which arises from the interaction between spins at equivalent lattice sites. Because of the assumed periodicity,  $C$  is independent of the spin configuration of the system and is given by

$$C = \sum_i \sum_{\alpha, \beta} \lim_{\vec{r} \rightarrow 0} \frac{\partial}{\partial r^\alpha} \frac{\partial}{\partial r^\beta} \sum_{\vec{G}} \frac{1}{|\vec{r}_i + \vec{G} - \vec{r}|}, \quad (3.2.6)$$

while  $\mathcal{W}^{\alpha\beta}(\vec{r}_{ij})$  is the effective interaction matrix. Using the Ewald summation technique, this interaction matrix is defined as

$$\begin{aligned}\mathcal{W}^{\alpha\beta}(\vec{r}_{ij}) &= \lim_{\vec{r} \rightarrow 0} \frac{\partial}{\partial r^\alpha} \frac{\partial}{\partial r^\beta} \sum_{\vec{G}} \frac{1}{|\vec{r}_{ij} + \vec{G} - \vec{r}|}, \\ &= \frac{1}{L} \lim_{\vec{r} \rightarrow 0} \frac{\partial}{\partial r^\alpha} \frac{\partial}{\partial r^\beta} \left( \sum_{\vec{G}} \frac{\text{Erfc}(\eta|(\vec{r}_{ij} - \vec{r})/L + \vec{G}|)}{|(\vec{r}_{ij} - \vec{r})/L + \vec{G}|} \right. \\ &\quad \left. + \sum_{\vec{G} \neq 0} \frac{\exp((2\pi i \vec{G} \cdot (\vec{r}_{ij} - \vec{r})/L)) \text{Erfc}(\frac{\pi|\vec{G}|}{\eta})}{|\vec{G}|} \right).\end{aligned}\quad (3.2.7)$$

This expression can be used to evaluate  $\mathcal{W}^{\alpha\beta}(\vec{r}_{ij})$  very efficiently, which is then stored as an array for use during the simulations. The details of the calculation based on a generalization of the Ewald summation technique can be found in the references [155, 156, 171].

Finally, Equation 3.2.5 can be expressed in terms of an effective field,  $H_{dd}^\alpha(\vec{r}_i)$ , at a lattice site,  $i$ , as

$$E_{dd} = \frac{gN}{2L^2} \left( C + \sum_i \sum_\alpha \sigma^\alpha(\vec{r}_i) H_{dd}^\alpha(\vec{r}_i) \right), \quad (3.2.8)$$

such that  $H_{dd}^\alpha(\vec{r}_i)$  is given by

$$H_{dd}^\alpha(\vec{r}_i) = \sum_{j \neq i} \sum_\beta \mathcal{W}^{\alpha\beta}(\vec{r}_{ij}) \sigma^\beta(\vec{r}_j). \quad (3.2.9)$$

By including the long-range dipolar energy of the system given by Equation 3.2.8 into the Monte Carlo simulations, the Metropolis algorithm described in the previous section needs to be modified as follows:

1. Start with an initial spin configuration,  $\nu_i$ .
2. Calculate the effective field given by Equation 3.2.9 at each site of the lattice.

3. Go through the lattice in a random way and pick a target spin,  $\vec{\sigma}(\vec{r}_i)$ .
4. Generate a new state,  $\nu_{l+1}$ , by randomly changing the orientation of the target spin,  $\vec{\sigma}(\vec{r}_i)$ , to

$$\vec{\sigma}'(\vec{r}_i) = \vec{\sigma}(\vec{r}_i) + \Delta\vec{\sigma}(\vec{r}_i). \quad (3.2.10)$$

5. Compute  $\Delta E$  such that

$$\Delta E = \sum_{\alpha} \Delta\sigma^{\alpha}(\vec{r}_i) H_{dd}^{\alpha}(\vec{r}_i) + \Delta E_{ex} + \Delta E_{\kappa}, \quad (3.2.11)$$

where  $\Delta E_{ex}$  and  $\Delta E_{\kappa}$  denote the change in the exchange interaction and the change in the magnetic surface anisotropy, respectively.

6. Calculate  $W(\nu_l \rightarrow \nu_{l+1})$  according to Equation 3.1.8.
7. Generate  $Z$ .
8. Compare  $Z$  with  $W(\nu_l \rightarrow \nu_{l+1})$ . If  $W(\nu_l \rightarrow \nu_{l+1})$  is greater than  $Z$  accept the move, otherwise leave the spin as it is and retain the old spin configuration.
9. If the new spin configuration is accepted, then the effective field at each site is updated to

$$H_{dd}^{\alpha}(\vec{r}_i) = H_{dd}^{\alpha}(\vec{r}_i) + \sum_{j \neq i} \sum_{\beta}^{L^2} \mathcal{W}^{\alpha\beta}(\vec{r}_{ij}) \Delta\sigma^{\beta}(\vec{r}_j). \quad (3.2.12)$$

10. Repeat steps 3 to 9 as required.
11. Store the necessary observable quantities of the system every  $n^{th}$  Monte Carlo step per lattice site to calculate the averages.

This algorithm has some important features. One of these features is that most of the simulation time is spent in updating the effective field at  $L^2$  sites after each accepted change of a spin. For this reason, the time required to complete one Monte Carlo step per site by accepting a new  $\nu_{l+1}$  state scales as  $L^4$  in 2-dimensional systems or as  $L^6$  in 3-dimensional systems. Of particular importance is the way in which a new state,  $\nu_{l+1}$ , is generated from state,  $\nu_l$ , by randomly changing the orientation of the target spin from  $\vec{\sigma}(\vec{r}_i)$  to  $\vec{\sigma}'(\vec{r}_i)$  as mentioned in Step 4 above. In this study, simulations are conducted on both plane rotator and Heisenberg systems. For simulations of the plane rotator system, the change in orientation of the target spin is made by randomly selecting the angle  $\phi$ , which the target spin makes with the  $x$ -axis. Thus, the selected orientations of all target spins are uniformly distributed along the arc of a ring with radius 1 as shown in Figure 3.2. In the case of the Heisenberg system, however, two parameters must be used to change the orientation of the target spin,  $\vec{\sigma}_i$ . These two parameters are  $\theta$  and  $\phi$  as shown in Figure 3.3. To obtain a uniform sampling,  $\theta$  and  $\phi$  are selected randomly through two uniform distribution random numbers,  $Z_1$  and  $Z_2$ , such that

$$\begin{aligned}\theta &= \cos^{-1}(2Z_1 - 1), \\ \phi &= 2\pi Z_2,\end{aligned}\tag{3.2.13}$$

where each of these two random numbers is between 0 and 1. During simulations of this system, the orientations of all the target spins are changed randomly, such that they are uniformly distributed over the surface of a sphere with radius 1 as shown in Figure 3.4.

Also worth mentioning is that the two-dimensional arrays are stored as one-dimensional arrays, because this process provides more efficient access to the arrays.

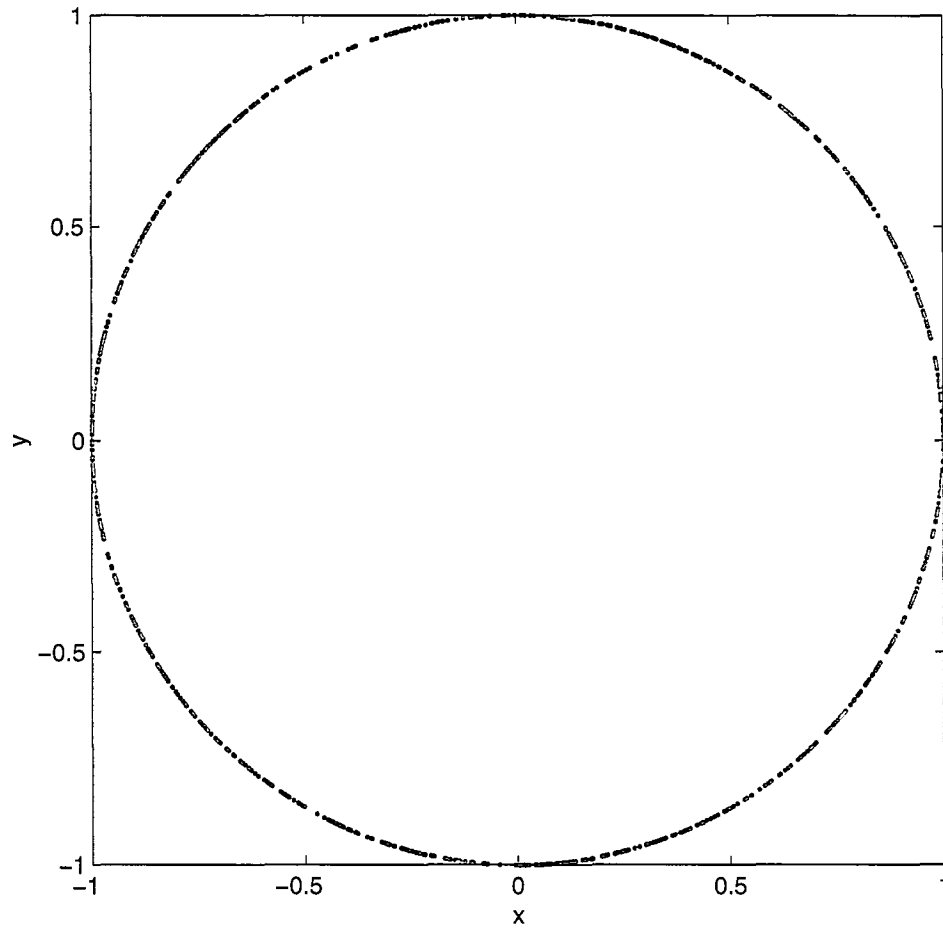


Figure 3.2: A uniform distribution of the randomly selected orientations of the target spins along the arc of a ring with radius 1.

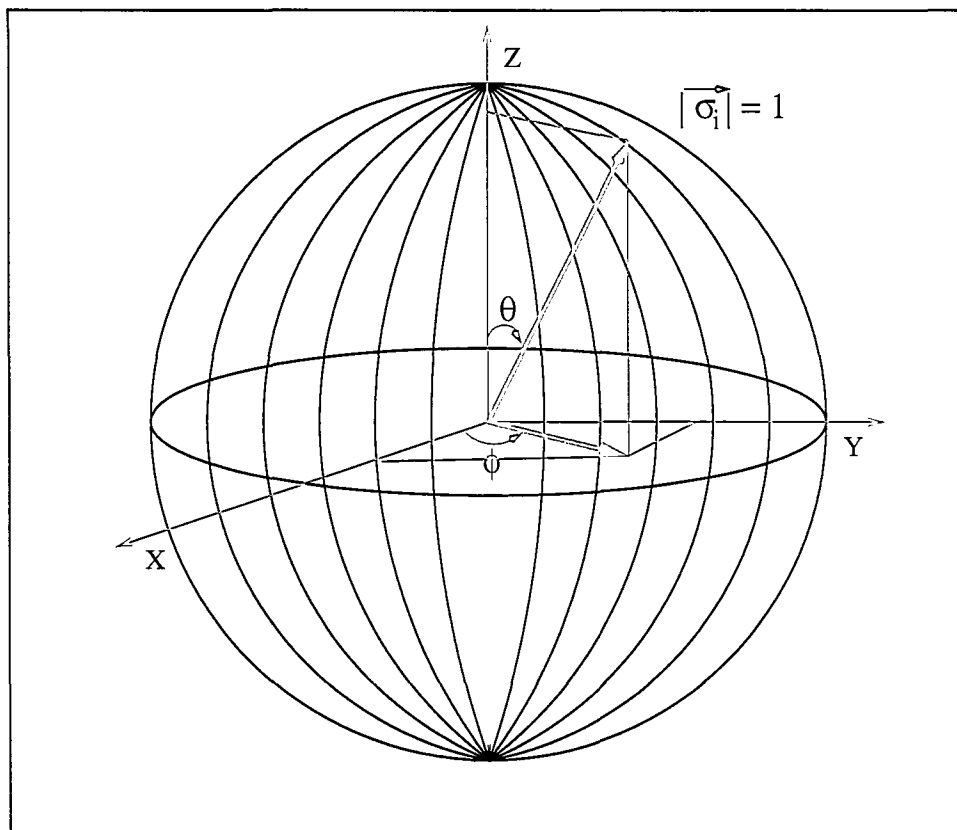


Figure 3.3: The spherical coordinates ( $|\vec{\sigma}_i|$ ,  $\theta$ , and  $\phi$ ) for the target spin,  $\vec{\sigma}_i$ .

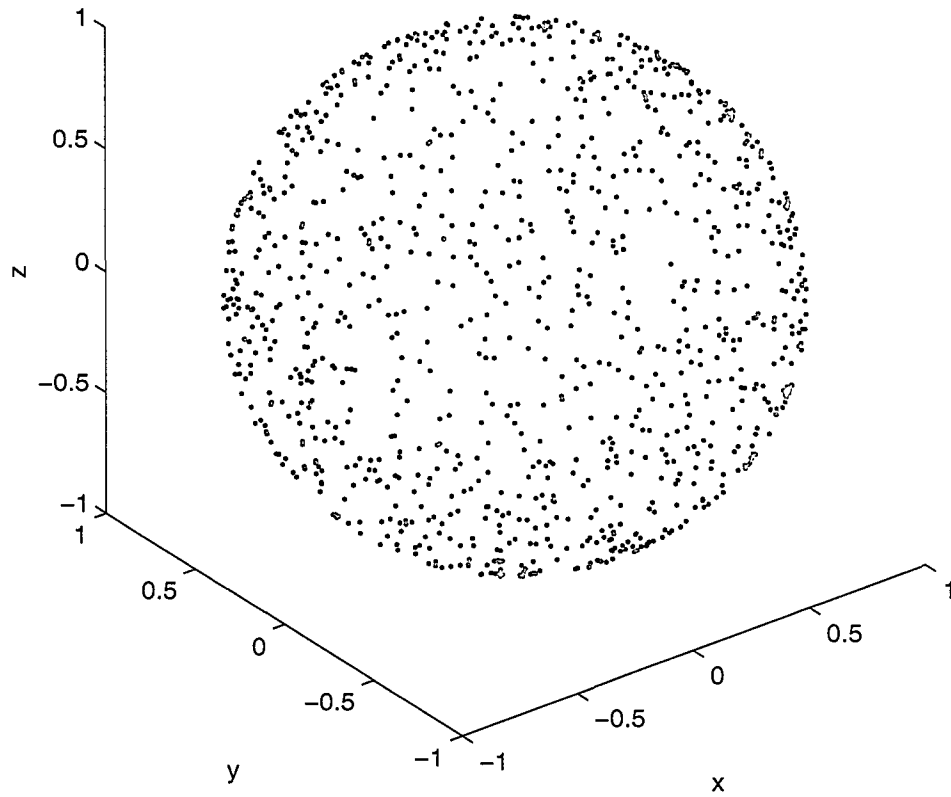


Figure 3.4: A uniform distribution of the randomly selected orientations of the target spins over the surface of a sphere with radius 1.

These computational details are comprehensively reviewed in a number of publications [155, 156].

### 3.3 Computational Aspects

As mentioned in chapter 2, in this study four systems of the basic model are examined that describe two-dimensional magnetic systems on a square lattice. In these systems the spins are treated classically and are represented by vectors of fixed magnitude. In the case of the plane rotator system the spins are constrained to lie in the plane, while in the Heisenberg system the spins are allowed to orient in any direction. The systems include the nearest neighbor antiferromagnetic exchange interaction, the long-range dipolar interaction, and the magnetic surface anisotropy, characterized respectively by the three coefficients  $J, g$ , and  $\kappa$ . Throughout this research, the two coupling parameters,  $J$  and  $\kappa$ , are measured in units of the parameter  $g$ . In addition, the temperature,  $T$ , is measured in units of  $1/k_B$  such that  $k_B$  is the Boltzmann constant. The calculations are performed on three different sizes of the square lattice ( $N = L \times L = 32^2, 64^2, 104^2$ ).

In determining the properties of these systems, equilibrium variables (e.g., energy and magnetization) that vary as a function of the model parameters ( $T/g, J/g, \kappa/g$ ) need to be considered. This permits the identification and study of the phase behavior of the system as a function of model parameters. In performing a temperature scan for example, the final state of the system at temperature,  $T/g$ , can be selected as the initial state for the next nearest temperature,  $T/g \pm \delta(T/g)$ . In performing the simulations over a range of increasing temperatures such as between  $T = 0.05g$  and  $T = 5.0g$  in steps of 0.05, the simulation would be initially performed at  $T = 0.05$

using the proper ground state. The final state of that simulation would then be used as the initial state for the simulation at  $T = 0.1g$ , and so on. The same technique is used in the process of cooling the system. In performing the simulations over a range of temperatures between  $T = 5.0g$  and  $T = 0.05g$  in steps of 0.05 for instance, the final state of that simulation at  $T = 5.0g$  would then be used as the initial state for the simulation at  $T = 4.95g$ , and so on. Using this technique for both heating and cooling reduces the time of the simulation because the equilibrium state (i.e., the state that contributes significantly to the thermal average) at  $T/g$  will be more similar to that at  $T/g \pm \delta(T/g)$ . A similar technique can also be used to scan with respect to other variables.

However, the question still remains as to how to determine the proper ground state spin configuration to be used as an initial state of the system at the beginning of the simulation. In the present study, this is done in the following manner. Before applying the simulation over a range of temperatures, all parameters of the energy involving a very low temperature (e.g.,  $T = 0.05g$ ) are specified. After that, a disordered state (i.e., random directions of the spins) is chosen as an initial state of the system. Then, the simulations are performed for a sufficient time allowing the system to relax using this low temperature. At the end of this simulation, the final spin configuration is obtained. From this spin configuration, the proper ground state of the system is determined. To ensure that the system relaxes to the proper ground state, other arbitrary initial states are used and the same procedure is repeated. Indeed, heating and then cooling the system gives additional evidence that the system relaxes to the same ground state spin configuration.

Before collecting the data, the system must be allowed to come to equilibrium.

Equilibrium means that the average probability of finding the system in any particular state,  $\nu$ , is proportional to the Boltzmann weight,  $\exp(-\beta E_\nu)$ , of that state. Therefore, at equilibrium the system spends the majority of its time in a small subset of states in which its internal energy and other properties take on a narrow range of values. In order to get a good estimate of the equilibrium value of any property of the system, it is necessary to generate a sufficient number of configurations until the system has found its way to one of the states that fall within this narrow range (i.e., until the image of the initial state is lost). The number of configurations required to bring the system to equilibrium is called the equilibration time,  $\tau_{eq}$ .

The normal practice in order to check whether or not the system has reached equilibrium is to plot a graph of some quantity of interest for the investigated system as a function of time (i.e.,  $MCS/site$ ) from the start of the simulation. From this graph,  $\tau_{eq}$  is estimated. As done in this research, the internal energy per spin is one of the interesting quantities plotted as a function of time. Samples of such curves are shown in Figure 3.5 for four different values of temperature,  $T = 0.05g, 0.1g, 0.15g, 0.2g$ , for the anisotropic Heisenberg model with  $J = -10.0g$ , and  $\kappa = -1.5g$ . At any of these fixed values of  $T/g$ , Figure 3.5 suggests that the system relaxes from an initial state to an equilibrium state in no more than  $10^4 MCS/site$ . Therefore, this is the value of  $\tau_{eq}$  used in this research.

Once the system has reached equilibrium, the observable quantities of interest need to be measured over a suitably long period of time,  $\tau$ , and averaged to obtain the best estimate of these observable quantities. In this research, the value of  $\tau$  used to calculate the averages, however, depends on both the size of the system and the temperature. For the results presented in this research, the simulations are

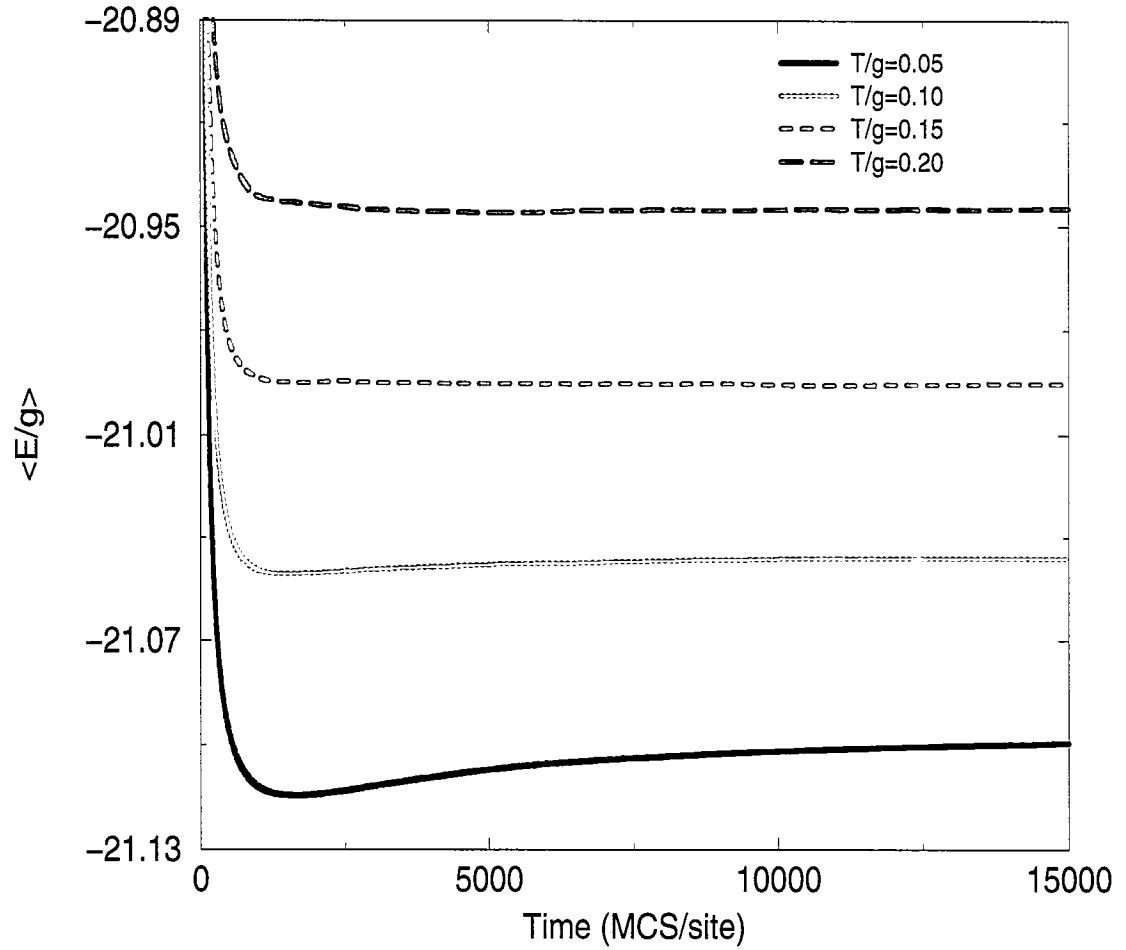


Figure 3.5: Average internal energy,  $\langle E/g \rangle$ , per spin as a function of time,  $MCS/site$ , for the Heisenberg model with  $J = -10.0g$ ,  $\kappa = -1.5g$ , and  $L = 64$  at four different values of temperature,  $T = 0.05g, 0.1g, 0.15g, 0.2g$ , from the start of the simulation. The final spin configuration at any of these fixed temperatures is considered as an initial state or the next nearest temperature.

applied over a range from  $10 \times 10^4$  *MCS/site* at high temperatures for the  $104 \times 104$  system, to  $29 \times 10^4$  *MCS/site* at low temperatures for the  $32 \times 32$  system. Physical properties after one *MCS/site* are very strongly correlated, particularly at all second-order phase transitions where the critical divergence of the correlation length is strongly distributed by the finite size and the periodicity of the system [155, 156, 172, 173, 176, 183, 175, 184]. Therefore, it may be better not to collect the desired observable quantities immediately after every *MCS/site*, but once every  $n^{\text{th}}$  *MCS/site* where  $n$  is some typical correlation time required to allow correlations to efficiently decay to zero. In this study, it is adequate to collect the interesting observable quantities of the system when calculating thermodynamic averages every 10 *MCS/site*.

Finally, the observable quantities of interest for the investigated systems need to be determined. In this research, the most likely candidates for these observable quantities are the internal energy and magnetization (order parameters). Given the internal energy,  $E$ , and the magnetization,  $M$ , every  $n^{\text{th}}$  *MCS/site*, these quantities can be averaged over the the whole time period of the simulation. Then, dividing these quantities by the number of spins,  $N$ , results in the average internal energy,  $\langle E \rangle$ , and average magnetization,  $\langle M \rangle$ , per spin. Also, the squares of the internal energy and magnetization per spin are averaged to find quantities like the specific heat,  $C_v$ , and the magnetic susceptibility,  $\chi$ , per spin

$$C_v = \frac{1}{NT^2}(\langle E^2 \rangle - \langle E \rangle^2), \quad (3.3.1)$$

$$\chi = \frac{1}{NT}(\langle M^2 \rangle - \langle M \rangle^2). \quad (3.3.2)$$

While it is possible to estimate thermal averages for model systems such as magnetization or internal energy using Monte Carlo techniques, it is less obvious how these techniques may be used to calculate the free energy,  $F$ , because it cannot be expressed as an ensemble average. However, it is easy to express the free energy difference,  $\Delta F$ , between the system of interest (with internal energy  $E$  at temperature  $T$ ) and a suitably chosen reference system (with internal energy  $E_o$  at temperature  $T_o$ ) as an ensemble average

$$\Delta F = -T \ln (\langle \exp - (E/T - E_o/T_o) \rangle_o), \quad (3.3.3)$$

where  $\langle \rangle_o$  denotes an average over a canonical ensemble of a reference system. The exact details of the derivation, however, are presented in Appendix A. This means that it is possible to estimate  $\Delta F$  with respect to some reference system by a conventional Monte Carlo technique using the Metropolis algorithm. This can be done by using non-equilibrium sampling technique [185, 186, 187]. From  $\Delta F$ , the free energy for the system of interest can be calculated over a particular range of a system parameter like  $T$ ,  $J$  or  $\kappa$  using the fact that the free energy is a continuous function.

In particular, some care must be given to the choice of reference system. In practice, Equation 3.3.3 is very useful for estimating the free energy differences between any two systems that are not too dissimilar as will be shown in chapter 5, where the simulation results of the dipolar plane rotator antiferromagnetic system will be presented and discussed.

### 3.4 Benchmarks

Monte Carlo simulations with long-range interactions require very high-performance computational resources which were generally not available before ten years ago. Since the present code included such interactions (dipolar interactions), the simulations presented in this thesis were run on a number of different computers using resources provided by many sources. At Memorial University of Newfoundland the code was run on an Alpha Server 4100, a set of Digital Alpha systems (Alcor, Alioth, Alphaid, and Mizar). Some of this research was done using a Silicon Graphics Onyx 3400 provided by Memorial University's Advanced Computation and Visualization Centre. A few jobs were run on a Silicon Graphics Origin 2000 provided by the High Performance Computing Center at the University of Alberta. However, the majority of the simulations presented in this thesis was done on the MACI Alpha Cluster (DS10, DS20E, XP1000, ES40, and ES45) which was provided by the High Performance Computing Center in Calgary.

To ensure that the code was functioning properly, in this research some independent results by Rastelli *et al.* [121] were replicated using the present code. The results taken from this reference are shown in Figure 3.6, where the heat capacity of the pure dipolar plane rotator system on a two-dimensional square lattice with  $L = 32$  as a function of temperature is plotted. Comparing the obtained results ( $\circ$ ) with the results ( $\star$ ) obtained by Rastelli *et al.*, shows an evidence of agreement between them (see Figure 3.6).

Other earlier results found by Gouvêa *et al.* [188] are shown in Figure 3.7, where the perpendicular order parameters,  $M_{\perp}$ , of the Heisenberg system on a two-dimensional square lattice with  $L = 64$ ,  $g = 0$ , and where  $J^x = J^y = \frac{1}{1.05}J^z$  as a

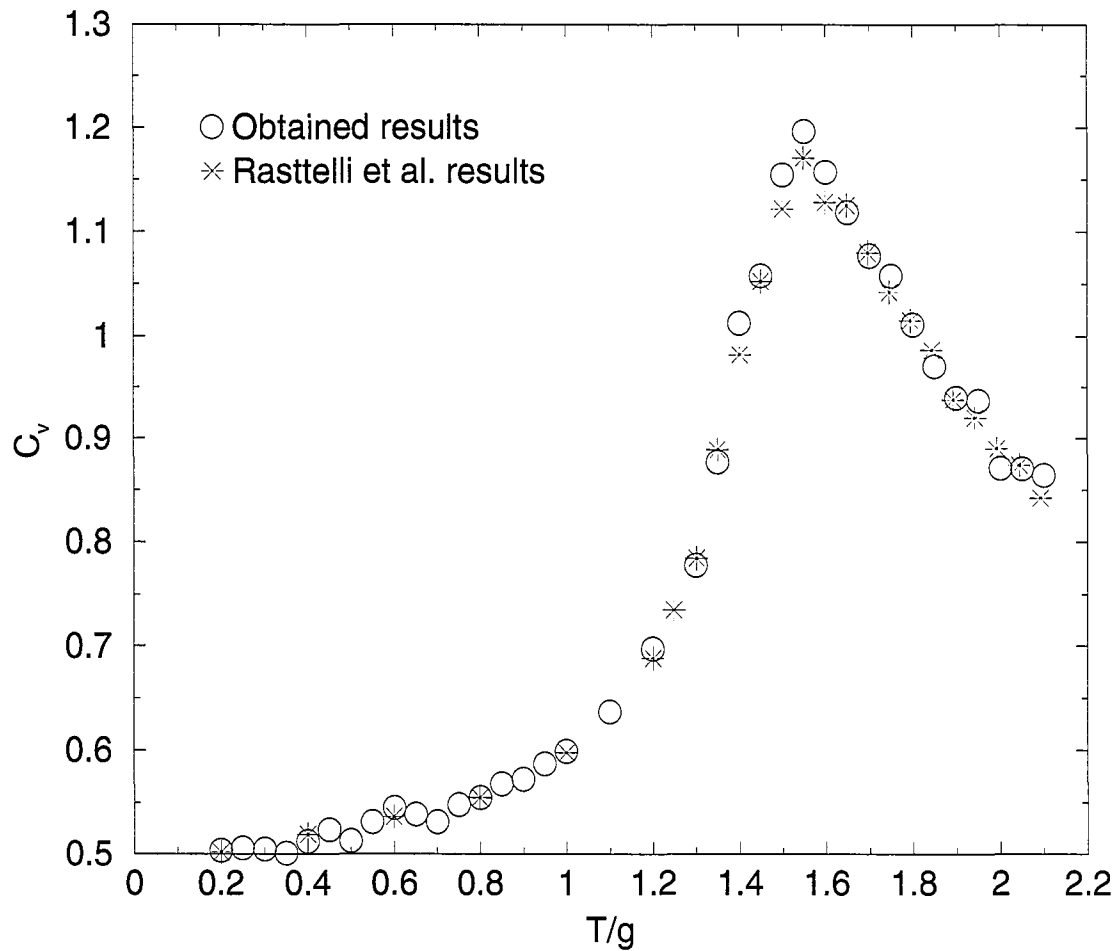


Figure 3.6: A comparison between the obtained (○) heat capacity,  $C_v$ , per spin as a function of temperature,  $T/g$ , and the results (★) obtained by Rastelli *et al.* for the pure dipolar plane rotator system on a two-dimensional square lattice with  $L = 32$ .

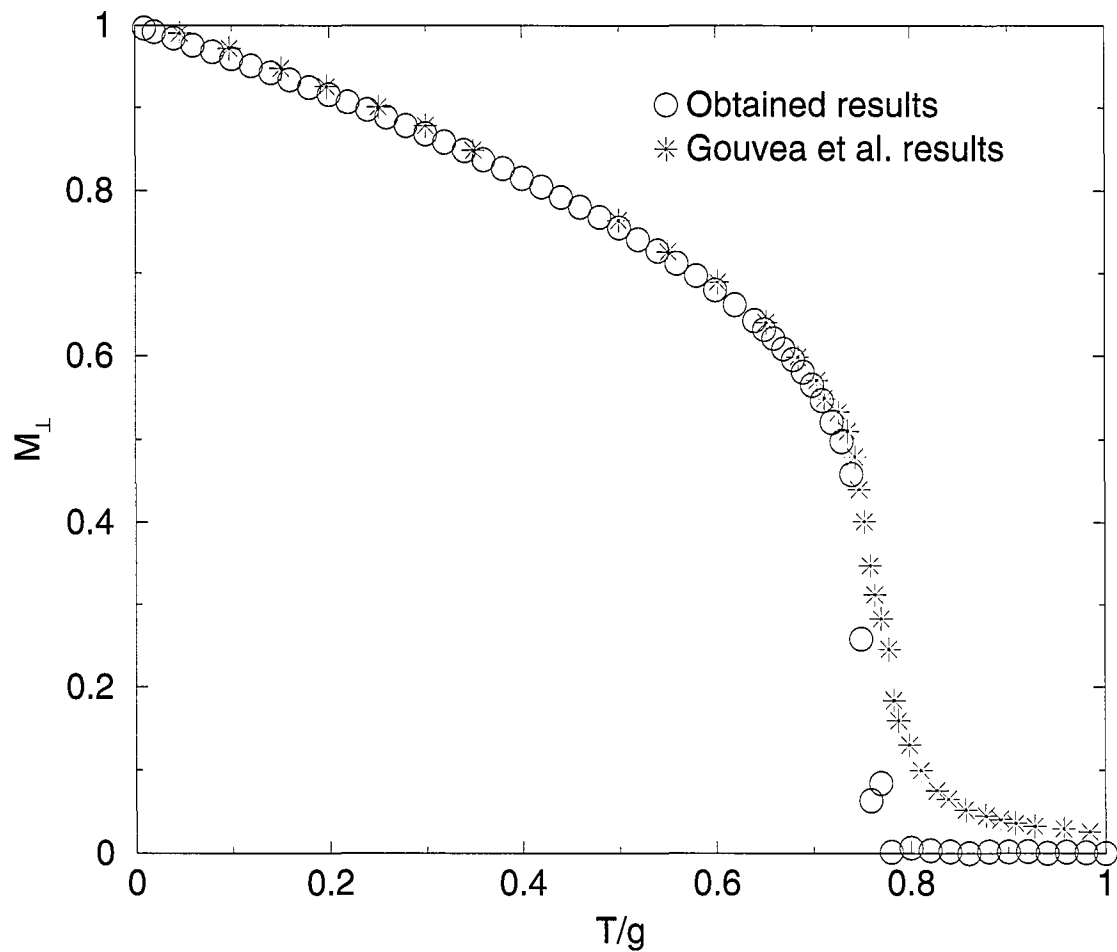


Figure 3.7: A comparison between the obtained ( $\circ$ ) perpendicular order parameter,  $M_{\perp}$ , per spin as a function of temperature,  $T/g$ , and the results ( $\star$ ) found by Gouvêa *et al.* for the Heisenberg system on a two-dimensional square lattice with  $L = 64$ ,  $g = 0$ , and where  $J^x = J^y = \frac{1}{1.05} J^z$ .

function of temperature is plotted. The results obtained in the present analysis (○) compare well with these obtained by Gouvêa *et al.* (★) except in the vicinity of the transition temperature (see Figure 3.7). This difference may be attributed to the differences in the implementation of the Monte Carlo algorithm in these two simulations. The code used in this research is based on the Metropolis single-spin moves, while Gouvêa *et al.* applied a combination of Metropolis single-spin moves, over-relaxation moves, and Wolff single-cluster operations in their code. This difference aside, the comparison shows generally good agreement between the present results and those of Gouvêa *et al.*

# Chapter 4

## The Heisenberg System

### 4.1 Introduction

In this chapter the phase behavior that can arise as a consequence of the competition between the dipolar and the exchange interaction in low-dimensional antiferromagnetic systems is examined for both zero and finite temperature. This chapter, therefore, does not include the effect of the magnetic surface anisotropy, although the system can be extended to incorporate it into the analysis as will be shown in chapters 6 and 7. This study is based on Monte Carlo simulations of a simple model of a two-dimensional antiferromagnetic system. The system consists of  $N$  classical spins of fixed magnitude arranged on a square lattice of length  $L$  ( $N = L \times L = 32^2, 64^2, 104^2$ ) which interact through a nearest neighbor antiferromagnetic exchange interaction and a long-range dipolar interaction. The two in-plane directions of the square lattice of the system are assumed to be  $\hat{x}$  and  $\hat{y}$ , and the direction perpendicular to the plane is  $\hat{z}$ .

In this system the energy of a particular spin configuration  $\{\vec{\sigma}_i\}$  is given by

$$E(\{\vec{\sigma}_i\}) = g \sum_{i \neq j} \left( \frac{\vec{\sigma}_i \cdot \vec{\sigma}_j}{r_{ij}^3} - 3 \frac{(\vec{\sigma}_i \cdot \vec{r}_{ij})(\vec{\sigma}_j \cdot \vec{r}_{ij})}{r_{ij}^5} \right) - J \sum_{\langle ij \rangle} \vec{\sigma}_i \cdot \vec{\sigma}_j. \quad (4.1.1)$$

Here,  $\vec{\sigma}_i$  is a three-dimensional classical spin vector with  $|\vec{\sigma}_i|^2 = 1$ , and the exchange interaction is assumed to be antiferromagnetic (i.e.,  $J < 0$ ).

In the following three sections both the zero and the finite temperature properties of the model are discussed and the results of the simulations including the phase diagram are presented. A brief discussion of the low temperature order parameter follows in section 4.5. A discussion of some potential applications of the results is presented in section 4.6, and the chapter finishes with a summary.

## 4.2 Ground State Properties

In the absence of an exchange interaction ( $J = 0$ ) the ground state spin configuration has the spins aligned in the plane of the system (the  $AF_{\parallel}$  phase). However, it has been noted by several authors that the planar ground state of the pure dipolar system is continuously degenerate [112, 114, 118]. Two examples of the dipolar ground state spin configurations are shown in Figure 4.1a and Figure 4.1b. Other ground state spin configurations can be generated by a transformation which continuously maps the spin configuration shown in Figure 4.1a into the spin configuration in Figure 4.1b by varying the angle  $\phi$  shown in Figure 4.2 [118]. The fact that the ground state is continuously degenerate is somewhat surprising since the dipolar interaction is not invariant under rotation. It can readily be shown that the energy of these states ( $AF_{\parallel}$  states) is not affected by the addition of the exchange interaction and is given by [50]

$$E_{AF_{\parallel}} = -5.0989g. \quad (4.2.1)$$

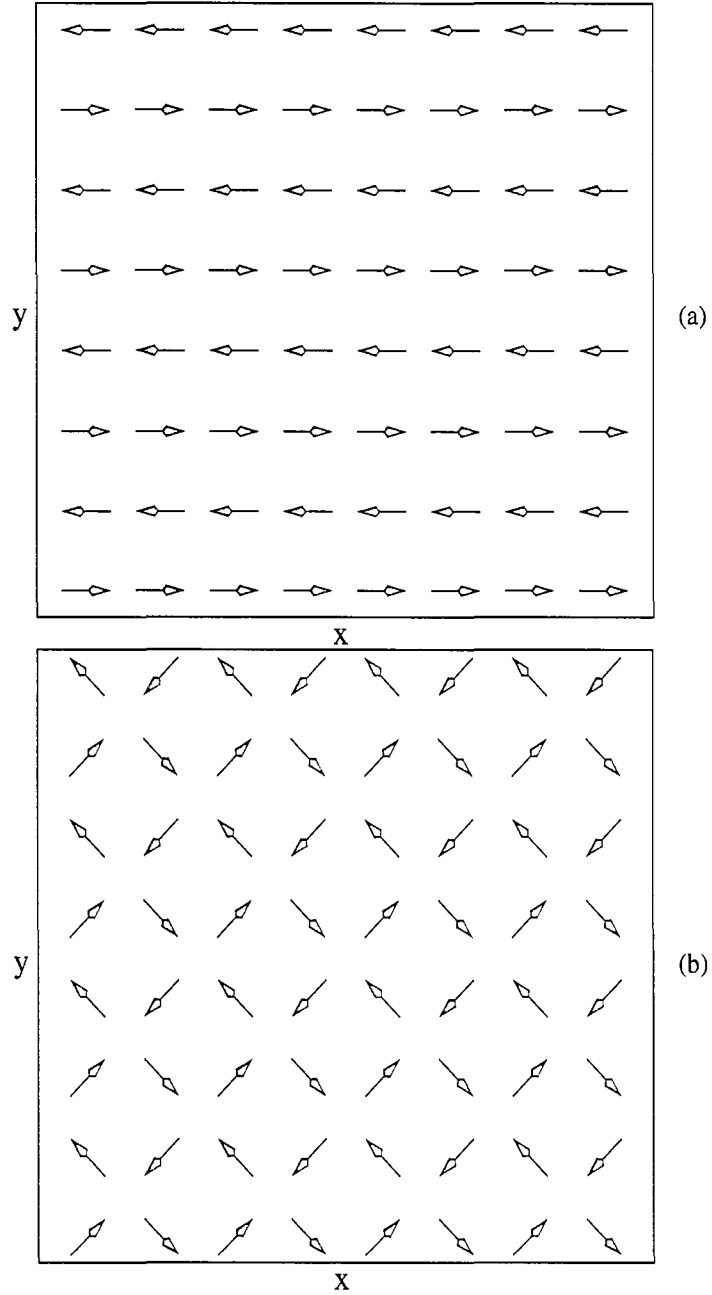


Figure 4.1: Two planar ground state spin configurations. In one (a) the spins are aligned along the x-axis in the other (b) they are oriented at  $\pm\pi/4$  to the x-axis.

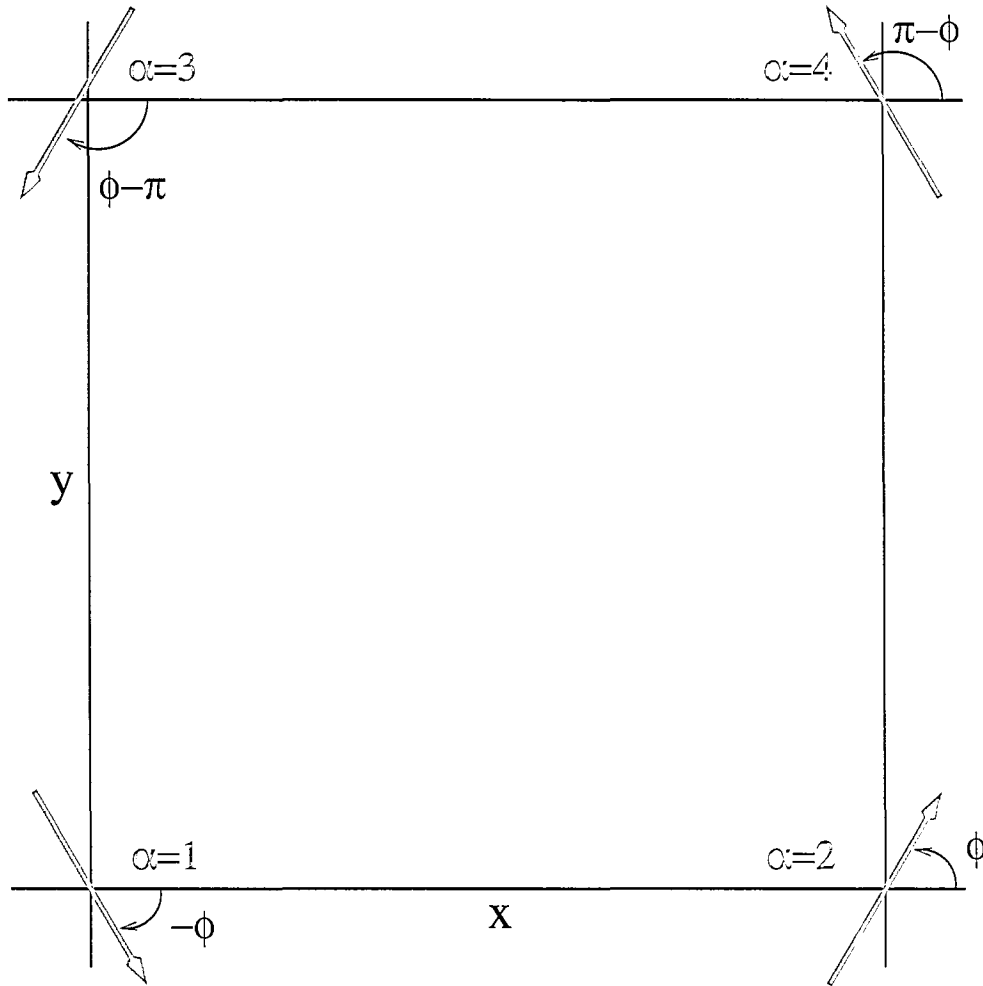


Figure 4.2: A schematic of the magnetic unit cell used to describe the magnetic order showing the four magnetic sub-lattices and labels attached to them. In this Figure,  $x$  and  $y$  denote the two in-plane directions of the square lattice. The energy of the spin configuration is independent of the angle  $\phi$  shown in the Figure.

For low values of  $|J|$  this manifold of degenerate states constitutes the ground state. However, if the strength of the antiferromagnetic exchange parameter is sufficiently large, the ground state spin configuration switches to one in which the spins are perpendicular to the plane of the system with each spin aligned anti-parallel to each of its nearest neighbors (the  $AA_{\perp}$  phase) as shown in Figure 4.3. The energy of this state is given by [50]

$$E_{AA_{\perp}} = -2.6459g + 2J. \quad (4.2.2)$$

Comparing the energies of the planar (Equation 4.2.1) and the perpendicular (Equation 4.2.2) spin configurations, it is seen that, at zero temperature, a transition from the degenerate parallel antiferromagnetic phase to the non-degenerate perpendicular antiferromagnetic phase occurs when  $|J| = J_0$ , with

$$\begin{aligned} J_0/g &= (5.0989 - 2.6459)/2 \\ &= 1.2265. \end{aligned} \quad (4.2.3)$$

Thus, the competition between the dipolar and the antiferromagnetic exchange interactions can give rise to a reorientation transition at zero temperature.

To construct order parameters for both of these states the lattice is divided into four sub-lattices [118], each of which is square with a lattice spacing twice that of the original lattice. The magnetic lattice, therefore, contains four sites per unit cell, each site corresponding to one of the sub-lattices. Denoting the four sites by  $\alpha \in \{1 \dots 4\}$ , as shown in Figure 4.2, the sub-lattice magnetizations,  $\vec{M}_{AF_{\parallel}}^{\alpha}$  and  $\vec{M}_{AA_{\perp}}^{\alpha}$ , may be

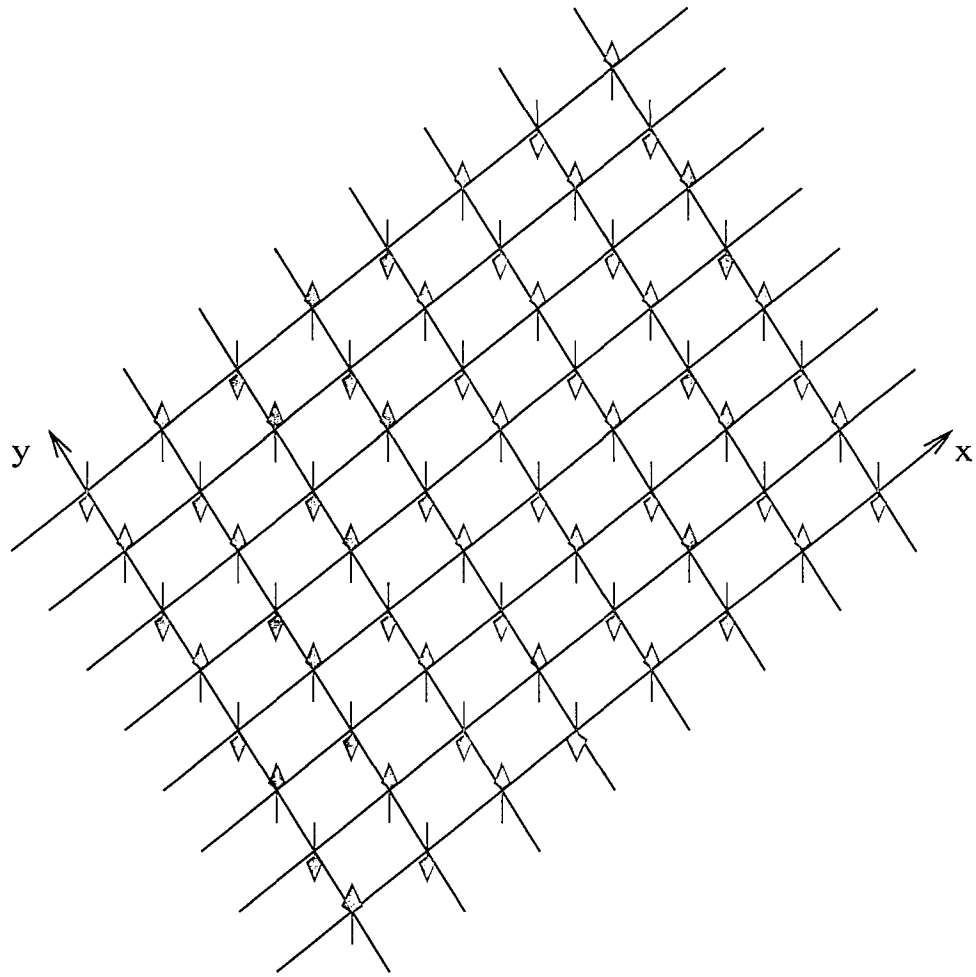


Figure 4.3: The perpendicular ground state spin configuration in the case of the large value of  $|J|/g$ , where  $x$  and  $y$  denote the two in-plane directions of the square lattice.

defined as

$$\begin{aligned}\vec{M}_{AF_{\parallel}}^{\alpha} &= M_x^{\alpha} \hat{x} + M_y^{\alpha} \hat{y} \\ &= \frac{4}{N} \left( \sum_{\vec{r}_{\alpha}} \sigma^x(\vec{r}_{\alpha}) \right) \hat{x} + \frac{4}{N} \left( \sum_{\vec{r}_{\alpha}} \sigma^y(\vec{r}_{\alpha}) \right) \hat{y}\end{aligned}\quad (4.2.4)$$

and

$$\begin{aligned}\vec{M}_{AA_{\perp}}^{\alpha} &= M_z^{\alpha} \hat{z} \\ &= \frac{4}{N} \sum_{\vec{r}_{\alpha}} \sigma^z(\vec{r}_{\alpha}) \hat{z},\end{aligned}\quad (4.2.5)$$

from which the order parameters,  $M_{AF_{\parallel}}$  and  $M_{AA_{\perp}}$ , may be defined as

$$M_{AF_{\parallel}} = \frac{1}{4} \left| (M_x^1 + M_x^2 - M_x^3 - M_x^4) \hat{x} + (M_y^1 + M_y^3 - M_y^2 - M_y^4) \hat{y} \right| \quad (4.2.6)$$

and

$$M_{AA_{\perp}} = \frac{1}{4} \left( |M_z^1| + |M_z^2| + |M_z^3| + |M_z^4| \right) \hat{z}. \quad (4.2.7)$$

For the planar ground state,  $|J| < J_0$ ,

$$M_{AF_{\parallel}} = 1$$

and

$$M_{AA_{\perp}} = 0,$$

while for the perpendicular ground state,  $|J| > J_0$ ,

$$M_{AF_{\parallel}} = 0$$

and

$$M_{AA_{\perp}} = 1.$$

### 4.3 Finite Temperature Properties

In the case of the pure dipolar system ( $J = 0$ ) Monte Carlo simulations clearly show the existence of long-range magnetic order for both the planar [118, 109] and the Heisenberg model [144] at low temperature. In both cases, the equilibrium spin configuration is antiferromagnetic, with the spins aligned along either the  $x$  or the  $y$ -axis, similar to the configuration shown in Figure 4.1a. Since the dipolar ground state is continuously degenerate, the existence of long-range magnetic order poses two interesting and subtle questions, both of which are relevant to the current work. Firstly, since the degeneracy of the ground state implies the existence of a gapless mode in the spin wave spectra, a result confirmed by spin wave calculations for both the Heisenberg [189] and the planar model [118], why does the amplitude of spin fluctuations not diverge and the magnetic order disappear at finite temperature as in the simple nearest neighbour Heisenberg model [102]? Secondly, if the long-range magnetic order does persist at finite temperature, how is the easy axis of magnetization determined if the ground state is continuously degenerate?

The answer to both of these questions lies in the fact that the degeneracy of the dipolar ground state does not arise as a result of a global symmetry. As a consequence, while the ground state energy is independent of the magnetization axis, the spectrum of energy excitations is not. This means that the thermal spin fluctuations break the degeneracy of the ground state and generate an effective potential that has the four fold symmetry of the underlying lattice [116, 117, 118]. This effective potential will manifest itself as a gap in the spin wave spectra [120, 109] that renders the amplitude finite [109] at finite temperature, and can serve to define an easy axis of magnetization.

A similar situation pertains in the case of the present system for  $|J| < J_0$  ( $J_0 = 1.2265g$ ). The order parameters  $M_{AF\parallel}$  and  $M_{AA\perp}$  for  $|J| = 0.4g$  and  $|J| = 1.0g$  defined by Equations 4.2.6 and 4.2.7 are shown in Figure 4.4 in terms of the thermally averaged sub-lattice magnetization given by

$$\vec{M}_{AF\parallel}^\alpha = \langle M_x^\alpha \rangle \hat{x} + \langle M_y^\alpha \rangle \hat{y} \quad (4.3.1)$$

and

$$\vec{M}_{AA\perp}^\alpha = \langle M_z^\alpha \rangle \hat{z}. \quad (4.3.2)$$

In both cases the data show a planar phase at low temperature  $M_{AF\parallel} \neq 0$  and  $M_{AA\perp} \approx 0$ . As the temperature is increased the order parameter decreases, dropping rapidly at around  $T = (1.4 \pm 0.05)g$  for both  $|J| = 0.4g$  and  $|J| = 1.0g$ , to indicate the transition from the ordered planar antiferromagnetic phase to the disordered paramagnetic phase. In both cases the transition sharpens as the system size increases, consistent with a second-order transition. The existence of a second-order phase transition is also reflected in the susceptibility (Figure 4.5), in the average internal energy (Figure 4.6), and in the heat capacity (Figure 4.7) data. It is interesting to note that, while the equilibrium phase at low temperature clearly shows long-range magnetic order, the heat capacity for the planar phase shows a transition that is relatively insensitive to system size. Qualitatively, the peak in the heat capacity resembles the peak in the heat capacity at the Kosterlitz Thouless transition temperature in the two-dimensional XY-model ( $g = 0$ ).

While the order parameter and other thermodynamic observations appear qualitatively similar for different values of  $J$  (Figures 4.4 - 4.7), the nature of the equilibrium spin configuration is nevertheless quite different. A sample spin configuration for each

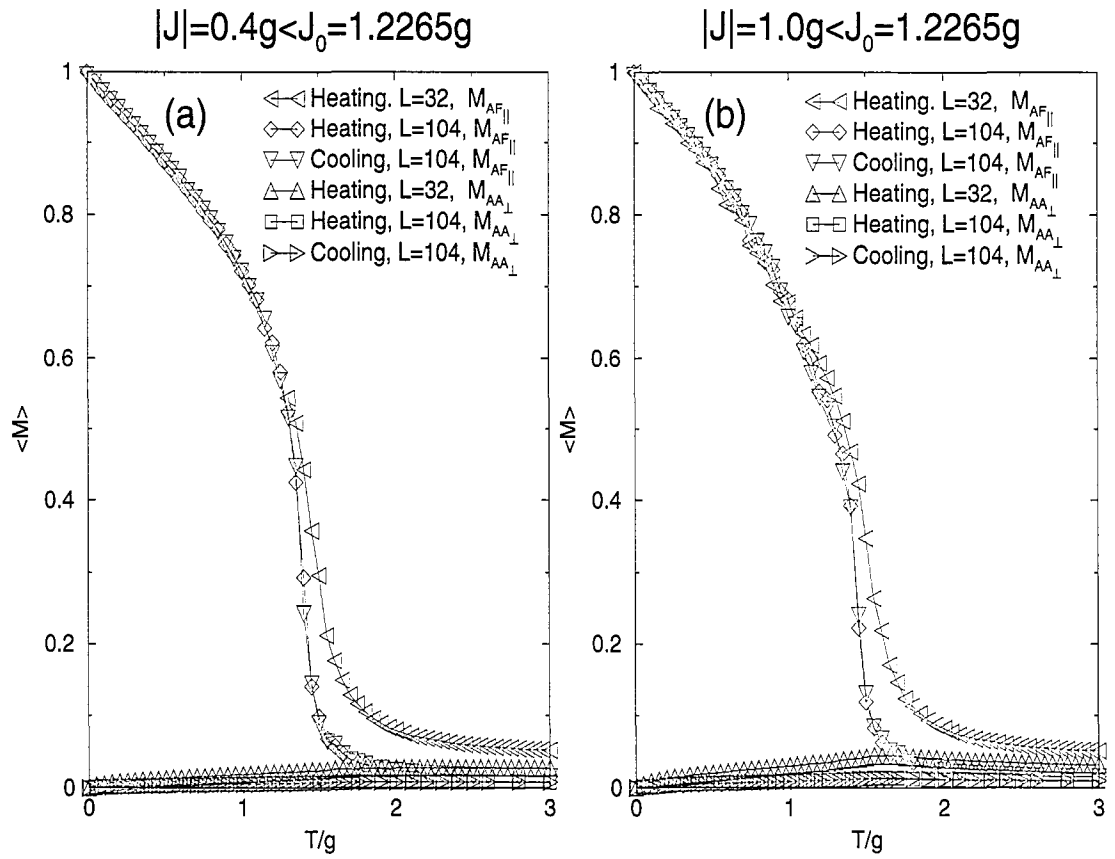


Figure 4.4: A plot of the parallel and perpendicular order parameters,  $M_{AF\parallel}$  and  $M_{AA\perp}$ , per spin as a function of temperature,  $T/g$ , for (a)  $|J| = 0.4g$  and (b)  $|J| = 1.0g$  with  $L = 32$  and  $104$ .

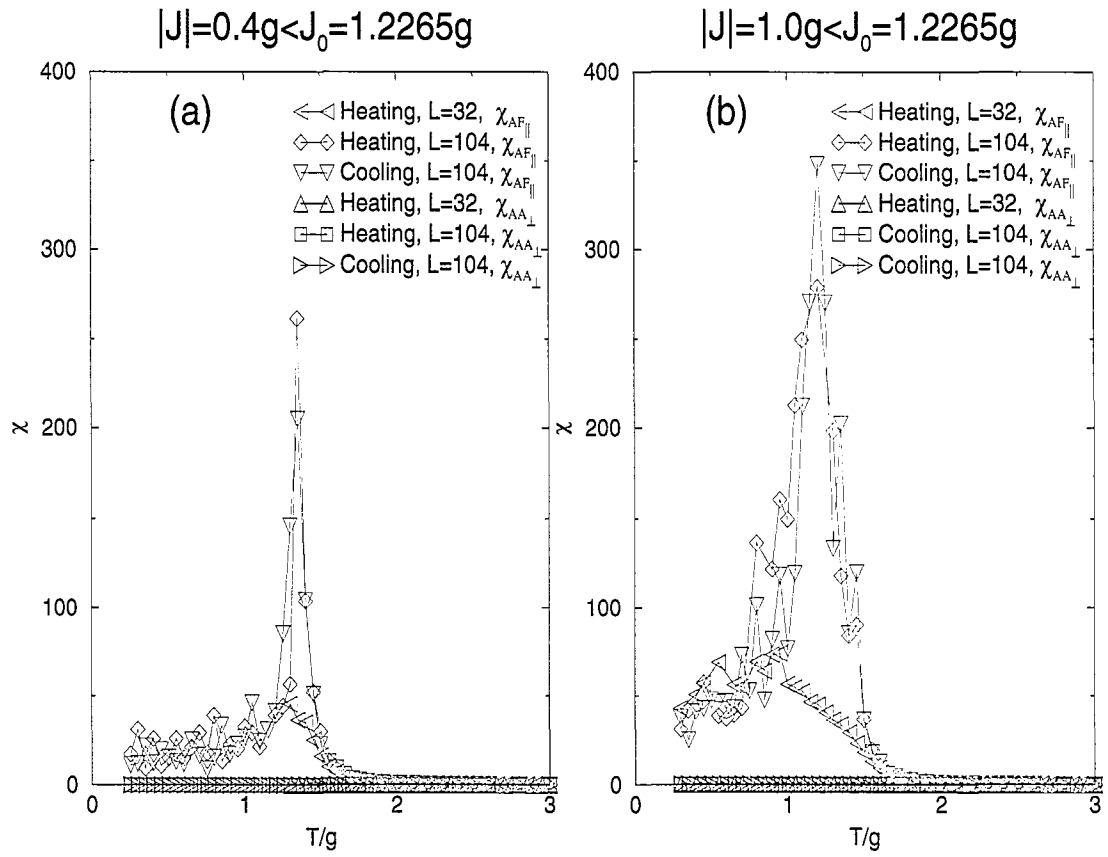


Figure 4.5: A plot of the parallel and perpendicular susceptibilities,  $\chi_{AF\parallel}$  and  $\chi_{AA\perp}$ , per spin as a function of temperature,  $T/g$ , for (a)  $|J| = 0.4g$  and (b)  $|J| = 1.0g$  with  $L = 32$  and  $104$ .

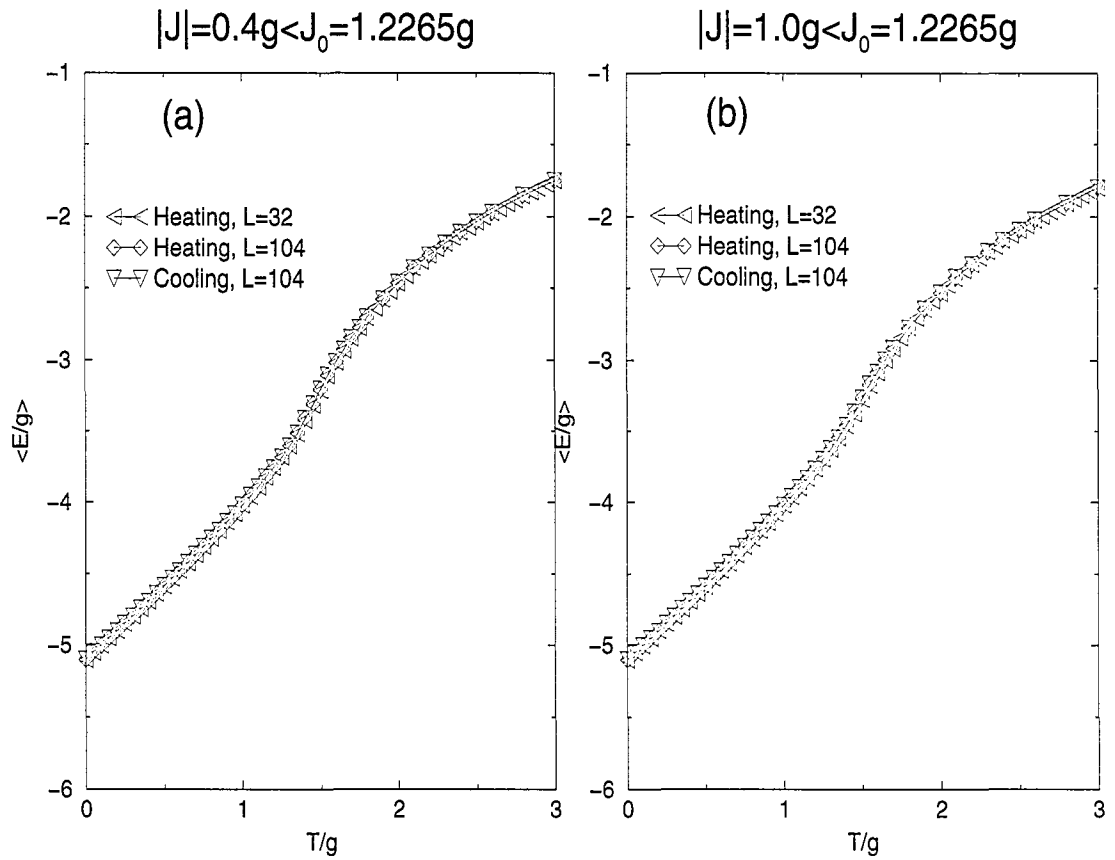


Figure 4.6: A plot of the average internal energy,  $\langle E/g \rangle$ , per spin as a function of temperature,  $T/g$ , for (a)  $|J| = 0.4g$  and (b)  $|J| = 1.0g$  with  $L = 32$  and  $104$ .

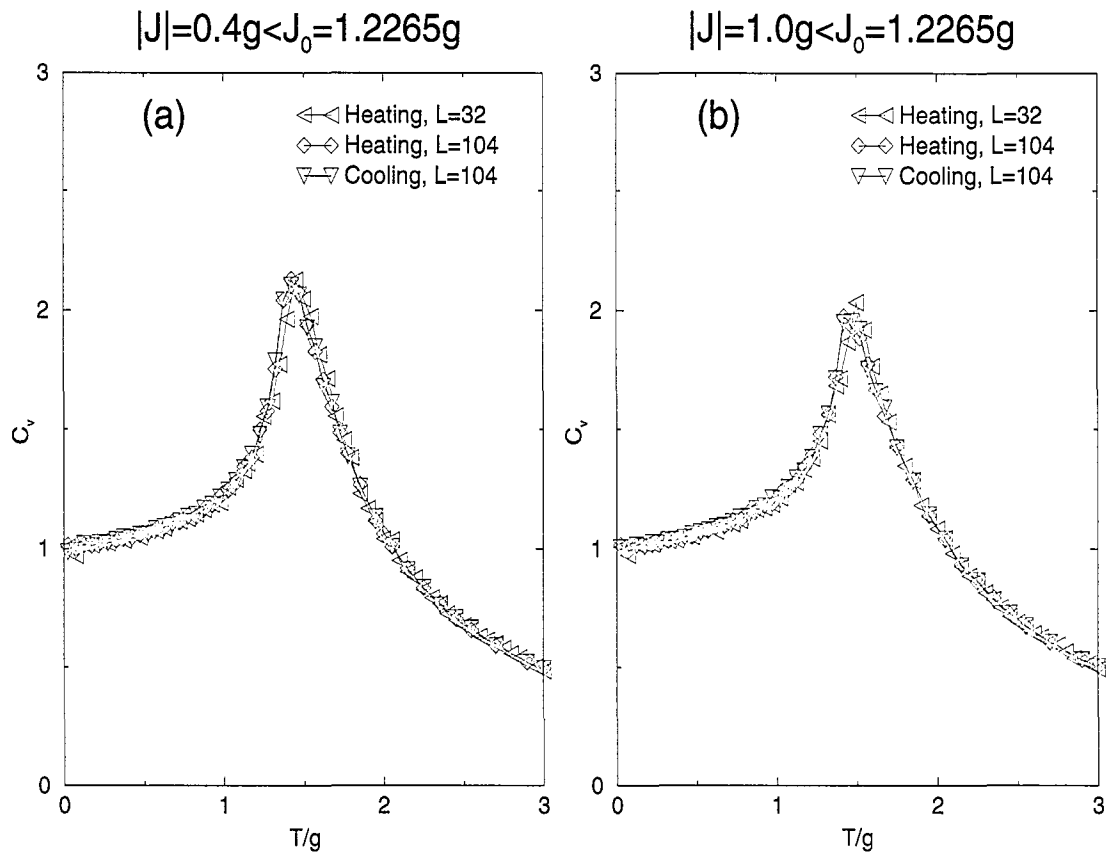


Figure 4.7: A plot of the heat capacity,  $C_v$ , per spin as a function of temperature,  $T/g$ , for (a)  $|J| = 0.4g$  and (b)  $|J| = 1.0g$  with  $L = 32$  and  $104$ .

value of  $J$  is shown in Figure 4.8 for  $T = 0.15g$ . The spin configuration in Figure 4.8a shows quite clearly that the sub-lattice magnetization for  $J = 0.4g$  is similar to that for the pure dipolar system,  $J = 0$ , with the spins aligned along either the  $x$ - or  $y$ -axis. In contrast, the spin configuration in Figure 4.8b shows that, for  $|J| = 1.0g$ , the sub-lattice magnetization is oriented at  $\pm\pi/4$  to the  $x$ -axis. This implies that two distinctly ordered planar phases exist.

The difference in the orientation of the equilibrium spin configuration is also apparent in Figure 4.9, which shows the angle  $\phi_\alpha$  as a function of the temperature,  $T/g$ , for two values of  $J$ , where  $\phi_\alpha$  is defined for each of the sub-lattices as

$$\phi_\alpha = \arctan \left( \frac{\langle M_y^\alpha \rangle}{\langle M_x^\alpha \rangle} \right). \quad (4.3.3)$$

The data are presented for cooling and show, at high temperature, that the spins on each of the four sub-lattices do not appear to exhibit any preferred orientation within the plane for both  $|J| = 0.4g$  and  $1.0g$ . As the temperature is lowered and the antiferromagnetic order is established, the spins in each of the magnetic sub-lattices begin to order along one of the symmetry axes. However, it is apparent from the data that the symmetry axis is different for the different values of  $|J|$ . For  $|J| = 0.4g$  the symmetry axis is along the  $x$ -axis, with  $\phi_1 = \phi_2 = 0$  and  $\phi_3 = \phi_4 = \pi$ , while for  $|J| = 1.0g$  the symmetry axis is oriented at  $\pi/4$  to the  $x$ -axis, with  $\phi_1 = \pi/4$ ,  $\phi_2 = 3\pi/4$ ,  $\phi_3 = 5\pi/4$  and  $\phi_4 = 7\pi/4$ .

For  $|J| > J_0$  the ground state spin configuration has the spins aligned perpendicular to the plane of the system. The two order parameters  $M_{AF\parallel}$  and  $M_{AA\perp}$ , earlier defined by Equations 4.2.6 and 4.2.7, are shown in Figure 4.10 for  $|J| = 2.0g$ , calculated using the thermally averaged sub-lattice magnetization given by Equations 4.3.1 and 4.3.2. The data show a perpendicular antiferromagnetic phase with each spin

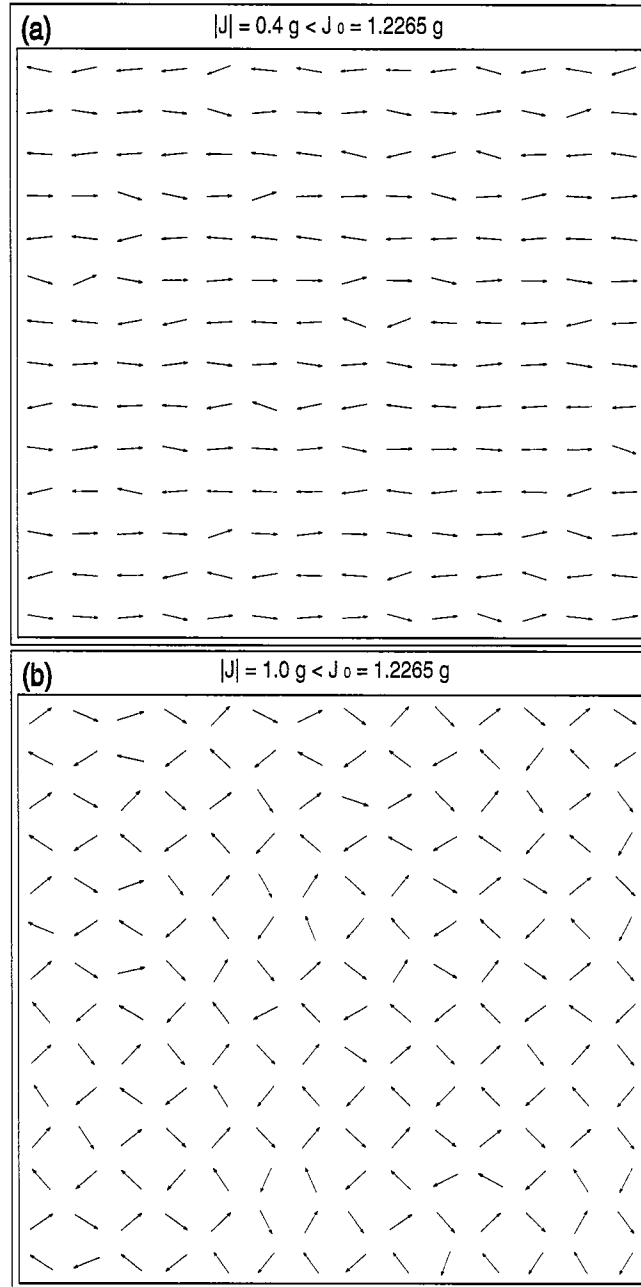


Figure 4.8: Snapshots of two typical spin configurations at  $T = 0.15g$  for (a)  $|J| = 0.4g$  and (b)  $|J| = 1.0g$  with  $L = 104$ .

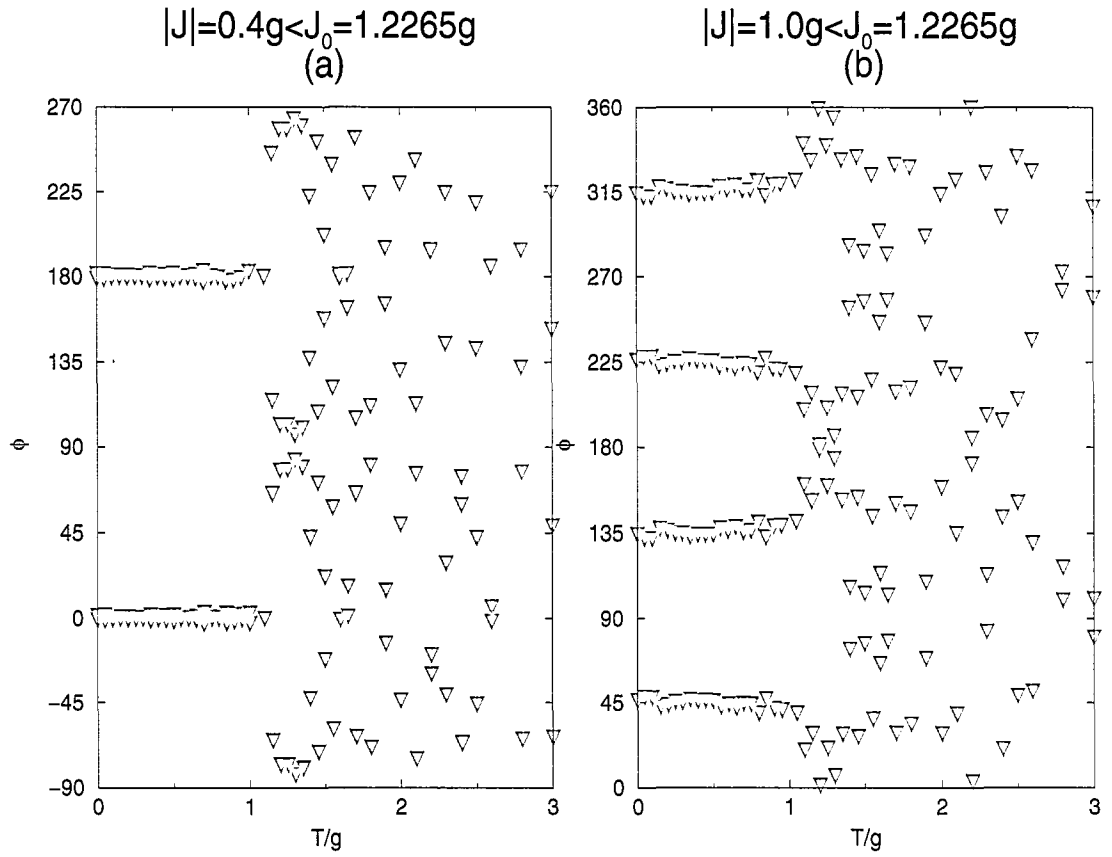


Figure 4.9: A plot of the angle  $\phi_\alpha$ , for each of the sub-lattice magnetization as a function of temperature,  $T/g$ , for (a)  $|J| = 0.4g$  and (b)  $|J| = 1.0g$  with  $L = 104$ .

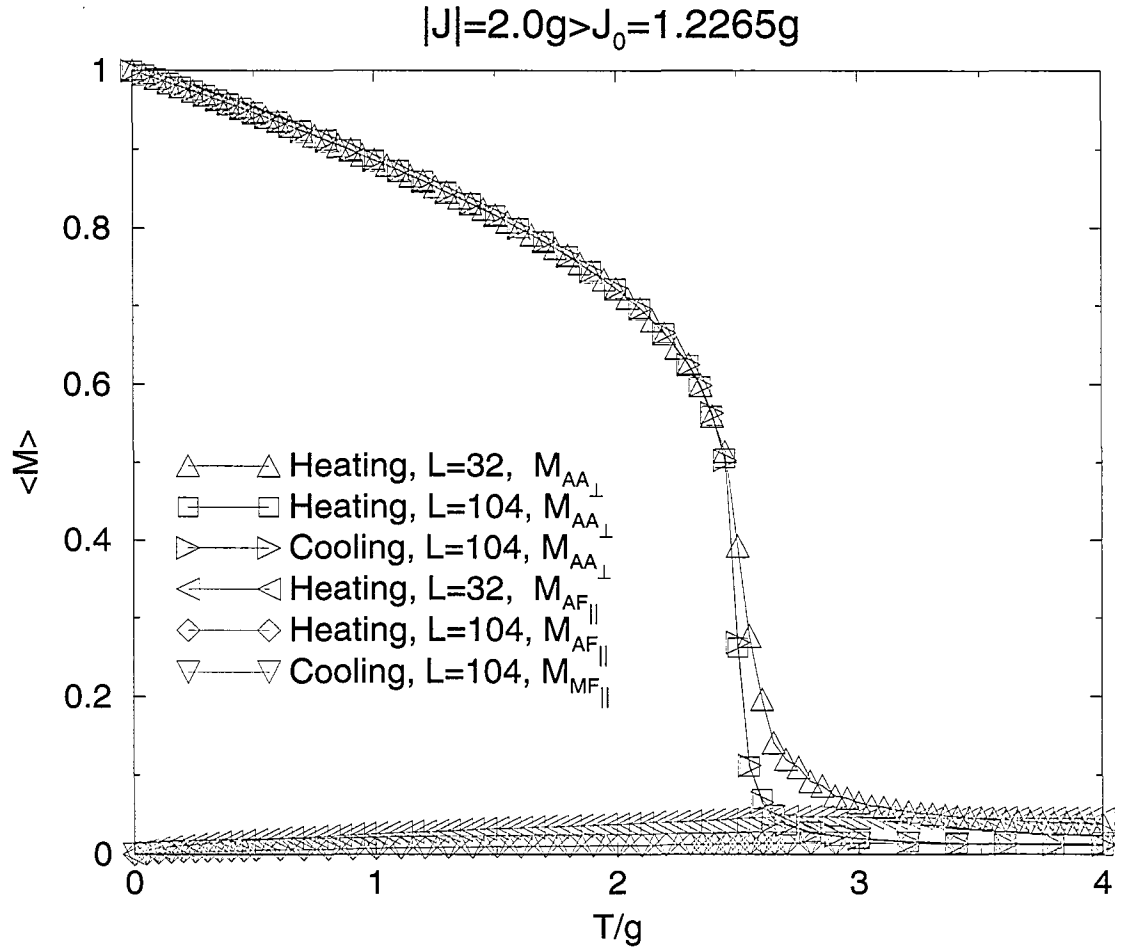


Figure 4.10: A plot of the perpendicular and parallel order parameters,  $M_{AA_{\perp}}$  and  $M_{AF_{\parallel}}$ , per spin as a function of temperature,  $T/g$ , for  $|J| = 2.0g$  with  $L = 32$  and 104.

aligned anti-parallel to its nearest neighbour. As the temperature is increased the order parameter decreases, dropping rapidly at around  $T = (2.5 \pm 0.05)g$  for  $|J| = 2.0g$ , indicating the transition from the ordered perpendicular antiferromagnetic phase to the disordered paramagnetic phase. As with the parallel phase discussed above, the order parameter data show the transition sharpening as the system size increases, consistent with a second-order transition. Comparing the heat capacity of Figure 4.11 for the perpendicular phase with that shown in Figure 4.7 for the parallel phase, it is worth noting that the peak in the heat capacity for the perpendicular phase shows a more pronounced size effect. This agrees with corresponding susceptibilities and average internal energy shown, respectively, in Figures 4.12, 4.13. The existence of the simple perpendicular antiferromagnetic phase in such systems was also confirmed by Deng *et al.* [153] using spin dynamics calculations with fast Fourier transformations.

The transition from the planar antiferromagnetic to the perpendicular antiferromagnetic phase is clearly seen in Figures 4.14, 4.15 and 4.16, which show how the order parameters  $M_{AF_{\parallel}}$  and  $M_{AA_{\perp}}$  (Figure 4.14), the total internal energy (Figure 4.15), and the dipolar and exchange energies (Figure 4.16) per spin change with increasing  $|J|/g$  for  $T = 0.4g$ . It is worth noting that while the data indicate that the transition from the planar to the perpendicular antiferromagnetic phase is first order, the latent heat at the transition is very small. Instead, the transition is characterized by a sharp change in the slope of the energy with respect to  $|J|$ . The discontinuous nature of the transition is clearly seen in Figure 4.16, in which the exchange and the dipolar energy are plotted with increasing  $|J|/g$ . The curves show that in the planar phase

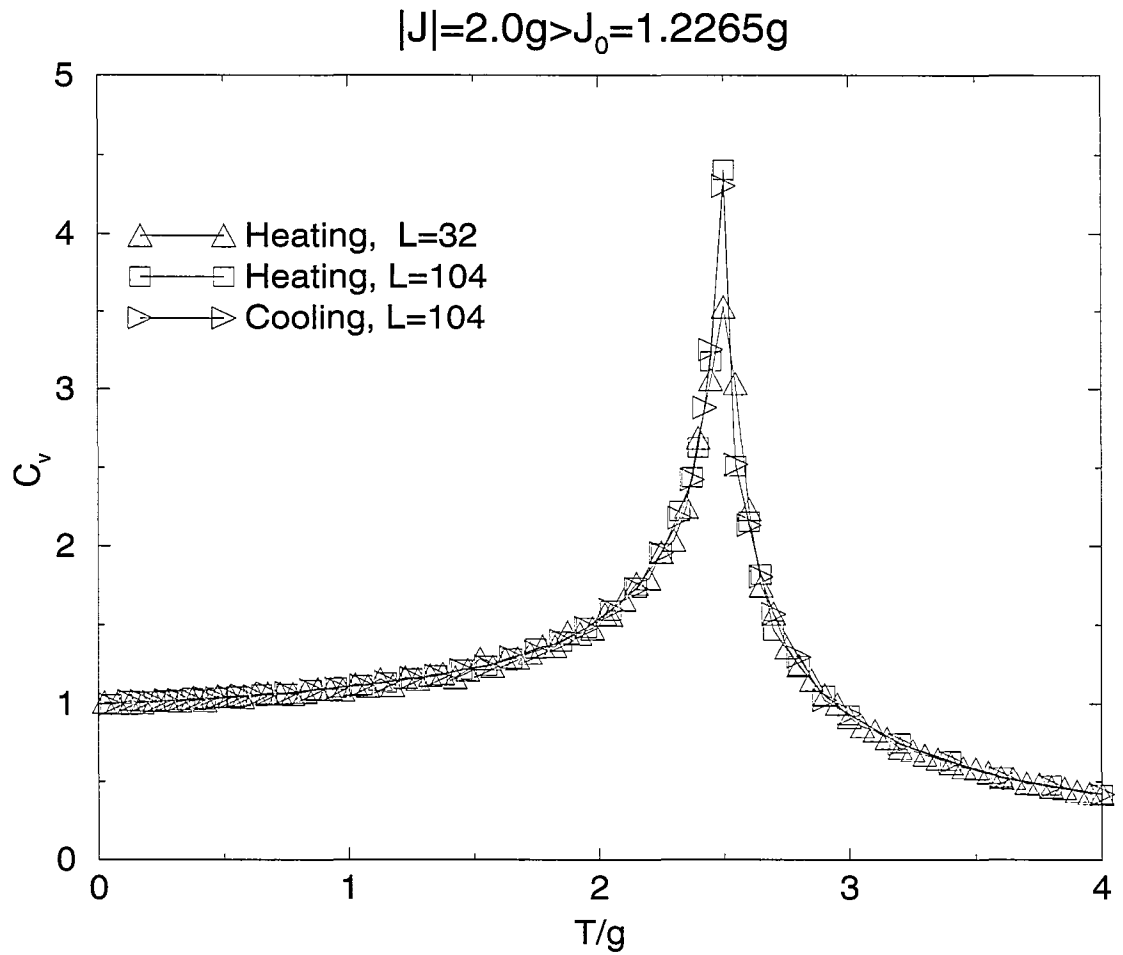


Figure 4.11: A plot of the heat capacity,  $C_v$ , per spin as a function of temperature,  $T/g$ , for  $|J| = 2.0g$  with  $L = 32$  and  $104$ .

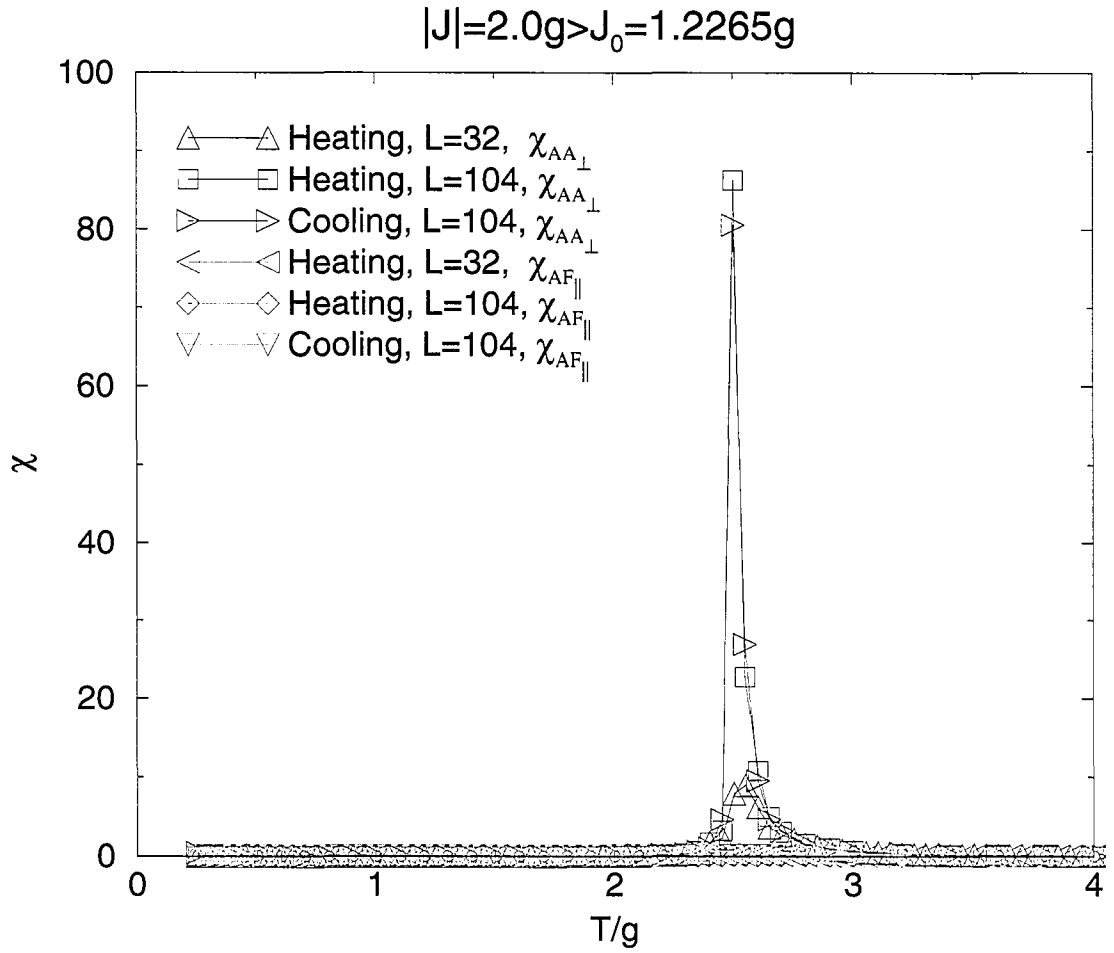


Figure 4.12: A plot of the perpendicular and parallel susceptibilities,  $\chi_{AA\perp}$  and  $\chi_{AF\parallel}$ , per spin as a function of temperature,  $T/g$ , for  $|J| = 2.0g$  with  $L = 32$  and  $104$ .

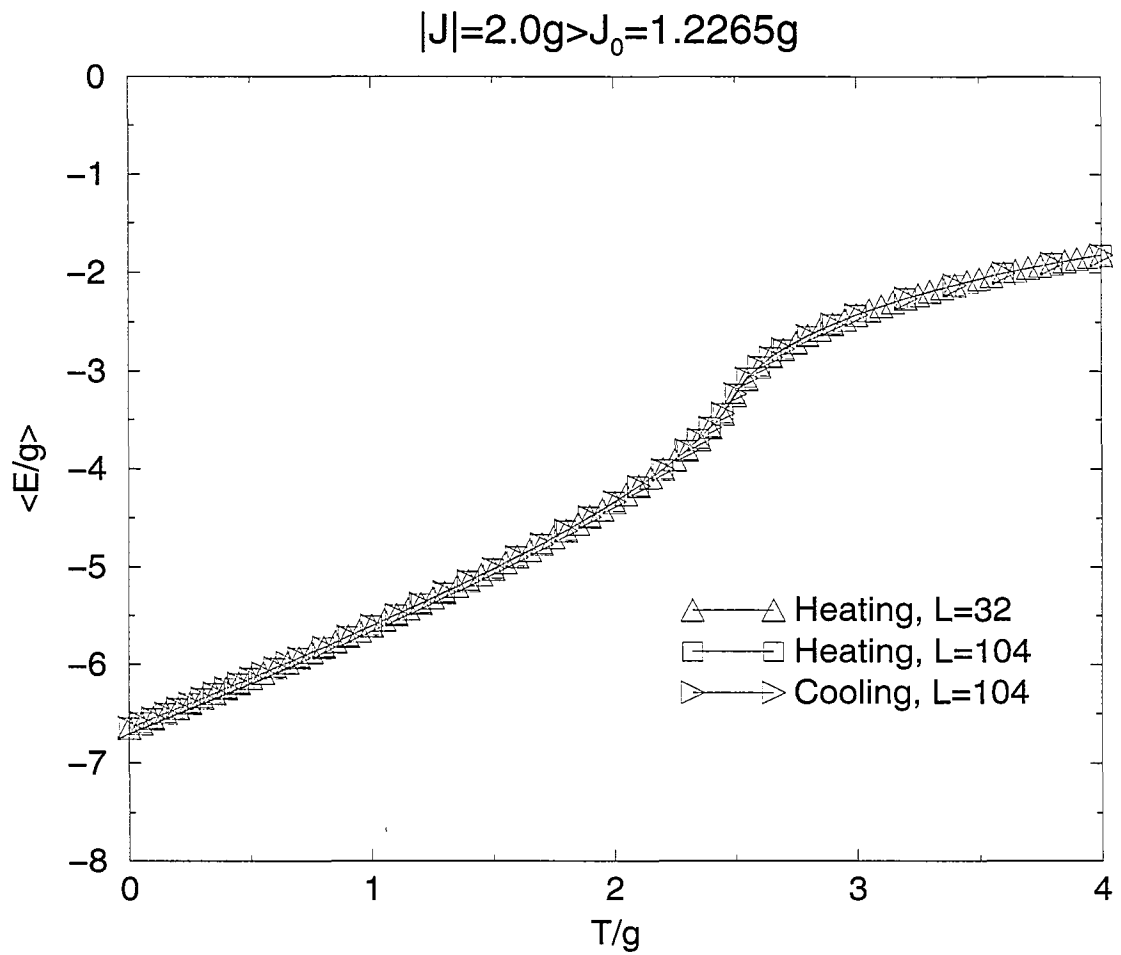


Figure 4.13: A plot of the average internal energy,  $\langle E/g \rangle$ , per spin as a function of temperature,  $T/g$ , for  $|J| = 2.0g$  with  $L = 32$  and  $104$ .

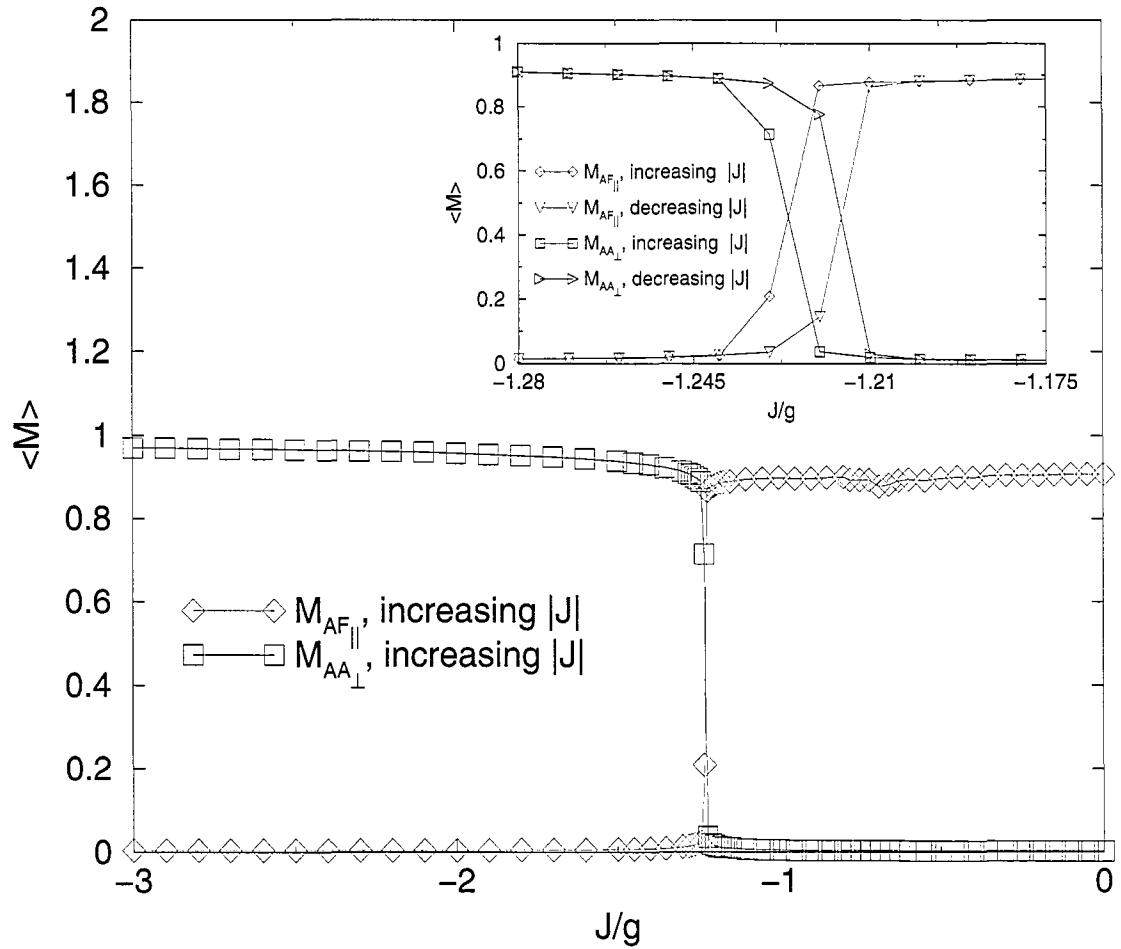


Figure 4.14: A plot of the parallel and perpendicular order parameters,  $M_{AA_{\perp}}$  and  $M_{AF_{\parallel}}$ , per spin as a function of the exchange constant,  $J/g$ , for  $T = 0.4g$  with  $L = 104$ .

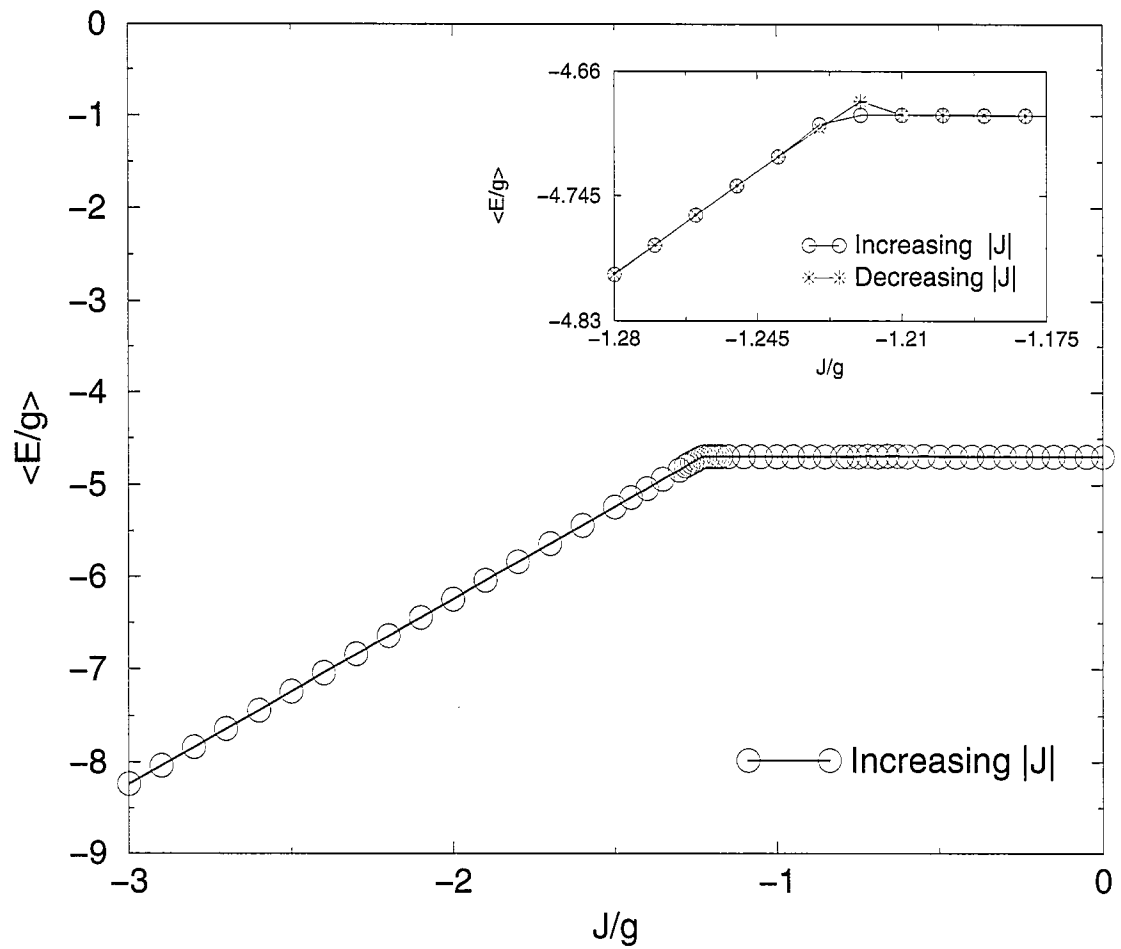


Figure 4.15: A plot of the average internal energy,  $\langle E/g \rangle$ , per spin as a function of the exchange constant,  $J/g$ , for  $T = 0.4g$  with  $L = 104$ .

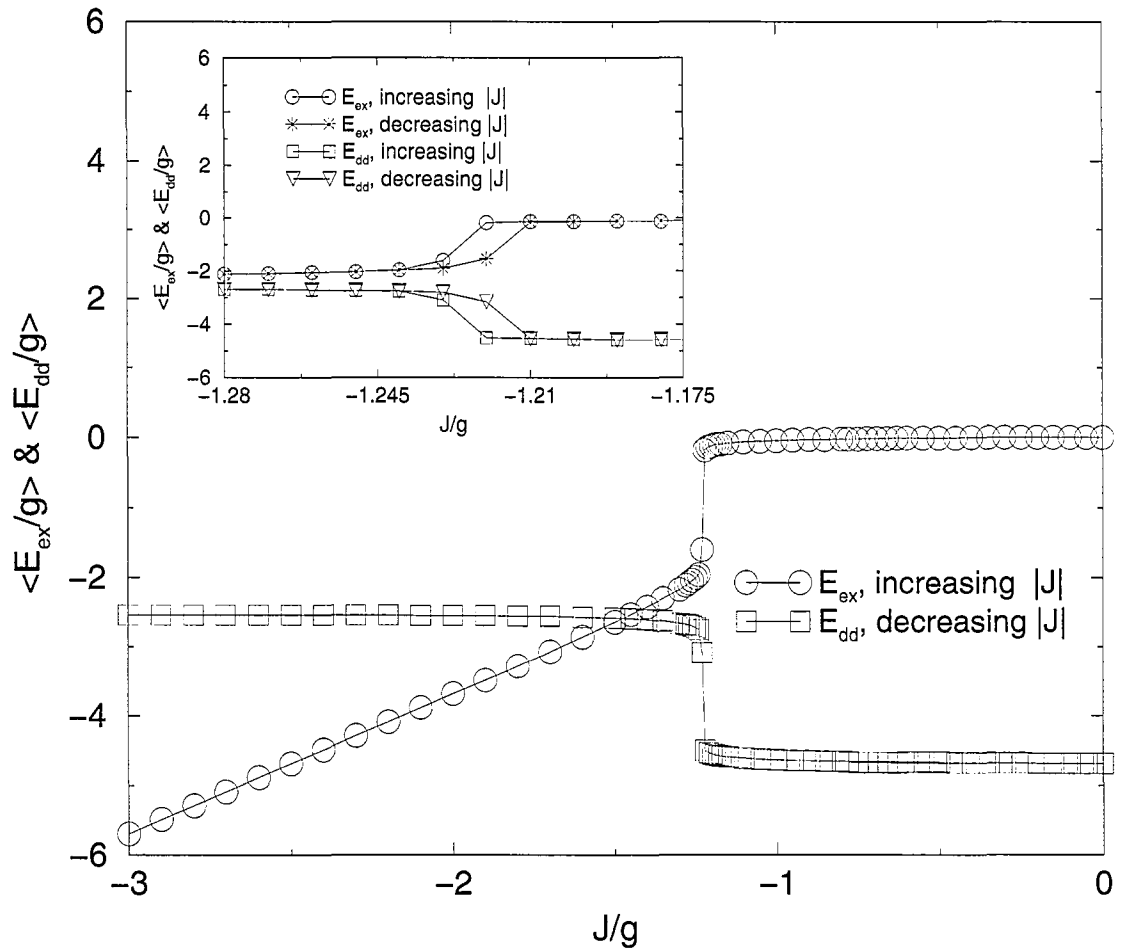


Figure 4.16: A plot of the exchange energy,  $\langle E_{ex}/g \rangle$ , and the dipolar energy,  $\langle E_{dd}/g \rangle$ , energies per spin as a function of the exchange constant,  $J/g$ , for  $T = 0.4g$  with  $L = 104$ .

( $|J| < J_0$ ), the energy of the system is almost entirely dipolar,  $E_{ex} \approx 0$ . At the transition,  $|J| = (1.2265 \pm 0.02)g$ , the system switches from the planar to the perpendicular phase and the exchange energy is seen to decrease abruptly and the dipolar energy increase. The data also indicate a small amount of hysteresis, consistent with the discontinuous nature of the transition. Further evidence for the transition between the two planar phases is also seen in the susceptibilities of the sub-lattice magnetization, shown in Figure 4.17, which shows not one but two distinct peaks. The first peak occurs at  $|J| = (0.69 \pm 0.02)g$  and corresponds to the reorientation transition from one planar phase to the other, and the second peak occurs at  $|J| = (1.23 \pm 0.02)g$  which represents the transition from the planar to the perpendicular phase.

## 4.4 The Phase Diagram

The phase diagram constructed from the Monte Carlo data is shown in Figure 4.18. The graph shows the three phase boundaries separating the dipolar planar antiferromagnetic phase (Region I), the perpendicular antiferromagnetic phase (Region II) and the paramagnetic phase (Region III). The dotted line in Region I, indicates the phase boundary separating the two planar phases. Within the accuracy of the simulations, the precise nature of this boundary and its location are difficult to determine precisely in the region where  $T > 1.0g$ .

The phase boundary separating the planar and the perpendicular antiferromagnetic phases appears, from the Monte Carlo data, to be first order. The order parameters  $M_{AA\perp}$  and  $M_{AF\parallel}$  change abruptly with increasing and decreasing  $|J|$  and the data show a small amount of hysteresis as shown in Figure 4.14. While the transition between the perpendicular and the parallel antiferromagnetic phases appears to be

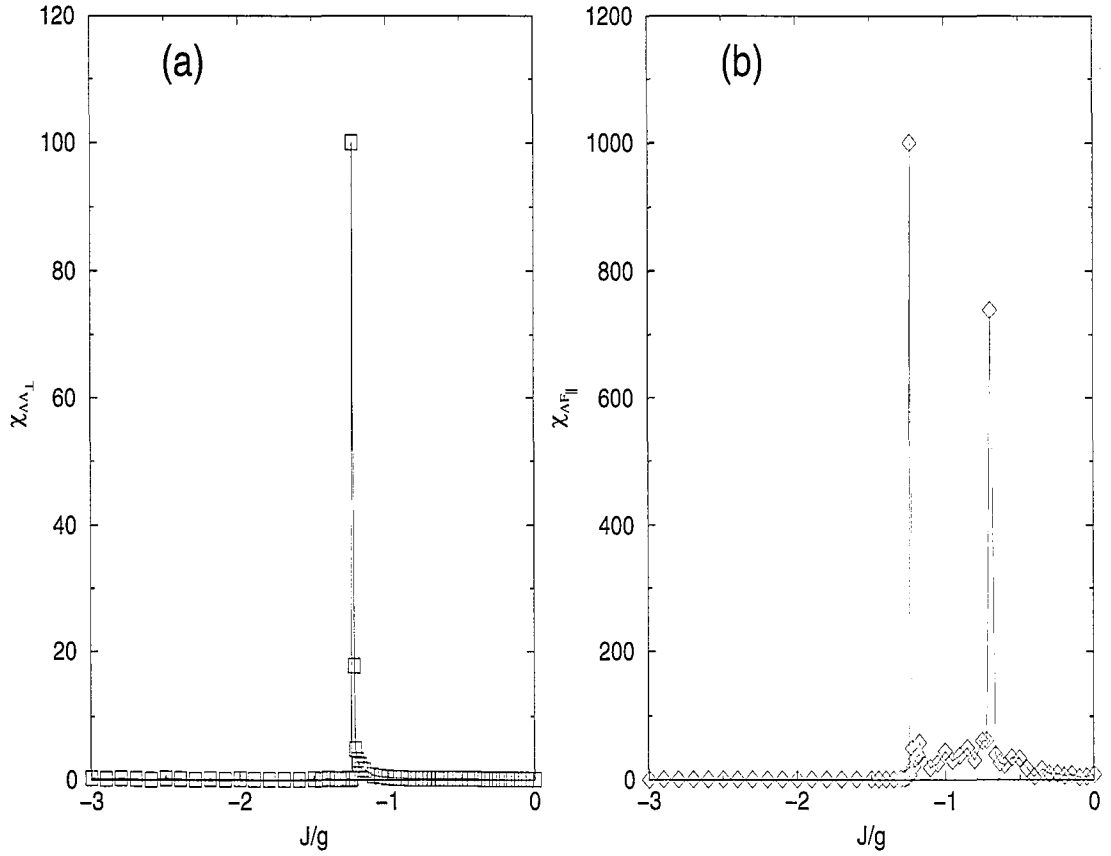


Figure 4.17: A plot of the perpendicular (a) and the parallel (b) susceptibilities,  $\chi_{AA\perp}$  and  $\chi_{AF\parallel}$ , per spin as a function of the exchange constant,  $J/g$ , for  $T = 0.4g$  with  $L = 104$ . Both the perpendicular and parallel susceptibilities exhibit peaks at the in-plane to out-of-plane transition. The parallel susceptibility exhibits a second peak corresponding to the in-plane reorientation transition.

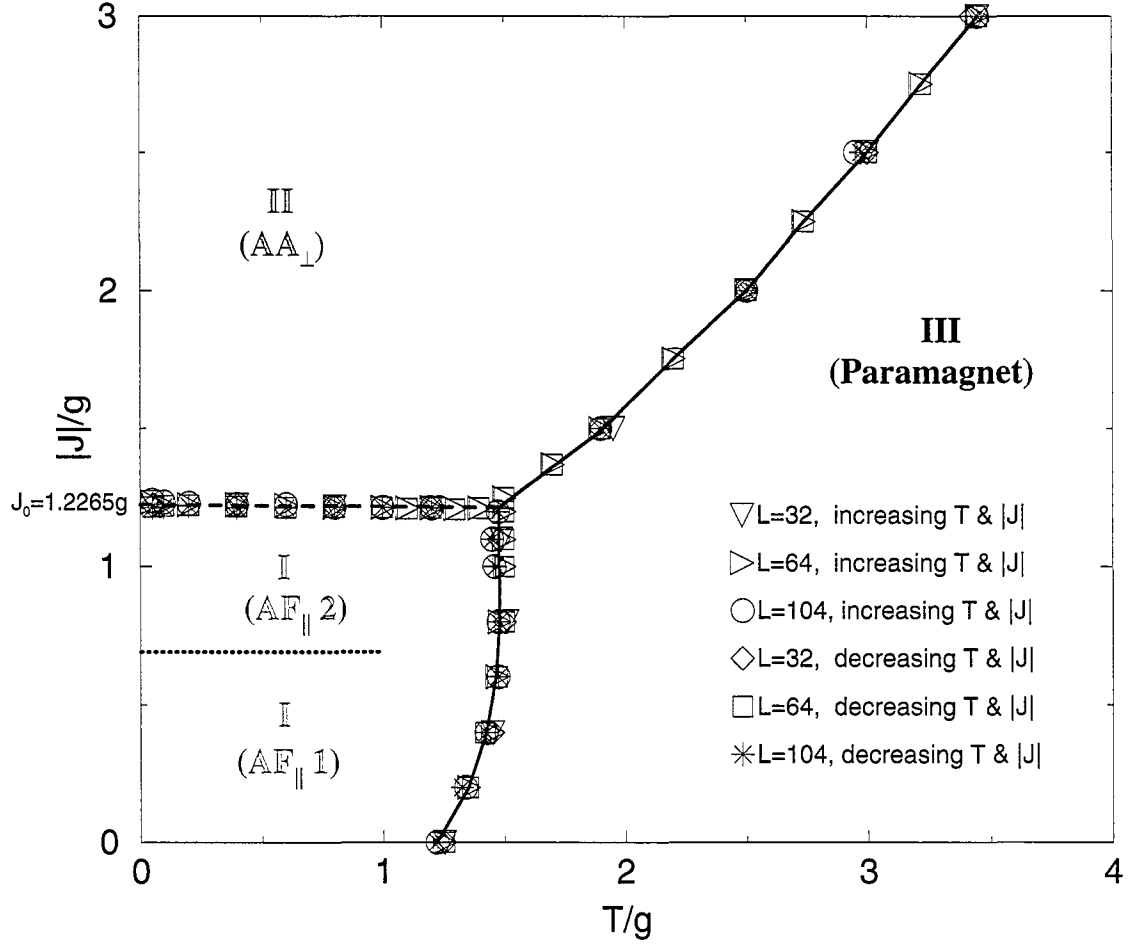


Figure 4.18: The magnetic phase diagram, based on the Monte Carlo simulations, for the dipolar antiferromagnetic Heisenberg system with  $\kappa = 0$  as a function of increasing and decreasing both  $|J|/g$  and  $T/g$  for  $N = L \times L = 32^2, 64^2, 104^2$ . Region I is the dipolar planar antiferromagnetic phase (AF<sub>||</sub> phase), Region II is the simple perpendicular antiferromagnetic phase (AA<sub>⊥</sub> phase), and Region III is the paramagnetic phase (disordered phase). The two solid lines highlight the two lines of second-order transitions from the paramagnetic phase to the two ordered phases. The dashed line highlight the line of first-order reorientation transition from one order state to the other (AF<sub>||</sub>, AA<sub>⊥</sub>). The dotted line separates the two planar phases (AF<sub>||</sub>1, AF<sub>||</sub>2).

first order, the latent heat of the transition is relatively small along the length of the phase boundary. This is consistent with the observation that the phase boundary separating Regions I and II is almost horizontal. Letting  $J_R(T)$  define the phase boundary, it can be readily shown that the slope of the coexistence line,  $dJ_R(T)/dT$ , is proportional to the latent heat,  $\Delta E$ , and is given by

$$\frac{dJ_R(T)}{dT} = \frac{J\Delta E}{T_R\Delta E_{ex}}, \quad (4.4.1)$$

where  $\Delta E_{ex}$  denotes the difference in the exchange energy between the equilibrium phases on the coexistence line. Preliminary estimates of the slope and the latent heat are consistent with this calculation, although the range of uncertainty is relatively large making a precise confirmation of this result difficult.

The phase boundary separating the perpendicular antiferromagnetic phase from the paramagnetic phase is determined by the peak position in the heat capacity of the system. Size effects, the continuous decrease in the order parameter, and the lack of any hysteresis suggest that this phase boundary defines a line of second-order transitions. This is consistent with the theoretical results of Pich and Schwabl [125]. Based on a generalized spin-wave theory, Pich and Schwabl obtained the following relationship for the Néel temperature,  $T_N$ , for  $|J| \gg g$  [125]

$$\frac{|J|}{T_N} = a \ln\left(\frac{|J|}{g}\right) + b. \quad (4.4.2)$$

To compare this relationship with the results of the Monte Carlo calculation,  $\ln(|J|/g)$  is plotted as a function of  $|J|/T_N$  in Figure 4.19. From this Figure it can be seen that the Monte Carlo data do indeed fall on a straight line for large values of  $|J|/g$ , as predicted by Pich and Schwabl. The solid line shown in the figure is the line of best fitting for the points  $|J| > 2.0g$ . The equation for the best fit line gives  $a = 0.1963$

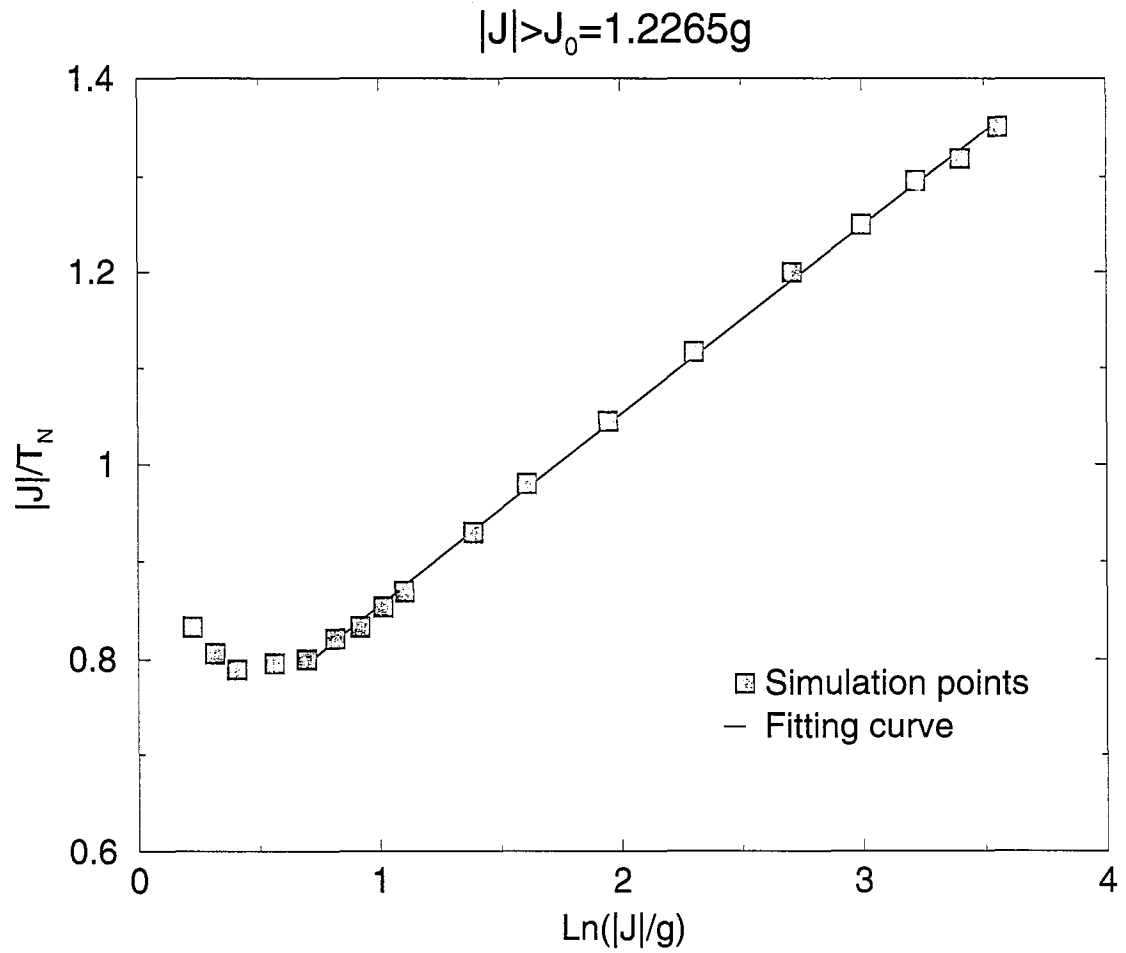


Figure 4.19: A plot of  $|J|/T_N$  as a function of  $\ln(|J|/g)$  for  $|J| > J_0$  with  $L = 104$ .

and  $b = 0.6599$ .

The phase boundary separating the planar  $AF_{\parallel}$  phase from the paramagnetic phase is also shown and, again, appears to describe a line of second-order phase transitions. At present, there do not appear to be any theoretical results for the Néel temperature for the planar  $AF_{\parallel}$  phase with which to compare our results.

The dotted line on the phase diagram represents the boundary between the two in-plane phases. For this study, the boundary was determined from the corresponding peak in the parallel susceptibility and, based on the results from the simulations, the transition is tentatively identified a discontinuous first-order transition.

## 4.5 Low Temperature Order Parameter

While the simulations are consistent with a first-order transition from the  $AA_{\perp}$  phase to the  $AF_{\parallel}$  phase with decreasing  $|J|$ , the low temperature order parameter data indicate a significant softening of the spin-wave spectra (i.e., decreasing in the spin-wave stiffness) as the transition is approached. In Figure 4.20, the perpendicular order parameter is plotted as a function of  $T$  for several values of  $|J| > J_0$ . The graphs show that the perpendicular order parameter decreases linearly with increasing temperature in the low temperature region (i.e.,  $T \rightarrow 0$ ). The linear decrease of the order parameter with temperature may be readily understood on the basis of classical linear spin-wave theory. The magnitude of the sublattice magnetisation,  $M^{\alpha}$ , may be written as

$$M^{\alpha} \equiv \left| \frac{4}{N} \sum_{\vec{r}_{\alpha}} \vec{\sigma}(\vec{r}_{\alpha}) \right| = 1 - \frac{4}{N} \sum_{\vec{r}_{\alpha}} \langle b^*(\vec{r}_{\alpha}) b(\vec{r}_{\alpha}) \rangle \quad (4.5.1)$$

where  $b_{\vec{r}_{\alpha}}$  denotes the complex amplitude associated with the spin fluctuations at the

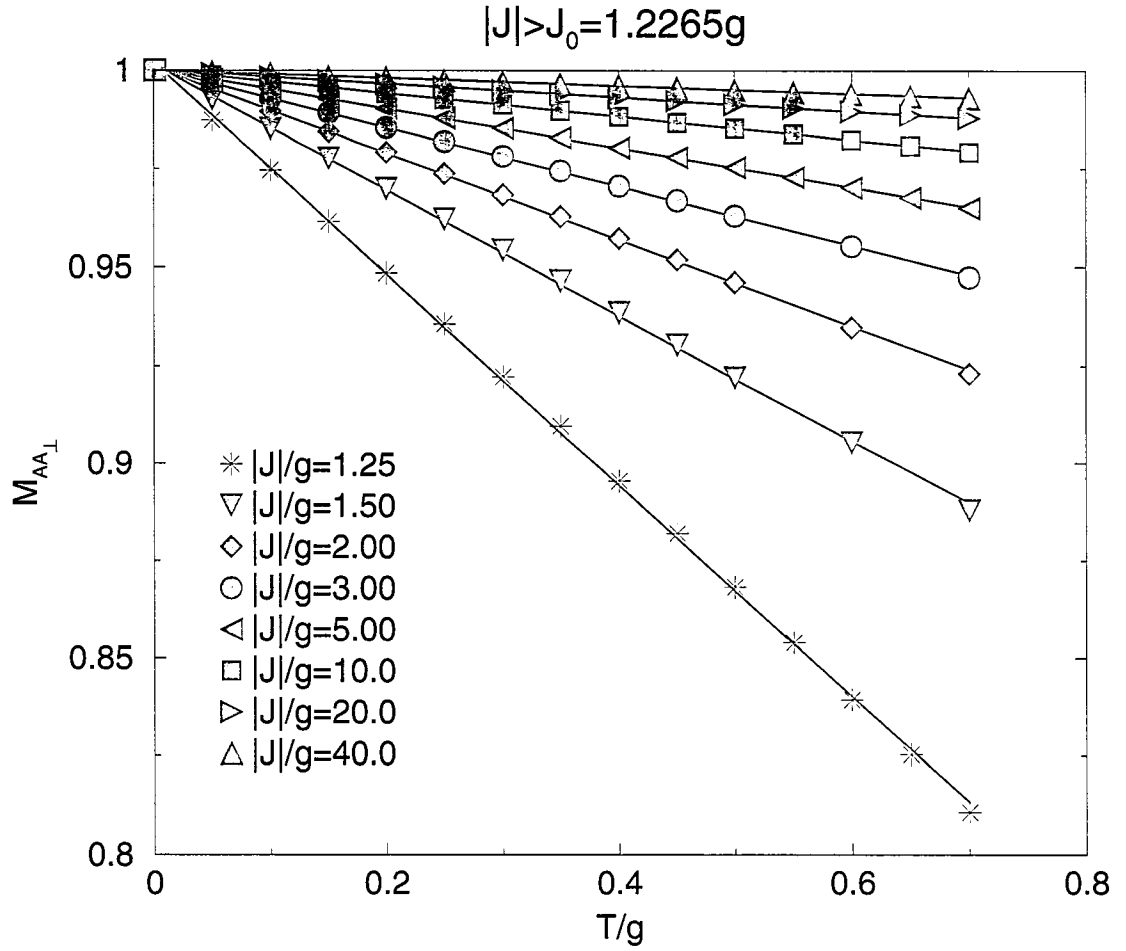


Figure 4.20: A plot of the perpendicular order parameter,  $M_{AA_{\perp}}$ , per spin as a function of the the temperature,  $T/g$ , for several values of  $|J| > J_0$  with  $L = 104$ .

site,  $\vec{r}_\alpha$ , in the  $\alpha$  sublattice. At low temperature the thermal average  $\langle b^*(\vec{r}_\alpha)b(\vec{r}_\alpha) \rangle$  may be calculated from linear spin-wave theory, provided the spin-wave spectra is not gapless. It can be readily shown that  $\langle b^*(\vec{r}_\alpha)b(\vec{r}_\alpha) \rangle \propto T$ . However, due to the presence of the dipolar interaction, the proportionality constant is quite difficult to calculate in general. It is clear from the graphs shown in Figure 4.20 that the slope of the perpendicular order parameter in the limit  $T \rightarrow 0$  decreases with decreasing  $|J|/g$ , reflecting a softening of the spin-wave stiffness.

A plot of  $\lim_{T \rightarrow 0} |dM_{AA_\perp}/dT|$ , as a function of  $|J|/g$  is shown in Figure 4.21. Since  $\lim_{T \rightarrow 0} |dM_{AA_\perp}/dT|$  is dependent on the exchange parameter, it shows a rapid increase in magnitude as the transition is approached. This compares with a phenomenological relationship

$$\lim_{T \rightarrow 0} \frac{|dM_{AA_\perp}|}{|dT|} = \frac{a}{((|J|/g)^b - c)^d} \quad (4.5.2)$$

where a regression analysis yields the following estimates:  $a = 0.1660$ ,  $b = 2.3835$ ,  $c = 1.4900$  and  $d = 0.3165$ . This relationship predicts that the slope of the order parameter diverges at  $|J|/g = 1.1805$ , which lies just below the phase boundary separating the perpendicular and the in-plane phases.

A similar analysis of the order parameter in the parallel phase is complicated by the fact that the temperature dependence of the sublattice magnetization appears to deviate systematically from linear behavior at low temperature. This is due to a gapless branch in the spin-wave spectra that arises as a consequence of the degeneracy of the ground state. In Figure 4.22,  $g(1 - M_{AF_\parallel})/T$  is plotted as a function of  $T/g$  for  $|J| = 0.2g$ . It can be seen that the points do not tend to a constant in the limit  $T \rightarrow 0$  as might be expected on the basis of simple linear spin-wave theory but, instead, show a steady increase as the temperature is reduced. This is consistent with the results

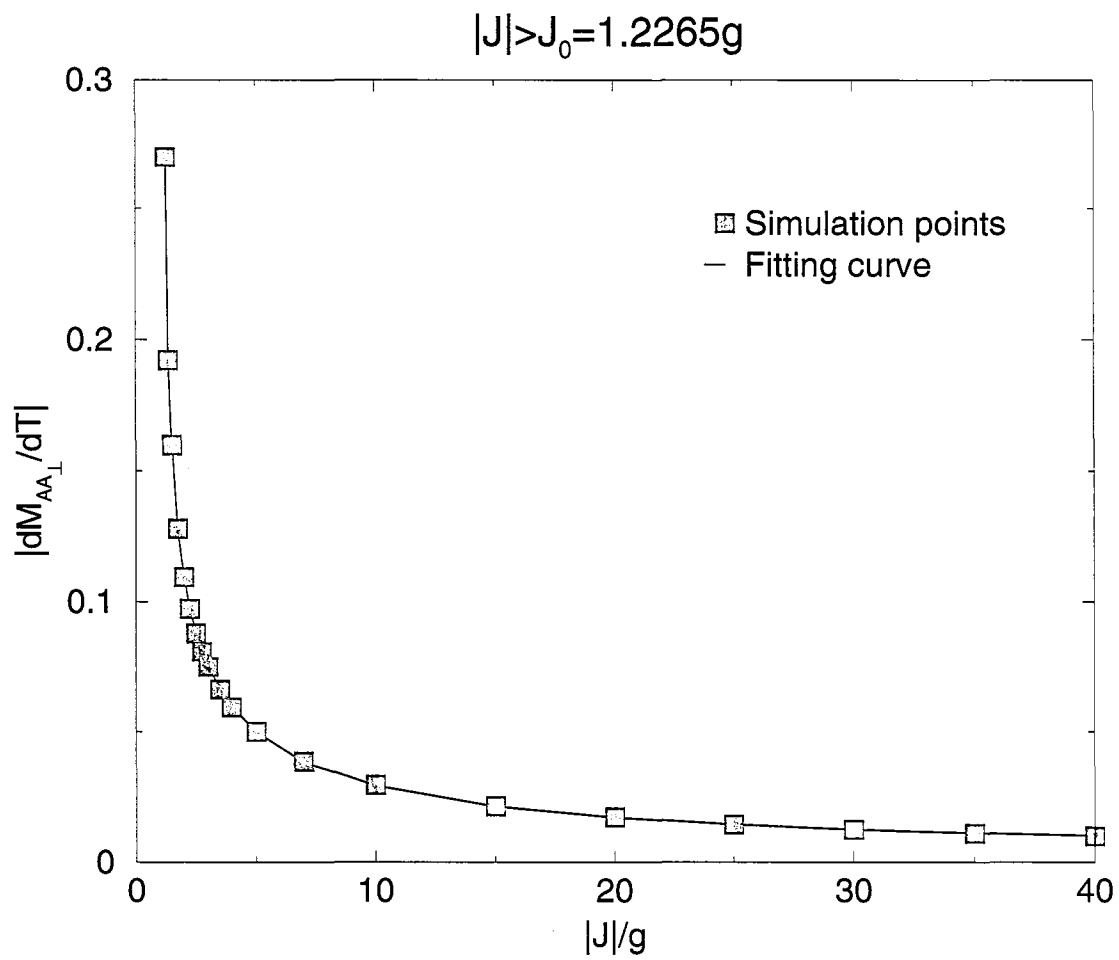


Figure 4.21: A plot of the low temperature slope,  $|dM_{AA_\perp}/dT|$ , as a function of the exchange interaction,  $|J|/g$ , for  $|J| > J_0$  with  $L = 104$ .

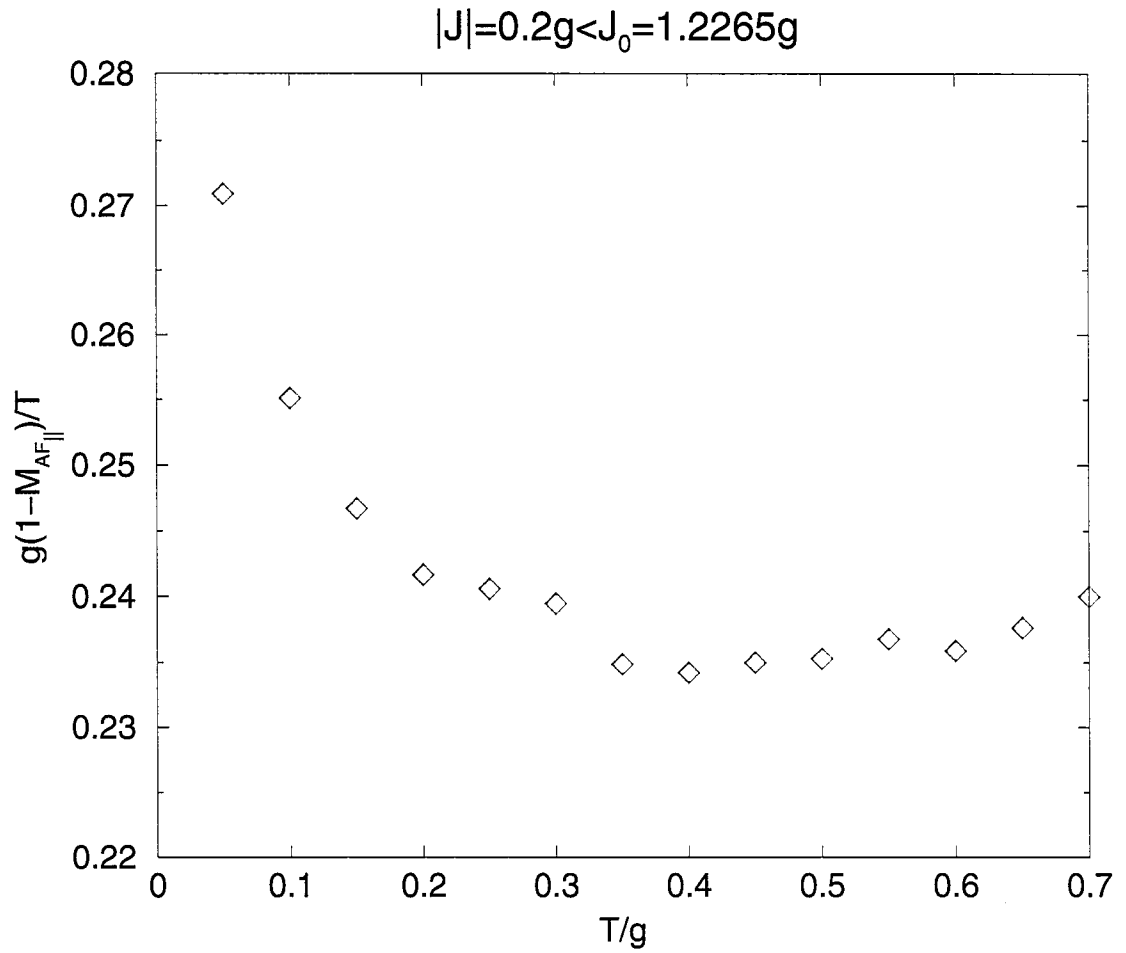


Figure 4.22: A plot of the ratio  $g(1 - M_{AF||})/T$  as a function of the the temperature,  $T/g$ , for  $|J| < J_0$  with  $L = 104$ .

of Carbognani *et al.* [109] for the planar model. In their study, Carbognani *et al.* go beyond the simple spin-wave approximation and they predict a low temperature order parameter of the form

$$\lim_{T \rightarrow 0} M_{AF\parallel} \simeq 1 - AT + BT \ln T, \quad (4.5.3)$$

where A and B are two constants. From Equation 4.5.3, one can see that at low temperature  $M_{AF\parallel}$  diverges logarithmically. This prediction arises as consequence of the result that the spin spectra becomes gapless in the limit  $T \rightarrow 0$ . The present results suggest that the degeneracy of the planar ground state of the Heisenberg model also gives rise to a similar non analytic temperature dependence of the order parameter,  $M_{AF\parallel}$ , in the limit  $T \rightarrow 0$ .

## 4.6 Discussion

Low-dimensional antiferromagnetic systems are interesting for a variety of reasons, not the least of which is that the competition between the antiferromagnetic exchange and the dipolar interaction is sufficient to induce a reorientation transition from a dipolar planar phase to a perpendicular phase.

The results from the simulations show that the function,  $J_R(T)$ , that describes the phase boundary between the dipolar planar and the perpendicular antiferromagnetic phases is only weakly dependent on the temperature, suggesting that the effective anisotropy that arises as a consequence of the exchange and the dipolar interaction is largely independent of temperature. Since it is not obvious how this result can be modified by the addition of an explicit magnetic surface anisotropy, this is the subject of chapter 6.

A subtle aspect of the phase behavior arises from the degeneracy of the dipolar planar ground state energy. The existence of long-range magnetic order and the orientation of the easy axis of magnetization is determined by the disorder produced by the thermal fluctuations. This provides an explicit example of the concept of “order from disorder” discussed by Henley [116]. However, Henley and Prakash [116, 117] have shown that the orientation of the magnetization axis generated by disorder is critically dependent on the precise nature of the disorder. In particular, in the case of the antiferromagnetic XY-model, the effective potential that arises as a consequence of the thermal fluctuations has a minimum on the  $x - y$  axis, while the disorder arising from the effects of dilution has a minima at  $\pm\pi/4$  to the  $x - y$  axis. It seems reasonable on the basis of the work by Henley to assume that it is the change in the nature of the disorder as the exchange interaction,  $|J|/g$ , is increased that gives rise to the reorientation transition within the dipolar planar phase which is observed in these simulations.

Further motivation to determine how thermal fluctuations can give rise to an in-plane reorientation transition is provided by a recent experimental observation of such an in-plane transition in a ferromagnetic system [190]. While it is by no means obvious how the results obtained in this study are relevant to the ferromagnetic case, it is possible that both arise as a consequence of the same underlying physical process.

The simulations also lend support to some of the predictions of non-linear spin-wave theory. In particular, the Néel temperature for the perpendicular phase appears to be consistent with the results of Pich and Schwabl [125], while an analysis of the low-temperature magnetization in the planar phase shows a non analytic dependence on  $T$  that is qualitatively similar to that predicted by Carbogani *et al.* [109]

for the planar model in the absence of an exchange interaction. Obviously a more quantitative comparison between spin-wave theory and the results obtained from the simulations would be useful and could include an analysis of the low-temperature magnetization in the perpendicular phase to examine the spin-wave spectra close to the phase boundary and the effect of the excitations on the magnetization.

As mentioned in chapter 1, one important class of quasi-two dimensional antiferromagnetic materials in which the dipolar energy is comparable to the exchange energy is the so-called high  $T_c$  superconductors,  $\text{REBa}_2\text{Cu}_3\text{O}_{7-\delta}$ , (RE = Rare Earth). The structure of these compounds is such that the rare earth ions reside on well-separated planes, replacing the yttrium (Y) ions of the parent compound  $\text{YBa}_2\text{Cu}_3\text{O}_{7-\delta}$ . The compounds in which dysprosium (Dy), gadolinium (Gd) or erbium (Er) are substituted for the yttrium have been most extensively studied [50]. At low temperature, the spins are aligned perpendicular to the plane in the case of Dy [57] and Gd [61] compounds, and parallel to the plane in the case of Er compounds [48].

The compound  $\text{GdBa}_2\text{Cu}_3\text{O}_{7-\delta}$  is of particular interest in the context of the present discussion since, as an S-wave ion, the crystalline electric field (CEF) anisotropy will disappear to leading order and, based on a simple scaling argument [50], it will have the strongest exchange interaction of the three compounds. Therefore, application of the present system to this compound would locate the low temperature phase of  $\text{GdBa}_2\text{Cu}_3\text{O}_{7-\delta}$  in Region II of the phase diagram shown in Figure 4.18. This is consistent with the experimental observations of the order parameter and, while the observed low temperature heat capacity is complicated by the quantum nature of the spins at low temperature, measurements nevertheless show a sharp peak at the transition similar to that presented in Figure 4.12 [60].

More intriguing is the case of  $\text{ErBa}_2\text{Cu}_3\text{O}_{7-\delta}$ . According to the simple scaling argument referred to above, the Er compound will have the weakest exchange interaction of the three compounds ( $J(\text{Er}) \approx J(\text{Gd})/9$ ). This is consistent with the fact that the moments are aligned in plane at low temperature. In the case of the orthorhombic superconducting phase of  $\text{ErBa}_2\text{Cu}_3\text{O}_{7-\delta}$  ( $\delta > 1/2$ ), the Er ions clearly order at low temperature along the  $a$ -axis, with the spins ordering as shown in Figure 4.1a [48], while the specific heat shows a sharp cusp at the Néel temperature [191]. In the tetragonal insulating phase ( $\delta < 1/2$ ), the specific heat is much more rounded and there does not appear to be any long-range magnetic order at low temperature [55]. Calculations of the CEF and the ground state of the Er ions show that, while the small orthorhombic distortion defines an easy axis of magnetization in the superconducting phase, in the tetragonal phase the magnetic moment of the Er ions is free to rotate in the plane [167]. While it is possible to argue that the rounded heat capacity observed experimentally is qualitatively similar to the heat capacity shown in Figure 4.7, it is difficult to reconcile the absence of long-range magnetic order with the results presented here. A possible explanation for the absence of an observed ordered state is that the highly degenerate nature of the planar equilibrium phases and the critical dependence of their stability on the nature of the disorder created by both the thermal fluctuations and any structural disorder (e.g., oxygen vacancies) results in frustration effects. These effects would prevent the system from realizing long-range magnetic order. Indeed it is possible that such effects would produce a glass-like phase of micro-domains that would be difficult to identify experimentally.

While the properties of the  $\text{GdBa}_2\text{Cu}_3\text{O}_{7-\delta}$  and  $\text{ErBa}_2\text{Cu}_3\text{O}_{7-\delta}$  compounds are consistent with certain aspects of the phase diagram shown in Figure 4.18, a more

complete picture of the magnetic properties of these compounds, and the others in this class, should include the magnetic anisotropy arising from the CEF and the effects of impurities.

## 4.7 Summary

In this chapter, the two-dimensional dipolar antiferromagnetic Heisenberg system on a square lattice with  $\kappa = 0$  has been studied for both zero and the finite temperatures. At low temperatures, the Monte Carlo results show that the system exhibits a reorientation transition from the dipolar planar ( $AF_{\parallel}$ ) phase to the perpendicular antiferromagnetic ( $AA_{\perp}$ ) phase as the antiferromagnetic exchange parameter increases. Indeed, the results show that the phase boundary separating these two order phases is weakly dependent on temperature, and intercepts the  $|J|/g$  axis at  $J_0 = 1.2265g$ . While this phase boundary appears to be a first-order transition with a small amount of hysteresis, the results show that the phase boundary separating the two ordered states ( $AF_{\parallel}, AA_{\perp}$ ) from the paramagnetic state appears to be a second-order transition.

A subtle aspect of the phase behavior for this system arises from the characteristics of the dipolar planar phase. In this phase, the Monte Carlo data indicates that there are two distinct phases. The first is labelled the  $AF_{\parallel}1$  phase (known also as the collinear or columnar phase) which occurs at low values of  $|J|/g$  ( $|J| \lesssim 0.7g$ ). In this phase the spins are aligned along either the  $x$  or the  $y$ -axis of the square lattice of the system. The second is the  $AF_{\parallel}2$  phase (known as the anticollinear or vortical phase) which occurs at the higher values of  $|J|/g$  ( $0.7g \lesssim |J| \lesssim 1.23g$ ). In this phase, the spins are aligned along the axis which oriented at  $\pm\pi/4$  to the  $x$ -axis of the square

lattice of the system. This provides an explicit example of the concept of “order from disorder” first pointed out by Henley [116]. In addition, the Monte Carlo results indicate that the phase boundary separating the  $AF_{\parallel}1$  from the  $AF_{\parallel}2$  phase appears to be a first-order transition.

Finally, two interesting and important issues arise in this chapter. The first is to identify the way in which the  $z$ -components of the spins can effect the characteristics of the dipolar planar phase of the system. The second is to determine the way in which the magnetic surface anisotropy affects the phase behaviour of the system. While the first issue will be addressed in chapter 5, where the Monte Carlo results of the dipolar antiferromagnetic plane rotator model is presented, the second issue will be explored in chapters 6 and 7 where the Monte Carlo results for the two-dimensional dipolar antiferromagnetic Heisenberg model on a square lattice with a planar anisotropy ( $\kappa < 0$ ) will be presented.

# Chapter 5

## The Plane Rotator System

### 5.1 Introduction

In the previous chapter, results from a series of Monte Carlo simulations were presented for the case of a two-dimensional Heisenberg system of magnetic ions arranged on a square lattice interacting only through an antiferromagnetic short-range exchange interaction and a long-range dipolar interaction. It was found that the two-dimensional dipolar antiferromagnetic Heisenberg system with zero  $\kappa$  exhibits a reorientation transition from an in-plane dipolar antiferromagnetic phase to an out-of-plane antiferromagnetic phase as the magnitude of the exchange coupling is increased. In addition, the in-plane dipolar antiferromagnetic ordering exhibits two phases: In one, the spins are aligned parallel to the square lattice axes; in the other, the staggered magnetization is rotated by  $\pi/4$  relative to the square lattice axes.

The appearance of in-plane magnetic ordering in these systems is a subtle effect since the planar ground state is continuously degenerate despite the anisotropic nature of the dipolar interaction [118]. The magnetic order arises as a consequence of the disorder created by the thermal fluctuations [158, 118], and provides an explicit

example of the “order from disorder” [192, 115, 116] phenomena which is known to give rise to magnetic ordering in a number of frustrated magnetic systems [193, 194]. Earlier theoretical studies on a truncated dipole-like interaction have shown that both thermal fluctuations and dilution can stabilise the antiferromagnetic state, with thermal fluctuations favouring ordering along the lattice axis and dilution favouring ordering aligned at  $\pi/4$  to the lattice axis [116, 117]. In chapter 4 it was conjectured that thermally activated, isolated out-of-plane spin flips would create a disorder similar to the effects of dilution, with a density controlled by the strength of the exchange interaction,  $J$ , and the temperature,  $T$ . It was therefore conjectured that these spin flips were the cause the reorientation transition from  $AF_{\parallel 1}$  to  $AF_{\parallel 2}$  with increasing  $|J|/g$ . The present chapter examines this conjecture since out-of-plane spin flips are absent in the plane rotator model. This chapter is also of interest as it may be considered to be another limiting case of the more general model that includes the on-site surface anisotropy. In this limiting case, the magnitude of the on-site anisotropy is effectively infinite ( $\kappa = -\infty$ ) and restricts the spins to being in-plane so that they may be treated as strictly planar rotors.

This chapter hence identifies differences and similarities between the results for this plane rotator system and the system studied in chapter 4. The results reported are based on Monte Carlo simulations of the square lattice model having the energy

$$E(\{\vec{\sigma}_i\}) = g \sum_{i \neq j} \left( \frac{\vec{\sigma}_i \cdot \vec{\sigma}_j}{r_{ij}^3} - 3 \frac{(\vec{\sigma}_i \cdot \vec{r}_{ij})(\vec{\sigma}_j \cdot \vec{r}_{ij})}{r_{ij}^5} \right) - J \sum_{\langle i,j \rangle} \vec{\sigma}_i \cdot \vec{\sigma}_j, \quad (5.1.1)$$

where  $\{\vec{\sigma}_i\}$  denotes the set of two-dimensional unit vectors that describe the orientation of the spins at the lattice sites  $\{\vec{r}_i\}$  within the plane of the lattice. In this system the exchange interaction is also assumed to be antiferromagnetic (i.e.,  $J < 0$ ).

## 5.2 Ground state properties

For low values of  $|J|/g$ , the ground state of the plane rotator system is the dipolar planar antiferromagnet ( $AF_{\parallel}$  phase) as described in chapter 4. The energy of this ground state is given by [50]

$$E_{AF_{\parallel}} = -5.0989g. \quad (5.2.1)$$

In contrast, for large values of  $|J|/g$ , the ground state of the system is a simple planar antiferromagnet in which each nearest neighbour pair is aligned antiparallel ( $AA_{\parallel}$  phase) as shown in Figure 5.1. The energy of this state is given by [50]

$$E_{AA_{\parallel}} = 1.3229g + 2J. \quad (5.2.2)$$

By comparing Equation 5.2.1 with Equation 5.2.2, a transition from the degenerate  $AF_{\parallel}$  phase to the non-degenerate  $AA_{\parallel}$  phase occurs when  $|J| = J_0$ , with

$$\begin{aligned} J_0/g &= (5.0989 + 1.3229)/2 \\ &= 3.2109. \end{aligned} \quad (5.2.3)$$

To construct order parameters for both of these two states the square lattice is decomposed into four sub-lattices as was done in chapter 4. Each sublattice is labeled by an index  $\alpha = 1, 2, 3, 4$ , defining for each sub-lattice a corresponding sub-lattice magnetization

$$\begin{aligned} \vec{M}_{\parallel}^{\alpha} &= M_x^{\alpha} \hat{x} + M_y^{\alpha} \hat{y} \\ &= \frac{4}{N} \left( \sum_{\vec{r}_{\alpha}} \sigma^x(\vec{r}_{\alpha}) \right) \hat{x} + \frac{4}{N} \left( \sum_{\vec{r}_{\alpha}} \sigma^y(\vec{r}_{\alpha}) \right) \hat{y}. \end{aligned} \quad (5.2.4)$$

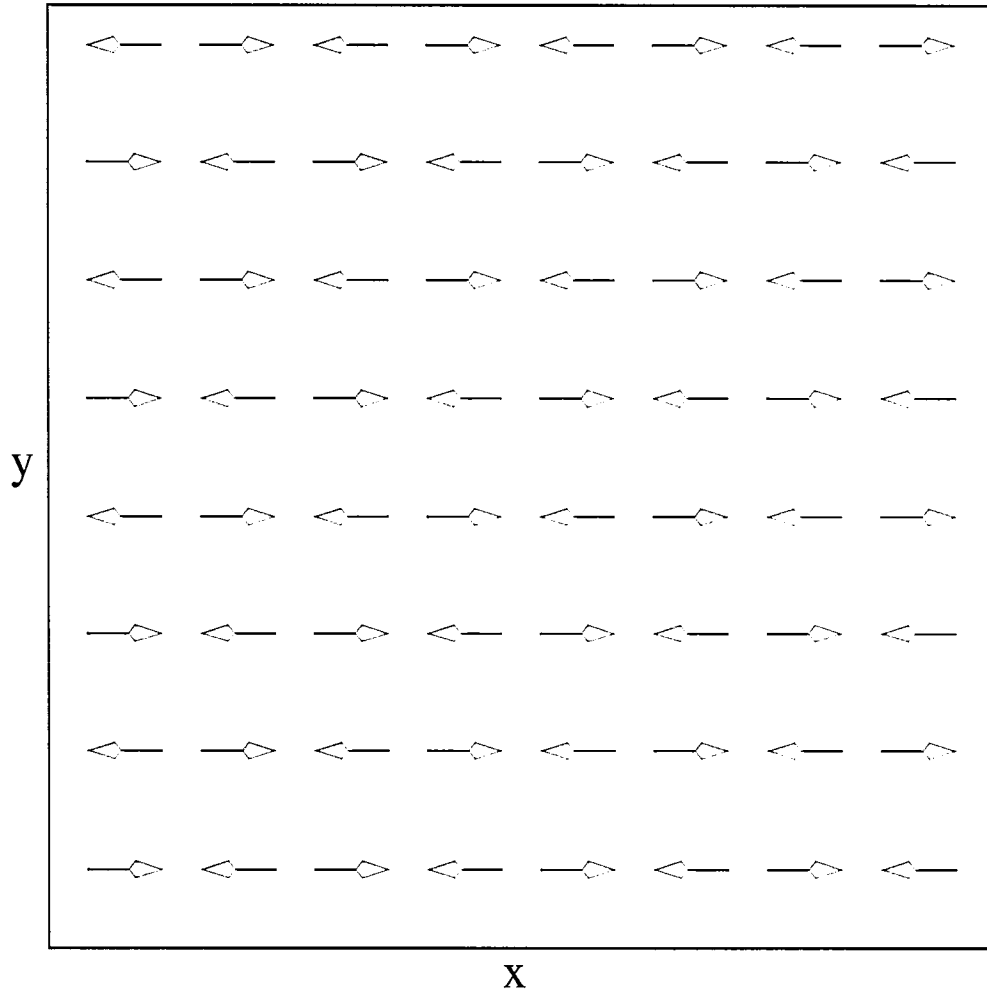


Figure 5.1: The planar antiferromagnetic ( $AA_{||}$ ) ground state spin configuration, where  $x$  and  $y$  denote the two in-plane directions of the square lattice.

From these sub-lattice magnetizations two order parameters are constructed

$$M_{AF_{\parallel}} = \frac{1}{4} |(M_x^1 + M_x^2 - M_x^3 - M_x^4)\hat{x} + (M_y^1 + M_y^3 - M_y^2 - M_y^4)\hat{y}| \quad (5.2.5)$$

and

$$M_{AA_{\parallel}} = \frac{1}{4} |(M_x^1 + M_x^4 - M_x^3 - M_x^2)\hat{x} + (M_y^1 + M_y^4 - M_y^3 - M_y^2)\hat{y}|. \quad (5.2.6)$$

The first of these order parameters,  $M_{AF_{\parallel}}$ , is the same as Equation 4.2.6 characterizes ordering in the ground state corresponding to the  $AF_{\parallel}$  phase [118]. It can be shown that the second-order parameter,  $M_{AA_{\parallel}}$ , is zero in this state. The second-order parameter,  $M_{AA_{\parallel}}$ , characterizes ordering in the ground state corresponding to the  $AA_{\parallel}$  phase. It can be shown that the first-order parameter,  $M_{AF_{\parallel}}$ , is zero in this state.

### 5.3 The phase diagram

At zero temperature, for  $|J| < J_0$  ( $J_0 = 3.2109g$ ), the  $AF_{\parallel}$  phase is energetically favoured, while for  $|J| > J_0$ , the  $AA_{\parallel}$  phase is energetically favoured. This critical value of  $|J|/g$  may be compared to the value of the exchange constant,  $|J_0|/g = 1.2265$ , at which the spins switch from the  $AF_{\parallel}$  ordering to the  $AA_{\perp}$  ordering in the case of the Heisenberg model studied in the previous chapter.

At finite temperature, the equilibrium phases of the system obtained from Monte Carlo simulations are summarised in the phase diagram shown in Figure 5.2. The phase diagram exhibits a phase in which the ordering corresponds to the  $AF_{\parallel}$  states (Region I), a phase in which the ordering corresponds to the  $AA_{\parallel}$  states (Region II), and a disordered phase (Region III). The transition from the  $AF_{\parallel}$  phase to the  $AA_{\parallel}$  phase appears to be first order with clear discontinuities in  $M_{AF_{\parallel}}$  and  $M_{AA_{\parallel}}$  (Fig. 5.3)

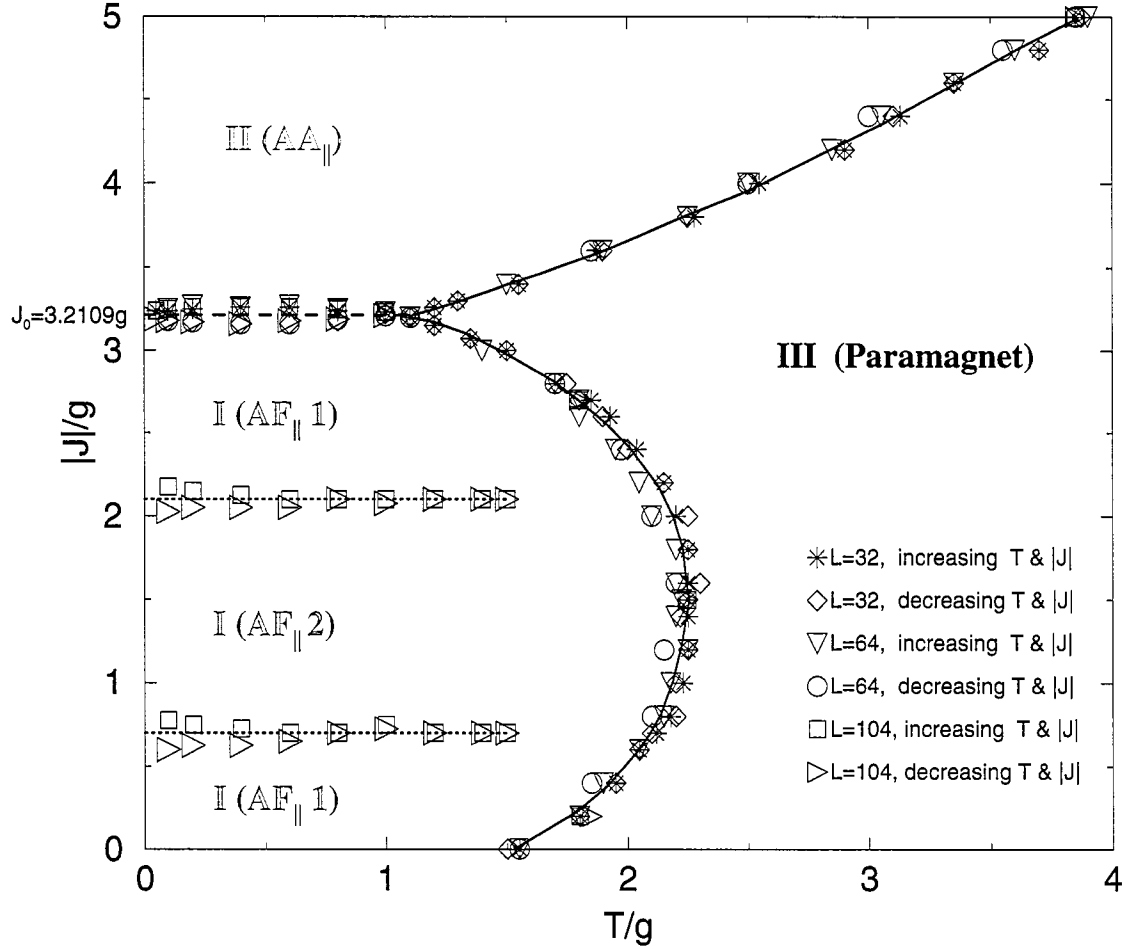


Figure 5.2: The magnetic phase diagram, based on the Monte Carlo simulations, for the dipolar antiferromagnetic plane rotator system as a function of increasing and decreasing both  $|J|/g$  and  $T/g$  for  $N = L \times L = 32^2, 64^2, 104^2$ . Region I is the dipolar planar antiferromagnetic phase ( $AF_{||}$  phase), Region II is the simple parallel antiferromagnetic phase ( $AA_{||}$  phase), and Region III is the paramagnetic phase (disordered phase). The two solid lines highlight the two lines of second-ordered transitions from the paramagnetic phase to the two ordered phases. The dashed line highlight the line of first-ordered reorientation transition from one order state to the other ( $AF_{||}, AA_{||}$ ). The two dotted lines separate the two planar phases ( $AF_{||}1, AF_{||}2$ ).

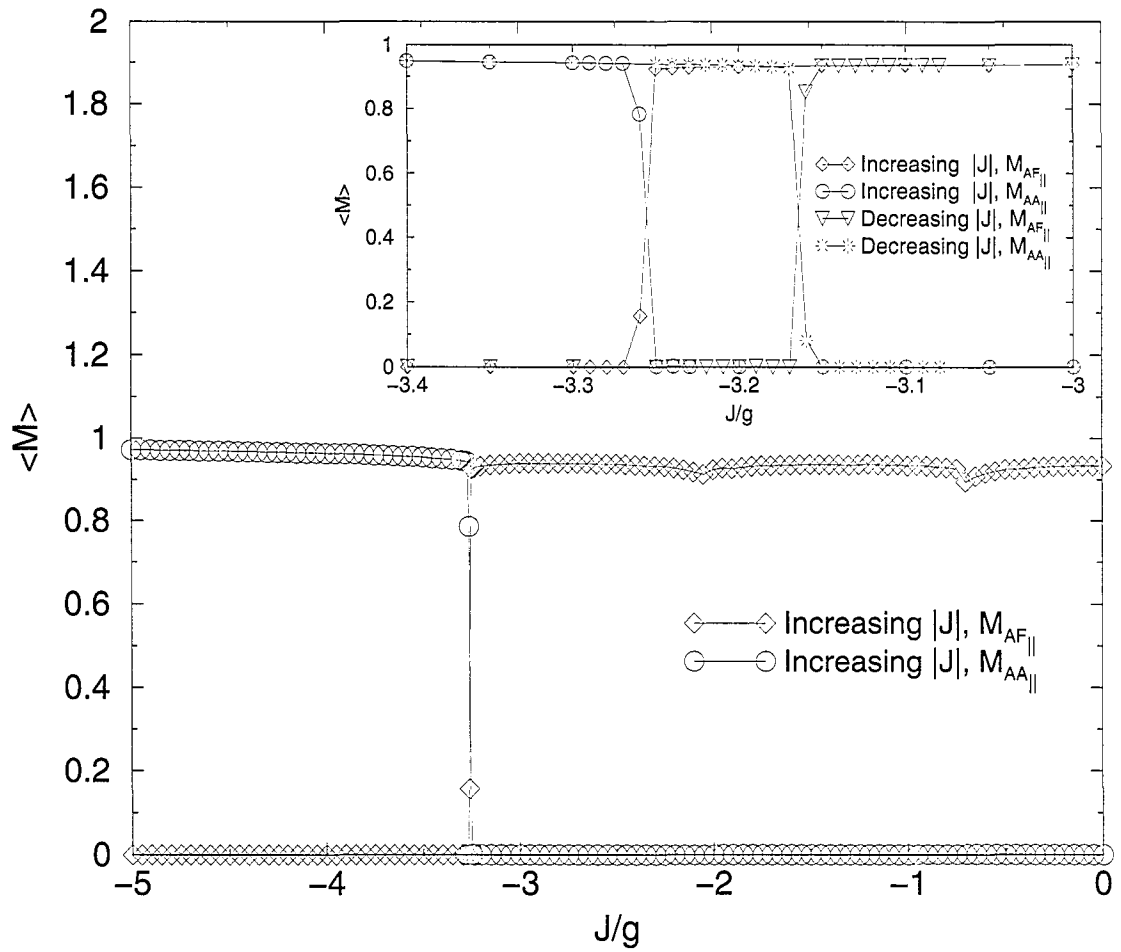


Figure 5.3: The two order parameters,  $M_{AF\parallel}$  and  $M_{AA\parallel}$ , per spin as a function of  $J/g$  for  $T = 0.4g$  with  $L = 104$ . The transition region is shown in the inset and displays the hysteresis characteristic of a first-order transition.

defined in terms of the thermally averaged sub-lattice magnetisation. Within the accuracy of the simulations, the value of  $J$  at which the transition between these two states occurs appears to be independent of temperature. The phase boundary separating the ordered phases,  $AF_{\parallel}$  (Region I) and  $AA_{\parallel}$  (Region II), from the paramagnetic phase (Region III) is obtained from the points at which the order parameters drop to zero (Fig. 5.4) as well as from the corresponding peak in the magnetic heat capacity (Fig. 5.5). These simulations indicate that the transition is second order.

In addition, there is evidence of two distinct  $AF_{\parallel}$  phases: In one ( $AF_{\parallel}1$ ) the order parameter is parallel to one of the axes of the square lattice. In the other ( $AF_{\parallel}2$ ), the order parameter is at an angle of  $\pi/4$  to the lattice axes. The existence of these two distinct phases is readily discerned by monitoring the angle ( $\phi_{\alpha}$ ) associated with the sub-lattice magnetisation for each of the four sub-lattices as defined by Equation 4.3.3. Figure 5.6 shows the behaviour of the sub-lattice magnetisation angle as a function of decreasing temperature for three typical simulations. A sample spin configuration for each value of  $J$  is shown in Figure 5.7 for  $T = 0.15g$ .

The two dotted lines in the phase diagram (Figure 5.2) indicate where transitions between the two  $AF_{\parallel}$  phases are clearly observed to occur in the simulations. In Region I for  $T \leq 1.5g$ , within the accuracy of the simulations, the value of  $J$  for each of these transitions is independent of temperature. For  $T \geq 1.5g$ , the phase behaviour in Region I becomes more difficult to determine and the phase boundary separating the two  $AF_{\parallel}$  phases is more difficult to discern. While it seems reasonable to suppose that the phase boundaries separating the two  $AF_{\parallel}$  phases in Region I remain distinct and terminate at the paramagnetic phase boundary, at this point other possibilities cannot be eliminated. Despite these details regarding the precise determination of

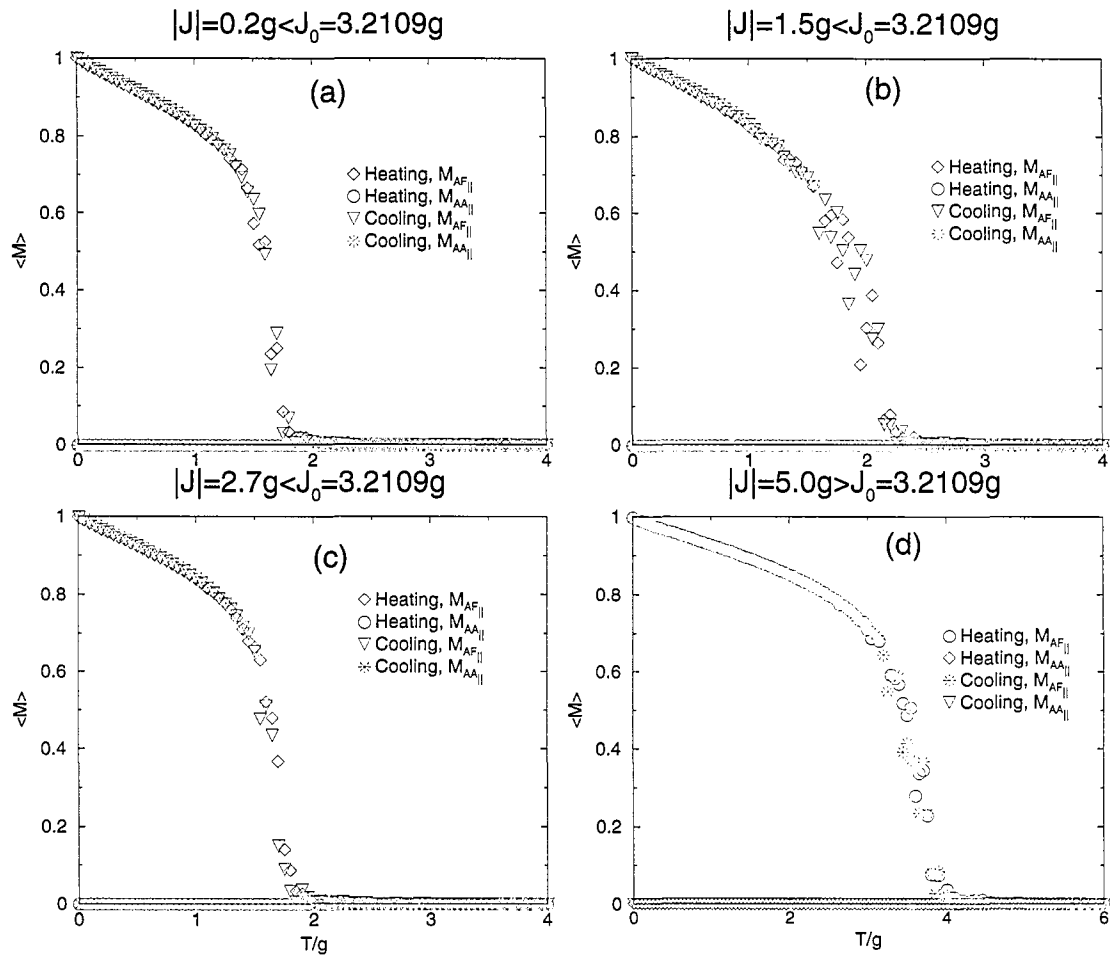


Figure 5.4: The two order parameters,  $M_{AF\parallel}$  and  $M_{AA\parallel}$ , per spin as a function of  $T/g$  for (a)  $|J| = 0.2g$ , (b)  $|J| = 1.5g$ , (c)  $|J| = 2.7g$ , and (d)  $|J| = 5.0g$  with  $L = 104$ .

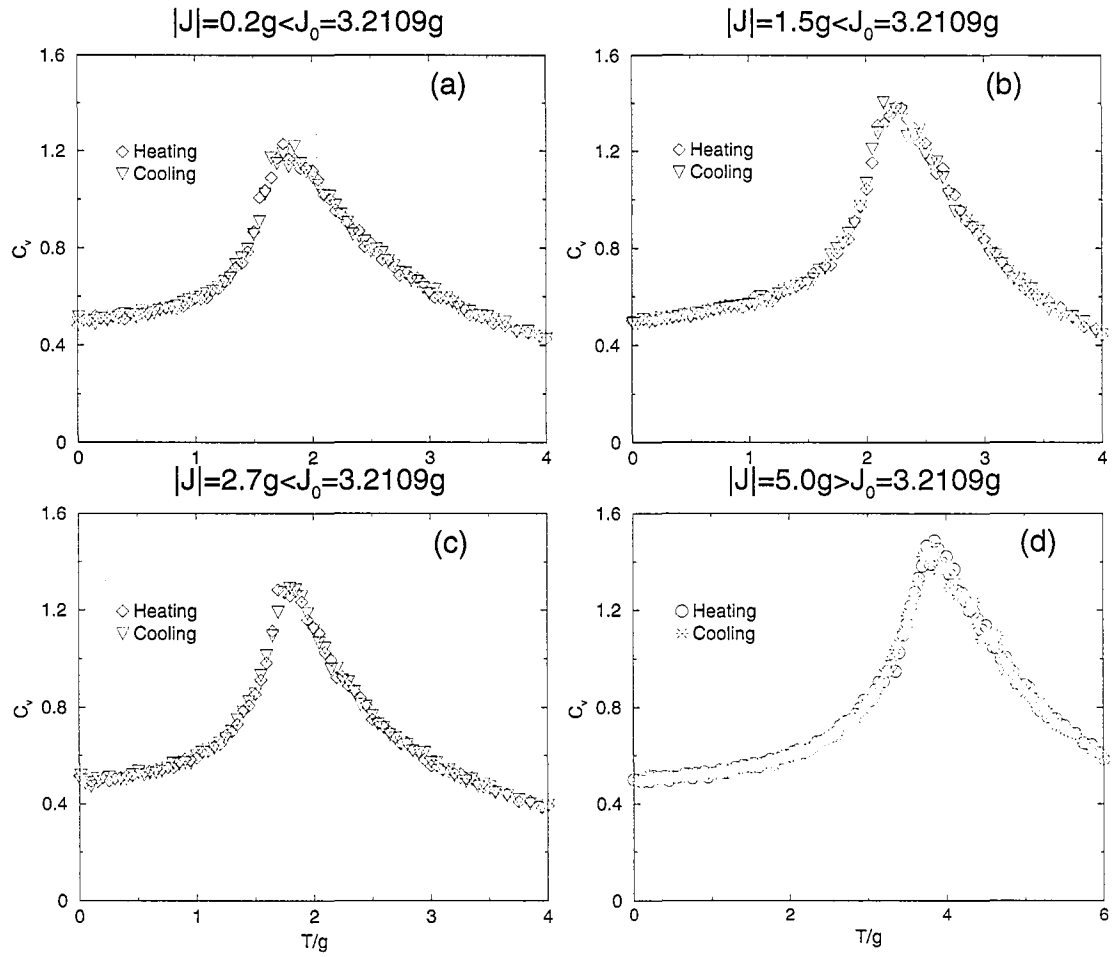


Figure 5.5: The heat capacity,  $C_v$ , per spin as a function of  $T/g$  for (a)  $|J| = 0.2g$ , (b)  $|J| = 1.5g$ , (c)  $|J| = 2.7g$  and, (d)  $|J| = 5.0g$  with  $L = 104$ .

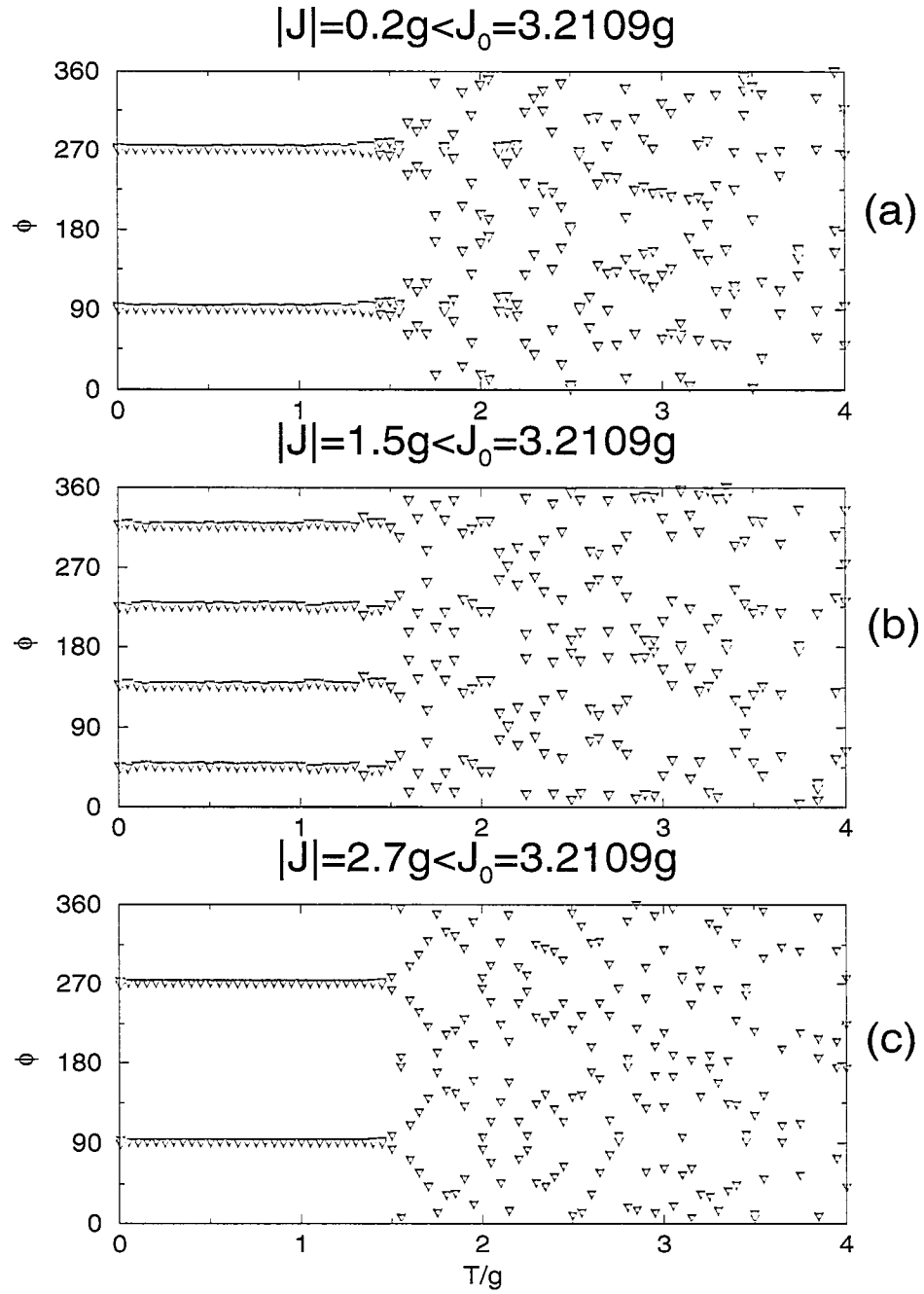


Figure 5.6: A plot of the angle  $\phi_\alpha$ , for each of the four sub-lattice magnetisations as a function of temperature,  $T/g$ , for (a)  $|J| = 0.2g$ , (b)  $|J| = 1.5g$ , and (c)  $|J| = 2.7g$  with  $L = 104$ .

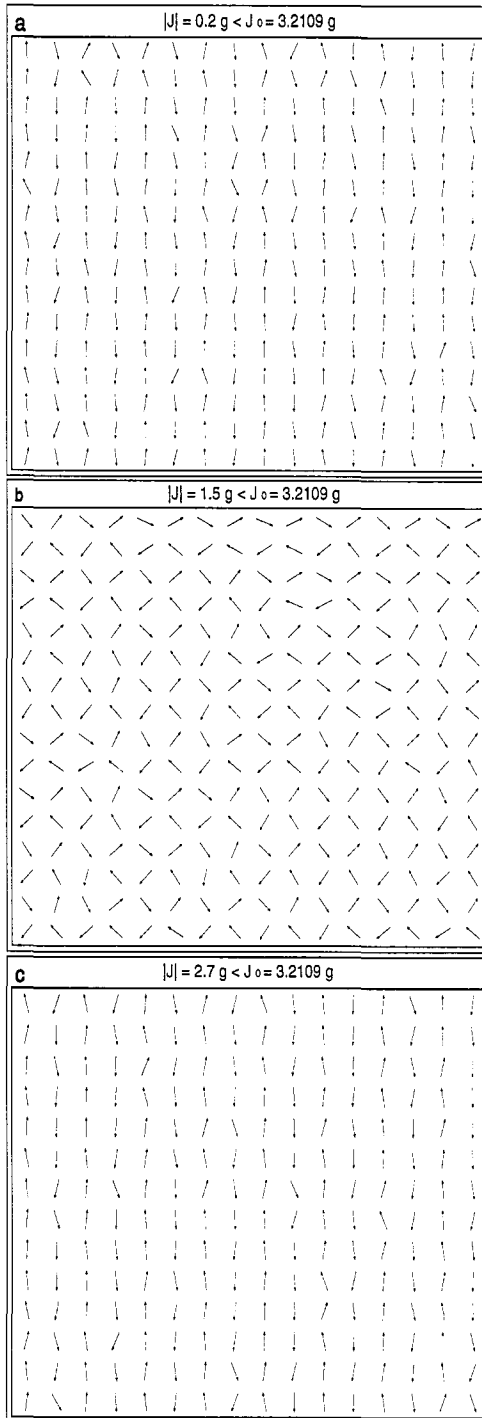


Figure 5.7: Snapshots of three typical spin configurations at  $T = 0.15g$  for (a)  $|J| = 0.2g$ , (b)  $|J| = 1.5g$ , and (c)  $|J| = 2.7g$  with  $L = 104$ .

the phase boundaries separating the  $AF_{\parallel}1$  and  $AF_{\parallel}2$  phases, the reentrant behaviour of the  $AF_{\parallel}$  phases in which the system is in the  $AF_{\parallel}1$  phase for small values of  $|J|/g$ , switches to the  $AF_{\parallel}2$  phase as  $|J|/g$  is increased and then back to the  $AF_{\parallel}1$  phase, before making a transition back to the  $AA_{\parallel}$  phase, is perhaps the most remarkable feature of this phase diagram. The two  $AF_{\parallel}$  phases can also be distinguished by noting that the magnetic order in the  $AF_{\parallel}$  phase arises as a consequence of an effective four-fold anisotropy induced by the thermal fluctuations which break the symmetry of the dipolar ground state manifold [116, 117, 118]. The effect of this thermally induced effective anisotropy on the magnetic order can be determined by calculating the mean value of the conjugate field to which it couples [118], i.e.

$$P(T) = \frac{1}{N} \left\langle \sum_{\vec{R}} (\sigma_x^4 + \sigma_y^4) \right\rangle. \quad (5.3.1)$$

At zero temperature,  $P = 1$  for the  $AF_{\parallel}1$  phase and  $P = 0.5$  for the  $AF_{\parallel}2$  phase, while in a paramagnetic phase  $P = 0.75$ . Figure 5.8 shows the variation of  $P$  with temperature for three values of  $|J|/g$  in the  $AF_{\parallel}$  phases, as presented for decreasing temperature. The three graphs in Figure 5.8 show evidence of two distinct behaviours. For  $|J| = 0.2g$  and  $2.7g$  the curve starts at high temperature in the paramagnetic phase with  $P = 0.75$ . As the temperature is reduced,  $P$  evolves towards a value of 1 in the limit  $T \rightarrow 0$ . For  $|J| = 1.5g$  the behaviour is quite different. Starting at high temperature in the paramagnetic phase,  $P$  decreases with decreasing temperature, reaching a value of 0.5 in the limit  $T \rightarrow 0$ . This is consistent with the phase diagram shown in Figure 5.2.

A noticeable feature of the curves for  $|J| = 0.2g$  and  $2.7g$  is that  $P$  reaches a value of 0.75, the expected value of  $P$  for a paramagnetic system, at  $T \approx 1.4g$ , just below the Néel temperature. A similar feature was noted in the analysis of the pure dipolar

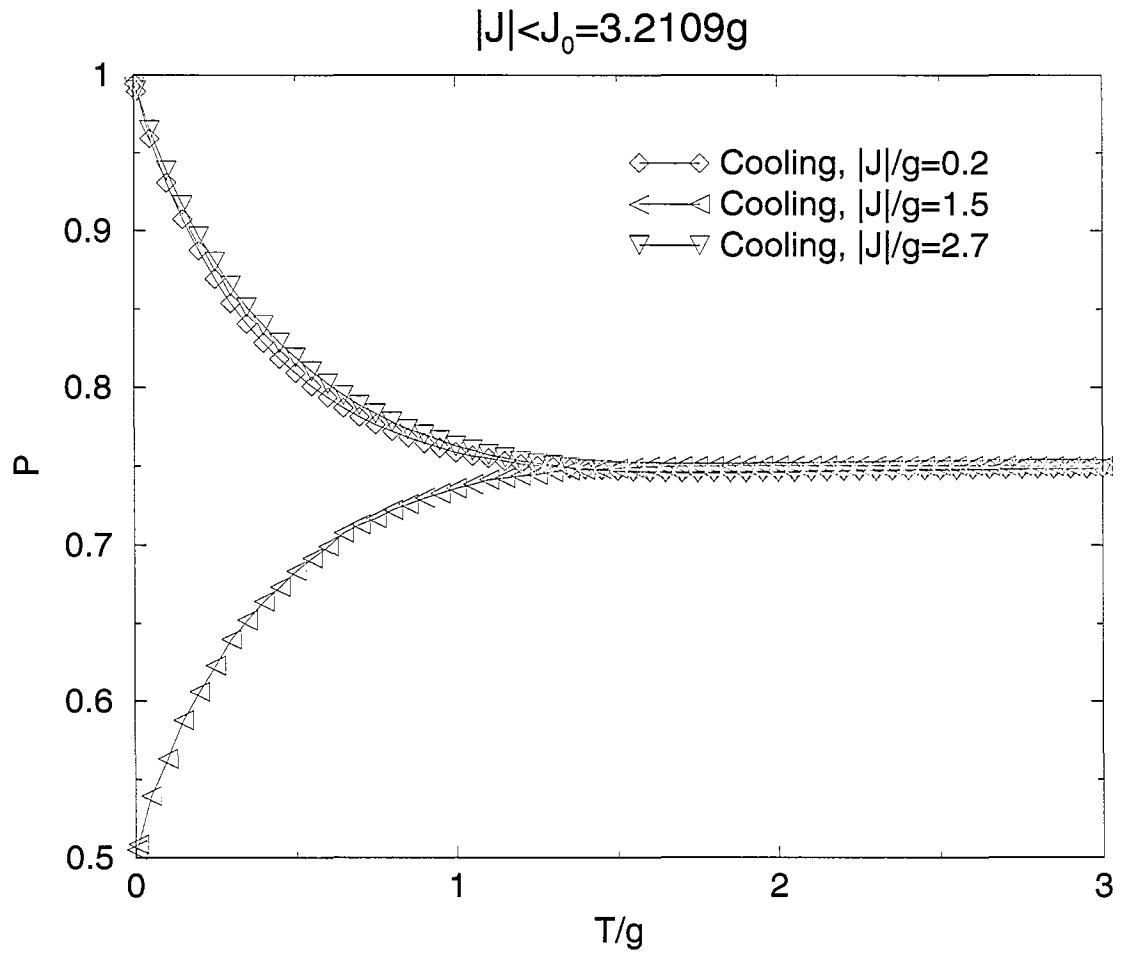


Figure 5.8: The conjugate field,  $P$ , per spin as a function of temperature,  $T/g$ , for several values of  $|J|/g$  with  $L = 104$ .

system [118]. The significance of this result and its implications for the magnetic order are not fully understood.

## 5.4 Free energy

The existence of the  $AF_{\parallel}1$  and the  $AF_{\parallel}2$  phases in Region I of the phase diagram suggests that the free energy in the  $AF_{\parallel}$  phase has two branches, one branch corresponding to the  $AF_{\parallel}1$  phase and the other to the  $AF_{\parallel}2$  phase. The reentrant behaviour in which the antiferromagnetic  $AF_{\parallel}$  phase changes not once but twice with increasing  $|J|/g$  places constraints on the nature of the free energy surfaces describing the  $AF_{\parallel}$  phases and how they intersect. It is therefore instructive to evaluate the free energy of the  $AF_{\parallel}$  phase as a function of the exchange constant,  $|J|/g$ , for a fixed temperature,  $T/g$ .

While the absolute free energy of a system cannot be calculated directly from Monte Carlo simulations as mentioned in chapter 3, it is possible, using non-equilibrium sampling technique, to calculate the difference in free energy with respect to some reference state. It can be shown that the difference in free energy,  $\Delta F$ , between two systems with different exchange constants,  $\Delta J = J_o - J$ , can be expressed as

$$\Delta F = -T \ln \left( \left\langle \exp\left(-\Delta J \sum_{\langle i,j \rangle} \vec{\sigma}_i \cdot \vec{\sigma}_j / T\right) \right\rangle_{J_o} \right), \quad (5.4.1)$$

where the ensemble average,  $\langle \rangle_{J_o}$ , is calculated using the exchange constant,  $J_o$ , in the thermal average. The exact details of the derivation, however, are presented in Appendix A.

In practice, reasonable results can be obtained from Monte Carlo simulations

provided  $\Delta J$  is not too large. However, by calculating  $\Delta F$  as a function of  $J$  for several values of  $J_0$ , the free energy can be calculated over a particular range of  $J$  using the fact that the free energy is a continuous function of  $J$  (more details are presented in Appendix A). Results are shown for  $T = 0.2g$  in Figure 5.9. The data show that the free energy curves for both the  $AF_{\parallel 1}$  and the  $AF_{\parallel 2}$  phases are concave, with a maximum of  $|J| \approx 1.5g$ , and consistent with the reentrant behaviour obtained from the current simulations implicit shown in the phase diagram in Figure 5.2. Note, however, that the solid lines shown in Figure 5.9 are simply a guide to the eye.

## 5.5 Summary

In this chapter the dipolar antiferromagnetic rotator model on a square lattice has been studied for both zero and finite temperature. At low temperatures, the Monte Carlo results show that the competition between the long-range dipolar and the short-range antiferromagnetic interactions in this system can lead to a reorientation transition from the dipolar planar antiferromagnetic ( $AF_{\parallel}$ ) phase to the simple planar antiferromagnetic ( $AA_{\parallel}$ ) phase as the antiferromagnetic exchange constant increases. The results also show that the phase boundary separating these two ordered phases is weakly dependent on temperature and intercepts the  $|J|/g$  axis at  $J_0 = 3.2109g$ . This phase boundary also appears to be a first-order transition involving a small amount of hysteresis. Moreover, the Monte Carlo results show that the phase boundary separating the two ordered states ( $AF_{\parallel}, AA_{\parallel}$ ) from the paramagnetic state appear to be a second-order transitions.

The present results also demonstrate that a purely planar model can exhibit both the  $AF_{\parallel 1}$  and  $AF_{\parallel 2}$  phases, with a transition between them, as the relative strength

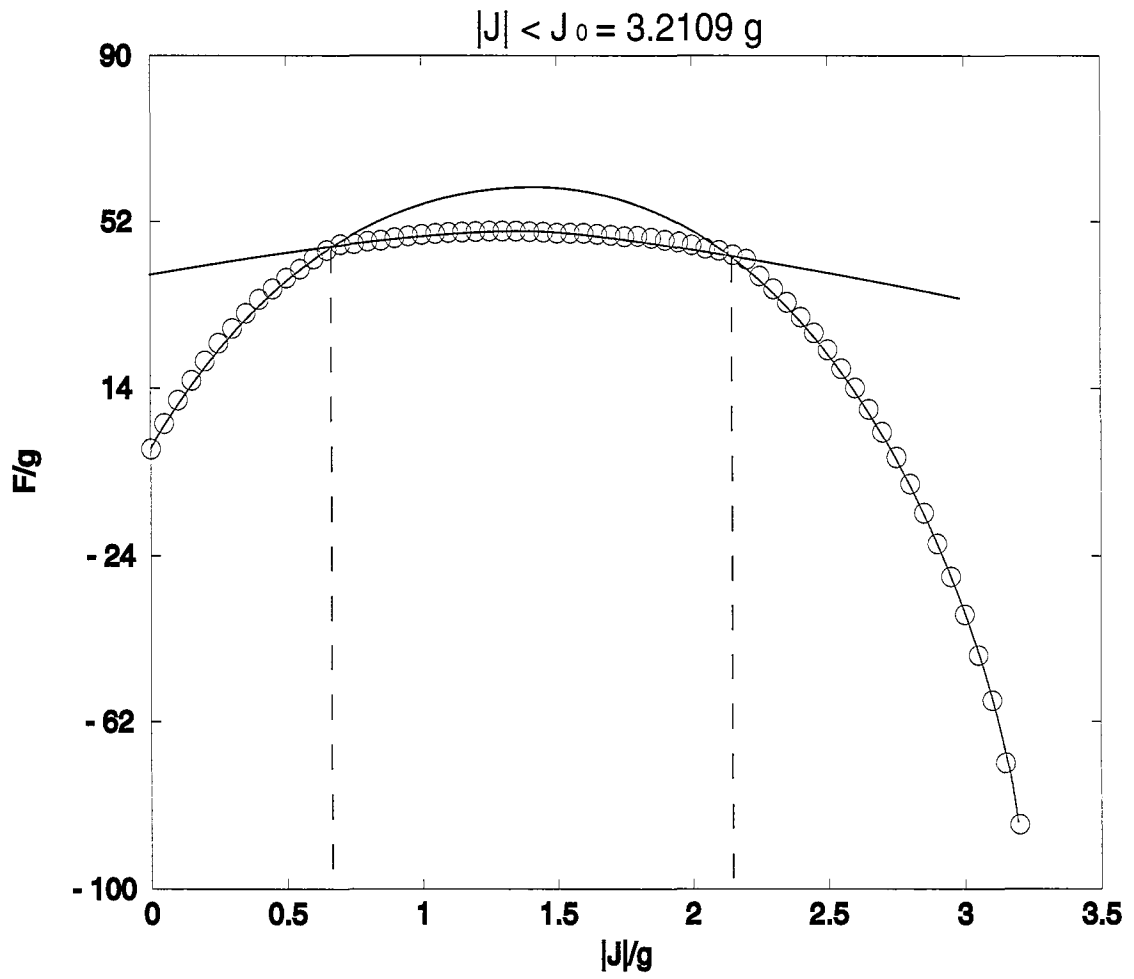


Figure 5.9: The free energy as a function of the exchange constant,  $|J|/g$ , for  $T = 0.2g$  with  $L = 64$ . (The solid lines shown in the figure are simply a guide to the eye.)

of the exchange interaction is varied. While the  $AF_{\parallel}1$  phase occurs in the two regions where  $|J| \lesssim 0.7g$  and  $2.1g \lesssim |J| \lesssim 3.21g$ ,  $AF_{\parallel}2$  occurs in the region where  $0.7g \lesssim |J| \lesssim 2.1g$ . This means that the out-of-plane degree of freedom of the magnetic moments, present in the study described in chapter 4 but absent here, does not play a critical role in determining the easy axis of the magnetisation in the  $AF_{\parallel}$  phase. The presence of the  $AF_{\parallel}1$  and  $AF_{\parallel}2$  phases in the square plane rotator model having a long-range isotropic antiferromagnetic and long-range dipolar interactions is also confirmed by Rastelli *et al.* using renormalized spin-wave theory as well as Monte Carlo simulations [121]. The question of how the presence of the exchange interaction modifies the thermal randomness so that this effect is observed remains to be answered.

Furthermore, the present study indicates that reentrant phenomena between the  $AF_{\parallel}$  phases occurs as the relative strength of the exchange interaction is increased. This was not observed in the study reported in chapter 4, presumably because the in-plane to out-of-plane reorientation transition occurs before the system can reenter the  $AF_{\parallel}1$  phase. The low temperature properties of the dipolar planar antiferromagnetic system, therefore, provide a particularly intriguing example of the phenomena of “order from disorder”. It would be interesting to examine how the antiferromagnetic order for the planar antiferromagnet would be affected by other types of disorder, such as dilution. As the present work clearly demonstrates, the form of the ordered state is extremely sensitive to the precise nature of the disorder that gives rise to it.

# Chapter 6

## The Anisotropic Heisenberg System: Fixed $\kappa$

### 6.1 Introduction

In chapter 4, it was concluded from the Monte Carlo results that, at low temperatures, the competition between the short-range antiferromagnetic exchange and the long-range dipolar interactions for the two-dimensional Heisenberg system on a square lattice with zero magnetic surface anisotropy could lead to a reorientation transition between the dipolar planar antiferromagnetic and the perpendicular antiferromagnetic phases. It was also found that the coexistence line between these two order phases appears to be weakly dependent on the temperature. Moreover, the results suggested that the phase boundary between the low temperature ordered phase and the high temperature paramagnetic phase appears to be a second-order transition. Interestingly, the results demonstrated that the dipolar planar phase consists of two distinct phases,  $AF_{\parallel 1}$  and  $AF_{\parallel 2}$ . While in the  $AF_{\parallel 1}$  phase the spins are ordered along either the  $x$  or  $y$ -axis of the lattice, in the  $AF_{\parallel 2}$  phase they are aligned at  $\pm\pi/4$  to the  $x$ -axis.

In chapter 5, the Monte Carlo results for the magnetic properties of the dipolar antiferromagnetic plane rotator system were presented. It can be concluded from these results that the out-of-plane degree of freedom of the magnetic spins does not seem to play a critical role in determining the easy axis of the magnetisation in the  $AF_{\parallel}$  phase.

Typically, low-dimensional magnetic systems include the on-site magnetic anisotropy in addition to the exchange and the dipolar interactions. Thus, the magnetic properties of such systems depend on the subtle interplay between these three interactions. Hence, the question which arises as to how the magnetic surface anisotropy can affect the phase behavior of the system presented in chapter 4. To answer this question, in this chapter the two-dimensional dipolar antiferromagnetic Heisenberg system on a square lattice having a weak planar magnetic surface anisotropy is investigated. The chapter examines the phase behaviour that arises as a consequence of the competition between the long-range dipolar, and the nearest-neighbour antiferromagnetic exchange interactions in the presence of a weak planar anisotropy for the two-dimensional Heisenberg system on this lattice. Differences and similarities between the results for this system and the system studied in chapter 4 are presented and discussed in the following sections.

Again, the results reported are primarily based on Monte Carlo simulations. The system consists of  $N$  classical spins arranged on a square lattice of length  $L$  with an energy given by

$$\begin{aligned}
 E(\{\vec{\sigma}_i\}) = & g \sum_{i \neq j} \left( \frac{\vec{\sigma}_i \cdot \vec{\sigma}_j}{r_{ij}^3} - 3 \frac{(\vec{\sigma}_i \cdot \vec{r}_{ij})(\vec{\sigma}_j \cdot \vec{r}_{ij})}{r_{ij}^5} \right) - J \sum_{\langle i, j \rangle} \vec{\sigma}_i \cdot \vec{\sigma}_j \\
 & - \kappa \sum_i (\sigma_i^z)^2,
 \end{aligned} \tag{6.1.1}$$

where  $\{\vec{\sigma}_i\}$  denotes the set of three-dimensional unit vectors that describe the orientation of the magnetic moments at the lattice sites  $\{\vec{r}_i\}$ . In this system, a specific value of the in-plane surface anisotropy,  $\kappa = -1.0g$ , and an antiferromagnetic exchange constant (i.e.,  $J < 0$ ) are considered.

## 6.2 The Ground State

The ground state of the system is dependent on the value of  $|J|/g$ . For low values of  $|J|/g$ , the ground state is the dipolar planar antiferromagnet ( $AF_{\parallel}$ ) described in chapter 4, and its energy is given by [50]

$$E_{AF_{\parallel}} = -5.0989g. \quad (6.2.1)$$

For large values of  $|J|/g$ , the ground state is the simple perpendicular antiferromagnet ( $AA_{\perp}$ ), and its energy is given by [50]

$$E_{AA_{\perp}} = -2.6459g + 2J - \kappa. \quad (6.2.2)$$

Comparing Equation 6.2.1 with Equation 6.2.2, at  $T = 0$ , the system switches from the degenerate  $AF_{\parallel}$  phase to the non-degenerate  $AA_{\perp}$  phase at  $J = -J_0$ , with

$$J_0/g = (5.0989g - 2.6459g - \kappa)/2. \quad (6.2.3)$$

For  $\kappa = -1.0g$ , Equation 6.2.3 then gives

$$J_0/g = 1.7265. \quad (6.2.4)$$

Comparing this value with the value of the exchange constant,  $|J|/g = 1.2265$ , at which the spins switch from the  $AF_{\parallel}$  phase to the  $AA_{\perp}$  phase for  $\kappa = 0$ , one can see

that the presence of a weak planar magnetic surface anisotropy stabilizes the planar phase and causes the switching value of the exchange constant to shift toward a higher value.

### 6.3 Finite Temperature Properties

Similar to the system discussed in chapter 4, the equilibrium phases of interest are the  $AF_{\parallel}$  and the  $AA_{\perp}$  phases. These can be characterised by the order parameters,  $M_{AF_{\parallel}}$  and  $M_{AA_{\perp}}$ , given by Equations 4.2.6 and 4.2.7, respectively. In Figure 6.1, both  $M_{AF_{\parallel}}$  and  $M_{AA_{\perp}}$ , defined in terms of the thermally averaged sublattice magnetisation given by Equations 4.3.1 and 4.3.2, are plotted as a function of both increasing and decreasing temperature for different values of  $|J|/g$  in an  $N = 104^2$  system. In Figure 6.1a,  $|J| = 0.2g$  and the data show that there is a continuous transition between the  $AF_{\parallel}$  phase and the paramagnetic phase at  $T_N = (1.38 \pm 0.05)g$ . In Figure 6.1b,  $|J| = 1.2g$  and the data show qualitatively similar behaviour, except that the continuous transition between the  $AF_{\parallel}$  phase and the paramagnetic phase occurs at  $T_N = (1.58 \pm 0.05)g$ . For low values of  $|J|/g$  the order parameters for this system behave similarly to that found for the Heisenberg system in chapter 4 (see Figures 4.4a and 4.4b) and to that found for the plane rotator system in chapter 5 (see Figures 5.4a, 5.4b, and 5.4c). As in the previous two systems, this suggests that the phase boundary between the  $AF_{\parallel}$  ordered phase and the disordered phase defines a line of second-order transitions. In Figure 6.1d,  $|J| = 2.5g$ , and the data show similar behaviour to that shown in Figures 6.1a and 6.1b, except that now the transition that occurs at  $T_N = (2.7 \pm 0.05)g$  is between the  $AA_{\perp}$  phase and the paramagnetic phase. For large values of  $|J|/g$ , the order parameters in Figure 6.1d behave similarly to that

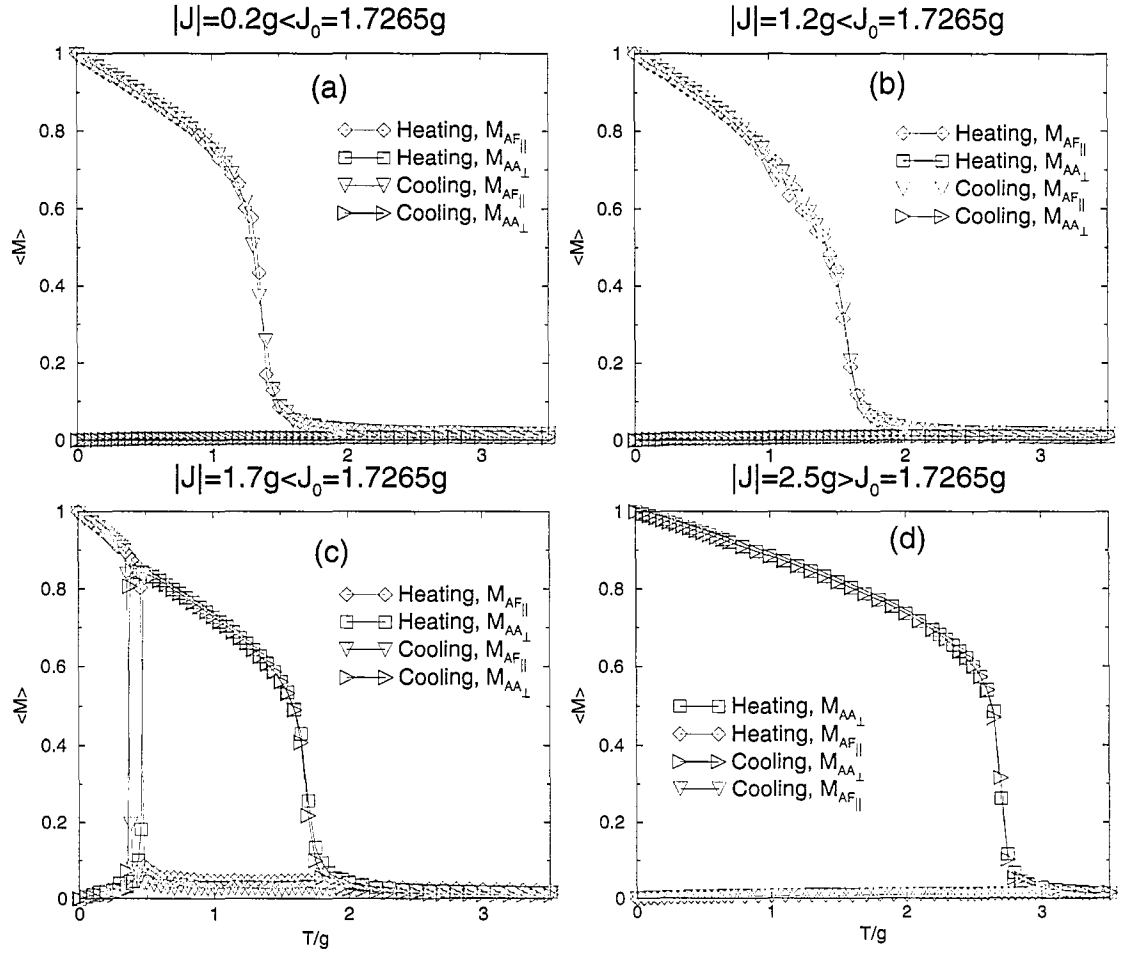


Figure 6.1: The two order parameters,  $M_{AF\parallel}$  and  $M_{AA\perp}$ , per spin as a function of the temperature  $T/g$  for (a)  $|J| = 0.2g$ , (b)  $|J| = 1.2g$ , (c)  $|J| = 1.7g$ , and (d)  $|J| = 2.5g$  with  $L = 104$ .

shown in chapter 4 for the Heisenberg system (see Figure 4.10). This also suggests that the phase boundary between the  $AA_{\perp}$  ordered phase and the paramagnetic phase defines another line of second-order transitions.

However, in Figure 6.1c,  $|J| = 1.7g$  and the data indicate that the two order parameters,  $M_{AF_{\parallel}}$  and  $M_{AA_{\perp}}$ , now behave differently from that shown in Figures 6.1a, 6.1b, and 6.1d. At  $T = 0$  and for this value of  $|J|/g$ , the system is completely in the dipolar ( $AF_{\parallel}$ ) phase. As the temperature is increased, the system switches such that the  $AF_{\parallel}$  order parameter effectively drops to zero while the  $AA_{\perp}$  order parameter becomes non-zero at  $T_R = (0.47 \pm 0.02)g$ . As the temperature is increased further, the system exhibits a continuous transition from the  $AA_{\perp}$  to the paramagnetic phase at  $T_N = (1.68 \pm 0.05)g$ . Similar behaviour is observed on cooling except that the discontinuity in the order parameter occurs at a slightly lower temperature,  $T_R = (0.37 \pm 0.02)g$ . This hysteresis, together with the discontinuous change in the order parameters for both heating and cooling, indicates that the reorientation transition is first order. The hysteresis at the transition is shown in more detail in Figure 6.2, which shows the order parameters and the internal energy as a function of both increasing and decreasing temperature in the region near the transition temperature. This is evidence that the reorientation transition is first-order.

Further evidence for the first-order reorientation transition between the two ordered states is also seen in the susceptibilities of the sub-lattice magnetization data, shown in Figure 6.3. While the perpendicular susceptibility (Figure 6.3a) shows two narrow peaks corresponding to the reorientation transition on heating and cooling, the parallel susceptibility (Figure 6.3b) shows three distinct peaks. The two narrow peaks correspond to the reorientation transition on heating and cooling, while the

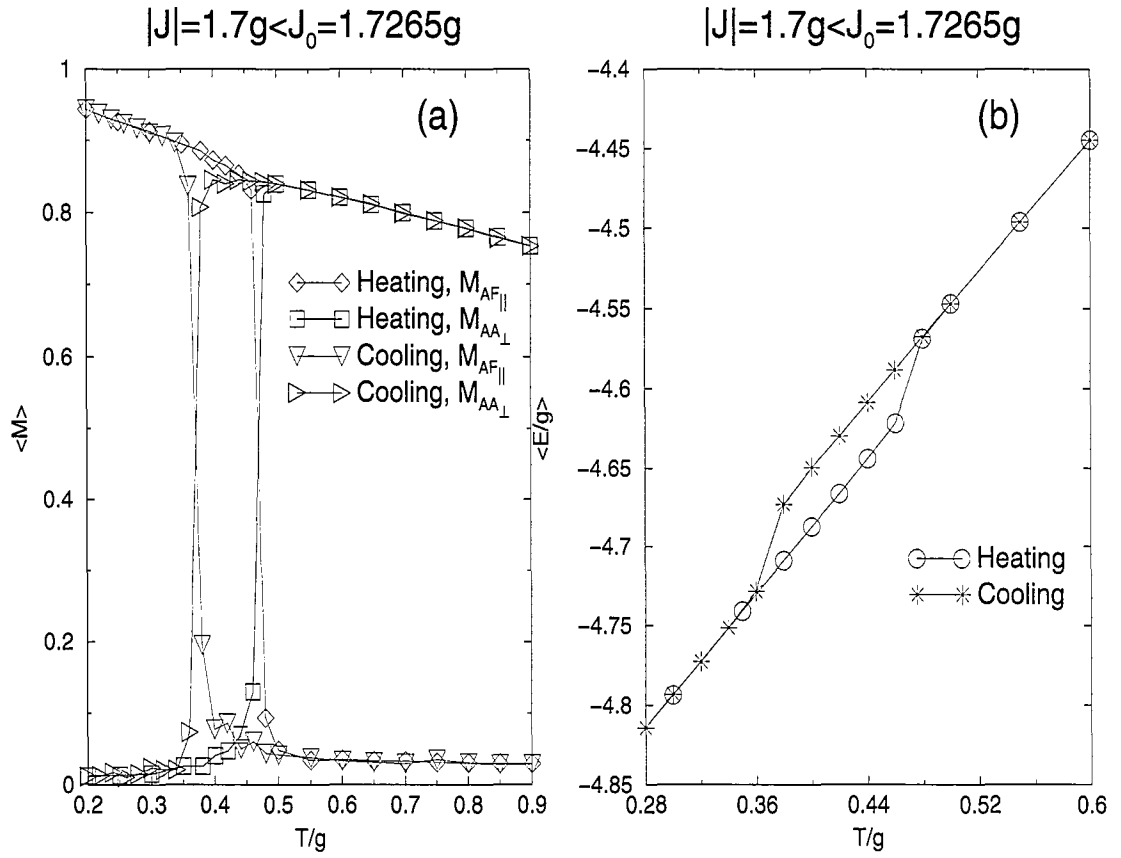


Figure 6.2: A plot of the (a) two order parameters,  $M_{AA\perp}$  and  $M_{AF||}$ , and (b) the total average internal energy,  $\langle E/g \rangle$ , per spin as a function of temperature,  $T/g$ , for  $|J| = 1.7g$  with  $L = 104$ .

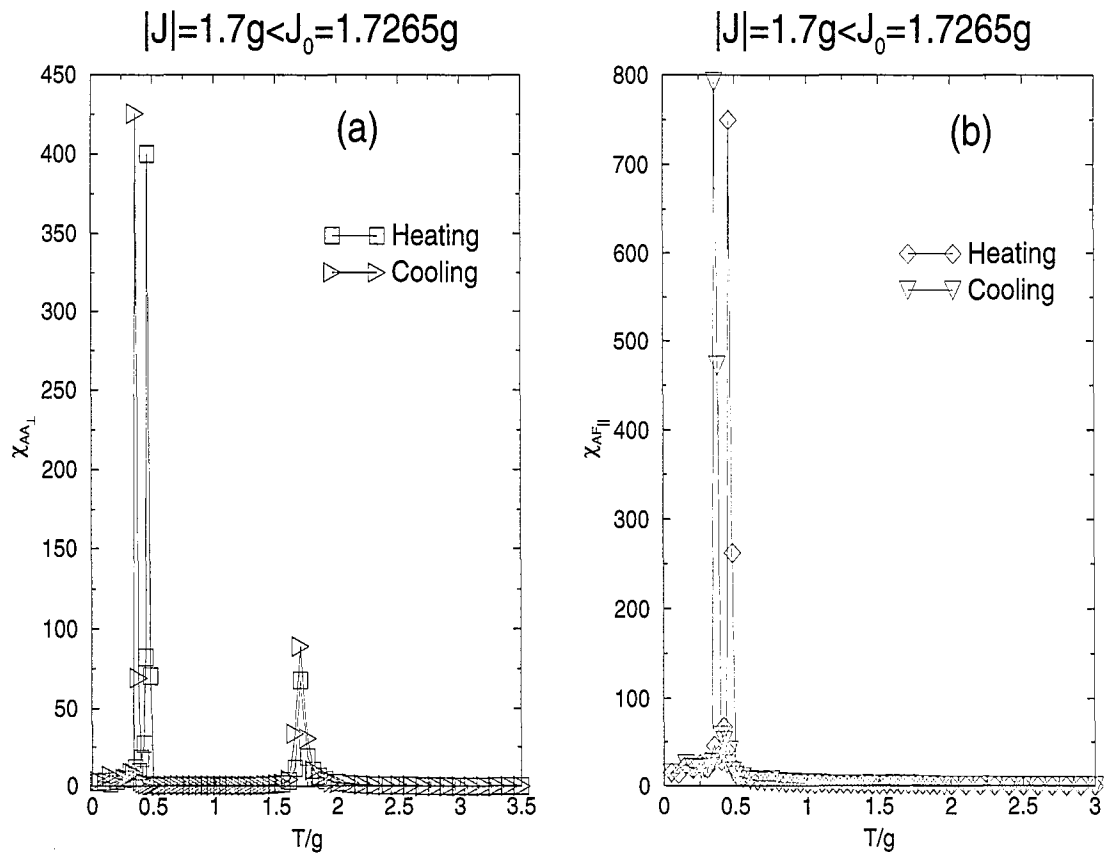


Figure 6.3: A plot of the (a) parallel and (b) the perpendicular susceptibilities,  $\chi_{AA_{\perp}}$  and  $\chi_{AF_{\parallel}}$ , per spin as a function of temperature,  $T/g$ , for  $|J| = 1.7g$  with  $L = 104$ .

broad peak in the perpendicular susceptibility data corresponds to the continuous transition between the perpendicular phase and the paramagnetic phase.

The temperature dependence of the two order parameters shown in Figure 6.1, is consistent with the heat capacity data shown in Figure 6.4 for the same values of  $|J|/g$  mentioned earlier (i.e.,  $|J|/g = 0.2, 1.2, 1.7, 2.5$ ). For  $|J|/g = 0.2, 1.2, 2.5$  shown in Figures 6.4a, 6.4b, and 6.4d, respectively, the heat capacity data show only one peak which corresponds to the continuous transition between the two order states and the paramagnetic state. The heat capacity data for  $|J| = 1.7g$  in Figure 6.4c shows three distinct peaks. The two narrow peaks correspond to the reorientation between the two ordered states on heating and cooling, while the broad peak corresponds to the continuous transition between the perpendicular phase and the paramagnetic phase.

Similar to what was found in the previous two systems, the nature of the equilibrium spin configurations for the  $AF_{\parallel}$  phase depends on the value of  $|J|/g$ . A sample spin configuration for each value of  $|J|/g$  (i.e.,  $|J| = 0.2g, 1.2g$ ) is shown in Figure 6.5 for  $T = 0.15g$ . The spin configuration in Figure 6.5a shows that for  $|J| = 0.2g$ , the sub-lattice magnetisation is aligned along either the  $x$  or  $y$ -axis (the  $AF_{\parallel 1}$  phase) similar to that found for both the Heisenberg and plane rotator systems in the region where  $|J| \lesssim 0.7g$  (see Figure 4.8a, Figures 5.7a). In contrast, the spin configuration in Figure 6.5b shows that for  $|J| = 1.2g$ , the sub-lattice magnetisation is oriented at  $\pi/4$  to the  $x$ -axis (the  $AF_{\parallel 2}$  phase) similar to that found in the Heisenberg system in the region where  $0.7g \lesssim |J| \lesssim 1.23g$  (see Figure 4.8b), and to that found in the plane rotator system in the region where  $0.7g \lesssim |J| \lesssim 2.1g$  (see Figure 5.7b).

The difference in the orientation of the equilibrium spin configuration is also apparent in Figure 6.6, which shows the angle  $\phi_{\alpha}$  for each of the sub-lattices, defined

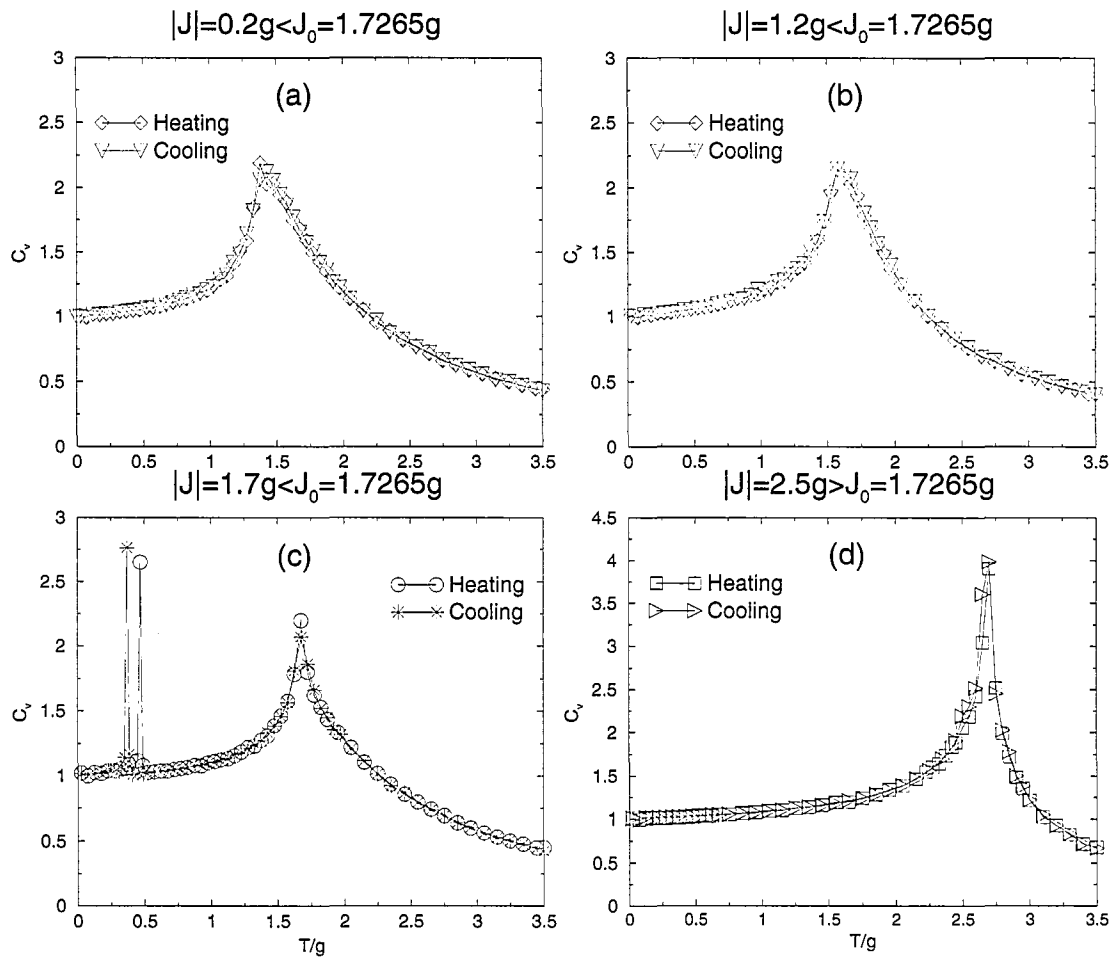


Figure 6.4: The heat capacity,  $C_v$ , per spin as a function of temperature,  $T/g$ , for (a)  $|J| = 0.2g$ , (b)  $|J| = 1.2g$ , (c)  $|J| = 1.7g$  and (d)  $|J| = 2.5g$  with  $L = 104$ .

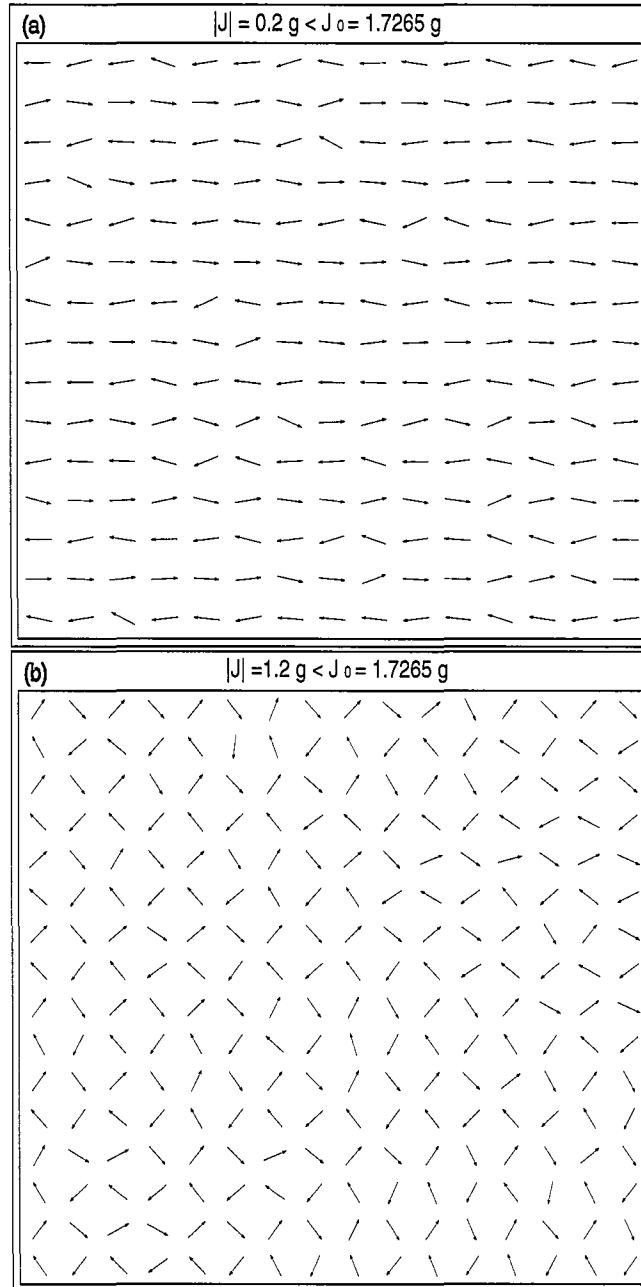


Figure 6.5: Snapshots of two typical spin configurations at  $T = 0.15g$  for (a)  $|J| = 0.2g$  and (b)  $|J| = 1.2g$  with  $L = 104$ .

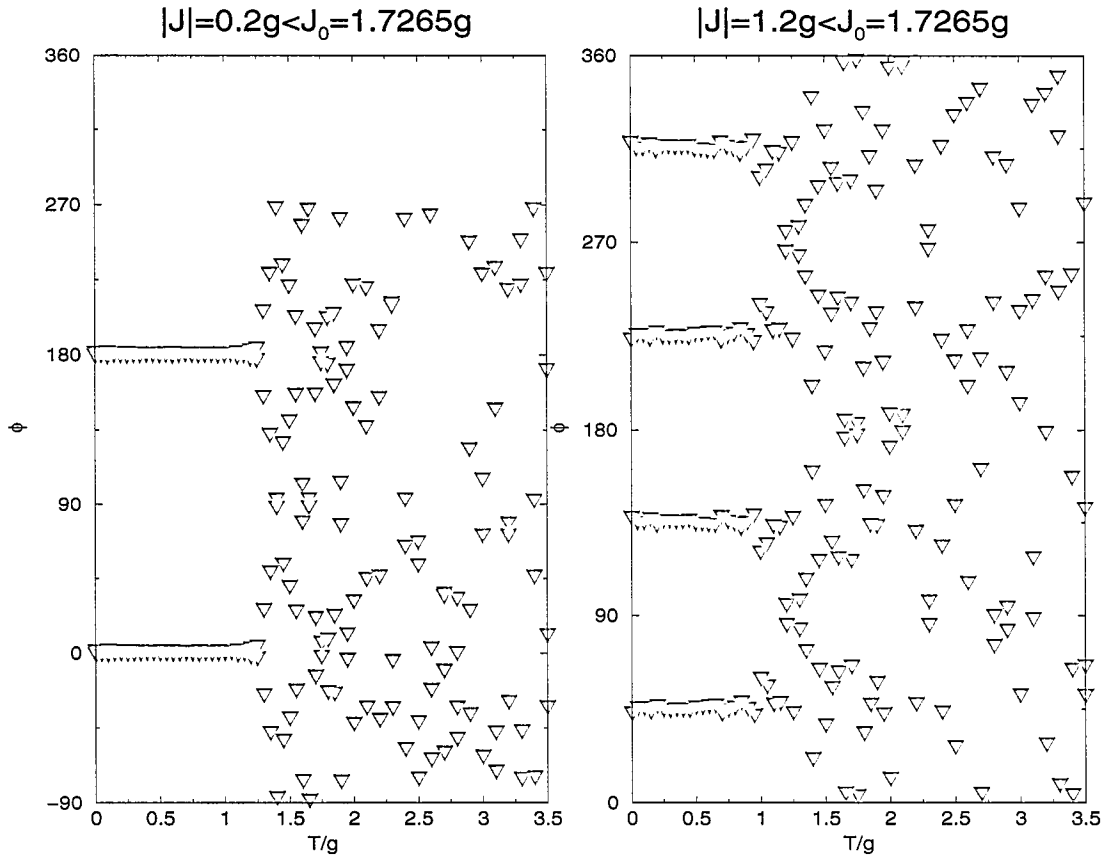


Figure 6.6: The angle  $\phi_\alpha$ , for each of the four sub-lattice magnetisations as a function of temperature,  $T/g$ , for (a)  $|J| = 0.2g$ , and (b)  $|J| = 1.2g$  with  $L = 104$ .

by Equation 4.3.3, as a function of decreasing temperature,  $T/g$ , for the two values of  $|J|/g$ . It is apparent from the data that the symmetry axis is different for the different values of  $|J|/g$ , similar to what was found in the Heisenberg (see Figure 4.9) and plane rotator (see Figure 5.6) systems. For  $|J| = 0.2g$  the symmetry axis is along the  $x$ -axis, with  $\phi_1 = \phi_2 = 0$  and  $\phi_3 = \phi_4 = \pi$ , while for  $|J| = 1.2g$  the symmetry axis is oriented at  $\pi/4$  to the  $x$ -axis, with  $\phi_1 = \pi/4$ ,  $\phi_2 = 3\pi/4$ ,  $\phi_3 = 5\pi/4$  and  $\phi_4 = 7\pi/4$ .

## 6.4 The Phase Diagram

In Figure 6.7, the results of Monte Carlo simulations have been collected to form a phase diagram. It includes the results presented earlier as well as a large number of other simulations done at various values of both  $|J|/g$  and  $T/g$ , and on a number of different size systems ( $N = L \times L = 32^2, 64^2, 104^2$ ). This phase diagram shows three distinct magnetic regions. Region I is the dipolar planar antiferromagnetic ( $AF_{\parallel}$ ) phase, Region II is the perpendicular antiferromagnetic ( $AA_{\perp}$ ) phase, and Region III is the paramagnetic phase. While the two solid lines indicate phase boundaries of second-order transitions between the two ordered states (Region I and Region II) and the paramagnetic state (Region III), the dashed line indicates the phase boundary of first-order transitions between the two ordered phases ( $AF_{\parallel}$  and  $AA_{\perp}$ ). The dotted line in the  $AF_{\parallel}$  region indicates the phase boundary separating the two planar phases,  $AF_{\parallel}1$  and  $AF_{\parallel}2$ .

To compare the results presented in this chapter with those presented for the system with zero magnetic surface anisotropy in chapter 4, the two phase diagrams shown in Figures 4.18 and 6.7 are redrawn schematically in Figures 6.8a and 6.8b,

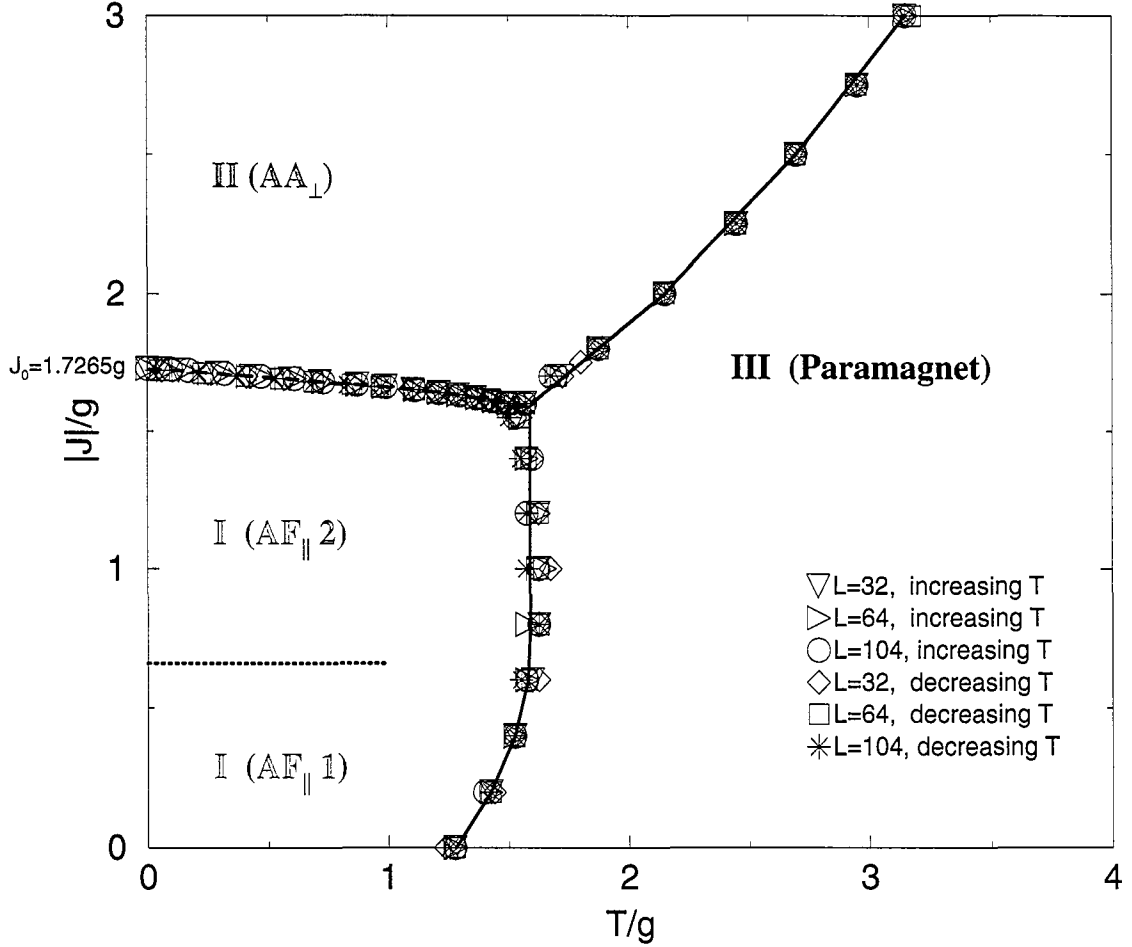


Figure 6.7: The magnetic phase diagram, based on the Monte Carlo simulations, for the dipolar antiferromagnetic Heisenberg system with  $\kappa = -1.0g$  as a function of increasing and decreasing both  $|J|/g$  and  $T/g$  for  $N = L \times L = 32^2, 64^2, 104^2$ . Region I is the dipolar planar antiferromagnetic phase (AF<sub>||</sub> phase), Region II is the simple perpendicular antiferromagnetic phase (AA<sub>⊥</sub> phase), and Region III is the paramagnetic phase (disordered phase). The two solid lines highlight the two lines of second-order transitions from the paramagnetic phase to the two ordered phases. The dashed line highlights the line of first-ordered reorientation transitions from one ordered state to the other (AF<sub>||</sub>, AA<sub>⊥</sub>). The dotted line separates the two planar phases (AF<sub>||</sub>1, AF<sub>||</sub>2).

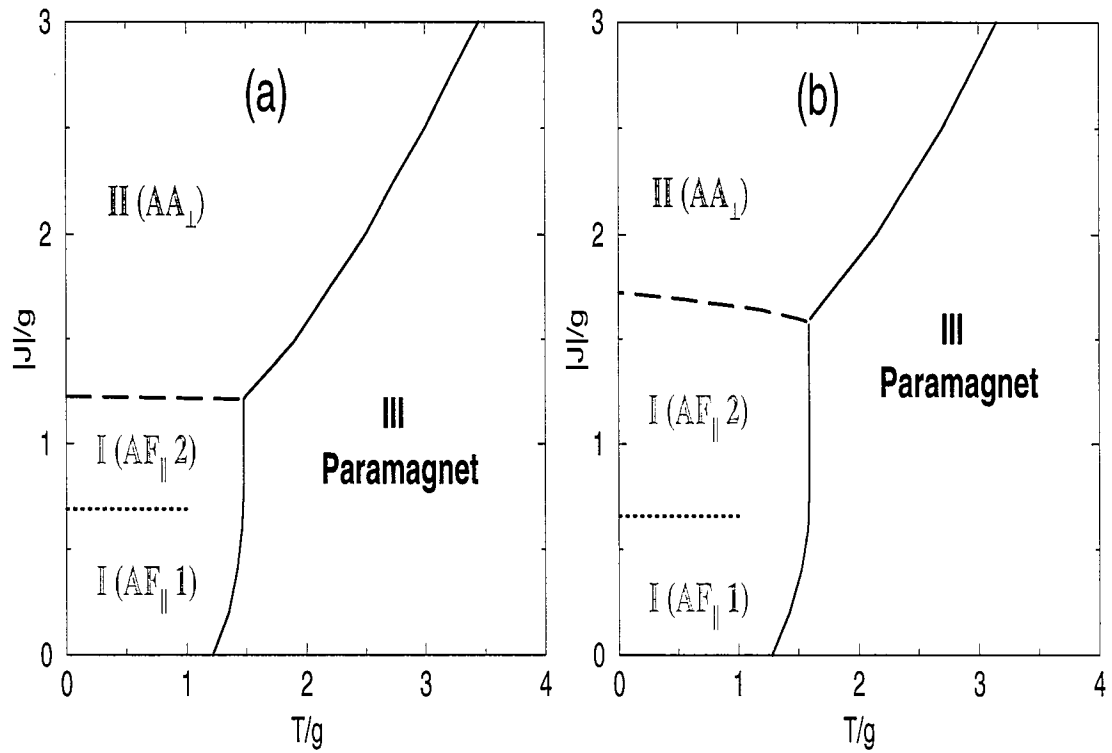


Figure 6.8: A schematic phase diagrams for (a)  $\kappa = 0$  and (b)  $\kappa = -1.0g$  as a function of both  $|J|/g$  and  $T/g$ . Region I is the dipolar planar antiferromagnetic ordered phase ( $AF_{\parallel}$ ), Region II is the simple out-of-plane antiferromagnetic ordered phase ( $AA_{\perp}$ ), and Region III is the paramagnetic phase (disordered phase).

respectively. At low temperatures, the two diagrams show the  $AF_{\parallel}$  phase for low values of  $|J|/g$ , and the  $AA_{\perp}$  phase for large values of  $|J|/g$ . In both systems, the  $AF_{\parallel}$  phase consists of the two distinct phases,  $AF_{\parallel}1$  and  $AF_{\parallel}2$ . Moreover, the transition from the  $AF_{\parallel}1$  phase to the  $AF_{\parallel}2$  phase with increasing  $|J|/g$  occurs at  $|J| \approx 0.7g$  in both cases. While the two phase diagrams show certain similarities, there are two important differences. The first is that the weak planar anisotropy causes the reorientation transition from the  $AF_{\parallel}$  phase to the  $AA_{\perp}$  phase, at zero temperature, to be at higher values of  $|J|/g$ . The second is that the phase boundary separating the two ordered states ( $AF_{\parallel}$ ,  $AA_{\perp}$ ) of the system includes the weak planar magnetic surface anisotropy which is temperature dependent with a negative slope. Therefore, the system with the weak planar magnetic surface anisotropy exhibits a reorientation transition from the dipolar planar antiferromagnetic phase to the perpendicular antiferromagnetic phase with increasing temperature. This means that the weak planar anisotropy plays a critical role in determining the characteristic properties of the phase boundary separating the two ordered states,  $AF_{\parallel}$  and  $AA_{\perp}$ . In addition, the presence of the reentrant phenomena between the  $AF_{\parallel}$  phases presented in chapter 5 for the plane rotator system and its absence in this system occurs presumably because the in-plane to out-of-plane reorientation transition takes place before the system can reenter the  $AF_{\parallel}1$  phase.

## 6.5 The Low Temperature Order Parameter

In Figure 6.9 the perpendicular order parameter is plotted as a function of  $T/g$  for several values of  $|J| > J_0$ . The graphs show that the perpendicular order parameter decreases linearly with increasing temperature at low  $T$  with a slope that decreases

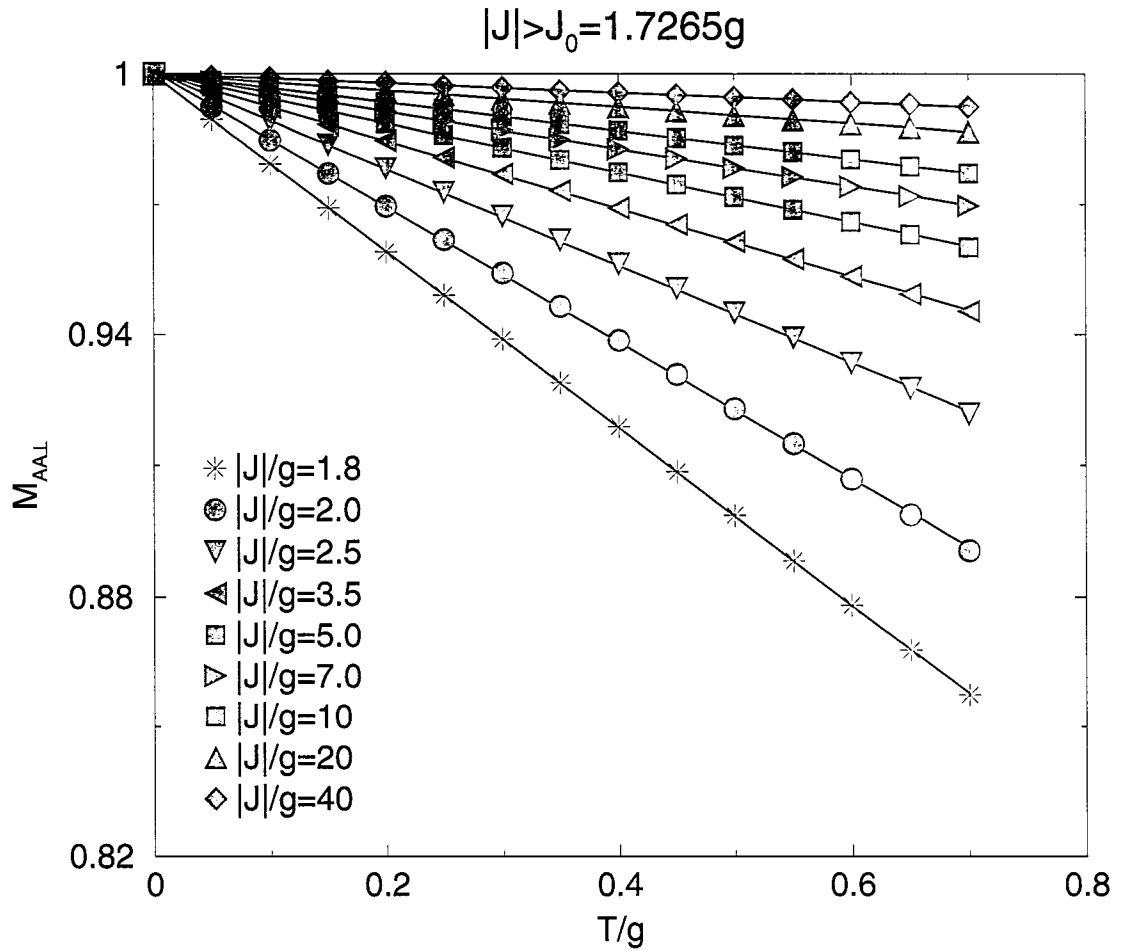


Figure 6.9: A plot of the perpendicular order parameter,  $M_{AA_{\perp}}$ , per spin as a function of the temperature,  $T/g$ , for several values of  $|J| > J_0$  with  $L = 104$ .

with decreasing  $|J|/g$ , reflecting a decreasing of the spin-wave stiffness, similar to what was found in chapter 4 for the Heisenberg system.

A plot of the  $\lim_{T \rightarrow 0} |dM_{AA_{\perp}}/dT|$ , as a function of  $|J|/g$  is shown in Figure 6.10. This Figure shows a comparison with the phenomenological relationship

$$\lim_{T \rightarrow 0} \frac{|dM_{AA_{\perp}}|}{|dT|} = \frac{a}{((|J|/g)^b - c)^d}, \quad (6.5.1)$$

where a regression analysis yields the following estimates  $a = 0.1991$ ,  $b = 2.3746$ ,  $c = 3.1045$  and  $d = 0.3329$ . This relationship predicts that the slope of the order parameter diverges at  $|J|/g = 1.6114$ , which lies just below the phase boundary separating the perpendicular and the in-plane phases.

As presented in chapter 4, a similar analysis of the parallel order parameter is performed. In Figure 6.11,  $g(1 - M_{AF_{\parallel}})/T$  is plotted as a function of  $T/g$  for  $|J| = 0.2g$ . This is also evidence that the points do not tend toward a constant in the limit  $T \rightarrow 0$ , as predicted by linear spin-wave theory, but instead, show a steady increase as the temperature is reduced.

## 6.6 Summary

The magnetic properties for the two-dimensional dipolar antiferromagnetic Heisenberg model on a square lattice with a weak planar magnetic surface anisotropy ( $\kappa = -1.0g$ ) have been determined for both zero and finite temperatures. As in chapter 4, the present magnetic phase diagram demonstrates that the system with  $\kappa = -1.0g$  has three distinct magnetic phases: the dipolar planar antiferromagnetic phase, the perpendicular antiferromagnetic phase, and the paramagnetic phase. While the phase boundaries between the two ordered phases and the paramagnetic

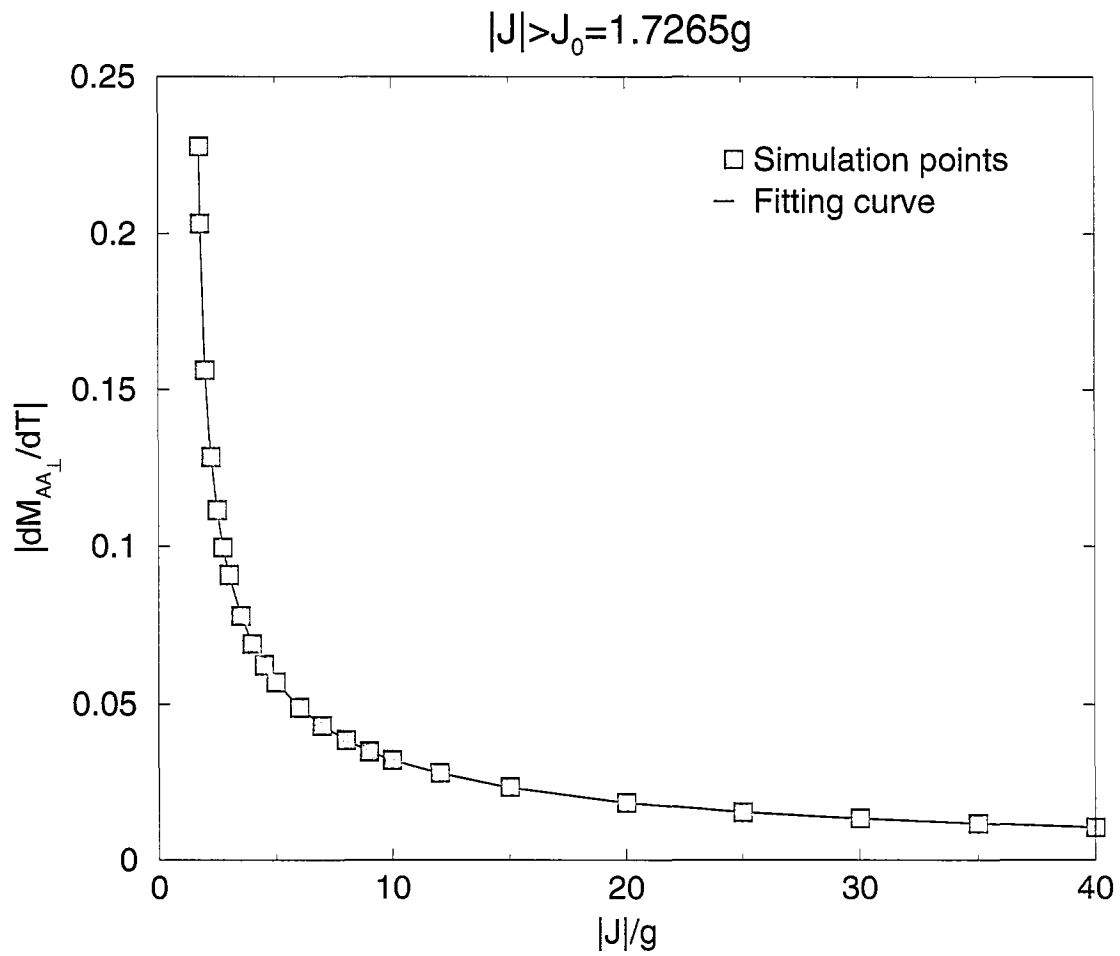


Figure 6.10: A plot of the low temperature slope,  $|dM_{AA_{\perp}}/dT|$ , as a function of the the exchange interaction  $|J|/g$ , for  $|J| > J_0$  with  $L = 104$ .

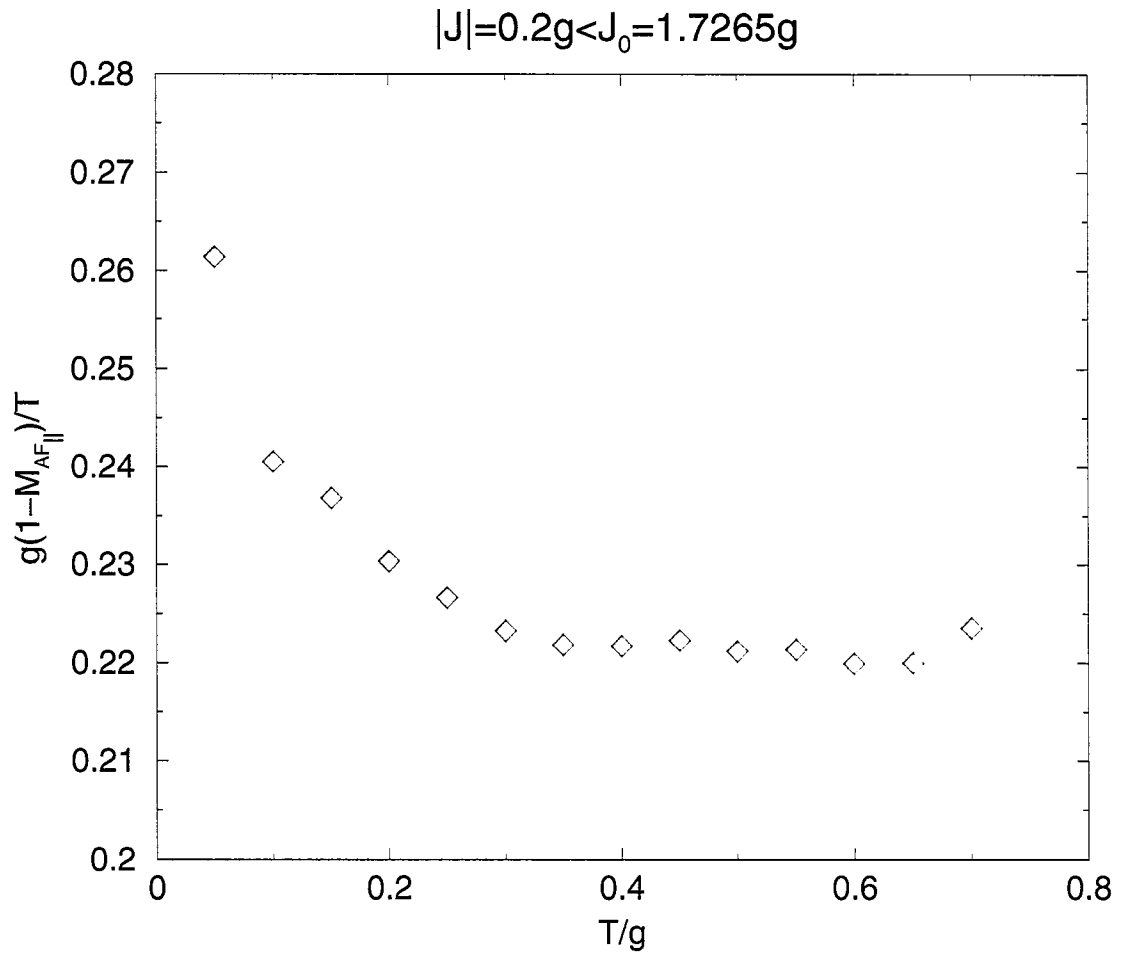


Figure 6.11: A plot of the ratio  $g(1 - M_{AF||})/T$  as a function of the temperature,  $T/g$ , for  $|J| < J_0$  with  $L = 104$ .

phase appear to be second-order transitions, the phase boundary between the two ordered phases appears to be a first-order transition. As with the previous examples, the planar ordered phase consists of two distinct phases: The  $AF_{\parallel}1$  phase which occurs at low values of  $|J|/g$ , in which the spins are aligned along the axes of the lattice, and the  $AF_{\parallel}2$  phase which occurs at higher values of  $|J|/g$ , in which the spins are aligned at  $\pm\pi/4$  to the x-axis.

In contrast to the results presented in chapter 4, the present study shows that the phase boundary separating the two ordered states appears to be temperature dependent with a negative slope. Therefore, these results demonstrate that the system can exhibit a reorientation transition from the dipolar planar antiferromagnetic phase to the perpendicular antiferromagnetic phase with increasing temperature. Indeed, the magnitude of the exchange interaction where the system exhibits a reorientation transition between the  $AF_{\parallel}$  and  $AA_{\perp}$  phases at zero temperature (i.e.,  $J_0$ ), is higher compared to that for a system with zero magnetic surface anisotropy. From Equation 6.2.3, one can also expect that the value of  $J_0$  will be higher as the value of  $|\kappa|/g$  increases. However, the  $\kappa$  dependence of the coexistence line between the  $AF_{\parallel}$  and  $AA_{\perp}$  phases can be determined using the Monte Carlo simulation results or other suitable method.

Again, the reentrant phenomena between the two  $AF_{\parallel}$  phases, as shown in chapter 5, was not observed in the study reported in this chapter. It may be that the in-plane to out-of-plane reorientation transition occurs before the system can reenter the  $AF_{\parallel}1$  phase.

# Chapter 7

## The Anisotropic Heisenberg System: Fixed $J$

### 7.1 Introduction

This chapter extends the study of the anisotropic Heisenberg model studied in the previous chapter. In the previous chapter the phase behaviour for different  $J$  values and for fixed  $\kappa$  was studied. In this chapter, the phase behaviour for different values of  $\kappa$  but for a fixed value of  $J$  is studied. As before only the case where  $\kappa < 0$  is considered (i.e., planar magnetic surface anisotropy). In the present system, the antiferromagnetic exchange constant is chosen such that  $J = -10.0g$ . Choosing the exchange interaction to be the dominant interaction provides a potentially useful comparison with experimental systems [7]. Therefore, this chapter presents results from simulations which examine the interplay of the planar magnetic surface anisotropy and the dipolar anisotropy in the exchange-dominated antiferromagnetic phase ( $|J| > 1.23g$ ) for the two-dimensional Heisenberg system on a square lattice with several lattice sizes in the range  $N = 32 \times 32$  to  $104 \times 104$ . In particular, the  $\kappa - T$  phase diagram for  $\kappa \leq 0$  and  $J = -10.0g$  is presented. Especially noteworthy

is the prediction of a reorientation transition from the planar antiferromagnetic phase to the perpendicular antiferromagnetic phase with increasing temperature.

The layout of this chapter is as follows. In the following section, the order parameters for the perpendicular and planar phases of interest are defined and the results obtained from simulations are presented. These results include the temperature dependence of the order parameters, the heat capacity and the energy for  $J = -10.0g$  and three values of  $\kappa$ . The data for  $\kappa = -4.1g$  are shown to exhibit a reorientation transition from the planar antiferromagnetic phase to the perpendicular antiferromagnetic phase with increasing temperature. The  $\kappa - T$  phase diagram for  $J = -10.0g$ , constructed from the results of the Monte Carlo simulations, is presented, and shows that the coexistence line separating the planar and the perpendicular phases satisfies an important thermodynamic relationship analogous to the Clausius-Clapeyron relationship in fluids. An analysis of the low temperature magnetisation is then presented, which suggests a softening of the spin-wave spectra in the long wavelength limit close to the reorientation transition. The chapter closes by summarising the results and discussing their significance.

## 7.2 Magnetic Properties

As shown in chapter 4 (see Figure 4.18), in the absence of the magnetic surface anisotropy, and with  $J = -10.0g$ , the ground state is the simple perpendicular antiferromagnetic state in which each spin is aligned perpendicular to the surface and antiparallel to each of its four nearest neighbours. This is referred to as the perpendicular antiferromagnetic,  $AA_{\perp}$ , phase (see Figure 4.3). When a finite magnetic surface anisotropy is included, then the energy of this ground state spin configuration

is given by[50]

$$E_{AA_{\perp}} = -2.6459g + 2J - \kappa. \quad (7.2.1)$$

If the magnetic surface anisotropy is such that it favours an in-plane orientation of the spins ( $\kappa < 0$ ), then the ground state energy of the perpendicular antiferromagnetic phase increases as the strength of the magnetic surface anisotropy increases. At some critical value, denoted by  $-\kappa_0$ , the perpendicular antiferromagnetic ground state will become unstable with respect to the planar antiferromagnetic,  $AA_{\parallel}$ , phase in which each spin is aligned parallel to the surface and antiparallel to each of its four nearest neighbours (see Figure 5.1). The ground state energy of the planar antiferromagnetic phase is given by[50]

$$E_{AA_{\parallel}} = 1.3229g + 2J. \quad (7.2.2)$$

Since the transition from the perpendicular to the planar antiferromagnetic phase occurs at  $T = 0$  when

$$E_{AA_{\perp}} = E_{AA_{\parallel}}, \quad (7.2.3)$$

then a value of  $\kappa_0$  is given by

$$\begin{aligned} \kappa_0 &= (2.646 + 1.323)g \\ &= 3.9688g. \end{aligned} \quad (7.2.4)$$

To construct order parameters for these two states, the lattice is divided into four magnetic sub-lattices as described in the previous three chapters. Each magnetic sublattice is a square with a lattice spacing twice that of the original lattice. The unit cell of the magnetic sublattice, therefore, contains four sites per unit cell, each

site corresponding to one of the sub-lattices, which is denoted by  $\alpha \in \{1 \dots 4\}$ , as shown in Figure 4.2. The sub-lattice magnetisations,  $\vec{M}_{AA_\perp}^\alpha$  and  $\vec{M}_{AA_\parallel}^\alpha$ , are then defined as

$$\begin{aligned}\vec{M}_{AA_\perp}^\alpha &= M_z^\alpha \hat{z} \\ &= \frac{4}{N} \sum_{\vec{r}_\alpha} \sigma^z(\vec{r}_\alpha) \hat{z}\end{aligned}\tag{7.2.5}$$

and

$$\begin{aligned}\vec{M}_{AA_\parallel}^\alpha &= M_x^\alpha \hat{x} + M_y^\alpha \hat{y} \\ &= \frac{4}{N} \left( \sum_{\vec{r}_\alpha} \sigma^x(\vec{r}_\alpha) \right) \hat{x} + \frac{4}{N} \left( \sum_{\vec{r}_\alpha} \sigma^y(\vec{r}_\alpha) \right) \hat{y},\end{aligned}\tag{7.2.6}$$

from which the order parameters,  $M_{AA_\perp}$ , are defined and  $M_{AA_\parallel}$  as

$$M_{AA_\perp} = \frac{1}{4} (|M_z^1| + |M_z^2| + |M_z^3| + |M_z^4|) \hat{z}.\tag{7.2.7}$$

and

$$M_{AA_\parallel} = \frac{1}{4} |(M_x^1 + M_x^4 - M_x^3 - M_x^2) \hat{x} + (M_y^1 + M_y^4 - M_y^3 - M_y^2) \hat{y}|.\tag{7.2.8}$$

For the ground state of the perpendicular antiferromagnetic phase ( $|\kappa| < \kappa_0$ ),

$$M_{AA_\perp} = 1$$

and

$$M_{AA_\parallel} = 0,$$

while for the ground state of the planar antiferromagnetic phase ( $|\kappa| > \kappa_0$ ),

$$M_{AA_\perp} = 0$$

and

$$M_{AA\parallel} = 1.$$

At finite temperature the order parameters are defined by the thermal averages of  $M_{AA\perp}$  and  $M_{AA\parallel}$  determined from Equations 7.2.7 and 7.2.8, respectively. The temperature dependence of each of the two order parameters is shown in Figures 7.1a and 7.1b as a function of both increasing and decreasing temperature for  $|\kappa| = 1.5g$  and  $|\kappa| = 7.0g$ .

These two graphs show an antiferromagnetic ordered state at low temperature, a disordered state at higher temperature, and a continuous transition between them. For  $|\kappa| = 1.5g$ , the ground state is the perpendicular antiferromagnetic state. As shown in Figure 7.1a, as the temperature is increased the perpendicular order parameter,  $M_{AA\perp}$ , decreases continuously, dropping rapidly to zero at around  $T_N = (8.40 \pm 0.05)g$ , while the planar order parameter,  $M_{AA\parallel}$ , remains effectively zero. In contrast, for  $|\kappa| = 7.0g$ , the ground state is the planar antiferromagnetic state. Figure 7.1b shows that as the temperature is increased, the planar order parameter,  $M_{AA\parallel}$ , decreases continuously with increasing temperature, dropping rapidly to zero at around  $T_N = (6.80 \pm 0.05)g$ , while the perpendicular order parameter,  $M_{AA\perp}$ , remains effectively zero.

The existence of a continuous transition between the antiferromagnetically ordered state and the disordered state, for both  $|\kappa| = 1.5g$  and  $|\kappa| = 7.0g$ , is consistent with the absence of the hysteresis in the two order parameters shown in Figure 7.1. This also agrees with data in which the heat capacity of the system is plotted as a function of both increasing and decreasing temperature for  $|\kappa| = 1.5g$  (Figure 7.2a) and for  $|\kappa| = 7.0g$  (Figure 7.2b) where both of which show a peak at the transition

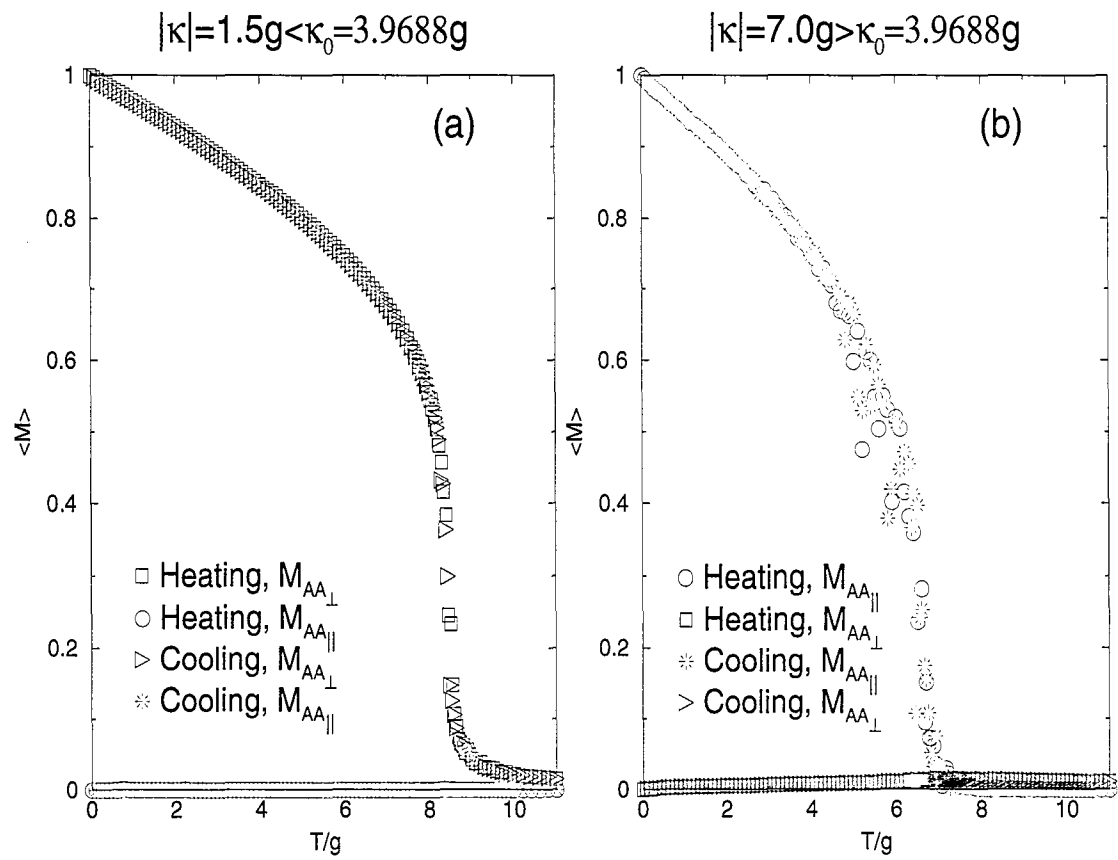


Figure 7.1: A plot of the two order parameters,  $M_{AA\perp}$  and  $M_{AA\parallel}$ , per spin as a function of temperature,  $T/g$ , for (a)  $|\kappa| = 1.5g$  and (b)  $|\kappa| = 7.0g$  with  $L = 104$ .

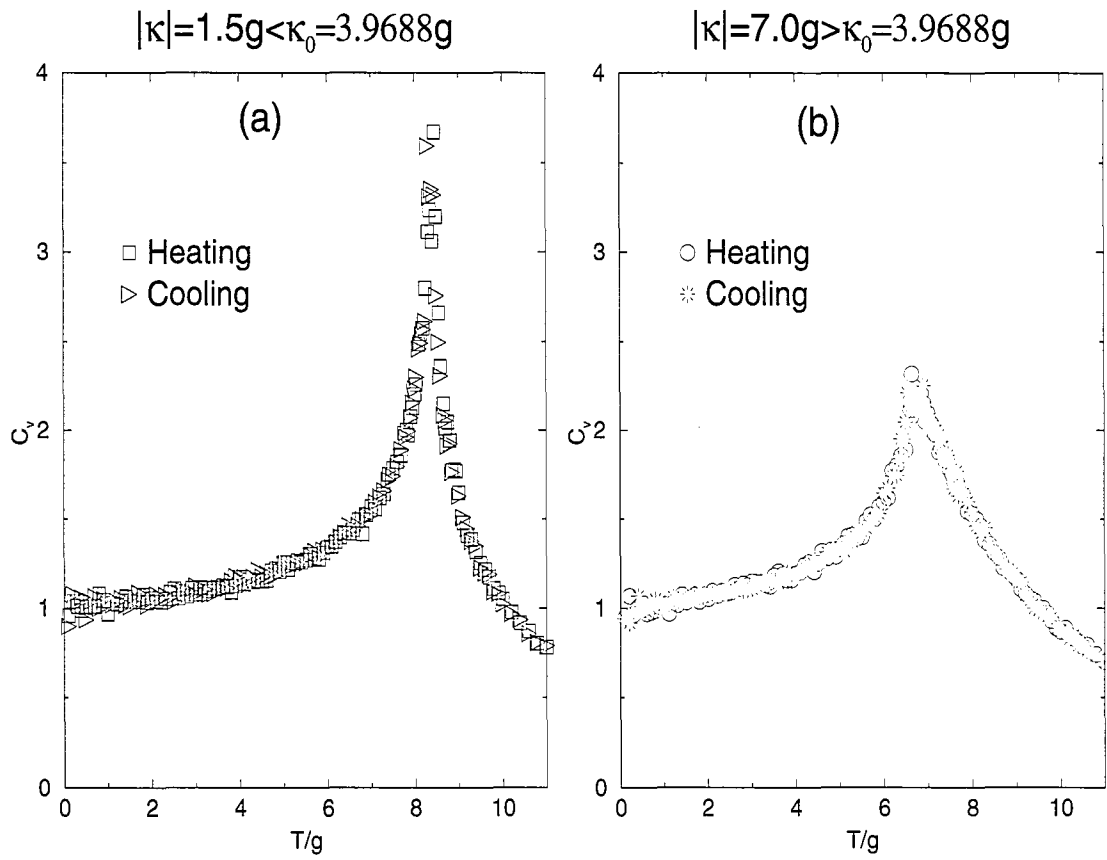


Figure 7.2: A plot of the heat capacity,  $C_v$ , per spin as a function of temperature,  $T/g$ , for (a)  $|\kappa| = 1.5g$  and (b)  $|\kappa| = 7.0g$  with  $L = 104$ .

temperature. The behaviour of the two order parameters along with the heat capacity as a function of temperature for  $|\kappa| = 1.5g$  and  $|\kappa| = 7.0g$  suggests that the system exhibits a second-order transition between the perpendicular antiferromagnetically ordered state and the disordered state for low values of  $|\kappa|/g$  ( $|\kappa| < \kappa_0$ ), and a second-order transition between the planar antiferromagnetically ordered state and the disordered state for large values of  $|\kappa|/g$  ( $|\kappa| > \kappa_0$ ).

The temperature dependence for the two order parameters,  $M_{AA\parallel}$  and  $M_{AA\perp}$ , are plotted as a function of temperature for  $\kappa = -4.1g$  as shown in Figure 7.3. At  $T = 0$ , the system is in the planar phase with  $M_{AA\parallel} = 1$  and  $M_{AA\perp} = 0$ . As the temperature initially increases  $M_{AA\parallel}$  decreases while  $M_{AA\perp}$  remains effectively zero until  $T_R = (1.42 \pm 0.02)g$ , at which point the order parameters change discontinuously with  $M_{AA\parallel}$  dropping effectively to zero and  $M_{AA\perp}$  increasing to approximately 0.9. As the temperature increases further, the system exhibits a continuous transition to the paramagnetic phase at  $T_N = (7.05 \pm 0.05)g$ . Similar behaviour is observed on cooling except that the discontinuity in the order parameter occurs at the slightly lower temperature,  $T_R = (1.16 \pm 0.02)g$ . This hysteresis, together with the discontinuous change in the order parameters, indicates that the reorientation transition is first order. This discontinuity observed during both heating and cooling corresponds to a reorientation transition.

The hysteresis at the transition is shown in more detail in Figure 7.4, which shows the changes in the order parameter and the internal energy as a function of both increasing and decreasing temperature, in the vicinity of the reorientation transition.

This sequence of transitions is also reflected in the heat capacity data shown in Figure 7.5, which shows three distinct peaks. The two narrow peaks correspond

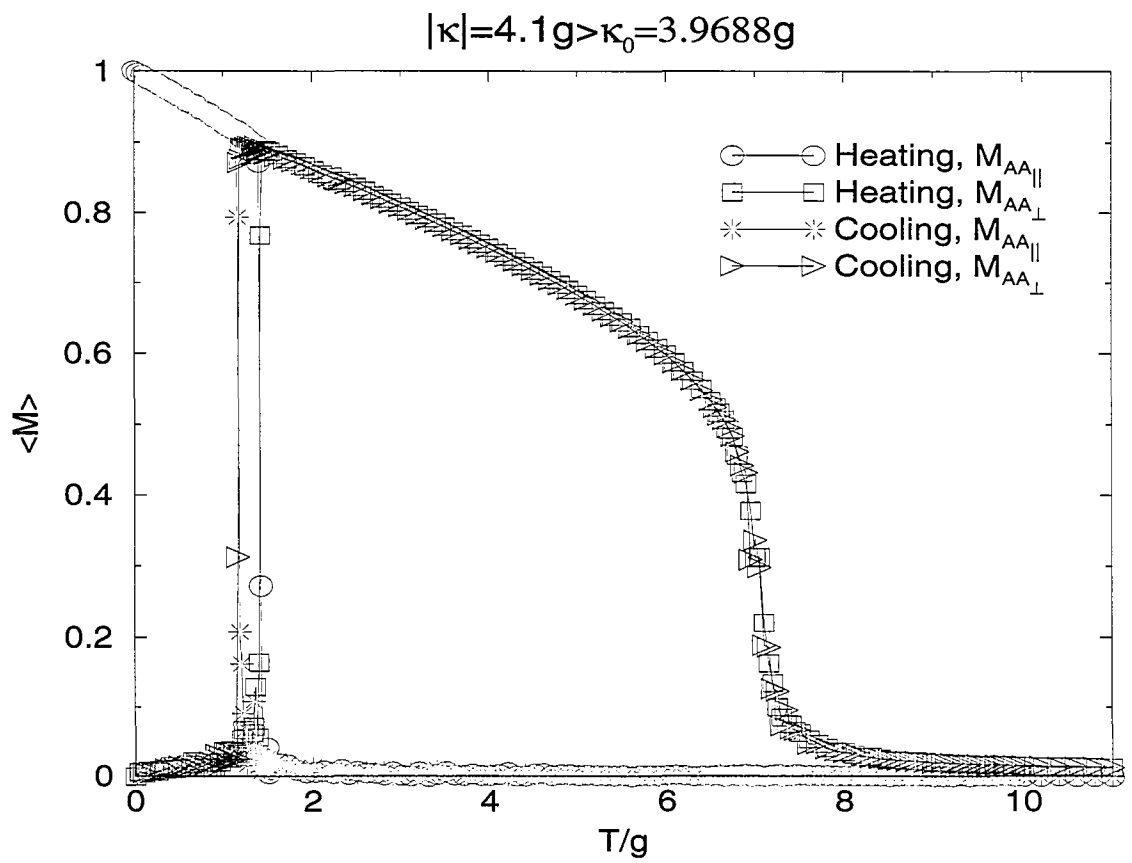


Figure 7.3: A plot of the two order parameters,  $M_{AA\perp}$  and  $M_{AA\parallel}$ , per spin as a function temperature,  $T/g$ , for  $|\kappa| = 4.1g$  with  $L = 104$ .

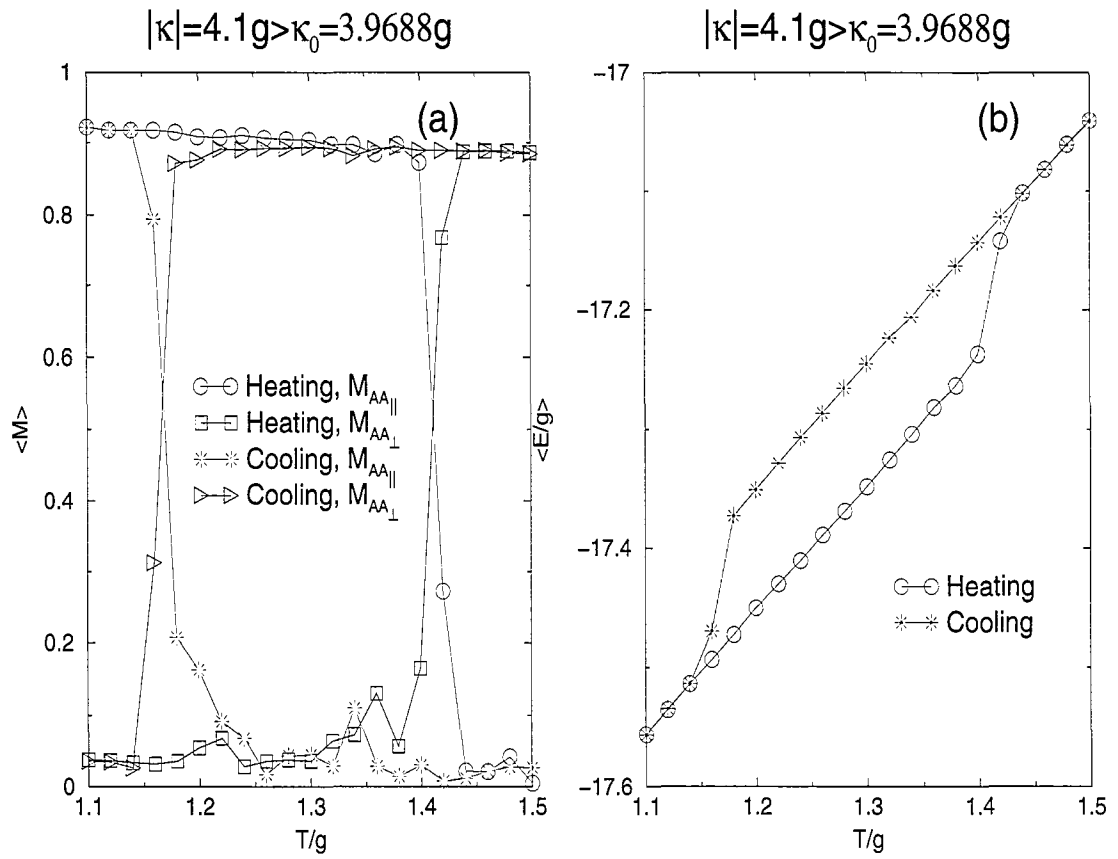


Figure 7.4: A plot of (a) the two order parameters,  $M_{AA\perp}$  and  $M_{AA\parallel}$ , and (b) the total average internal energy,  $\langle E/g \rangle$ , per spin as a function of both increasing and decreasing temperature for  $|\kappa| = 4.1g$  with  $L = 104$ .

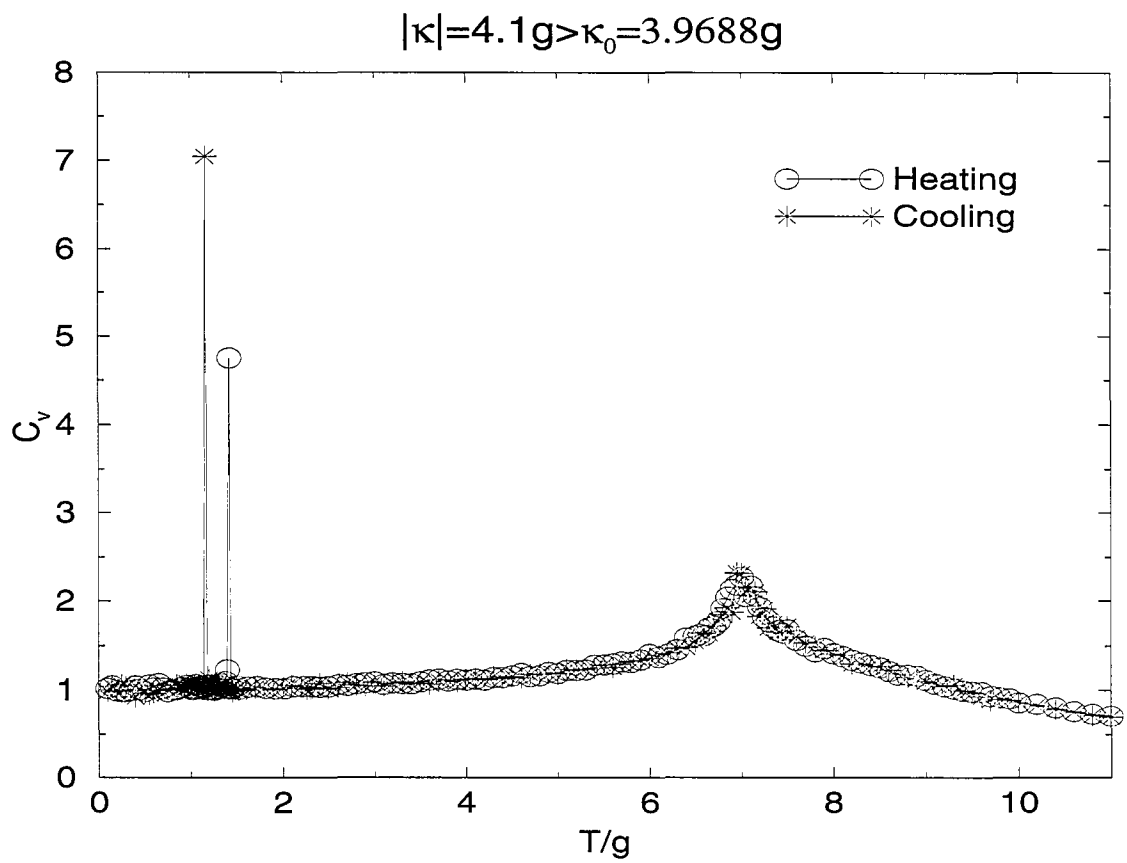


Figure 7.5: A plot of the heat capacity,  $C_v$ , per spin as a function temperature,  $T/g$ , for  $|\kappa| = 4.1g$  with  $L = 104$ .

to the reorientation transition on heating and cooling, while the broad peak corresponds to the continuous transition between the perpendicular phase and the paramagnetic phase. This is also consistent with the the susceptibility data shown in Figure 7.6, in which the parallel susceptibility (Figure 7.6a) shows two narrow peaks again corresponding to the reorientation transition on heating and cooling while the perpendicular susceptibility (Figure 7.6b) shows three distinct peaks. The two narrow peaks correspond to the reorientation on heating and cooling, while the broad peak corresponds to the continuous transition between the perpendicular phase and the paramagnetic phase.

Further evidence for the discontinuous nature of the reorientation transition is obtained from the  $xy$ -conjugate field,  $P_{xy}$ , and the  $z$ -conjugate field,  $P_z$ , defined respectively as [157]

$$P(T)_{xy} = \frac{1}{N} \left\langle \sum_{\vec{R}} (\sigma_x^4 + \sigma_y^4) \right\rangle \quad (7.2.9)$$

and

$$P(T)_z = \frac{1}{N} \left\langle \sum_{\vec{R}} \sigma_z^2 \right\rangle. \quad (7.2.10)$$

It can be readily shown that at zero temperature,  $P_{xy} = 1$  and  $P_z = 0$  for the planar phase, and  $P_{xy} = 0$  and  $P_z = 1$  for the perpendicular phase. If the system is completely disordered then  $P_{xy} = 2/5$  and  $P_z = 1/3$ . The temperature dependence of the two conjugate fields,  $P_{xy}$  and  $P_z$ , is shown in Figure 7.7 for both increasing and decreasing temperature. Both exhibit a discontinuity at the reorientation transition. At higher temperatures,  $P_{xy}$  extrapolates to  $2/5$  and  $P_z$  extrapolates to  $1/3$ , indicating that the system is in the disordered phase at high temperature.

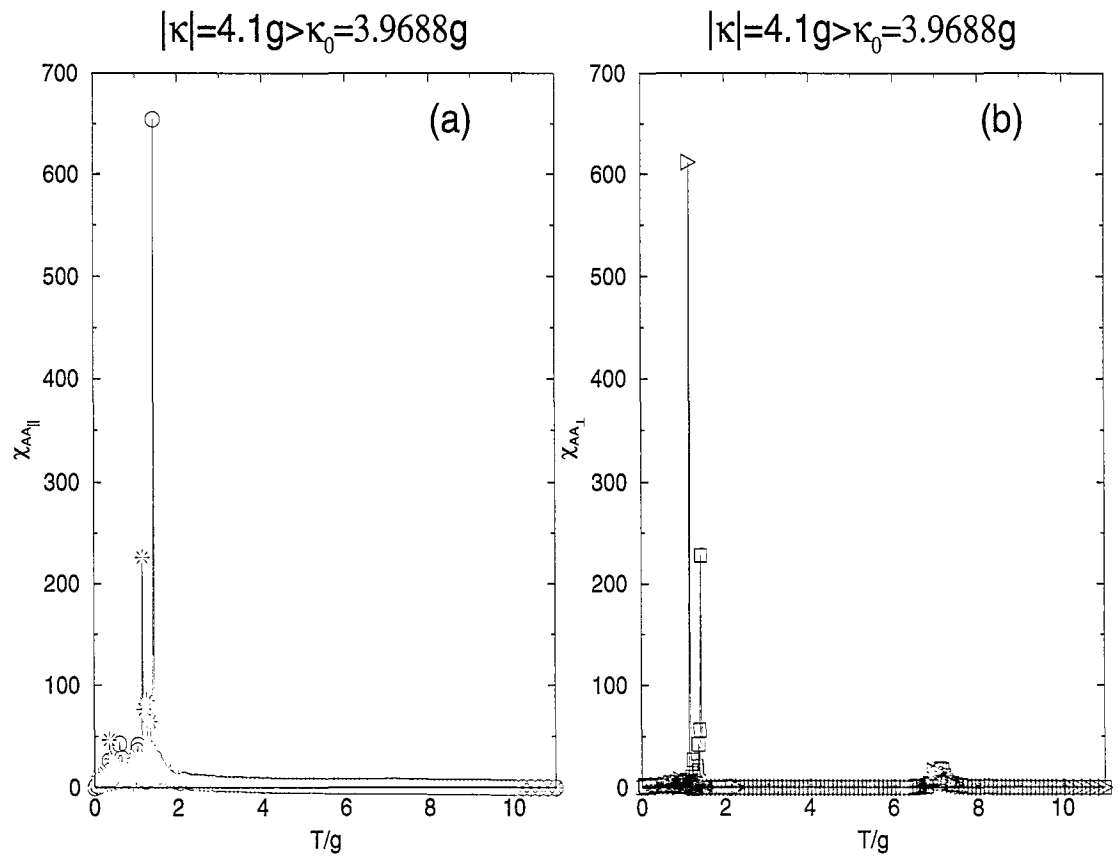


Figure 7.6: A plot of (a) the parallel susceptibility,  $\chi_{AA\parallel}$ , and (b) the perpendicular susceptibility,  $\chi_{AA\perp}$ , per spin as a function temperature,  $T/g$ , for  $|\kappa| = 4.1g$  with  $L = 104$ .

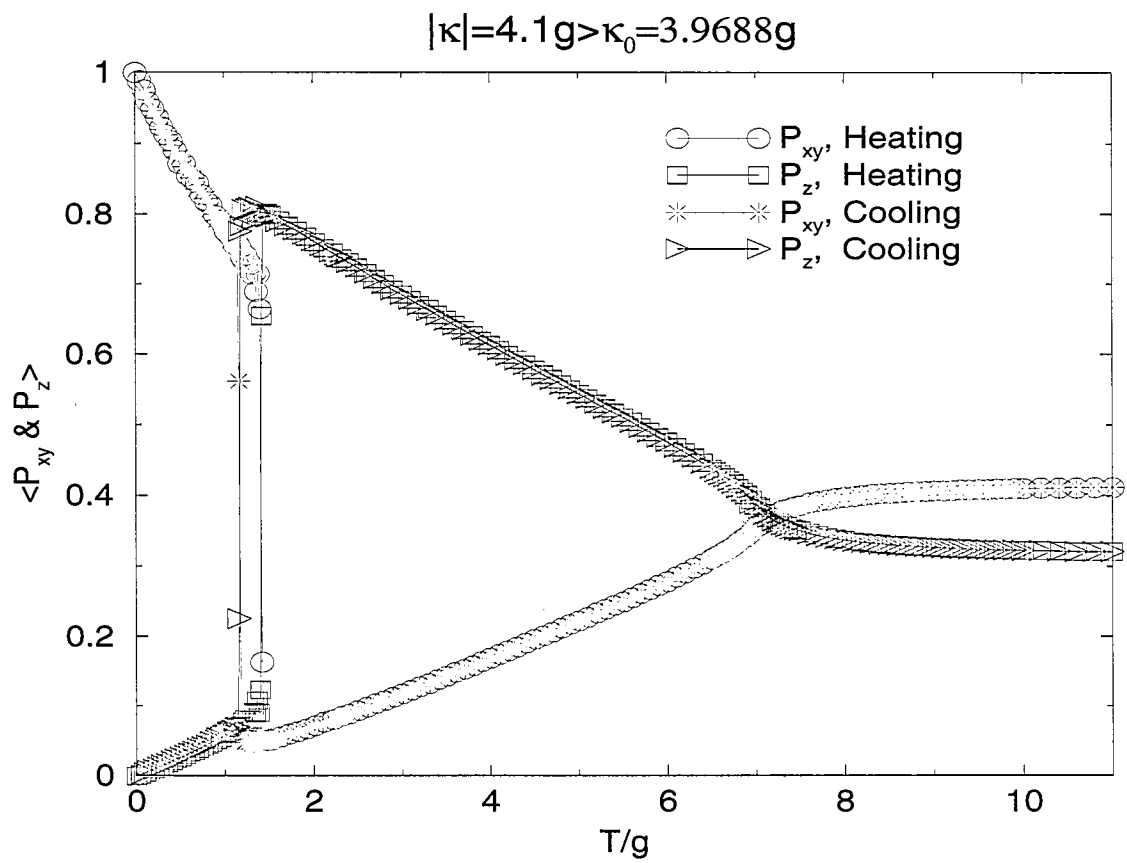


Figure 7.7: A plot of the two conjugate fields,  $P_{xy}$  and  $P_z$ , per spin as a function of temperature,  $T/g$ , for  $|\kappa| = 4.1g$  with  $L = 104$ .

It is interesting to contrast the reorientation transition reported in this work for antiferromagnetic systems and that reported in the ferromagnetic case. The most obvious difference is the homogeneous nature of the equilibrium phases in the case of the antiferromagnetic exchange interaction, in contrast to the inhomogeneous stripe phases observed in the case of the ferromagnetic exchange interaction. Another important difference lies in the fact that the sequence of transitions for the ferromagnetic reorientation transitions is from a perpendicular phase at low temperature to a planar phase at high temperature [135, 136]. This contrasts with the results reported in this chapter in which the sequence of transitions is from the planar phase at low temperature to the perpendicular phase at high temperature. This means that in the ferromagnetic case the dipolar interaction favours the in-plane antiferromagnetic phase while in the antiferromagnetic case the dipolar interaction favours the out-of-plane antiferromagnetic phase. However, the fact that the low temperature phases in both the ferromagnetic and the antiferromagnetic systems are stabilised by the magnetic surface anisotropy suggests that there are similarities between the two reorientation transitions that are not immediately apparent. At the most basic level, both reorientation transitions may be understood qualitatively as a weakening of the strength of the magnetic surface anisotropy relative to the dipolar interaction as a result of thermal fluctuations.

### 7.3 The Phase Diagram

In Figure 7.8, the results of the Monte Carlo simulations at finite temperature have been collected to form a phase diagram for both heating and cooling. This phase diagram shows three phase boundaries separating the perpendicular antiferromagnetic

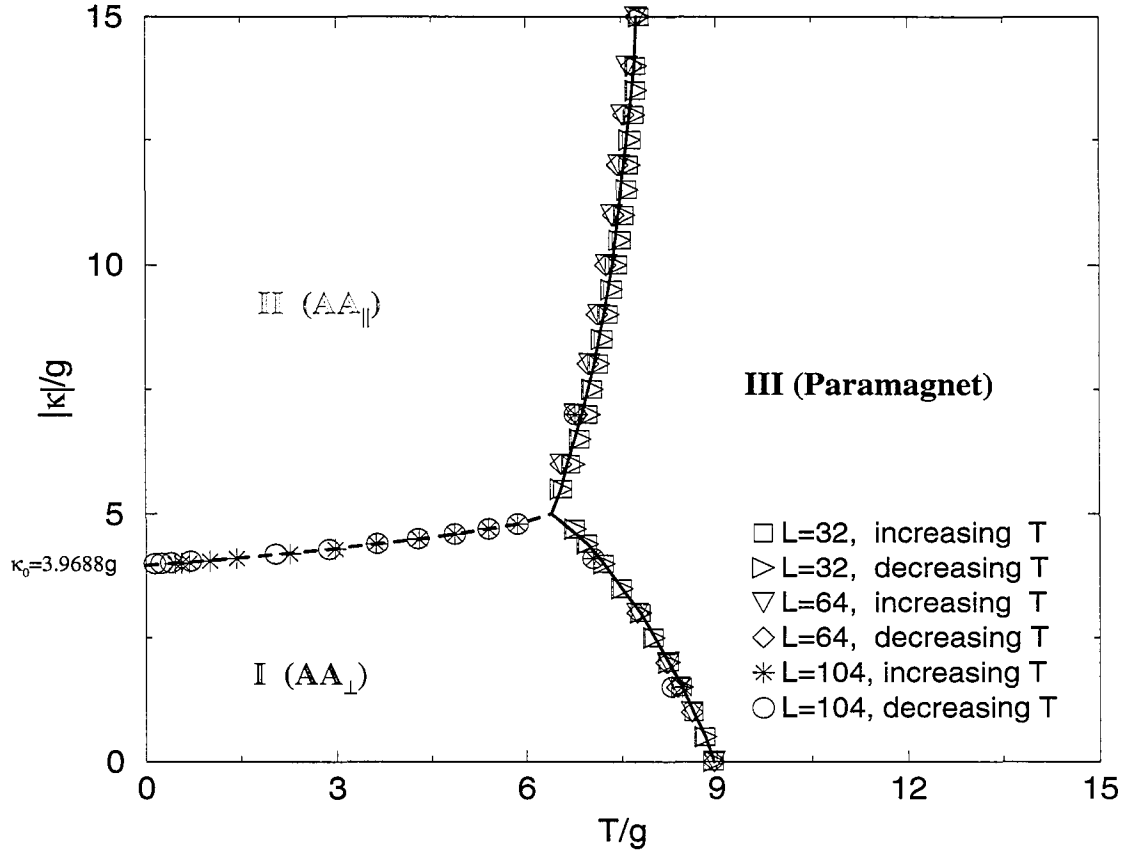


Figure 7.8: The magnetic phase diagram, based on the Monte Carlo simulations, for the dipolar antiferromagnetic Heisenberg system with  $\kappa \leq 0$  for  $J = -10.0g$  as a function of  $|\kappa|/g$  and  $T/g$  for  $N = L \times L = 32^2, 64^2, 104^2$ . Region I is the simple perpendicular antiferromagnetic phase ( $AA_{\perp}$  phase), Region II is the simple parallel antiferromagnetic phase ( $AA_{\parallel}$  phase), and Region III is the paramagnetic phase (disordered phase). The two solid lines highlight the two lines of second-ordered transitions from the paramagnetic phase to the two ordered phases. The dashed line highlight the line of first-ordered reorientation transition from one order state to the other ( $AA_{\perp}$ ,  $AA_{\parallel}$ ).

phase (Region I), the planar antiferromagnetic phase (Region II) and the paramagnetic phase (Region III). The two solid lines indicate second order transitions between the two antiferromagnetically ordered states and the disordered state, while the dashed line is the phase boundary separating the two antiferromagnetically ordered phases.

If the coexistence line separating the perpendicular and the planar phases is described by the function,  $\kappa_R(T)$ , the existence of the reorientation and the observed sequence of transitions are determined by the fact that  $d\kappa_R/dT > 0$ . The slope of the coexistence line can be expressed as

$$\frac{d\kappa_R(T)}{dT} = \frac{\kappa \Delta E}{T_R \Delta E_\kappa}, \quad (7.3.1)$$

where  $\Delta E$  denotes the latent heat of the transition and  $\Delta E_\kappa$  denotes the difference in the average anisotropic energy between the two equilibrium phases on the coexistence line. The total average internal energy (Figure 7.9a) and the average anisotropic energy (Figure 7.9b) are shown to change with increasing and decreasing temperature for  $|\kappa| = 4.2g$ . From these data it is possible to estimate that  $T_R = (2.25 \pm 0.02)g$ ,  $\Delta E = (0.142 \pm 0.003)g$ , and  $\Delta E_\kappa = (2.28 \pm 0.04)g$ , which yields  $d\kappa_R/dT = 0.116 \pm 0.013$  according to Equation 7.3.1. By comparison, for  $|\kappa| = 4.2g$  estimates of  $\kappa_R$  from the coexistence line yield a slope of  $d\kappa_R/dT = 0.128 \pm 0.006$ . The slope of the coexistence line provides a useful consistency check on the results obtained from the simulations on the nature of the reorientation transition.

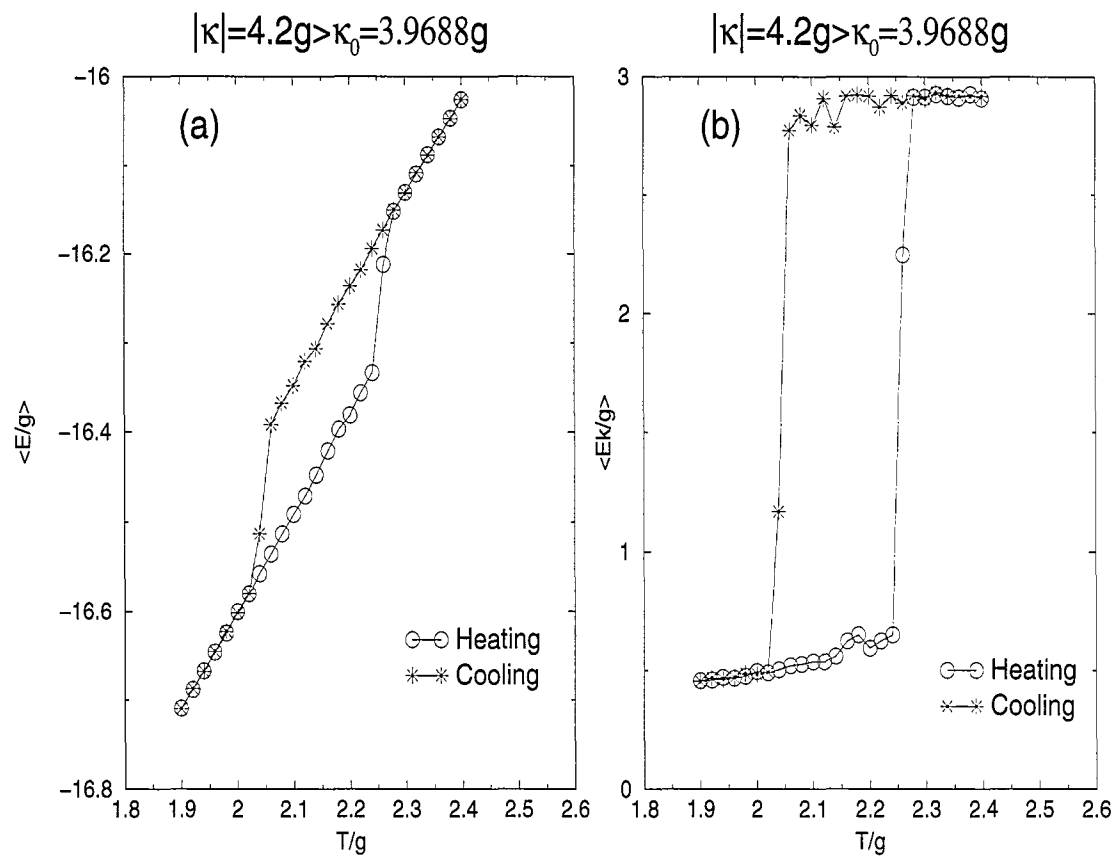


Figure 7.9: A plot of (a) the average internal energy,  $\langle E/g \rangle$ , and (b) the average magnetic surface anisotropy energy,  $\langle E_{\kappa/g} \rangle$ , per spin for  $|\kappa| = 4.2g$  as a function of temperature,  $T/g$ , with  $L = 104$ .

## 7.4 The Temperature Dependence of the Order Parameters in the Limit $T \rightarrow 0$

The temperature dependence of the order parameters,  $M_{AA_{\perp}}$  and  $M_{AA_{\parallel}}$ , are shown in Figures 7.10a and 7.10b, for the range  $0 < T/g < 1.5$  for several values of  $\kappa$ . The data show two interesting features. Firstly, the order parameter appears to decrease linearly with temperature, as would be expected on the basis of linearised spin-wave theory. Secondly, the magnitude of the slope,  $|dM_{AA_{\perp}}/dT|$ , increases as the reorientation transition is approached, for both the perpendicular and the planar phases, suggesting a softening of the spin-wave spectra close to the transition as discussed earlier.

Figure 7.11 shows a comparison between the slope  $\lim_{T \rightarrow 0} |dM_{AA_{\perp}}/dT|$ , as a function of  $\kappa$  for  $|\kappa| < \kappa_0$ , as obtained from the data shown in Figure 7.10a and the phenomenological relationship,

$$\lim_{T \rightarrow 0} \left| \frac{dM_{AA_{\perp}}}{dT} \right| = \frac{a}{[b - (|\kappa|/g)^c]^d} \quad (7.4.1)$$

where a regression analysis yields the following estimates:  $a = 0.0417$ ,  $b = 3.2553$ ,  $c = 0.7975$ , and  $d = 0.2762$ . This relationship predicts that the slope of the  $M_{AA_{\perp}}$  order parameter diverges at  $|\kappa| = 4.3930g$ , which lies just above  $\kappa_0$ . Also shown in Figure 7.11 for  $|\kappa| > \kappa_0$ , is a comparison between the slope,  $\lim_{T \rightarrow 0} |dM_{AA_{\parallel}}/dT|$ , as a function of  $\kappa$  for  $|\kappa| > \kappa_0$ , as obtained from the data shown in Figure 7.10b and the phenomenological relationship,

$$\lim_{T \rightarrow 0} \left| \frac{dM_{AA_{\parallel}}}{dT} \right| = \frac{a}{[(|\kappa|/g)^c - b]^d}, \quad (7.4.2)$$

where a regression analysis yields the following estimates:  $a = 0.0498$ ,  $b = 1.7385$ ,

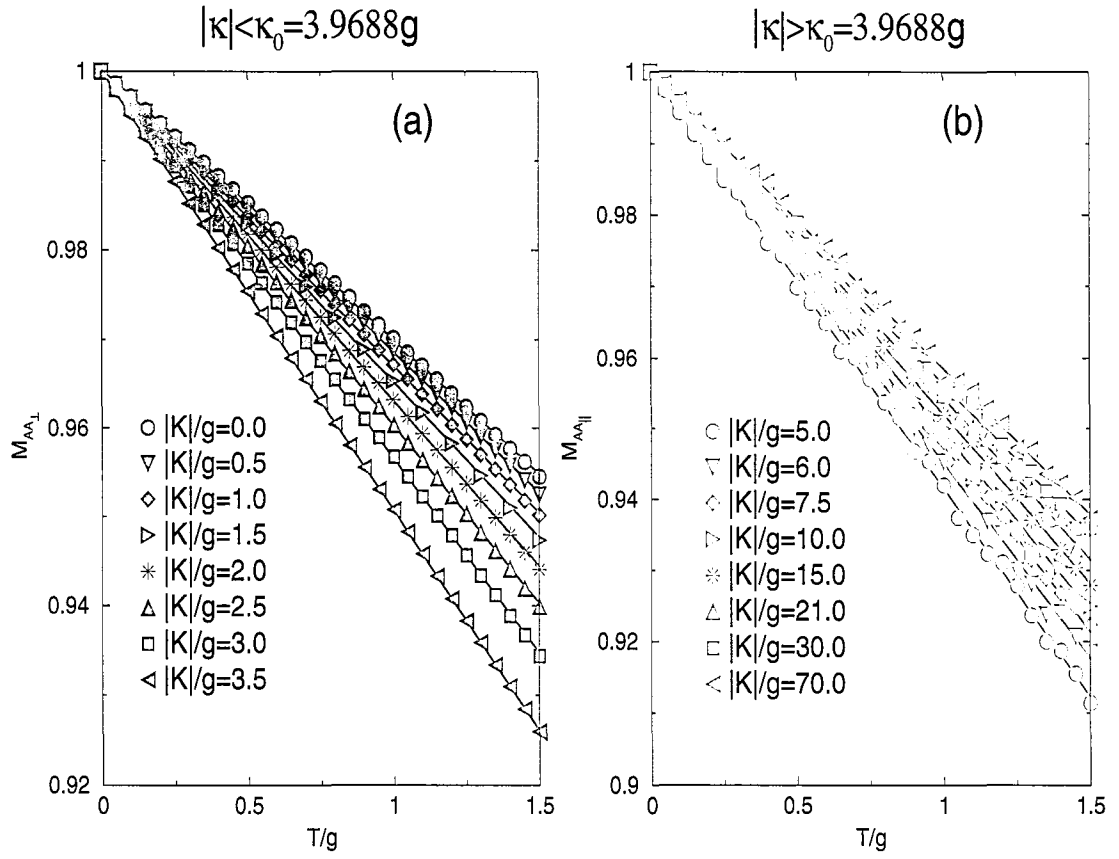


Figure 7.10: A plot of (a) the perpendicular order parameter,  $M_{AA\perp}$ , per spin for several values of  $|\kappa| < \kappa_0$  and (b) the planar order parameter,  $M_{AA\parallel}$ , per spin for several values of  $|\kappa| > \kappa_0$  as a function of temperature,  $T/g$ , with  $L = 104$ .

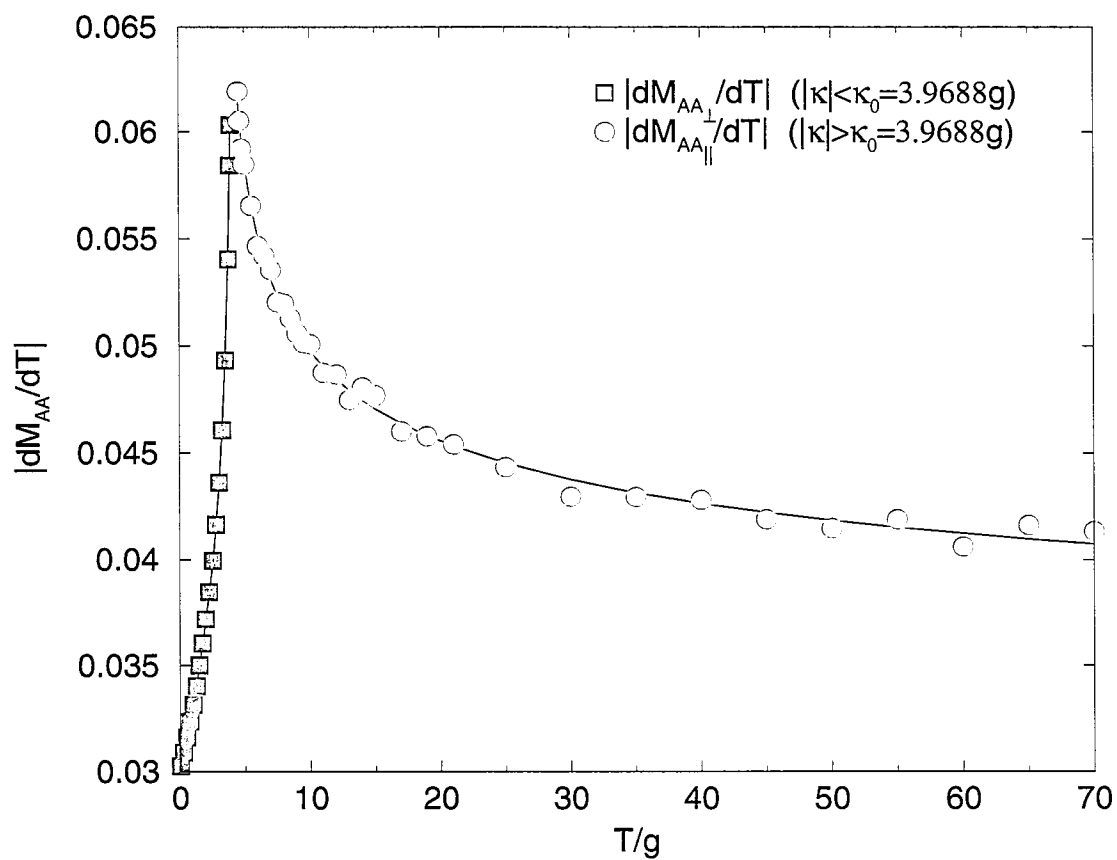


Figure 7.11: A plot of the low temperature slope,  $|dM_{AA\perp}/dT|$ , and the low temperature slope,  $|dM_{AA\parallel}/dT|$ , as a function of the anisotropy constant,  $|\kappa|/g$ , with  $L = 104$ .

$c = 0.4385$ , and  $d = 0.1293$ . This relation predicts that the slope of the  $M_{AA_{\parallel}}$  order parameter diverges at  $|\kappa| = 3.5296g$ , which lies just below  $\kappa_0$ .

## 7.5 Summary

The results from a series of Monte Carlo simulations of the classical Heisenberg model for a square lattice were presented. The spins were assumed to interact through an antiferromagnetic exchange, dipolar interaction, and the magnetic surface anisotropy. Choosing  $J = -10.0g$ , the relevant states are antiferromagnetic in which every spin is aligned in the opposite direction to its neighbours. The orientation of the antiferromagnetic state is determined by the strength of the dipolar interaction, which favours the perpendicular antiferromagnetic phase, and the magnetic surface anisotropy, which, for  $\kappa < 0$ , favours the planar antiferromagnetic state.

Simulations for small values of  $|\kappa|/g$  show a finite perpendicular antiferromagnetic order parameter which decreases with increasing temperature until the system undergoes a second-order phase transition to the paramagnetic phase at the Néel temperature, at which point the order parameter is effectively zero. A similar behaviour is observed for large values of  $|\kappa|$ , with the difference that the ordered phase is the planar phase.

For intermediate values of  $|\kappa|/g$  there exists a narrow range around  $|\kappa| \approx \kappa_0$  for which the system undergoes a first-order reorientation transition from the planar to the perpendicular phase with increasing temperature. As the temperature is further increased the system undergoes a second-order transition to the paramagnetic phase. These results are summarised in the phase diagram presented in Figure 7.8.

While the sequence of phases observed in the reorientation transition in the anti-ferromagnetic case is the opposite to that observed for the ferromagnetic case, both may be qualitatively understood as a reduction in the strength of the magnetic surface anisotropy relative to the dipolar interaction, due to the thermal fluctuations.

It was also noted that, despite the first-order nature of the reorientation transition, the low temperature magnetisation reveals a softening of the spin-wave spectra close to the transition. The prediction of the reorientation transition in antiferromagnetically thin films is perhaps the most interesting result to emerge from these studies.

## Chapter 8

# Conclusions and Future Research Directions

As mentioned in chapter 1, interest in low-dimensional magnetic systems has grown considerably in recent years. One important class of reduced dimensional systems is ultra-thin magnetic films, which consist of several mono-layers of magnetic atoms deposited on a non-magnetic substrate. The increased scientific interest in these materials is a consequence of advances in film fabrication and characterization techniques. In addition to the scientific interest, these materials are also of potential technological importance in data storage and processing [20]. Of particular importance in the context of the current work is the use of antiferromagnetic films, which are used in the construction of spin valves [1].

Another class of reduced dimensional magnetic system that is of increasing scientific and technological interest is micro-magnetic arrays which consist of high density arrays of nano-magnetic dots deposited on a non-magnetic substrate. Such systems can be fabricated to have a wide variety of structures [64, 66] and properties [65] that can be tuned in a continuous manner to give a variety of phase behavior.

The results obtained from studies on low-dimensional magnetic systems are also

relevant to certain layered compounds that contain weakly interacting planes of magnetic ions. One important recent example of such compounds is the class of rare earth superconductors, such as  $\text{REBa}_2\text{Cu}_3\text{O}_{7-\delta}$  (RE = rare earth). Several of these compounds exhibit an antiferromagnetic ordering of the rare earth ions at low temperature [58]. While experimental determination of the effective dimensionality of these compounds is difficult, they nevertheless exhibit certain behaviors characteristic of two-dimensional magnetic systems close to the Néel temperature [195, 57, 191, 60].

The wide range of phenomena that have been observed or predicted in these low-dimensional magnetic materials arise from the complex interplay between three fundamental interactions: the exchange interaction, the dipolar interaction, and the magnetic surface anisotropy. A model that includes these three interactions in a particular spin configuration,  $\{\vec{\sigma}_i\}$ , was described in terms of an energy,  $E(\{\vec{\sigma}_i\})$ , given by

$$E(\{\vec{\sigma}_i\}) = g \sum_{i \neq j} \left( \frac{\vec{\sigma}_i \cdot \vec{\sigma}_j}{r_{ij}^3} - 3 \frac{(\vec{\sigma}_i \cdot \vec{r}_{ij})(\vec{\sigma}_j \cdot \vec{r}_{ij})}{r_{ij}^5} \right) - J \sum_{\langle i, j \rangle} \vec{\sigma}_i \cdot \vec{\sigma}_j - \kappa \sum_i (\sigma_i^z)^2, \quad (8.0.1)$$

where  $\vec{\sigma}_i$  is the three-dimensional classical spin vector at the lattice site,  $i$ . In Equation 8.0.1, the first term denotes the dipolar interaction, the second the exchange interaction, and the third the magnetic surface anisotropy.

The magnetic properties of the low-dimensional magnetic systems differ significantly from those of bulk materials, in part because the isotropic exchange interaction cannot of itself sustain long-range magnetic order in these low-dimensional materials. Of particular importance is the anisotropic and long-range dipolar interactions; which play critical roles in determining the magnetic properties of these materials. In the

case of the two-dimensional dipolar planar ferromagnetic system on a square lattice, the long-range character of the dipolar interaction gives rise to a non-analytic contribution in the magnetic propagator. This modifies the spin-wave spectra in the dipolar planar ferromagnet in the long wavelength limit such that  $\lim_{q \rightarrow 0} \omega(q) \approx \sqrt{q}$ . This modification of the spin-wave spectra is sufficient to render the thermal spin-wave fluctuations finite and, hence, allow for the appearance of long-range magnetic order at finite temperature [124]. The dipolar interaction also plays an important role in the case of the uniaxial ferromagnetic Ising model, in which the spins are aligned perpendicularly to the surface. In this case, the interplay between the short-range ferromagnetic exchange interaction and the long-range antiferromagnetic dipolar interactions, destabilizes the ferromagnetic ground state in favor of a striped phase [87, 88, 89], an effect that has been confirmed experimentally [10, 6]. The region separating the planar ferromagnetic phase and the uniaxial striped phase is determined by the asymmetry between the in-plane and out-of-plane spin alignment that arises from the combined effect of the magnetic surface anisotropy and the dipolar interaction. The analysis of this region is complicated by the inhomogeneous character of the striped phase and the complexities that arise from the dipolar interaction. Analytical and simulation studies do, however, show that the temperature-dependent renormalisation of these interactions, due to the thermal spin fluctuations, can give rise to a reorientation transition whereby the magnetisation axis switches from in-plane to out-of-plane with changing temperature [135, 136, 133, 144].

While the low-dimensional ferromagnetic ( $J > 0$ ) systems have been studied extensively, less work has been done on the low-dimensional antiferromagnetic systems ( $J < 0$ ). However, the complex interplay between the exchange interaction, magnetic

surface anisotropy, and dipolar interaction, appears to provide an equally fascinating range of phenomena for the antiferromagnetic case as presented in this research. The systems studied in this research are important for gaining a better understanding of the magnetic properties of low-dimensional magnetic systems. Of particular interest is the magnetic phase diagram for a two-dimensional dipolar antiferromagnetic system on a square lattice. For each investigated system, the magnetic phase diagram is established for both zero and finite temperatures.

## 8.1 Summary of Results

In the case of the pure dipolar system ( $J = 0$ ,  $\kappa = 0$ ) the ground state for the square lattice is a dipolar planar antiferromagnetic state, referred to as the  $AF_{\parallel}$  state. Surprisingly, despite the anisotropic character of the dipolar interaction, the ground state of the square lattice is continuously degenerate [118, 109], a fact that had been noted earlier for the honeycomb lattice [114]. The spin configurations that comprise this ground-state manifold are described in terms of a magnetic sub-lattice consisting of four lattice sites, with the spin at each lattice site oriented in terms of the angle  $\phi$  as was shown in Figure 4.2 [118]. This degeneracy gives rise to a gapless mode in the spin-wave spectra at zero temperature.

While the ground-state energy is continuously degenerate, the excitation spectrum depends on the angle,  $\phi$ , that characterizes the ground-state spin configuration. This implies that the entropy, and hence the free energy, are not continuously degenerate, but instead manifest the fourfold symmetry of the underlying lattice. In the case of the pure dipolar system the thermal fluctuations are such that the minimum in free energy has the spins aligned parallel to one of the axes of the lattice [118]. This state

is referred to as the  $AF_{\parallel}1$  state [157] or the columnar state [121]. The mechanism that stabilizes the formation of long-range antiferromagnetic order at finite temperature is an example of the phenomenon known as establishing “order from disorder” [116].

Extending the pure dipolar model to include the isotropic exchange interaction does not remove the degeneracy of the dipolar planar ground-state spin configurations. Thus, in the case of an antiferromagnetic exchange interaction ( $J < 0$ ), the continuously degenerate manifold of dipolar planar ground-state spin configurations continues to define the ground-state manifold for  $|J| \lesssim 1.23g$  [157]. Monte Carlo simulations, however, show that the antiferromagnetic exchange interaction does modify the character of the spin fluctuations such that the angle,  $\phi$ , that characterizes the equilibrium spin configuration switches from  $\phi = 0$  (or  $\phi = \pi/2$ ) to  $\phi = \pi/4$  at  $|J| \approx 0.7g$ . This state is referred to as the  $AF_{\parallel}2$  state [157] or the microvortex state [121]. For  $|J| \gtrsim 1.23g$ , the ground state is given by the non-degenerate antiferromagnetic phase in which the spins are aligned perpendicular to the plane, with each spin antiparallel to each of its nearest neighbors. This phase is referred to as the  $AA_{\perp}$  phase. Simulations reveal that the phase boundary separating the dipolar planar  $AF_{\parallel}2$  phase from the perpendicular  $AA_{\perp}$  phase is almost independent of temperature and, therefore, while the transition is first order, the latent heat associated with the transition is extremely small [157]. The  $J - T$  phase diagram for  $J < 0$  and  $\kappa = 0$  was shown in Figure 4.18.

Originally, it was postulated that the switching from the dipolar planar  $AF_{\parallel}1$  phase to the dipolar planar  $AF_{\parallel}2$  phase arose as a consequence of isolated spins being aligned perpendicular to the plane [157] so that, in this region, the system behaves analogously to a diluted dipolar planar system [117]. However, a similar dependence

of the equilibrium spin configuration on the strength of the exchange constant has also been observed in simulations and linearized spin-wave calculations for the dipolar antiferromagnetic plane rotator model in which the spins are constrained to lie in the plane [158, 121]. These results demonstrate that a purely plane rotator model can exhibit both the  $AF_{\parallel}1$  and  $AF_{\parallel}2$  phases, with a transition between them, as the relative strength of the exchange interaction is varied. In the two regions where  $|J| \lesssim 0.7g$  and  $2.1g \lesssim |J| \lesssim 3.21g$ , the dipolar planar phase is the  $AF_{\parallel}1$  phase, while in the region where  $0.7g \lesssim |J| \lesssim 2.1g$ , the dipolar planar phase is the  $AF_{\parallel}2$  phase [158]. Therefore, the out-of-plane degree of freedom of the magnetic spins present in the study of the dipolar antiferromagnetic Heisenberg model with zero magnetic surface anisotropy does not appear to play a critical role in determining the easy axis of the magnetization in the  $AF_{\parallel}$  phase as was originally supposed.

For  $|J| \gtrsim 3.21g$  the ground state of this purely rotator system is the planar antiferromagnetic phase where each spin is aligned antiparallel to its four nearest neighbors, a phase referred to as the  $AA_{\parallel}$  phase. The Monte Carlo data indicate that the phase boundary separating the dipolar planar  $AF_{\parallel}2$  phase and the planar  $AA_{\parallel}$  phase is almost independent of temperature, and hence, while the transition is first order, the latent heat associated with the transition is extremely small [158]. Further data on the plane rotator model indicate that reentrant phenomena between the  $AF_{\parallel}$  phases may occur as the relative strength of the exchange interaction is increased. This was not observed in the study reported on the Heisenberg system with zero  $\kappa$ , presumably because the in-plane to out-of-plane reorientation transition occurs before the system can reenter the  $AF_{\parallel}1$  phase. Again, this suggests that the exchange interaction modifies the nature of the disorder produced by the thermal

fluctuations in a further subtle, and as yet unexplained manner. The  $J - T$  phase diagram for the dipolar antiferromagnetic planar system was shown in Figure 5.2.

Extending the dipolar antiferromagnetic Heisenberg model to include a weak planar magnetic surface anisotropy ( $\kappa = -1.0g$ ), the Monte Carlo results indicate that the system exhibits similar behavior to that of a system with zero magnetic surface anisotropy, except that the coexistence line between the dipolar planar  $AF_{\parallel}$  and the perpendicular  $AA_{\perp}$  phases is now temperature dependent and has a negative slope. Therefore, turning on the planar magnetic surface anisotropy can lead the system to exhibit a reorientation transition from the  $AF_{\parallel}$  phase to the  $AA_{\perp}$  phase with increasing temperature. The value of  $|J|/g$  in which the system switches from the  $AF_{\parallel}$  ground state to the  $AA_{\perp}$  ground state occurs at  $J_0 \approx 1.73g$ . The  $J - T$  phase diagram of this system was given in Figure 6.7.

To obtain a better understanding of this reorientation transition, the interplay of the planar magnetic surface anisotropy and the long-range dipolar anisotropy in the exchange dominated antiferromagnetic phase ( $J = -10.0g$ ) was examined [159]. In particular, the  $\kappa - T$  phase diagram for  $\kappa \leq 0$  and  $J = -10.0g$ , constructed from the results from the Monte Carlo simulations, was presented in Figure 7.8. This phase diagram shows three distinct magnetic phases: The  $AA_{\perp}$  phase which occurs at both low temperatures and at low values of  $|\kappa|/g$ ; the  $AA_{\parallel}$  phase which occurs at both the low temperatures and at high values of  $\kappa/g$ , and the paramagnetic phase which occurs at high temperatures regardless of the value of  $|\kappa|/g$ . Of special note is the prediction of a reorientation transition from the planar  $AA_{\parallel}$  antiferromagnetic phase to the perpendicular  $AA_{\perp}$  antiferromagnetic phase with increasing temperature. Therefore, the phase diagram shows that the coexistence line separating the planar and the

perpendicular phases satisfies an important thermodynamic relationship analogous to the Clausius-Clapeyron relationship in fluids.

## 8.2 Future Research Directions

This research has been able to provide answers to a number of questions about two-dimensional antiferromagnetic systems. Nevertheless, several intriguing and important questions remain to be answered. For example, one important challenge will be to determine how the presence of the antiferromagnetic exchange interaction modifies the thermal fluctuations of the system that leads to the presence of the  $AF_{\parallel}1$  and  $AF_{\parallel}2$  phases. One approach that may provide further insight into the role of the exchange interaction in determining the  $AF_{\parallel}$  equilibrium phases mentioned above would be to investigate the free energy of such a system as a function of  $\phi$  using the umbrella sampling method. The results obtained then could be compared to those results obtained from the linearized spin-wave method that was presented in [121]. Another important calculation that might provide some insight into the nature of the reorientation transition would be a comparison of the results reported in the low temperature magnetisation shown in Figure 7.11, which shows a softening close to the transition, with those obtained from spin-wave theory.

As an extension to the work of this thesis, our research group has started to investigate the effects of impurities as well as of polydispersity in the plane rotator systems. The preliminary analyses show interesting results which again show the subtle effects that arise from disorder. In addition, our group has begun to explore the Clausius-Clapeyron relationship that determines the coexistence line that separates the planar from the perpendicular phases. Our research group also plans to extend

the current work to analyse multilayered systems, and has started to parallelise the code used in the present work. This would permit an investigation of a number of very interesting systems including models of spin valves. Some preliminary work evaluating the critical exponents for both the planar and perpendicular phases has already been done. However, more detailed studies are still required in order to determine the precise nature of the transition to the paramagnetic phase in these systems. It will be interesting, for example, to compare the critical exponents at the transition from the paramagnetic phase to the parallel phase with corresponding values for the perpendicular phase. The effect of an applied magnetic field has not been considered at all in the present research, and needs to be considered if one hopes to gain a full understanding of the model and its potential applications.

# Appendix A

## Free Energy

The free energy,  $F$ , for a system can be written as

$$F = -T \ln \left( \sum_{\nu} \exp(-E_{\nu}/T) \right), \quad (\text{A.0.1})$$

where  $T$  is the temperature in units of  $1/k_B$ , such that  $k_B$  is the Boltzmann constant, and  $E_{\nu}$  is the energy of the system in a state  $\nu$ . The free energy difference,  $\Delta F$ , between the system of interest, with internal energy  $E$  at temperature  $T$ , and a reference system, with internal energy  $E_o$  at temperature  $T_o$ , is then given by

$$\begin{aligned} \Delta F &= F - F_o, \\ &= -T \ln \left( \frac{\sum_{\nu} \exp(-E/T)}{\sum_{\nu} \exp(-E_o/T_o)} \right), \\ &= -T \ln \left( \frac{\sum_{\nu} \exp(-E/T + E_o/T_o) \exp(-E_o/T_o)}{\sum_{\nu} \exp(-E_o/T_o)} \right), \\ &= -\ln(\langle \exp(-E/T + E_o/T_o) \rangle_o), \end{aligned} \quad (\text{A.0.2})$$

where  $\langle \rangle_o$  denotes an average over a canonical ensemble of reference system. In the case where  $T = T_o$ , Equation A.0.2 then gives

$$\begin{aligned}\Delta F &= -\ln(\langle \exp(-E/T + E_o/T) \rangle_o), \\ &= -\ln(\langle \exp(-\Delta E/T) \rangle_o),\end{aligned}\tag{A.0.3}$$

where  $\Delta E = E - E_o$ .

The energy of the dipolar plane rotator system in a particular spin configuration,  $\{\vec{\sigma}_i\}$ , at an exchange constant,  $J$ , is given by

$$\begin{aligned}E(J) &= E_{dd} + E_{ex}, \\ &= E_{dd} - J \sum_{\langle ij \rangle} \vec{\sigma}_i \cdot \vec{\sigma}_j, \\ &= E_{dd} + JA_{ex},\end{aligned}\tag{A.0.4}$$

such that

$$A_{ex} = - \sum_{\langle ij \rangle} \vec{\sigma}_i \cdot \vec{\sigma}_j.\tag{A.0.5}$$

Substituting Equation A.0.4 into Equation A.0.3, the expression for the free energy difference at temperature  $T$  between the system of interest, with internal energy  $E(J)$ , and a reference system, with internal energy  $E(J_o)$ , is then given by

$$\begin{aligned}\Delta F &= F(J) - F(J_o), \\ &= -T \ln(\langle \exp(-(J - J_o)A_{ex}/T) \rangle_{J_o}), \\ &= -T \ln(\langle \exp(-\Delta J A_{ex}/T) \rangle_{J_o}).\end{aligned}\tag{A.0.6}$$

Since the free energy results obtained from Monte Carlo simulations will be reliable only for values of  $J$  close to  $J_o$ , the free energy of the system with respect to  $F_o$  can

be calculated by evaluating  $\Delta F$  for several values of  $J_o$  over a range of values of  $J$ , and then combining the results to yield a free energy curve as a continuous function of  $J$ . The first region to consider is  $0 < |J| < 0.7g$ . Over this region, Monte Carlo simulations are applied using Equation A.0.6 to calculate  $\Delta F = F(J) - F(J_o)$  over this range of values of  $J/g$  for different values of  $J_o/g$ , as shown in Figure A.1 at a particular value of temperature,  $T = 0.2g$ . For each value of  $J_o$  six points are selected in the region around  $J_o$ , with the exception of  $J_o = 0.0$  for which only three points are selected. From these points the free energy relative to a common value,  $F_o$ , is established over the range  $0 < |J| < 0.7g$ . These selected points are shown in Figure A.2 with suitable labelling of each point.

Using the fact that the free energy is a continuous function of  $J$ , the selected points for one curve are combined with the points of the next curve, and so on. The following procedure is used to obtain the combination of the selected points over the chosen range of  $J/g$ . The selected points from the curve where  $J_o = 0.0$  are combined with those selected from the curve where  $J_o = -0.2g$  by adding a constant,  $f_1$ , to the points for  $J_o = -0.2g$ . The constant,  $f_1$ , which is needed to be added to the points of the second curve to align them with the points of the first curve is determined by minimizing the standard deviation,  $s$ , between the points mentioned above. The standard deviation between these points can be written as

$$s = (a_1 - (b_1 + f_1))^2 + (a_2 - (b_2 + f_1))^2 + (a_3 - (b_3 + f_1))^2, \quad (\text{A.0.7})$$

To minimize  $s$ , the derivative of both sides of Equation A.0.7 is taken first and the result gives

$$ds = (6f_1 + 2b_1 + 2b_2 + 2b_3 - 2a_1 - 2a_2 - 2a_3)df_1. \quad (\text{A.0.8})$$

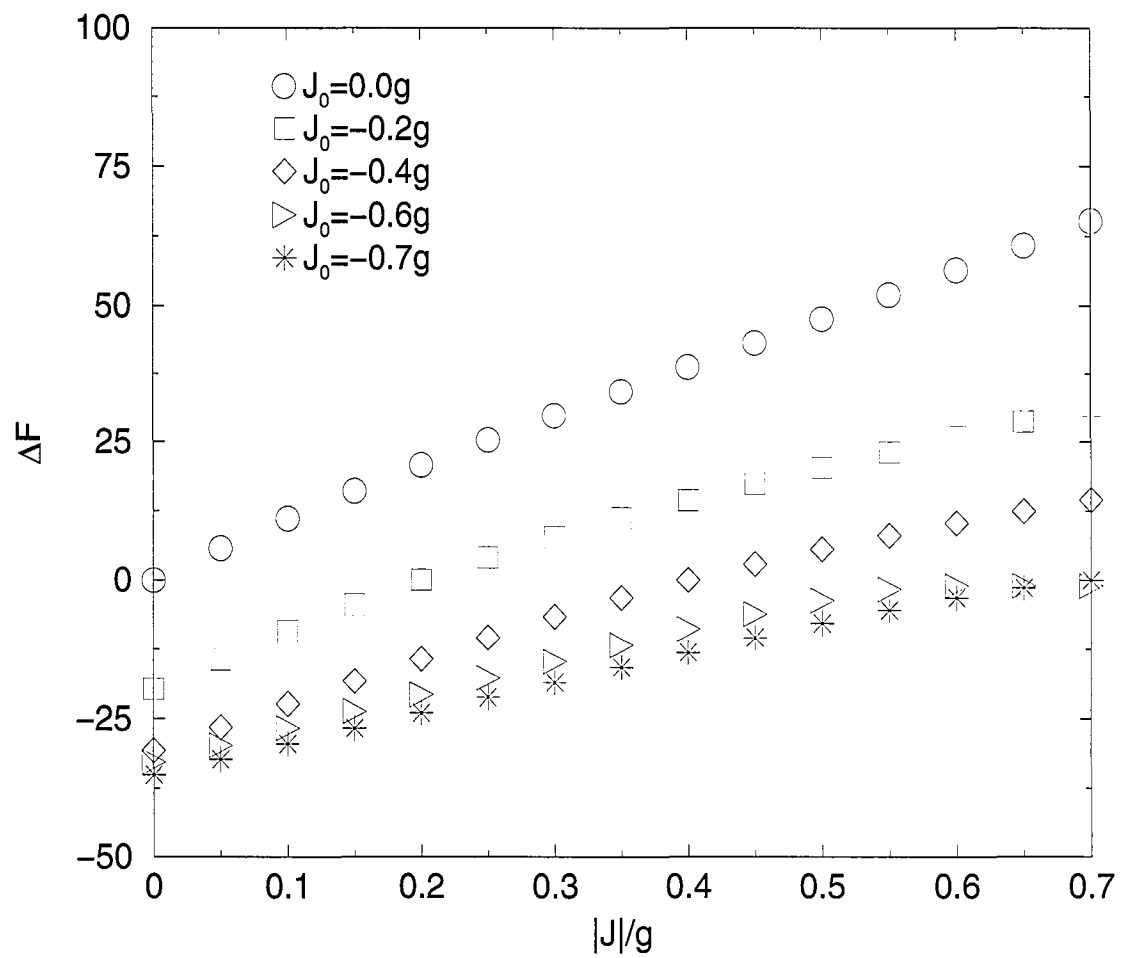


Figure A.1: The change in the free energy as a function of the exchange constant over the range where  $0 < |J| < 0.7g$ , for several values of  $J_0/g$  at  $T = 0.2g$  with  $L = 64$ .

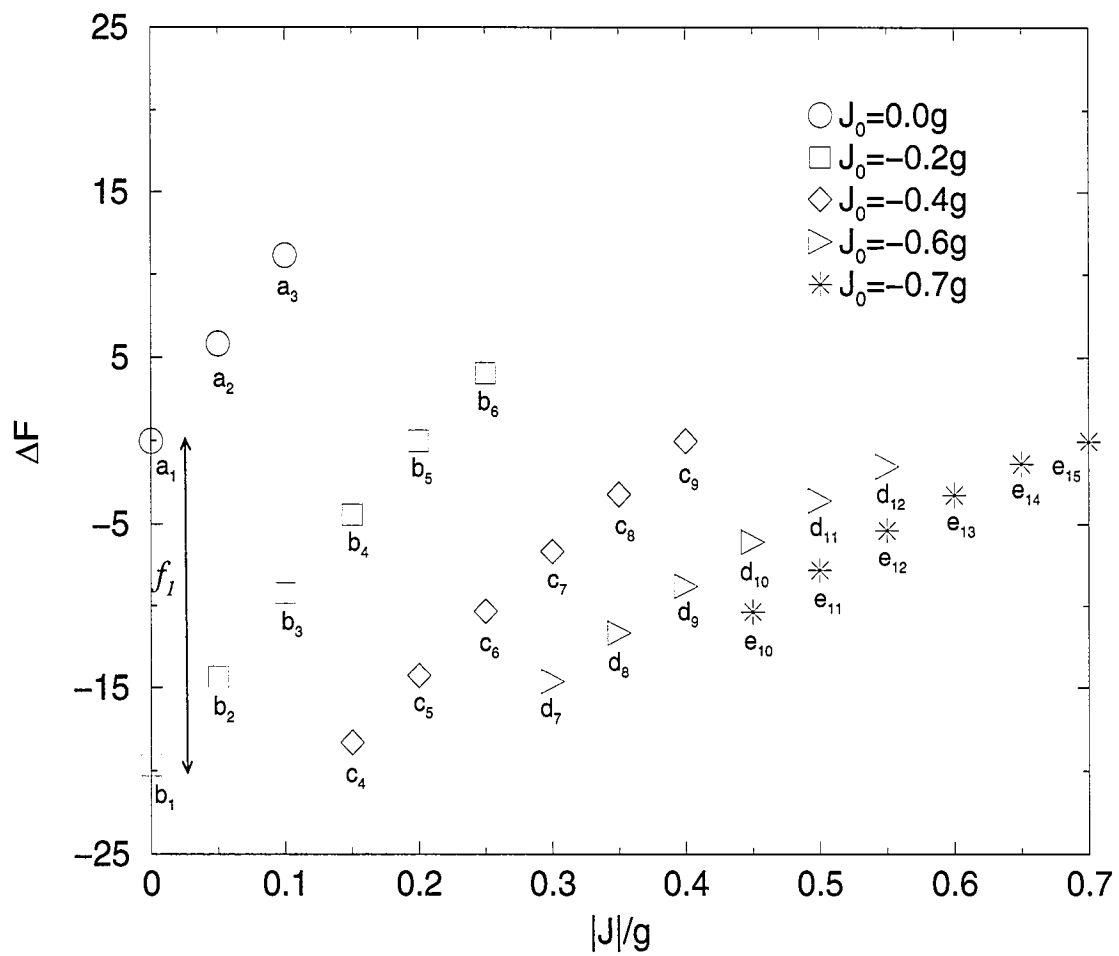


Figure A.2: The change in the free energy for the points selected from the curves shown in Figure A.1 at  $T = 0.2g$  with  $L = 64$ , where lower case letters denote these selected points.

Then, the left hand side of Equation A.0.8 is taken to be zero and this gives

$$0 = (6f_1 + 2b_1 + 2b_2 + 2b_3 - 2a_1 - 2a_2 - 2a_3)df_1. \quad (\text{A.0.9})$$

Solving for  $f_1$ , Equation A.0.9 yields

$$f_1 = \frac{1}{3} ((a_1 + a_2 + a_3) - (b_1 + b_2 + b_3)). \quad (\text{A.0.10})$$

These results are shown in Figure A.3 where new labels (denoted by  $B_4, B_5, B_6$ ) are attached to the new set of points produced from the previous step. This new set of points is then combined with the six points selected from the curve where  $J_o = -0.4g$ , by adding a constant,  $f_2$ , to the points for  $J_o = -0.4g$ . The constant,  $f_2$ , is determined using the same method that was used in calculating  $f_1$ , and is given by

$$f_2 = \frac{1}{3} ((B_4 + B_5 + B_6) - (c_4 + c_5 + c_6)). \quad (\text{A.0.11})$$

These results are shown in Figure A.4 where the new labels (denoted by  $C_7, C_8, C_9$ ) are attached to the new set of points produced from the previous step. The same calculations are then performed for each subsequent set of six points over the remaining values of  $J_o/g$ . The final collapsed results are shown in Figure A.5 where the corrected free energy with respect to  $F_o$  is plotted over the chosen range of  $|J|/g$ .

The same procedures are repeated for the other two regions where  $0.7g < |J| < 2.1g$  and  $2.1g < |J| < 3.2g$ . While Figure A.6 shows the free energy with respect to a common value,  $F_o$ , over the region where  $0.7g < |J| < 2.1g$ , Figure A.7 shows the free energy over the region where  $2.1 < |J|/g < 3.2$ .

By gathering the selected points from the curves shown in Figures A.5, A.6, and A.7, the free energy of the system with respect to  $F_o$  is obtained over a range of values of  $J/g$ , as shown in Figure A.8. From Figure A.8, the increase in free energy

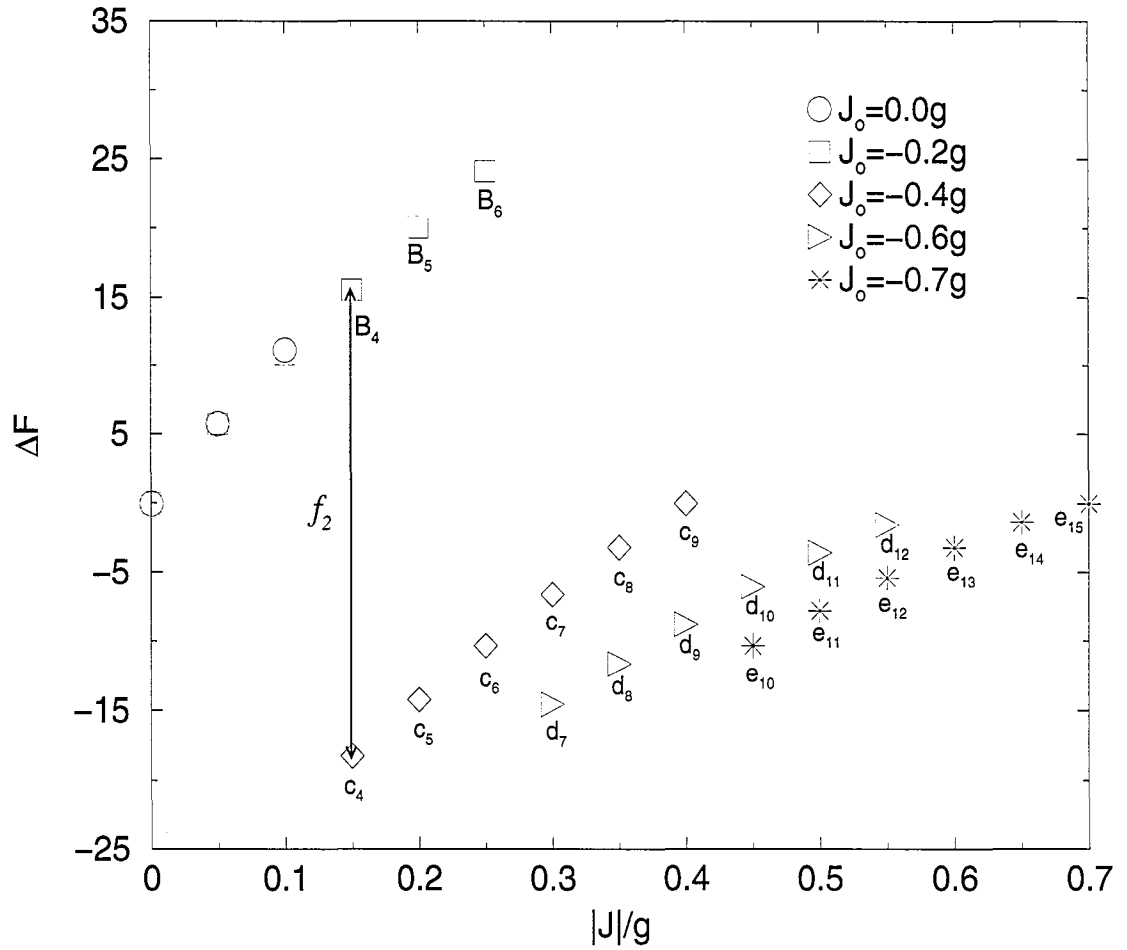


Figure A.3: The change in the free energy for the points selected from the curves shown in Figure A.1 after the combination of the points selected for the curve where  $J_0 = 0.0$  with the points selected from the curve where  $J_0 = -0.2g$  at  $T = 0.2g$  with  $L = 64$ .

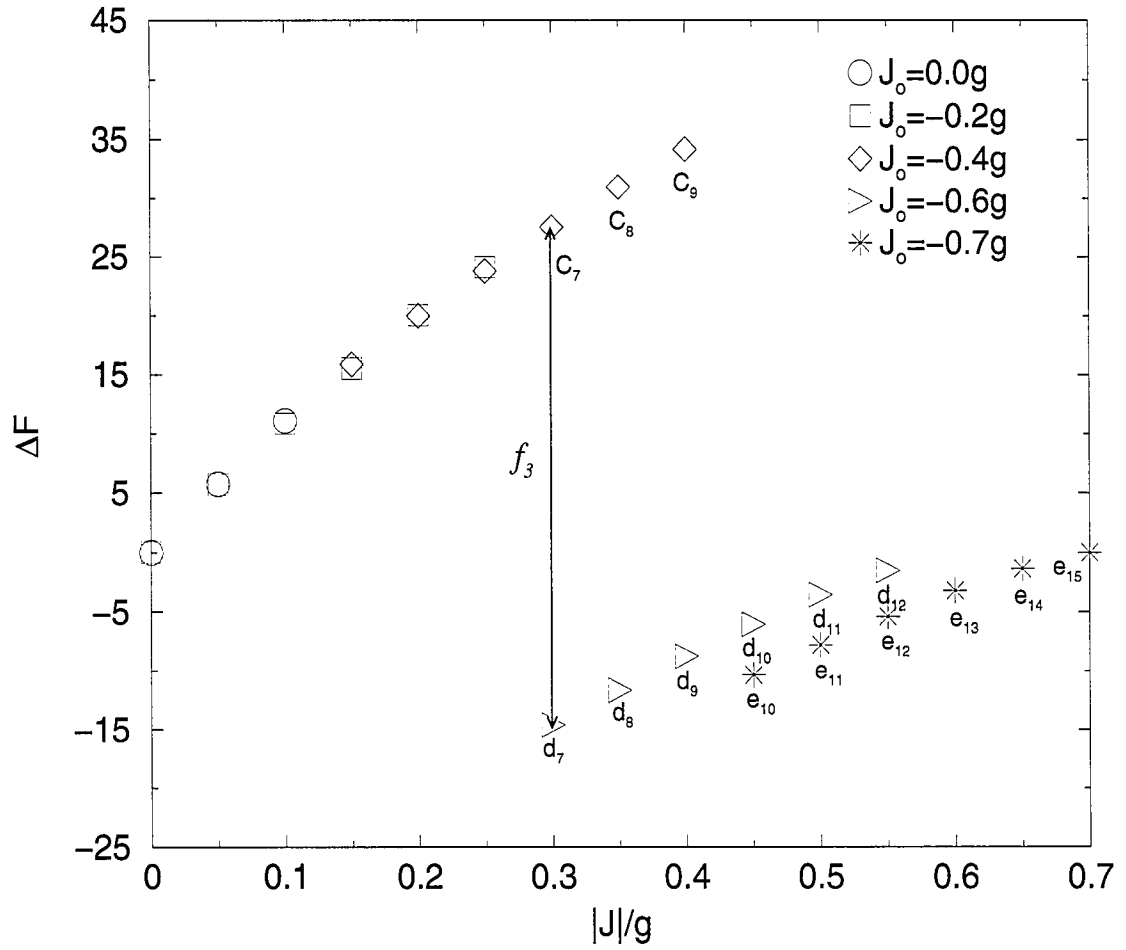


Figure A.4: The change in the free energy for the points selected from the curves shown in Figure A.1 after the combination of the new points selected from the curve where  $J_o = -0.2g$  with the points selected from the curve where  $J_o = -0.4g$  at  $T = 0.2g$  with  $L = 64$ .

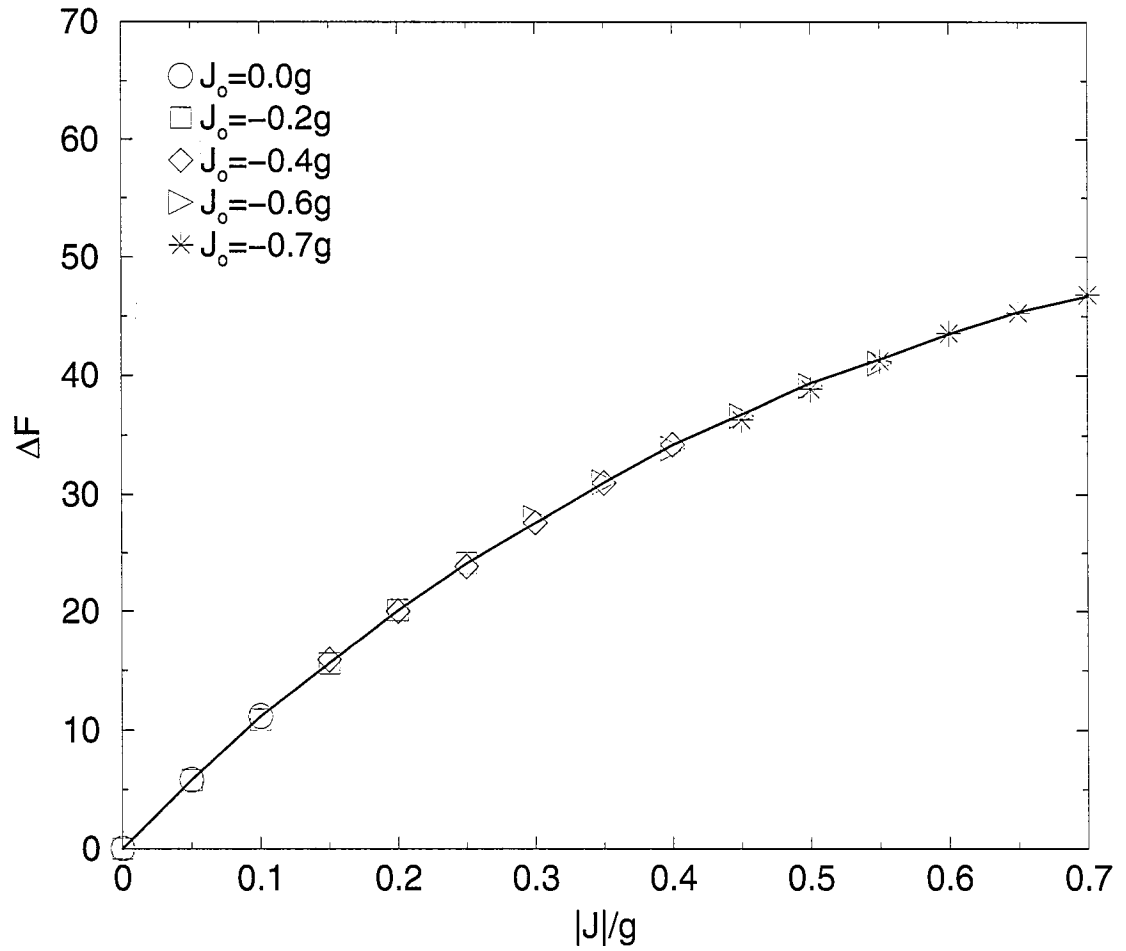


Figure A.5: The corrected free energy as a function of the exchange constant over the range  $0 < |J| < 0.7g$ , for several values of  $J_0/g$  at  $T = 0.2g$  with  $L = 64$ .

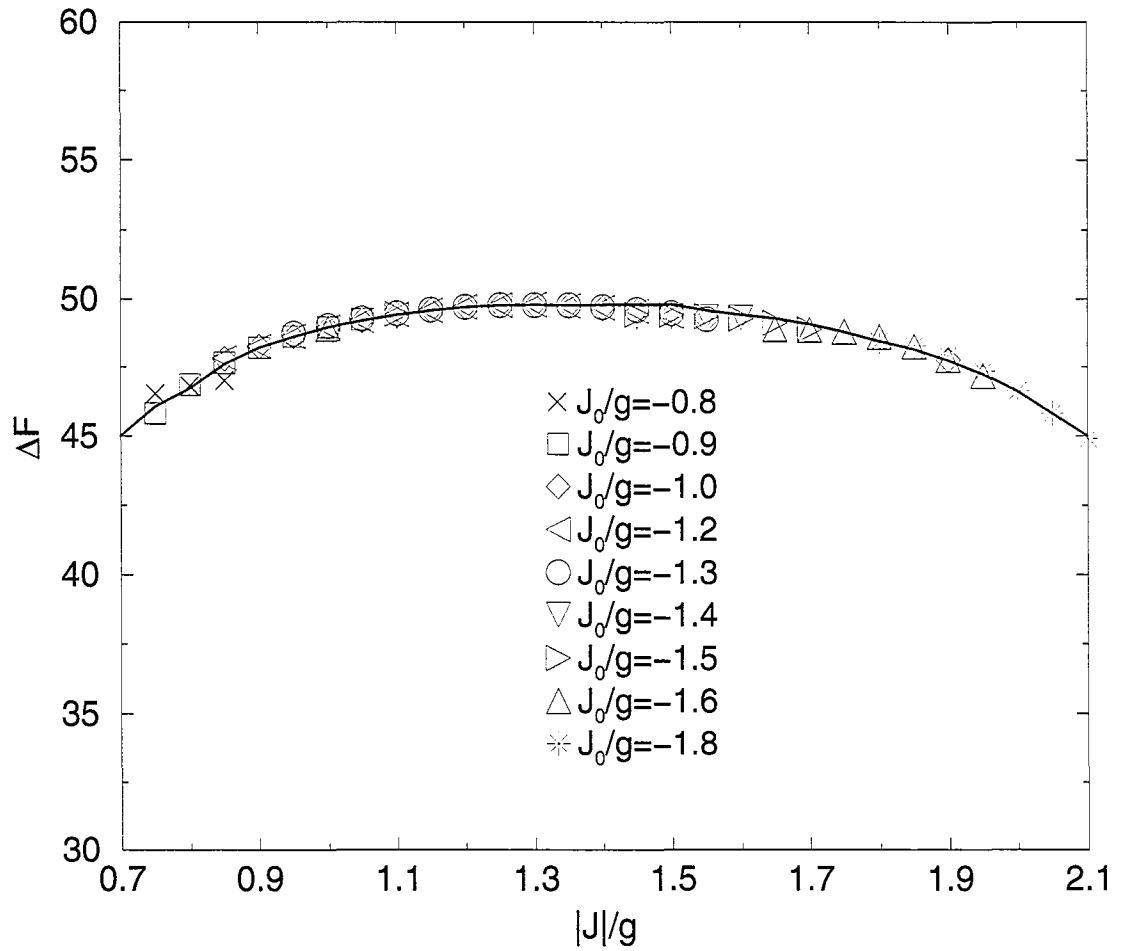


Figure A.6: The corrected free energy as a function of the exchange constant over the range  $0.7g < |J| < 2.1g$ , for several values of  $J_0/g$  at  $T = 0.2g$  with  $L = 64$ .

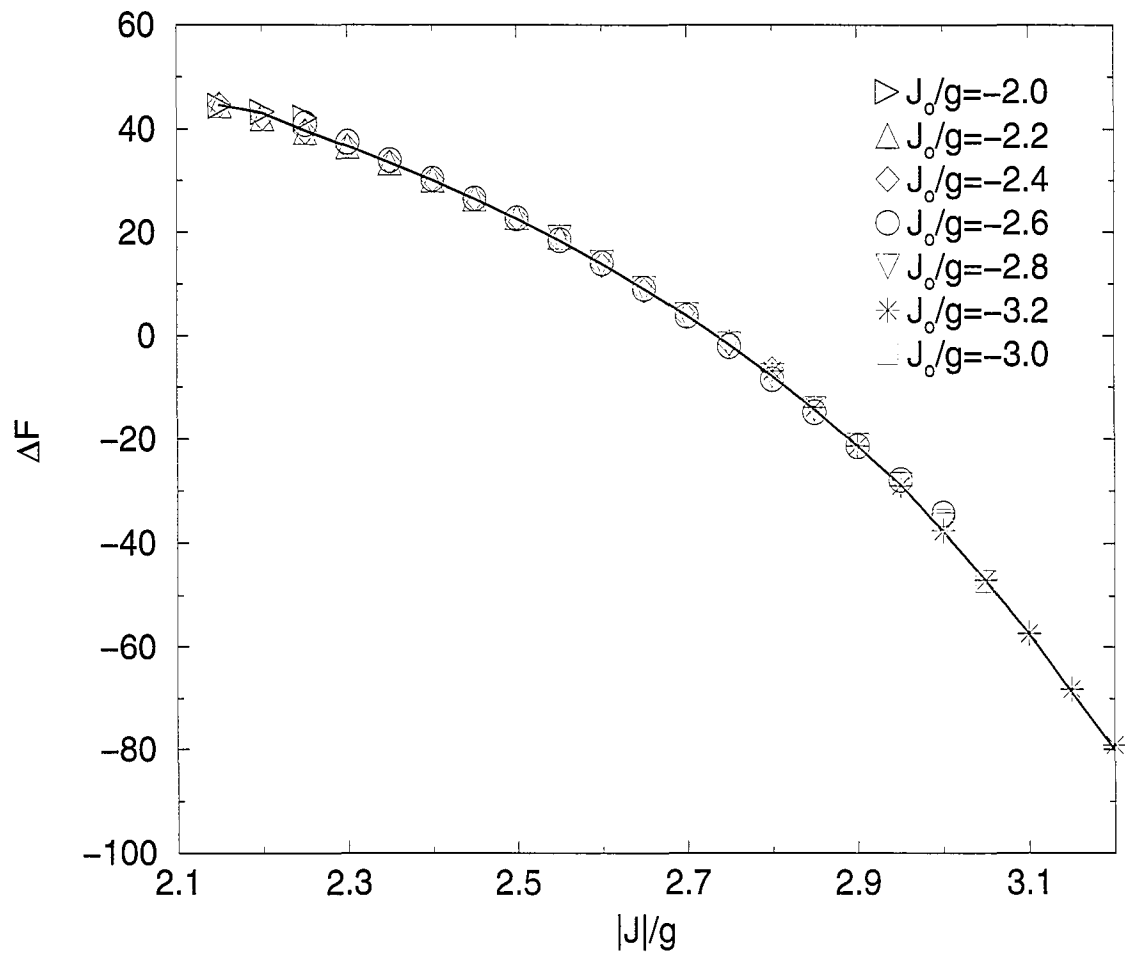


Figure A.7: The corrected free energy as a function of the exchange constant over the range  $2.1 < |J|/g < 3.2$ , for several values of  $J_0/g$  at  $T = 0.2g$ .

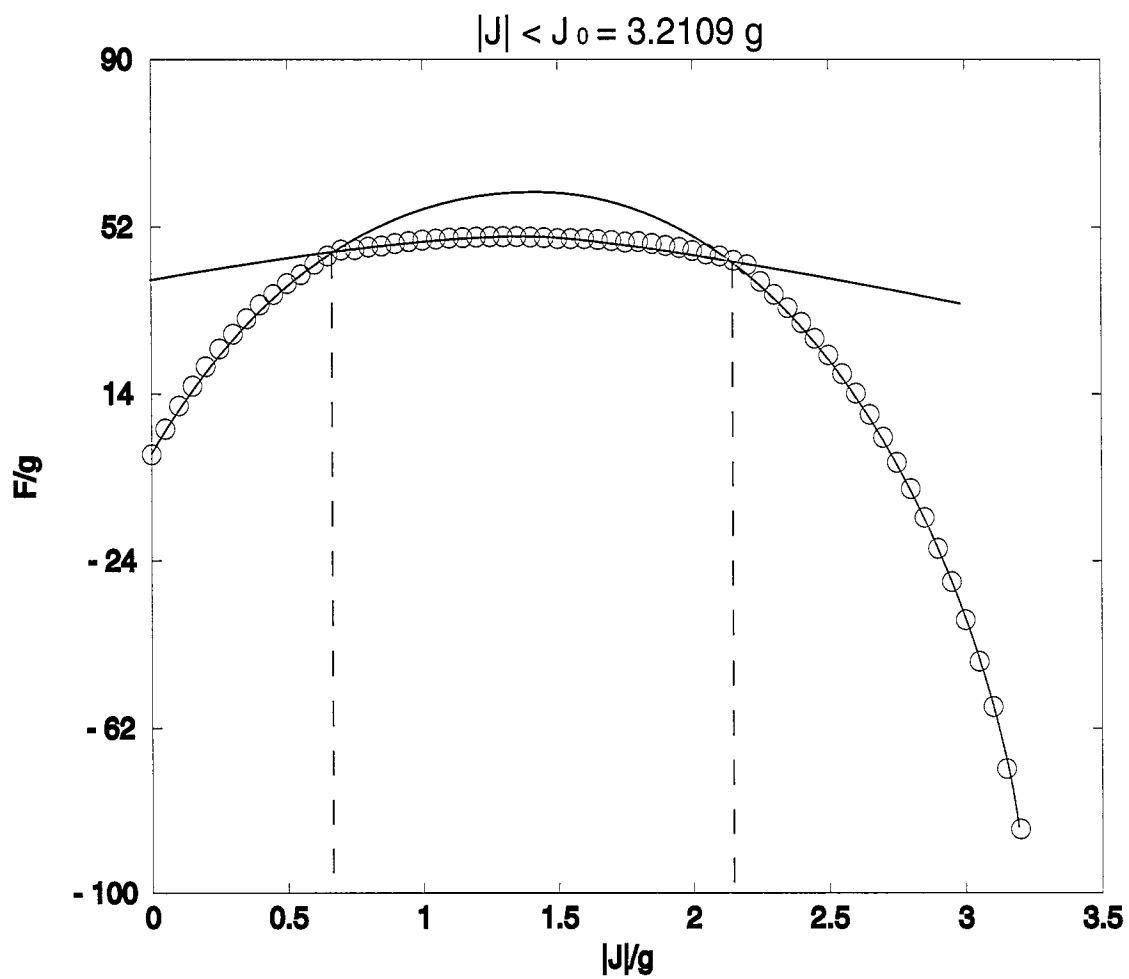


Figure A.8: The free energy with respect to a common value,  $F_0$ , as a function of the exchange constant at  $T = 0.2g$ . (The solid lines shown in the figure are simply a guide to the eye.)

from  $|J| = 0.0$  to approximately  $|J| = 0.7g$  denotes the first phase ( $AF_{||1}$  phase). The second phase ( $AF_{||2}$  phase) is illustrated by the relatively level free energy from  $|J| = 0.7g$  to approximately  $|J|/g = 2.1$ . The system reverts back to the  $AF_{||1}$  phase, as indicated by the decrease in the free energy starting from approximately  $|J|/g = 2.1$  to approximately  $|J|/g = 3.2$ . This calculation for the free energy of the dipolar plane rotator system was done in cooperation with summer student Paul Chafe [196].

# Appendix B

## Slope of the Coexistence Line

### B.1 Slope of the Coexistence Line: $J_R(T)$

As described in Appendix A, the free energy,  $F$ , for a given value of the exchange constant,  $J$ , and temperature,  $T$  (in units of  $1/k_B$ ), may be written as

$$F(J, T) = -T \ln \left( \sum_{\{\vec{\sigma}_i\}} \exp(-E(\{\vec{\sigma}_i\})/T) \right), \quad (\text{B.1.1})$$

where  $E(\{\vec{\sigma}_i\})$  is the energy of the system in a particular spin configuration  $\{\vec{\sigma}_i\}$  which is given by

$$E(\{\vec{\sigma}_i\}) = g \sum_{i \neq j} \left( \frac{\vec{\sigma}_i \cdot \vec{\sigma}_j}{r_{ij}^3} - 3 \frac{(\vec{\sigma}_i \cdot \vec{r}_{ij})(\vec{\sigma}_j \cdot \vec{r}_{ij})}{r_{ij}^5} \right) - J \sum_{\langle i, j \rangle} \vec{\sigma}_i \cdot \vec{\sigma}_j. \quad (\text{B.1.2})$$

From the energy given in Equation B.1.2 we obtain the following expression for the variation in the ratio  $F/T$  induced by a variation in the exchange constant  $J$  and the temperature  $T$

$$d \left( \frac{F}{T} \right) = \left( \frac{1}{T} \frac{\partial F}{\partial T} - \frac{F}{T^2} \right) dT + \frac{1}{T} \frac{\partial F}{\partial J} dJ. \quad (\text{B.1.3})$$

From equations B.1.1 and B.1.2,  $\frac{\partial F}{\partial J}$  is given by

$$\begin{aligned}\frac{\partial F}{\partial J} &= -\sum_{\langle ij \rangle} \vec{\sigma}_i \cdot \vec{\sigma}_j, \\ &= \frac{1}{J} E_{ex}.\end{aligned}\tag{B.1.4}$$

Because

$$dF = dE - TdS - SdT,\tag{B.1.5}$$

$\frac{\partial F}{\partial T}$  is then given by

$$\frac{\partial F}{\partial T} = -S.\tag{B.1.6}$$

Substituting Equations B.1.4 and B.1.6, Equation B.1.3 then gives

$$\begin{aligned}d\left(\frac{F}{T}\right) &= -\frac{1}{T} \left( \frac{ST - F}{T} dT - \frac{E_{ex}}{J} dJ \right), \\ &= -\frac{1}{T} \left( \frac{E}{T} dT - \frac{E_{ex}}{J} dJ \right).\end{aligned}\tag{B.1.7}$$

Let us consider two states which we label  $a$  and  $b$  respectively. We have that

$$d\left(\frac{F^{(a)}}{T}\right) = -\frac{1}{T} \left( \frac{E^{(a)}}{T} dT - \frac{E_{ex}^{(a)}}{J} dJ \right)\tag{B.1.8}$$

and

$$d\left(\frac{F^{(b)}}{T}\right) = -\frac{1}{T} \left( \frac{E^{(b)}}{T} dT - \frac{E_{ex}^{(b)}}{J} dJ \right).\tag{B.1.9}$$

Subtracting we obtain

$$d\left(\frac{\Delta F}{T}\right) = -\frac{1}{T} \left( \frac{\Delta E}{T} dT - \frac{\Delta E_{ex}}{J} dJ \right).\tag{B.1.10}$$

At the phase boundary separating the planar and the perpendicular phase, the two phases coexist and have the same free energy. Therefore, along the phase boundary

we have  $\Delta F/T = 0$  and therefore  $d(\Delta F/T) = 0$ , from which we obtain the following relationship for the difference between the exchange energy and the total energy of the two phases

$$\frac{\Delta E}{T} dT = \frac{\Delta E_{ex}}{J} dJ. \quad (\text{B.1.11})$$

Since the two phases have the same free energy then  $\Delta E$  is the latent heat, and hence we obtain the following expression for the slope quoted in the chapter 4 (Equation 4.4.1)

$$\frac{dJ_R}{dT} = \frac{J\Delta E}{T\Delta E_{ex}}. \quad (\text{B.1.12})$$

## B.2 Slope of the Coexistence Line: $\kappa_R(T)$

As described above, the free energy,  $F$ , for a given value of the magnetic surface anisotropy  $\kappa$  and temperature  $T$  (in units of  $1/k_B$ ) may be written as

$$F = -T \ln \left( \sum_{\{\vec{\sigma}_i\}} \exp(-E(\{\vec{\sigma}_i\})/T) \right), \quad (\text{B.2.1})$$

where  $E(\{\vec{\sigma}_i\})$  is the energy of the system in a particular spin configuration  $\{\vec{\sigma}_i\}$  which is given by

$$\begin{aligned} E(\{\vec{\sigma}_i\}) = & g \sum_{i \neq j} \left( \frac{\vec{\sigma}_i \cdot \vec{\sigma}_j}{r_{ij}^3} - 3 \frac{(\vec{\sigma}_i \cdot \vec{r}_{ij})(\vec{\sigma}_j \cdot \vec{r}_{ij})}{r_{ij}^5} \right) - J \sum_{\langle i,j \rangle} \vec{\sigma}_i \cdot \vec{\sigma}_j \\ & - \kappa \sum_i (\sigma_i^z)^2. \end{aligned} \quad (\text{B.2.2})$$

From the energy given in Equation B.2.2 we obtain the following expression for the variation in the ratio  $F/T$  induced by a variation in the magnetic surface anisotropy

constant  $\kappa$  and the temperature  $T$

$$d\left(\frac{F}{T}\right) = \left(\frac{1}{T}\frac{\partial F}{\partial T} - \frac{F}{T^2}\right) dT + \frac{1}{T}\frac{\partial F}{\partial \kappa} d\kappa. \quad (\text{B.2.3})$$

From equations B.2.1 and B.2.2,  $\frac{\partial F}{\partial \kappa}$  is given by

$$\begin{aligned} \frac{\partial F}{\partial \kappa} &= -\kappa \sum_i (\sigma_i^z)^2, \\ &= \frac{1}{\kappa} E_\kappa. \end{aligned} \quad (\text{B.2.4})$$

Substituting Equations B.1.6 and B.2.4 into Equation B.1.3 then gives

$$\begin{aligned} d\left(\frac{F}{T}\right) &= -\frac{1}{T} \left( \frac{ST - F}{T} dT - \frac{E_\kappa}{\kappa} d\kappa \right), \\ &= -\frac{1}{T} \left( \frac{E}{T} dT - \frac{E_\kappa}{\kappa} d\kappa \right). \end{aligned} \quad (\text{B.2.5})$$

Let us consider two states which we label  $a$  and  $b$  respectively. We have that

$$d\left(\frac{F^{(a)}}{T}\right) = -\frac{1}{T} \left( \frac{E^{(a)}}{T} dT - \frac{E_\kappa^{(a)}}{\kappa} d\kappa \right) \quad (\text{B.2.6})$$

and

$$d\left(\frac{F^{(b)}}{T}\right) = -\frac{1}{T} \left( \frac{E^{(b)}}{T} dT - \frac{E_\kappa^{(b)}}{\kappa} d\kappa \right). \quad (\text{B.2.7})$$

Subtracting we obtain

$$d\left(\frac{\Delta F}{T}\right) = -\frac{1}{T} \left( \frac{\Delta E}{T} dT - \frac{\Delta E_\kappa}{\kappa} d\kappa \right). \quad (\text{B.2.8})$$

At the phase boundary separating the planar and the perpendicular phase, the two phases coexist and have the same free energy. Therefore along the phase boundary we have  $\Delta F/T = 0$  and therefore  $d(\Delta F/T) = 0$ , from which we obtain the following

relationship for the difference between the exchange energy and the total energy of the two phases

$$\frac{\Delta E}{T} dT = \frac{\Delta E_{\kappa}}{\kappa} d\kappa. \quad (\text{B.2.9})$$

Since the two phases have the same free energy then  $\Delta E$  is the latent heat, and hence we obtain the following expression for the slope quoted in chapter 7 (Equation 7.3.1)

$$\frac{d\kappa_R}{dT} = \frac{\kappa \Delta E}{T \Delta E_{\kappa}}. \quad (\text{B.2.10})$$

# Bibliography

- [1] S. A. Wolf, D. D. Awschalom, R. A. Buhrman, J. M. Daughton, S. von Molnár, M. L. Roukes, A. Y. Chtchelkanova, and D. M. Treger. Spintronics: A spin-based electronics vision for the future. *Science*, 294:1488–1495, 2001.
- [2] M. R. Freeman and B. C. Choi. Advances in magnetic microscopy. *Science*, 294:1484–1488, 2001.
- [3] L. M. Falicov, F. Mejia-Lira, and J. L. Morán-López, editors. *Magnetic properties of low-dimensional systems II*. Springer-Verlag, Berlin, 1990.
- [4] M. Prutton. *Introduction to surface physics*. Clarendon Press, Oxford, 1994.
- [5] T. L. Jones and D. Venus. Structural and magnetic characterization of thin iron films on a tungsten (001) substrate. *Surface Science*, 302:126–140, 1994.
- [6] D. P. Pappas, K.-P. Kämper, and H. Hopster. Reversible transition between perpendicular and in-plane magnetization in ultrathin films. *Physical Review Letters*, 64(26):3179–3182, 1990.
- [7] R. Allenspach and A. Bischof. Magnetization direction switching in Fe/Cu(100) epitaxial films: Temperature and thickness dependence. *Physical Review Letters*, 69(23):3385–3388, 1992.

- [8] Z. Q. Qiu, J. Pearson, and S. D. Bader. Asymmetry of the spin reorientation transition in ultrathin Fe films and wedges grown on Ag(100). *Physical Review Letters*, 70(7):1006–1009, 1993.
- [9] A. Berger and H. Hopster. Magnetization reversal properties near the reorientation phase transition of ultrathin Fe/Ag(100) films. *Journal of Applied Physics*, 79(8):5619–5621, 1996.
- [10] R. Allenspach, M. Stampanoni, and A. Bischof. Magnetic domains in thin epitaxial Co/Au(111) films. *Physical Review Letters*, 65(26):3344–3347, 1990.
- [11] M. Speckmann, H. P. Oepen, and H. Ibach. Magnetic domain structures in ultrathin Co/Au(111): On the influence of film morphology. *Physical Review Letters*, 75(10):2035–2038, 1995.
- [12] C. Liu and S. D. Bader. Perpendicular surface magnetic anisotropy in ultrathin epitaxial Fe films. *Journal of Vacuum Science and Technology A*, 8(3):2727–2731, 1990.
- [13] B. Schulz and K. Baberschke. Crossover from in-plane to perpendicular magnetization in ultrathin Ni/Cu(001) films. *Physical Review B*, 50(18):13467–13471, 1994.
- [14] K. Baberschke. The magnetism of nickel monolayers. *Applied Physics A*, 62:417–427, 1996.
- [15] M. Farle, W. Platow, A. N. Anisimov, B. Schulz, and K. Baberschke. The temperature dependence of magnetic anisotropy in ultra-thin films. *Journal of Magnetism and Magnetic Materials*, 165:74–77, 1997.
- [16] B. Heinrich and J. F. Cochran. Ultrathin metallic magnetic films: Magnetic anisotropies and exchange interactions. *Advances in Physics*, 42(5):523–639, 1993.

- [17] J. A. C. Bland and B. Heinrich. *Ultrathin magnetic films*, volume I, II. Springer-Verlag, Berlin, 1994.
- [18] B. T. Jonker, S. A. Chambers, R. F. C. Farrow, C. Chappert, R. Clarke, W. J. M. de Jonge, T. Egami, P. Grünberg, K. M. Krishnan, E. E. Marinero, C. Rau, and S. Tsunashima. *Magnetic Ultrathin Films*, volume 313. Material Research Society, Pennsylvania, 1993.
- [19] J. B. Kortright D. D. Awschalom, J. Stöhr, S. D. Bader, Y. U. Idzerda, S. S. P. Parkin, Ivan K. Schuller, and H.-C. Siegmann. Research frontiers in magnetic materials at soft X-ray synchrotron radiation facilities. *Journal of Magnetism and Magnetic Materials*, 207:7–44, 1999.
- [20] G. A. Prinz. Magnetoelectronics. *Science*, 282:1660–1663, 1998.
- [21] H. J. Richter. Recent advances in the recording physics of thin-film media. *Journal of Physics D: Applied Physics*, 32(21):R147–R168, 1999.
- [22] C. Roland and M. Grant. Lack of self-averaging, multiscaling, and  $1/f$  noise in the kinetics of domain growth. *Physical Review Letters*, 63(5):551–554, 1989.
- [23] C. Roland and R. C. Desai. Kinetics of quenched systems with long-range repulsive interactions. *Physical Review B*, 42(10):6658–6669, 1990.
- [24] C. Sagui and R. C. Desai. Kinetics of phase separation in two-dimensional systems with competing interactions. *Physical Review E*, 49(3):2225–2244, 1994.
- [25] M. M. Hurley and S. J. Singer. Domain energies of the dipolar lattice gas. *Journal of Physical Chemistry*, 96(4):1938–1950, 1992.
- [26] J. Nogués and I. K. Schuller. Exchange bias. *Journal of Magnetism and Magnetic Materials*, 192:203–232, 1999.

- [27] B. Dieny, V. S. Speriosu, S. S. P. Parkin, B. A. Gurney, D. R. Wilhoit, and D. Mauri. Giant magnetoresistance in soft ferromagnetic multilayers. *Physics Review B*, 43(1):1297–1300, 1991.
- [28] S. S. P. Parkin, K. P. Roche, M. G. Samant, P. M. Rice, R. B. Beyers, R. E. Scheuerlein, E. J. O’Sullivan, S. L. Brown, J. Bucchigano, D. W. Abraham, Y. Lu, M. Rooks, P. L. Trouilloud, R. A. Wanner, and W. J. Gallagher. Exchange-biased magnetic tunnel junctions and application to nonvolatile magnetic random access memory (invited). *Journal of Applied Physics*, 85(8):5828–5833, 1999.
- [29] C. Tsang, R. E. F., Tsann Lin, D. E. Heim, V. S. Speriosu, B. A. Gurney, and M. L. Williams. Design, fabrication, and testing of spin-valve read heads for high density recording. *IEEE Transactions on Magnetism*, 30(6):3801–3806, 1994.
- [30] S. S. P. Parkin and D. Mauri. Spin engineering: Direct determination of the Ruderman-Kittler-Kasuya-Yosida far-field range function in ruthenium. *Physical Review B*, 44(13):7131–7134, 1991.
- [31] J. Daughton, J. Brown, E. Chen, R. Beech, A. Pohm, and W. Kude. Magnetic field sensors using GMR multilayer. *IEEE Transactions on Magnetism*, 30(6):4608–4610, 1994.
- [32] J. A. Borchers, R. W. Erwin, S. D. Berry, D. M. Lind, J. F. Ankner, E. Lochner, K. A. Shaw, and D. Hilton. Long-range magnetic order in  $\text{Fe}_3\text{O}_4/\text{NiO}$  superlattices. *Physical Review B*, 51(13):8276–8286, 1995.
- [33] W. L. Roth. Neutron and optical studies of domains in NiO. *Journal of Applied Physics*, 31(11):2000–2011, 1960.

- [34] G. A. Slack. Crystallography and domain walls in antiferromagnetic NiO crystals. *Journal of Applied Physics*, 31(9):1571–1582, 1960.
- [35] D. Spanke, V. Solinus, D. Knabben, F. U. Hillebrecht, F. Ciccacci, L. Gregoratti, and M. Marsi. Evidence for in-plane antiferromagnetic domains in ultrathin NiO films. *Physical Review B*, 58(9):5201–5204, 1998.
- [36] J. Baruchel. X-ray and neutron topographical of magnetic materials. *Physica B*, 192:79–93, 1993.
- [37] J. Stöhr, A. Scholl, J. Lüning, M. R. Scheinfein, H. A. Padmore, and R. L. White. Images of the antiferromagnetic structure of a NiO surface by means of x-ray magnetic linear dichroism spectromicroscopy. *Physical Review Letters*, 83(9):1862–1865, 1999.
- [38] A. Scholl, J. Stöhr, J. Lüning, J. W. Seo, J. Fompeyrine, H. Siegwart, J.-P. Locquet, F. Nolting, S. Anders, E. E. Fullerton, M. R. Scheinfein, and H. A. Padmore. Observation of antiferromagnetic domains in epitaxial thin films. *Science*, 287:1014–1016, 2000.
- [39] M. K. Wu, J. R. Ashburn, C. J. Torng, P. H. Hor, R. L. Meng, L. Gao, Z. J. Huang, Y. Q. Wang, and C. W. Chu. Superconductivity at 93 K in a new mixed-phase Y-Ba-Cu-O compound system at ambient pressure. *Physical Review Letters*, 58(9):908–910, 1987.
- [40] P. H. Hor, R. L. Meng, Y. Q. Wang, L. Gao, Z. J. Huang, J. Bechtold, K. Forster, and C. W. Chu. Superconductivity above 90 K in the square planar compound system  $\text{ABa}_2\text{Cu}_3\text{O}_{6+x}$  with  $\text{A}=\text{Y, La, Nd, Sm, Eu, Gd, Ho, Er, and Lu}$ . *Physical Review Letters*, 58(18):1891–1894, 1987.

- [41] K. Kitazawa, K. Kishio, H. Takagi, T. Hasegawa, S. Kanbe, S. Uchida, S. Tanaka, and K. Fueki. Superconductivity at 95 K in the new Yb-Ba-Cu oxide system. *Japanese Journal of Applied Physics*, 26:L339–L341, 1987.
- [42] J. M. Tarascon, W. R. McKinnon, L. H. Greene, G. W. Hull, and E. M. Vogel. Oxygen and rare-earth doping of the 90-K superconducting perovskite  $\text{YBa}_2\text{Cu}_3\text{O}_{7-x}$ . *Physical Review B*, 36(1):226–234, 1987.
- [43] E. A. Hayri, K. V. Ramanujachary, S. Li, M. Greenblatt, S. Simizu, and S. A. Friedberg. Superconductivity in the Ln-Ba-Cu-O (Ln=Y, Ho, Er). *Solid State Communications*, 64(2):217–226, 1987.
- [44] J. O. Willis, Z. Fisk, J. D. Thompson, S-W. Cheong, R. M. Aikin, J. L. Smith, and E. Zirngiebl. Superconductivity above 90 K in magnetic rare earth-barium-copper oxides. *Journal of Magnetism and Magnetic Materials*, 67:L139–L142, 1987.
- [45] D. W. Murphy, S. Sunshine, R. B. van Dover, R. J. Cava, B. Batlogg, S. M. Zahurak, and L. F. Schneemeyer. New superconducting cuprate perovskites. *Physical Review Letters*, 58(18):1888–1890, 1987.
- [46] M. B. Maple, Y. Dalichaouch, J. M. Ferreira, R. R. Hake, B. W. Lee, J. J. Neumeier, M. S. Torikachvili, K. N. Yang, H. Zhou, R. P. Guertin, and M. V. Kuric.  $\text{RBa}_2\text{Cu}_3\text{O}_{7-\delta}$  (R=rare earth) high- $T_c$  magnetic superconductors. *Physica B*, 148:155–162, 1987.
- [47] B. W. Lee, J. M. Ferreira, Y. Dalichaouch, M. S. Torikachvili, K. N. Yang, and M. B. Maple. Long-range magnetic ordering in the high- $T_c$  superconductors  $\text{RBa}_2\text{Cu}_3\text{O}_{7-\delta}$  (R = Nd, Sm, Gd, Dy and Er). *Physical Review B*, 37(4):2368–2371, 1988.

- [48] J. W. Lynn, T. W. Clinton, W-H. Li, R. W. Erwin, J. Z. Liu, K. Vandervoort, and R. N. Shelton. 2D and 3D magnetic behavior of Er in  $\text{ErBa}_2\text{Cu}_3\text{O}_7$ . *Physical Review Letters*, 63(23):2606–2609, 1989.
- [49] K. De’Bell and J. P. Whitehead. The dipole-dipole contribution to the magnetic propagator in the  $\text{REBa}_2\text{Cu}_3\text{O}_{7-\delta}$  compounds. *Journal of Physics : Condensed Matter*, 3:2431–2439, 1991.
- [50] K. De’Bell, A. B. MacIsaac, and J. P. Whitehead. Dipolar effects in magnetic thin films and quasi-two-dimensional systems. *Review of Modern Physics*, 72(1):225–257, 2000.
- [51] J. W. Lynn, W-H. Li, Q. Li, H. C. Ku, H. D. Yang, and R. N. Shelton. Magnetic fluctuations and two-dimensional ordering in  $\text{ErBa}_2\text{Cu}_3\text{O}_7$ . *Physical Review B*, 36(4):2374–2377, 1987.
- [52] J. W. Lynn. *High Temperature Superconductivity*. Springer-Verlag, New York, 1990.
- [53] T. W. Clinton and J. W. Lynn. Magnetic ordering of Er in powder and single crystals of  $\text{ErBa}_2\text{Cu}_3\text{O}_7$ . *Physica C*, 174:487–490, 1991.
- [54] J. W. Lynn. Two-dimensional behavior of the rare earth ordering in oxide superconductors. *Journal of Alloys and Compounds*, 181, 1992.
- [55] T. W. Clinton, J. W. Lynn, J. Z. Liu, Y. X. Jia, T. J. Goodwin, R. N. Shelton, B. W. Lee, M. Buchgeister, M. B. Maple, and J. L. Peng. Effects of oxygen on the magnetic order of the rare-earth ions in  $\text{RBa}_2\text{Cu}_3\text{O}_{6+x}$  (R=Dy, Er, Nd). *Physical Review B*, 51(21):15429–15447, 1995.
- [56] S. Skanthakumar and J. W. Lynn. Spin dynamics of  $\text{Er}^{3+}$  in  $\text{ErBa}_2\text{Cu}_3\text{O}_{7-\delta}$ . *Journal of Applied Physics*, 81(8):4934–4936, 1997.

- [57] T. W. Clinton and J. W. Lynn. Magnetic order of Dy in  $\text{DyBa}_2\text{Cu}_3\text{O}_7$ . *Journal of Applied Physics*, 70(10):5751–5753, 1991.
- [58] S. E. Brown, J. D. Thompson, J. O. Willis, R. M. Aikin, E. Zirngiebl, J. L. Smith, Z. Fisk, and R. B. Schwarz. Magnetic and superconducting properties of  $\text{RBa}_2\text{Cu}_3\text{O}_x$  compounds. *Physical Review B*, 36(4):2298–2300, 1987.
- [59] M. E. Reeves, D. S. Citrin, B. G. Pazol, T. A. Friedmann, and D. M. Ginsberg. Specific heat of  $\text{GdBa}_2\text{Cu}_3\text{O}_{7-\delta}$  in the normal and superconducting states. *Physical Review B*, 36(13):6915–6919, 1987.
- [60] B. D. Dunlap, M. Slaski, Z. Sungaila, D. G. Hinks, K. Zhang, C. Segre, S. K. Malik, and E. E. Alp. Magnetic ordering of Gd and Cu in superconducting and nonsuperconducting  $\text{GdBa}_2\text{Cu}_3\text{O}_{7-\delta}$ . *Physical Review B*, 37(1):592–594, 1988.
- [61] D. M. Paul, H. A. Mook, A. W. Hewat, B. C. Sales, L. A. Boatner, J. R. Thompson, and M. Mostoller. Magnetic ordering in the high-temperature superconductor  $\text{GdBa}_2\text{Cu}_3\text{O}_7$ . *Physical Review B*, 37:2341, 1988.
- [62] M. Knobel, L. C. Sampaio, E. H. C. P. Sinnecker, P. Vargas, and D. Altbir. Dipolar magnetic interactions among magnetic microwires. *Journal of Magnetism and Magnetic Materials*, 249:60–72, 2002.
- [63] L. C. Sampaio, R. Hyndman, F. S. de Menezes, J. P. Jamet, P. Meyer, J. Gierak, C. Chappert, V. Mathet, and J. Ferré. Power-law relaxation decay in two-dimensional arrays of magnetic dots interacting by long-range dipole-dipole interactions. *Physical Review B*, 64(18):184440(1)–184440(7), 2001.
- [64] R. P. Cowburn, A. O. Adeyeye, and M. E. Welland. Controlling magnetic ordering in coupled nanomagnet arrays. *New Journal of Physics*, 1(6):1–9, 1999.

- [65] R. P. Cowburn. Property variation with shape in magnetic nanoelements. *Journal of Physics D: Applied Physics*, 33:R1–R16, 2000.
- [66] M. Giersig and M. Hilgendorff. The preparation of ordered colloidal magnetic particles by magnetophoretic deposition. *Journal of Physics D: Applied Physics*, 32:L111–L113, 1999.
- [67] R. Hyndman, A. Mougin, L. C. Sampaio, J. Ferré, J. P. Jamet, P. Meyer, V. Mathet, C. Chappert, D. Mailly, and J. Gierak. Magnetization reversal in weakly coupled magnetic patterns. *Journal of Magnetism and Magnetic Materials*, 240:34–36, 2002.
- [68] E. H. C. P. Sinnecker, F. S. de Menezes, L. C. Sampaio, M. Konbel, and M. Vázquez. Tailoring coercivity in an array of glass-coated microwires. *Journal of Magnetism and Magnetic Materials*, 226-230:1467–1469, 2001.
- [69] M. Vázquez and A. Hernando. A soft magnetic wire for sensor applications. *Journal of Physics D*, 29:939–949, 1996.
- [70] H. Chiriac and T. A. Óvári. Amorphous glass-covered magnetic wires: Preparation, properties, applications. *Progress in Materials Science*, 40:333–407, 1996.
- [71] L. C. Sampaio, E. H. C. P. Sinnecker, G. R. C. Cernicchiaro, M. Knobel, M. Vázquez, and J. Velázquez. Magnetic microwires as macrospins in a long-range dipole-dipole interaction. *Physical Review B*, 61(13):8976–8983, 2000.
- [72] M. Hehn, K. Ounadjela, R. Ferré, W. Grange, and F. Rousseaux. Reorientational magnetic transition in mesoscopic cobalt dots. *Applied Physics Letters*, 71(19):2833–2835, 1997.
- [73] R. L. Stamps and R. E. Camley. Magnetization processes and reorientation transition for small magnetic dots. *Physical Review B*, 60(16):11694–11699, 1999.

- [74] W. Weber, C. H. Back, A. Bischof, D. Pescia, and R. Allenspach. Magnetic switching in cobalt films by adsorption of copper. *Nature*, 374(27):788–790, 1995.
- [75] J-J Weis. Simulation of quasi-two-dimensional dipolar systems. *Journal of Physics: condensed Matter*, 15:s1471–s1495, 2003.
- [76] B. M. McCoy and T. T. Wu. *The Two-dimensional Ising Model*. Harvard University Press, USA, 1973.
- [77] E. Ising. Beitrag zur theories des ferromagnetismus. *Zeitschrift für Physik*, 31(3-4):253–258, 1925.
- [78] L. Onsager. Crystal statistics. I. A two-dimensional model with an order-disorder transition. *Physical Review*, 65(3-4):117–149, 1944.
- [79] C. Herring and C. Kittel. On the theory of spin waves in ferromagnetic media. *Physical Review*, 81(5):869–880, 1951.
- [80] W. Döring. Über den ferromagnetismus des flächengitters. *Zeitschrift für Naturforschg*, 16a:1008–1016, 1961.
- [81] W. Döring. Die sättigungsmagnetisierung dünner schichten. *Zeitschrift für Naturforschg*, 16a:1146–1152, 1961.
- [82] A. Corciovei. Spin-wave theory of ferromagnetic thin films. *Physical Review*, 130(6):2223–2229, 1963.
- [83] A. B. MacIsaac, J. P. Whitehead, K. De’Bell, and K. S. Narayanan. Monte Carlo study of two-dimensional Ising dipolar antiferromagnets as a model for rare-earth ordering in the R-Ba-Cu-O compounds (R = rare earth). *Physical Review B*, 46(10):6387–6394, 1992.

- [84] A. Abanov, V. Kalatsky, V. L. Pokrovsky, and W. M. Saslow. Phase diagram of ultrathin ferromagnetic films with perpendicular anisotropy. *Physical Review B*, 51(2):1023–1038, 1995.
- [85] Y. Yafet and E. M. Gyorgy. Ferromagnetic strip domains in an atomic monolayer. *Physical Review B*, 38(13):9145–9151, 1988.
- [86] M. B. Taylor and B. L. Gyorffy. A ferromagnetic monolayer with model spin-orbit and dipole-dipole interactions. *Journal of Physics : Condensed Matter*, 5:4527–4540, 1993.
- [87] T. Garel and S. Doniach. Phase transitions with spontaneous modulation- the dipolar Ising ferromagnet. *Physical Review B*, 26(1):325–329, 1982.
- [88] B. Kaplan and G. A. Gehring. The domain structure in ultrathin magnetic films. *Journal of Magnetism and Magnetic Materials*, 128:111–116, 1993.
- [89] A. B. MacIsaac, J. P. Whitehead, M. C. Robinson, and K. De’Bell. Striped phases in two-dimensional dipolar ferromagnets. *Physical Review B*, 51(22):16033–16045, 1995.
- [90] J. P. Whitehead and K. De’Bell. Stability of striped phases in two-dimensional dipolar systems. *Journal of Physics: Condensed Matter*, 6:L731–L734, 1994.
- [91] A. B. Kashuba and V. L. Pokrovsky. Stripe domain structures in a thin ferromagnetic film. *Physical Review B*, 48(14):10335–10344, 1993.
- [92] I. Booth, A. B. MacIsaac, J. P. Whitehead, and K. De’Bell. Domain structures in ultrathin magnetic films. *Physical Review Letters*, 75(5):950–953, 1995.
- [93] L. C. Sampaio, M. P. Albuquerque, and F. S. de Menezes. Magnetic relaxation and formation of magnetic domains in ultrathin films with perpendicular anisotropy. *Physical Review B*, 54(9):6465–6472, 1996.

- [94] A. Kashuba and V. L. Pokrovsky. Stripe domain structures in a thin ferromagnetic film. *Physical Review Letters*, 70(20):3155–3158, 1993.
- [95] M. Seul and R. Wolfe. Evolution of disorder in two-dimensional stripe patterns: “Smectic” instabilities and disinclination unbinding. *Physical Review Letters*, 68(16):2460–2463, 1992.
- [96] C. S. Arnold and D. Venus. Evidence for domain-condensation near the ferromagnetic to paramagnetic transition in the perpendicularly magnetized ultrathin Fe/2 ML Ni/W(110) films. *IEEE Transactions on Magnetics*, 34(4):1039–1041, 1998.
- [97] S. Simizu, S. A. Friedberg, E. A. Hayri, and M. Greenblatt. Low-dimensional magnetism in the high- $T_c$  superconductor  $LBa_2Cu_3O_{7-y}$  ( $L=Gd, Ho, Er$ ): Heat-capacity study. *Physical Review B*, 36(13):7129–7132, 1987.
- [98] Y. Nakazawa, M. Ishikawa, and T. Takabatake. Low-temperature specific heat of orthorhombic and tetragonal phases of  $Ba_2(RE)Cu_3O_{7-\delta}$  ( $RE=Gd, Dy, Ho, Er$  and  $Tm$ ). *Physica B*, 148:404–407, 1987.
- [99] M. W. Dirken and L. J. de Jongh. Magnetic specific heat of  $Dy^{3+}$  in  $DyBa_2Cu_3O_{7-\delta}$  compared to the 2-d,  $S=1/2$  Ising model prediction. *Solid State Communications*, 64(9):1201–1202, 1987.
- [100] J. van den Berg, C. J. van der Beek, P. H. Kes, J. A. Mydosh, G. J. Nieuwenhuys, and L. J. de Jongh. Superconductivity and 2-dimensional magnetism in orthorhombic and tetragonal  $GdBa_2Cu_3O_{7-\delta}$ . *Solid State Communications*, 64(5):699–703, 1987.
- [101] F. Bloch. Zur theorie des ferromagnetismus. *Zeitschrift für Physik*, 49:206–219, 1928.

- [102] N. D. Mermin and H. Wagner. Absence of ferromagnetism or antiferromagnetism in one- or two-dimensional isotropic Heisenberg models. *Physical Review Letters*, 17(22):1133–1136, 1966.
- [103] J. M. Kosterlitz and D. J. Thouless. Ordering, metastability and phase transitions in two-dimensional systems. *Journal of Physics C: Solid State Physics*, 6:1181–1203, 1973.
- [104] J. M. Kosterlitz. The critical properties of the two-dimensional xy-model. *Journal of Physics C: Solid State Physics*, 7:1046–1060, 1974.
- [105] P. Butera and M. Comi. Quantitative study of the Kosterlitz-Thouless phase transition in a system of two-dimensional plane rotators (XY model): High-temperature expansions to order  $\beta^{20}$ . *Physical Review B*, 47(18):11969–11979, 1993.
- [106] J. F. Fernández, M. F. Ferreira, and J. Stankiewicz. Critical behavior of the two-dimensional XY model: A Monte Carlo simulation. *Physical Review B*, 34(1):292–300, 1986.
- [107] R. Gupta, J. DeLapp, G. G. Batrouni, G. C. Fox, C. F. Baillie, and J. Apostolakis. Phase transition in the 2D XY model. *Physical Review Letters*, 61(17):1996–1999, 1988.
- [108] M. E. Fisher, S. Ma, and B. G. Nickel. Critical exponents for long-range interactions. *Physical Review Letters*, 29(14):917–920, 1972.
- [109] A. Carbognani, E. Rastelli, S. Regina, and A. Tassi. Dipolar interaction and long-range in the square planar rotator model. *Physical Review B*, 62(2):1015–1021, 2000.
- [110] S. Romano. Two-dimensional-lattice spin models with long-range antiferromagnetic interactions. *Physical Review B*, 44(13):7066–7069, 1991.

- [111] E. Rastelli, A. Carbognani, S. Regina, and A. Tassi. Long range order in two-dimensional spin models with long range interactions. *Journal of Applied Physics*, 85(8):6082–6084, 1999.
- [112] P. I. Belobrov, R S. Gekht, and V. A. Ignatchenko. Ground state in systems with dipole interaction. *Soviet Physics JETP*, 57(3):636–642, 1983.
- [113] J. M. Luttinger and L. Tisza. Theory of dipole interaction in crystals. *Physical Review*, 70(11-12):954–964, 1946.
- [114] G. O. Zimmerman, A. K. Ibrahim, and F. Y. Wu. Planar classical dipolar system on a honeycomb lattice. *Physical Review B*, 37(4):2059–2065, 1988.
- [115] C. L. Henley. Ordering by disorder: Ground-state selection in fcc vector antiferromagnets. *Journal of Applied Physics*, 61(8):3962–3964, 1987.
- [116] C. L. Henley. Ordering due to disorder in a frustrated vector antiferromagnet. *Physical Review Letters*, 62(17):2056–2059, 1989.
- [117] S. Prakash and C. L. Henley. Ordering due to disorder in dipolar magnets on two-dimensional lattices. *Physical Review B*, 42(10):6574–6589, 1990.
- [118] K. De’Bell, A. B. MacIsaac, I. N. Booth, and J. P. Whitehead. Dipolar-induced planar anisotropy in ultrathin magnetic films. *Physical Review B*, 55(22):15108–15118, 1997.
- [119] E. Rastelli, A. Carbognani, S. Regina, and A. Tassi. Order by thermal disorder in 2D planar rotator model with dipolar interaction. *The European Physical Journal B*, 9:641–649, 1999.
- [120] J. P. Whitehead. Spin wave renormalization and thermally induced order in two-dimensional dipolar systems. *Physics Essays*, 9(4):609–616, 1996.

- [121] E. Rastelli, S. Regina, A. Tassi, and A. Carbognani. Long-range isotropic and dipolar spin-spin interactions in the square planar rotator model. *Physical Review B*, 65(9):094412(1)–094412(16), 2002.
- [122] M. Bander and D. L. Mills. Ferromagnetism of ultrathin films. *Physical Review B*, 38(16):12015–12018, 1988.
- [123] R. P. Erickson and D. L. Mills. Anisotropy-driven long-range order in ultrathin ferromagnetic films. *Physical Review B*, 43(13):11527–11530, 1991.
- [124] S. V. Maleev. Dipole forces in two-dimensional and layered ferromagnets. *Soviet Physics JETP*, 43(6):1240–1247, 1976.
- [125] C. Pich and F. Schwabl. Order of two-dimensional isotropic dipolar antiferromagnets. *Physical Review B*, 47(13):7957–7960, 1993.
- [126] D. Pescia and V. L. Pokrovsky. Perpendicular versus in-plane magnetization in a 2D Heisenberg monolayer at finite temperatures. *Physical Review Letters*, 65(20):2599–2601, 1990.
- [127] P. Politi, A. Rettori, and M. G. Pini. Comment on “perpendicular versus in-plane magnetization in a 2D Heisenberg monolayer at finite temperatures”. *Physical Review Letters*, 70(8):1183–1183, 1993.
- [128] A. P. Levanyuk and N. Garcia. Comment on “Perpendicular versus in-plane magnetization in a 2D Heisenberg monolayer at finite temperatures”. *Physical Review Letters*, 70(8):1184–1184, 1993.
- [129] K. Ried, Y. Millev, M. Fähnle, and H. Kronmüller. Phase transitions in ferromagnets with dipolar interactions and uniaxial anisotropy. *Physical Review B*, 51(21):15229–15249, 1995.

- [130] A. Moschel and K. D. Usadel. Influence of the dipole interaction on the direction of the magnetization in thin ferromagnetic films. *Physical Review B*, 49(18):12868–12871, 1994.
- [131] A. Moschel and K. D. Usadel. Reorientation transitions of first and second order in thin ferromagnetic films. *Physical Review B*, 51(22):16111–16114, 1995.
- [132] A. Moschel and K. D. Usadel. Influence of the film thickness on the direction of the magnetization in thin ferromagnetic films. *Journal of Magnetism and Magnetic Materials*, 140-144:649–650, 1995.
- [133] A. Hucht and K. D. Usadel. Reorientation transition of ultrathin ferromagnetic films. *Physical Review B*, 55(18):12309–12312, 1997.
- [134] K. D. Usadel and A. Hucht. Anisotropy of ultrathin ferromagnetic films and the spin reorientation transition. *Physical Review B*, 66(2):024419(1)–024419(6), 2002.
- [135] S. T. Chui. Phase boundaries in ultrathin magnetic films. *Physical Review B*, 50(17):12559–12567, 1994.
- [136] A. Hucht, A. Moschel, and K. D. Usadel. Monte-Carlo study of the reorientation transition in Heisenberg models with dipole interactions. *Journal of Magnetism and Magnetic Materials*, 148:32–33, 1995.
- [137] A. Hucht and K. D. Usadel. Characterization of the reorientation transition in classical Heisenberg models with dipole interaction. *Journal of Magnetism and Magnetic Materials*, 156:423–424, 1996.
- [138] E. Y. Vedmedenko, H. P. Oepen, and J. Kirschner. Microstructure of the spin reorientation transition in second-order approximation of magnetic anisotropy. *Physical Review B*, 66(21):214401(1)–214401(5), 2002.

- [139] L. Ying, C. Nanxian, Z. Hongmin, and W. Chengwen. Monte Carlo simulation of the reorientation transition in Heisenberg model with dipolar interactions. *Solid state Communications*, 126:223–227, 2003.
- [140] J. A. C. Bland, C. Daboo, G. A. Gehring, B. Kaplan, A. J. R. Ives, R. J. Hicken, and A. D. Johnson. Magnetization of ultrathin ferromagnetic films at finite temperatures. *Journal of Physics: Condensed Matter*, 7:6467–6476, 1995.
- [141] Y. Yafet, J. Kwo, and E. M. Gyorgy. Dipole-dipole interactions and two-dimensional magnetism. *Physical Review B*, 33(9):6519–6522, 1986.
- [142] R. L. Stamps and B. Hillebrands. Dipolar interactions and the magnetic behavior of two-dimensional ferromagnetic systems. *Physical Review B*, 44(22):12417–12423, 1991.
- [143] P. Bruno. Spin-wave theory of two-dimensional ferromagnets in the presence of dipolar interactions and magnetocrystalline anisotropy. *Physical Review B*, 43(7):6015–6021, 1991.
- [144] A. B. MacIsaac, J. P. Whitehead, K. De’Bell, and P. H. Poole. Phase diagram for a magnetic thin film with dipolar interactions and magnetic surface anisotropy. *Physical Review Letters*, 77(4):739–742, 1996.
- [145] P. J. Jensen and K. H. Bennemann. Direction of the magnetization of thin films and sandwiches as a function of temperature. *Physical Review B*, 42(1):849–855, 1990.
- [146] P. J. Jensen and K. H. Bennemann. On direction of the magnetization of thin films and sandwiches as a function of temperature-II. *Solid State Communications*, 83(12):1057–1059, 1992.

- [147] P. Bruno. Tight-binding approach to the orbital magnetic moment and magnetocrystalline anisotropy of transition-metal monolayers. *Physical Review B*, 39(1):865–868, 1989.
- [148] L.Szunyogh, B. Újfalussy, and P. Weinberger. Magnetic anisotropy of iron multilayers on Au (001): First-principles calculations in terms of the fully relativistic spin-polarized screened KKR method. *Physical Review B*, 51(15):9552–9559, 1995.
- [149] A. Lessard, T. H. Moos, and W. Hübner. Magnetocrystalline anisotropy energy of transition-metal thin films: A nonperturbative theory. *Physical Review B*, 56(5):2594–2604, 1997.
- [150] S. Müller, P. Bayer, C. Reischl, K. Heinz, B. Feldmann, H. Zillgen, and M. Wuttig. Structural instability of ferromagnetic fcc Fe films on Cu(100). *Physical Review Letters*, 74(5):765–768, 1995.
- [151] M. Zharnikov, A. Dittschar, W. Kuch, C. M. Schneider, and J. Kirschner. Magnetic order-disorder transition mediated by a temperature-driven structural transformation. *Physical Review Letters*, 76(24):4620–4623, 1996.
- [152] C. Pich and F. Schwabl. Néel temperature for quasi-two-dimensional dipolar antiferromagnets. *Physical Review B*, 49(1):413–416, 1994.
- [153] D. S. Deng, X. F. Jin, and Ruibao Tao. Antiferromagnetic domains in a two-dimensional Heisenberg square lattice. *Physical Review B*, 65(13):132406(1)–132406(4), 2002.
- [154] D. Schmalz, R. Richter, and J. Schulenburg. Ground-state phases in a system of two competing square-lattice Heisenberg antiferromagnets. *Journal of Physics: Condensed Matter*, 15:2667–2679, 2003.

- [155] A. B. MacIsaac. Monte Carlo study of the two-dimensional dipolar Ising model. Master's thesis, Memorial University, 1992.
- [156] A. B. MacIsaac. *The magnetic properties of a model two-dimensional dipolar thin film*. PhD thesis, Memorial University, 1997.
- [157] A. M. Abu-Labdeh, J. P. Whitehead, K. De'Bell, and A. B. MacIsaac. Phase behavior of antiferromagnetic ultrathin magnetic films. *Physical Review B*, 65(2):24434(1)–24434(10), 2001.
- [158] A. M. Abu-Labdeh, N. P. Chafe, J. P. Whitehead, K. De'Bell, and A. B. MacIsaac. Phase behaviour of the antiferromagnetic plane rotator model. *Journal of Physics: Condensed Matter*, 14:7155–7163, 2002.
- [159] A. M. Abu-Labdeh, J. P. Whitehead, K. De'Bell, and A. B. MacIsaac. Evidence for a reorientation transition in the phase behaviour of a two-dimensional dipolar antiferromagnet. *Journal of Physics: Condensed Matter*, *To be published*, 2003.
- [160] N. Goldenfeld. *Lectures on phase transitions and the renormalization group*. Addison-Wesley Publishing Company, Reading, 1st edition, 1993.
- [161] N. W. Ashcroft and N. D. Mermin. *Solid state physics*. Holt, Rinehart and Winston, Orlando, 1976.
- [162] Charles Kittel. *Introduction to solid state physics*. John Wiley and Sons, New York, 1986.
- [163] D. H. Martin. *Magnetism in solids*. M.I.T. Press, 1967.
- [164] L. Néel. L'approche a la saturation de la magnétostriction. *Journal de physique*, 15:376–378, 1954.

- [165] J. G. Gay and Roy Richter. Spin anisotropy of ferromagnetic films. *Physical Review Letters*, 56(25):2728–2731, 1986.
- [166] R. Lorenz and J. Hafner. Uniaxial and planar magnetic anisotropy of thin transition-metal films. *Journal of Physics: Condensed matter*, 7:L253–L259, 1995.
- [167] K. De’Bell and J. P. Whitehead. Crystalline electric fields in  $\text{ErBa}_2\text{Cu}_3\text{O}_{7-\delta}$  and  $\text{DyBa}_2\text{Cu}_3\text{O}_{7-\delta}$ . *Physica B*, 194-196:179–180, 1994.
- [168] M. T. Hutchings. Point-charge calculations of energy levels of magnetic ions in crystalline electric fields. In F. Seitz and D. Turnbull, editors, *Solid state physics*, volume 16, pages 227–273. Academic, New York, 1964.
- [169] Amnon Aharony and Michael E. Fisher. Critical behavior of magnets with dipolar interaction. I. Renormalisation group near four dimensions. *Physical Review B*, 8(7):3323–3341, 1973.
- [170] M. E. Fisher and Amnon Aharony. Dipolar interactions at ferromagnetic critical points. *Physics Review Letters*, 30(12):559–562, 1973.
- [171] N. M. Fujiki, K. De’Bell, and D. J. W. Geldart. Lattice sums for dipolar systems. *Physical Review B*, 36(16):8512–8516, 1987.
- [172] D. P. Landau and K. Binder. *A guide to Monte Carlo simulations in statistical physics*. Cambridge University Press, Cambridge, 2000.
- [173] M. E. J. Newman and G. T. Barkma. *Monte Carlo methods in statistical physics*. Clarendon Press, Oxford, 1999.
- [174] V. M. Bedanov. Long-range order in a classical two-dimensional dipole system. *Journal of Physics: Condensed Matter*, 4:75–82, 1992.

- [175] K. Binder and D. W. Heermann. *Monte Carlo simulation in statistical physics*. Springer-Verlag, Berlin, second corrected edition, 1993.
- [176] K. Binder. Introduction: Theory and “technical” aspects of Monte Carlo simulations. In K. Binder, editor, *Monte Carlo Methods in Statistical Physics*, pages 1–46. Springer-Verlag, Berlin, 1979.
- [177] C. Bowen, D. L. Hunter, and N. Jan. Monte Carlo simulation of the two-dimensional planar model. *Journal of Statistical Physics*, 69(5-6):1097–1113, 1992.
- [178] N. Metropolis, A. W. Rosenbluth, M. N. Rosenbluth, A. H. Teller, and E. Teller. Equation of state calculations by fast computing machines. *The Journal of Chemical Physics*, 21(6):1087–1092, 1953.
- [179] K. Binder and D. W. Heermann. *Monte Carlo simulation in statistical physics*. Springer-Verlag, Berlin, fourth edition, 2002.
- [180] M. N. Barber. Finite size scaling. In C. Domb and J. L. Lebowitz, editors, *Phase transitions and critical phenomena*, volume 8. Academic Press, New York, 1983.
- [181] V. Privman. *Finite size scaling and numerical simulation of statistical systems*. World Scientific Publishing Co. Pte. Ltd., Singapore, 1st edition, 1990.
- [182] R. Kretschmer and K. Binder. Ordering and phase transitions in Ising systems with competing short range and dipolar interactions. *Z. Physik B.*, 34:375–392, 1979.
- [183] K. Binder and D. Stauffer. A simple introduction to Monte Carlo simulation and some specialized topics. In K. Binder, editor, *Applications of the Monte Carlo method in statistical physics*, pages 1–36. Springer-Verlag, Berlin, 1984.

- [184] R. W. Swendsen, J.-S. Wang, and A. M. Ferrenberg. New Monte Carlo methods for improved efficiency of computer simulations in statistical mechanics. In K. Binder, editor, *Topics in applied physics: The Monte Carlo method in condensed matter physics*, volume 71, pages 75–91. Springer-Verlag, Berlin, 1992.
- [185] G. M. Torrie and J. P. Valleau. Monte carlo free energy estimates using non-boltzmann sampling: Application to the sub-critical Lennard-Jones fluid. *Chemistry Physics Letter*, 28:578, 1974.
- [186] G. M. Torrie and J. P. Valleau. Nonphysical sampling distributions in Monte Carlo free-energy estimation: Umbrella sampling. *Journal of Computational Physics*, 23:187–199, 1977.
- [187] D. Frenkel and B. Smit. *Understanding molecular simulation*. Academic Press, USA, 1996.
- [188] M. E. Gouvêa, G. M. Wysin, S. A. Leonel, A. S. T. Pires, T. Kampeter, and F. G. Mertens. Low-temperature static and dynamic behavior of the two-dimensional easy-axis Heisenberg model. *Physical Review B*, 59(9):6229–6238, 1999.
- [189] L. R. Corruccini and Steven J. White. Dipolar antiferromagnetism in the spin-wave approximation. *Physical Review B*, 47(2):773–777, 1993.
- [190] E. Vescovo. (private communication). 2001.
- [191] S. Simizu, G. H. Bellesis, J. Lukin, S. A. Friedberg, H. S. Lessure, S. M. Fine, and M. Greenblatt. Low-dimensional magnetic ordering and Ising- and XY-like anisotropy of  $\text{Er}^{3+}$  in the system  $\text{ErBa}_2\text{Cu}_3\text{O}_x$  with  $6 < x < 7$ . *Physical Review B*, 39(13):9099–9107, 1989.
- [192] J. Villain, R. Bidaux, J-P. Carton, and R. Conte. Order as an effect of disorder. *Journal of Physics (France)*, 41:1263–1272, 1980.

- [193] C. L. Henley. Effective Hamiltonians and dilution effects in Kagome and related anti-ferromagnets. *Canada Journal of Physics*, 79:1307–1321, 2001.
- [194] L. Bellier-Castella, M. J. P. Gingras, P. C. W. Holdsworth, and R. Moessner. Frustrated order by disorder: The pyrochlore anti-ferromagnetic with bond disorder. *Canada Journal Physics*, 79:1365–1371, 2001.
- [195] J.W. Lynn, T. W. Clinton, W-H. Li, R. W. Erwin, J. Z. Liu, R.N. Shelton, and P. Klavins. Two-dimensional magnetic order of Er in  $\text{ErBa}_2\text{Cu}_3\text{O}_7$ . *Journal of Applied Physics*, 67(9), 1990.
- [196] P. Chafe. Magnetic thin films (summer research summary). 2001.





